UNIVERSITY OF CAMBRIDGE

Pathogenesis and Therapy of Mitochondrial Diseases

Pedro Filipe da Silva Pinheiro

This dissertation is submitted for the degree of Doctor of Philosophy
September 2021

MRC Mitochondrial Biology Unit

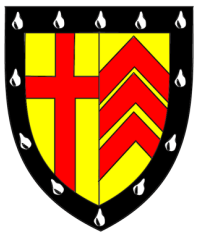

Mitochondrial Medicine Laboratory
&
Mitochondrial Genetics Laboratory

Clare College

Declaration

This dissertation describes the results of my own work, except for the experiments performed by collaborators, which are specified in the figure legends. The work was carried out at the Medical Research Council (MRC) Mitochondrial Biology Unit, under the supervision of Prof. Massimo Zeviani and Dr. Carlo Viscomi, between May 2017 and January 2020 and later under the supervision of Dr. Michal Minczuk between February 2020 and September 2021. Part of the work was also carried at the Department of Medical Biochemistry and Cell Biology at the University of Gothenburg, under the supervision of Prof. Maria Falkenberg between November 2018 and April 2019, as part of my individual training program from the Marie Sklodowska-Curie ITN-REMIX [721757].

This thesis has not been submitted, in whole or in part, for a degree at this or any other institution and the length of it does not exceed the prescribed word limit.

The results described in Chapter 4 led to a publication:
Silva-Pinheiro, Pedro, et al. "DNA polymerase gamma mutations that impair holoenzyme stability cause catalytic subunit depletion." Nucleic Acids Research 49.9 (2021): 5230-5248.

The results described in Chapter 5 led to a publication:
Silva-Pinheiro, Pedro, et al. "A Single Intravenous Injection of AAV-PHP.B-h*NDUFS4* Ameliorates the Phenotype of *Ndufs4*−/− Mice." Molecular Therapy-Methods & Clinical Development 17 (2020): 1071-1078.

Pedro Filipe da Silva Pinheiro,
Cambridge (UK), September 2021.

Abstract

Pedro Filipe da Silva Pinheiro

Pathogenesis and Therapy of Mitochondrial Diseases

Mitochondria are highly dynamic organelles found in most eukaryotic cells, with a fundamental role in the generation of cellular energy through oxidative phosphorylation (OXPHOS). Critical for their function, mitochondria have retained their own genome the mitochondrial DNA, mtDNA. In mammals, replication of mtDNA is ensured by the DNA polymerase POLγ, which is composed by one catalytic subunit POLγA and two accessory subunits POLγB.

Mutations in the nuclear-encoded *POLG* gene, coding for POLγA, are a common cause of human disease leading to a spectrum of disorders characterised by mtDNA instability, thus compromising mitochondrial function. Despite being relatively frequent, the molecular pathogenesis of *POLG*-related diseases is poorly understood and efficient treatments are missing, partly due to the lack of relevant *in vivo* models. Here, I describe the generation of two mouse models: 1) the *Polg*$^{A449T/A449T}$ mouse, which reproduces the A467T change, the most common human recessive mutation of *POLG* and 2) the *Polg*$^{WT/Y933C}$ mouse, which reproduces the Y955C change, the most common human dominant mutation of *POLG*. I focused on the use of the *Polg*$^{A449T/A449T}$ mouse and complementary *in vitro* techniques to provide insights into the molecular pathogenic mechanism of this *POLG* mutation. I describe the data showing that the mouse A449T mutation impairs DNA binding and mtDNA synthesis activities of POLγ, leading to a stalling phenotype. Most importantly, the A449T mutation also strongly impairs interaction with POLγB, the accessory subunit of the POLγ holoenzyme. This allows the free POLγA to become a substrate for LONP1 protease degradation, leading to dramatically reduced levels of POLγA in A449T mouse tissues, with consequences for the pathogenesis of the disease.

In the second part of the dissertation, I explore a gene therapy approach for mitochondrial diseases associated with mutations in nuclear-encoded genes. In particular, I test the use of a novel adeno-associated virus (AAV) capsid (PHP.B) as a gene therapy platform to ameliorate the neurological symptoms of a pre-clinical mouse model of mitochondrial disease, the *Ndufs4* knockout (*Ndufs4*$^{-/-}$) mouse. A single injection with AAV-PHP.B to express the human *NDUFS4* in *Ndufs4*$^{-/-}$ mice, improved lifespan, body weight gain, motor coordination and several molecular and histological features of the brain. These data provide promising proof-of-concept for the use of AAV-mediated gene therapy as a therapeutic option for the number of patients with, currently incurable, mitochondrial disease.

Acknowledgments

I would like to thank Massimo Zeviani and Carlo Viscomi for giving me the opportunity to carry my PhD studies under their expert supervision. In particular, I would like to thank Carlo for his time, patience and dedication in the lab during these last 4 years. I would also like to thank Michal Minczuk for welcoming me in his group and allowing me to conclude this work while providing exceptional support.

I would like to thank Maria Falkenberg for a very welcoming environment in her lab as part of my secondment, which greatly improved this work. Special thanks go to Carlos Pardo and Bertil Macao who supported me during my stay in Sweden.

Thanks goes to everyone in the Mitochondrial Medicine group which in one way or the other contributed to the development of this work. Special thanks go to Aurelio who shared his knowledge and assisted me with very "complicated" assays during this work. I would also like to thank Raffaele for his assistance in all histological analysis but more importantly, for being a good friend along the way and of course, for all the "nuts" provided which were important to perform this work.

Thanks go also to all my MBU friends and colleagues (they know who they are) who assisted me during the PhD and contributed to "watch the time fly" by providing a pleasant environment.

I am extremely grateful to all my family and friends back in Portugal for all their support, but in particularly I would like to thank my best other half, Ângela, who left everything behind to follow me in this adventure and made a lot easier to see Cambridge as the place I call "home". For that and everything else, thank you.

I dedicate this thesis to my loving Father Filipe, who I last hugged in the airport before flying to Cambridge for the first time. Despite knowing he would probably never see me again, he encouraged me to follow my dreams and ambitions. Wherever you are now, this one is for you!

Contents

Abbreviations

2D-AGE	Neutral two-dimensional agarose gel electrophoresis
AAP	Assembly activating protein
AAV	Adeno-associated virus
ADA	Adenosine deaminase
ADP	Adenosine diphosphate
AHS	Alpers-Huttenlocher syndrome
ALT	Alanine aminotransferase
ATP	Adenosine triphosphate
BBB	Blood-brain barrier
BNGE	Blue native PAGE
BrdU	Bromodeoxyuridine
BSA	Bovine serum albumin
CCl_4	Carbon Tetrachloride
CI	Mitochondrial complex I
CII	Mitochondrial complex II
CIII	Mitochondrial complex III
CIV	Mitochondrial complex IV
CLAMS	Comprehensive Lab Animal Monitoring System
ClpXP	Caseinolytic peptidase XP
CMV	Cytomegalovirus (promoter)
CN	Catalogue number
CNS	Central nervous system
CoA	Coenzyme A
CoQ	Coenzyme Q
COX	Cytochrome C Oxidase
CPEO	Chronic progressive external ophthalmoplegia
CPTs	Carnitine palmitoyltransferases
CS	Citrate synthase
CSBs	Conserved sequence blocks
CSF	Cerebrospinal fluid
CV	Mitochondrial complex V
D-loop	Displacement-loop
DAB	Diaminobenzidine
ddC	2',3'-dideoxycytidine
dg	Diploid genome
DMEM	Dulbecco's Modified Eagle Medium
dNTP	Deoxynucleoside triphosphate
DPX	Dibutylphthalate polystyrene xylene
dsDNA	double-stranded DNA
DTNB	5-dithio-bis-(2)-nitrobenzoic acid
EdU	5-ethynyl-2′-deoxyuridine
EMSA	Electrophoresis Mobility Shift Assay
ES	Embryonic stem
EtBr	Ethidium Bromide
ETC	Electron transport chain

FACS	Fluorescence-activated cell sorting
$FADH_2$	Flavine adenine dinucleotide (reduced)
FAO	Fatty Acid β-Oxidation
FBS	Fetal bovine serum
Fe/S	Heme and iron-sulphur (clusters)
FEN1	Flap endonuclease 1
Fw	Forward
GFP	Green fluorescent protein
gRNA	Guide RNA
GTP	Guanosine triphosphate
H&E	Hematoxylin and eosin
HDR	Homology directed repair
HSP	H-strand promoter
ICC	Immunocytochemistry
IGA	In-Gel Activity
IHC	Immunohistochemistry
IMM	Inner mitochondrial membrane
IMS	Intermembrane space
ITRs	Inverted terminal repeats
LHON	Leber's hereditary optic neuropathy
LONP1	Lon peptidase 1
LSP	L-strand promoter
LY6A	Lymphocyte antigen 6 complex, locus A
MCHS	Myocerebrohepatopathy spectrum
MEFs	Mouse embryonic fibroblasts
MELAS	Mitochondrial encephalopathy, lactic acidosis, and stroke-like episodes
MEMSA	Myoclonic epilepsy myopathy sensory ataxia
MGME1	Mitochondrial genome maintenance exonuclease 1
MNGIE	Mitochondrial neuro-gastro-intestinal leukoencephalopathy
MOMP	Mitochondrial outer membrane permeabilisation
MRC	Mitochondrial respiratory complex
mtDNA	Mitochondrial DNA
MTERF1	Mitochondrial termination factor 1
MTS	Mitochondrial targeting sequence
mtSSB	Mitochondrial single-stranded DNA-binding protein
NADH	Nicotinamide adenine dinucleotide
NADH	Nicotinamide adenine dinucleotide
NBF	Neutral buffered formalin
NBT	Nitroblue tetrazolium
NCR	Non-coding region (in the mitochondrial DNA)
nDNA	Nuclear DNA
Ndufs4	NADH dehydrogenase ubiquinone iron-sulphur protein 4
NHEJ	Non-homologous end joining
NRTIs	Nucleoside reverse transcriptase inhibitors
nt	Nucleotide(s)
NUMTs	Nuclear mitochondrial DNAs

OCT	Optimal cutting temperature compound
OMM	Outer mitochondrial membrane
OriH	H-strand replication
OriL	L-strand replication
OTC	Ornithine transcarbamylase
OXPHOS	Oxidative phosphorylation
PCR	Polymerase Chain Reaction
PFA	Paraformaldehyde
PG	Pathogreen staining
Pi	Inorganic phosphate
PKA	cAMP-dependent protein kinase
PMF	Proton-motive force
POLRMT	Mitochondrial DNA-dependent RNA polymerase
POLγ	DNA polymerase γ
RER	Respiratory exchange ratio
RFLP	Restriction fragment length polymorphism
RIs	Replication intermediates (mitochondrial)
RITOLS	Ribonucleotide incorporation throughout the lagging strand
ROS	Reactive oxygen species
rRNAs	Ribosomal RNAs
RT	Room temperature or Reverse transcription
Rv	Reverse
SAM	Sorting and assembly machinery
SANDO	Sensory ataxia neuropathy with dysarthria and ophthalmoplegia
SCAE	Spinocerebellar ataxia with epilepsy
SD	Standard deviation
SDH	Succinate dehydrogenase
SDS-PAGE	Sodium Dodecyl Sulfate Polyacrilamide Gel Electrophoresis
SEM	Standard error of mean
SKM	Skeletal muscle
ssDNA	single-stranded DNA
TAS	Termination-associated sequences
TCA	Tricarboxylic acid cycle
TEFM	Mitochondrial transcription elongation factor
TFAM	Mitochondrial transcription factor A
TFB2M	Mitochondrial transcription factor B2
TIM	Translocase of the inner membrane
TNB	Thionitrobenzoic acid
TOM	Translocase of the outer membrane
TOP1mt	Mitochondrial topoisomerase I
TP	Thymidine phosphorylase
tRNAs	Transfer RNAs
UCPs	Uncoupler proteins
URFs	Unidentified reading frames
v/v	volume/volume
VCO_2	Volume of carbon dioxide produced

VDAC	Voltage-dependent anion channel
vg	Viral genomes
VO_2	Volume of oxygen consumed
VPA	Valproic acid / Valproate
w/v	weight/volume
WES	Whole exome sequencing
WT	Wild-type
$\Delta\psi_M$	Mitochondrial membrane potential

Chapter 1 Introduction

1. Introduction

Mitochondria are highly dynamic organelles found in almost all eukaryotic cells, where they play a fundamental role in energy metabolism, biosynthesis of cellular components and signalling pathways. They produce most of cellular energy through oxidative phosphorylation (OXPHOS), the central set of reactions involved in ATP production (Vafai and Mootha, 2012).

Throughout evolution, mitochondria have retained their own genome (mitochondrial DNA, mtDNA), which encodes for 13 polypeptides of the OXPHOS system, as well as the 12S and 16S ribosomal RNAs (rRNAs) and the 22 transfer RNAs (tRNAs) necessary to translate them. Since mtDNA only encodes 13 proteins from over 1000 proteins present in mitochondria, 99% of the mitochondrial proteins are encoded by nuclear DNA (nDNA) and actively imported to create a functional organelle (Pearce et al., 2017). This sets mitochondrial homeostasis under a double genetic control of both nDNA and mtDNA. Therefore, disruptive mutations in any of the genes encoding mitochondrial proteins can lead to mitochondrial dysfunction and, consequently, to disease. Such group of disorders are collectively known as mitochondrial diseases.

1.1. Mitochondria in Animals

1.1.1. Mitochondria discovery and origins

Mitochondria were first described in 1890 by Richard Altmann, who recognised the ubiquitous presence of an organelle in eukaryotic cells, initially terming them “bioblasts”, and concluded that they were self-replicating "elementary organisms" within cells that carried out vital cellular functions (Altmann, 1894). The name “mitochondrion” was later introduced by Carl Benda in 1898, derived from “mitos” (“thread”) and “chondros” (“granule”), denoting the appearance of these structures by light microscopy as “threads dotted with grains” (Benda, 1898, Ernster and Schatz, 1981)

The phylogenetic roots of mitochondria trace back to an α-proteobacterium (Yang et al., 1985, Andersson et al., 1998), which during an endosymbiotic event blended

with an archaeal host cell more than 1.5 billion years ago (Sicheritz-Ponten et al., 1998). The idea that eukaryotic cellular organelles may have their origins in an ancient bacterial symbiosis was proposed over a hundred years ago (Mereschkowsky, 1905), however the theory only received broadened consideration in the 1960s giving rise to the "endosymbiotic theory" (Sagan, 1967).

The endosymbiotic theory (Sagan, 1967), and its proposed derivations between the 1970s and the 1990s, suggests that an anaerobic, early eukaryotic cell (Cavalier-Smith, 1987) engulfed a free-living, oxygen-consuming α-proteobacterium by phagocytosis (Doolittle, 1998), which escaped digestion and formed a mutually advantageous relationship with the host in an atmosphere with increasing levels of oxygen (Lane and Martin, 2010).

However, a new hypothesis based on studies of comparative biochemistry of energy metabolism, instead suggests that eukaryotes have arisen from the beneficial exchange of hydrogen between an anaerobic, hydrogen-dependent archaebacterium (host) cell and an α-proteobacterial (symbiont) facultative anaerobe, which synthesised hydrogen by fermentation and could also respire aerobically in the presence of oxygen (Martin and Muller, 1998, Koonin, 2010). In this "hydrogen hypothesis" (Martin and Muller, 1998), the endosymbiont supplied the host with the necessary hydrogen for its metabolism, and in turn, the host provided a safe environment to the mitochondrial ancestor. In addition, the hypothesis is supported by the finding that the Proterozoic ocean was mostly anoxic when eukaryotes developed (Mentel and Martin, 2008), and that mitochondria share the majority of their genes with hydrogenosomes (Embley and Martin, 2006), mitochondria-like organelles that generate hydrogen as a by-product of ATP synthesis (Lindmark and Muller, 1973). However, such theory implies that both aerobic and anaerobic metabolic pathways originated from the same bacterial symbiont, which is still under debate (Hug et al., 2010).

Nevertheless, it is unquestionable that mitochondria have been at the centre of the evolutionary transition from prokaryotes to eukaryotes and a core driver of the vast biodiversity present today.

1.1.2. Structure of mitochondria

Mitochondria were seen for decades as "threads dotted with grains", until the development of electron microscopy, in the 1950s, allowed for the first high-resolution images of the internal mitochondrial structure (Palade, 1953, Sjostrand, 1953).

Mitochondria are structurally delimited by two separate and functionally distinct membranes: the outer mitochondrial membrane (OMM) and the inner mitochondrial membrane (IMM) (Kuhlbrandt, 2015). The OMM defines the external barrier between the cytoplasm and the inside of the mitochondria, while the IMM constitutes an internal barrier that encapsulates the mitochondrial matrix, presenting a high number of invaginations known as cristae. The aqueous space between the OMM and IMM is denoted the intermembrane space (IMS) (Figure 1.1).

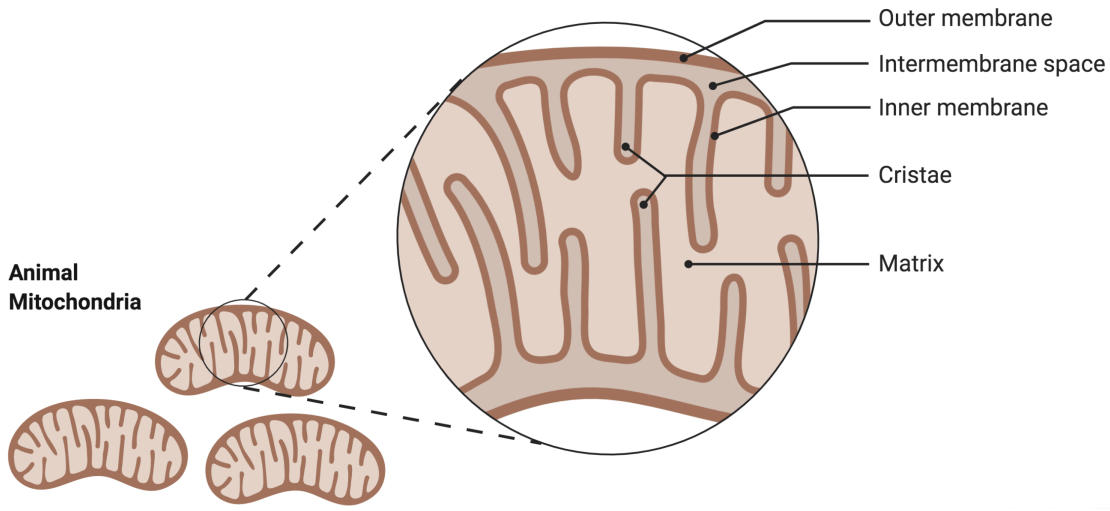

Figure 1.1. Animal mitochondria structure.
Schematic representation of animal mitochondria and its structure: Outer membrane; Intermembrane space; Inner membrane; Cristae; Matrix. Created with BioRender.com.

In support to the endosymbiotic origin of the organelle, the OMM is more similar in lipid composition to eukaryotic cell membranes, while the IMM resembles the cardiolipin-containing bacterial membranes (Cavalier-Smith, 2006). The two membranes also differ considerably in their permeability characteristics. The

OMM presents a high number of proteins called voltage-dependent anion channel (VDAC). These proteins are involved in the assembly of transmembrane aqueous channels that enables ions and other small molecules to get inside the mitochondria (Shoshan-Barmatz et al., 2010). In contrast, the IMM constitutes a very effective impermeable barrier, being permeable only to oxygen, carbon dioxide and water. The import, export or exchange of specific substrates and reaction products through the IMM is therefore accomplished by a sophisticated set of mitochondrial protein carriers embedded within the IMM (Kunji, 2004). The tightly regulated control of the permeability of the IMM is especially important in the formation of an electrochemical gradient across the membrane, which is necessary for production of adenosine triphosphate (ATP), the energy currency of the cell (discussed in detail in Section 1.1.3) (Nicholls, 1974).

The human mitochondrial proteome consists of over a thousand proteins (Pagliarini et al., 2008). Most of these proteins are encoded in the nucleus, translated by cytosolic ribosomes and actively imported to mitochondria with the assistance of a mitochondrial targeting sequence (MTS) (Wiedemann and Pfanner, 2017). The MTS is found at the N-terminus end of the protein and consist of a 10-70 amino acid long peptide with alternating pattern of hydrophobic and positively charged amino acids, forming an amphipathic helix (Bolender et al., 2008, Brix et al., 1997). Cleavage of the MTS is necessary to form the mature mitochondrial protein and is carried by specific peptidases and proteases with an essential role in mitochondrial homeostasis (Wiedemann and Pfanner, 2017).

Nuclear-encoded mitochondrial proteins cross the OMM through the translocase of the outer membrane (TOM) complex, and, depending upon the nature of the MTS, they may be directed to the mitochondrial matrix or into the OMM, IMM or IMS by other translocases and assembly machineries (Wiedemann et al., 2004). For example, the sorting and assembly machinery (SAM) complex regulates the insertion and assembly of β-barrel proteins directed to the OMM (Darshi et al., 2011). The IMM also contains its own protein import machinery for proteins that must be inserted in the IMM or imported into the mitochondrial matrix. Such task

is accomplished by the translocase of the inner membrane (TIM) complexes TIM22 and TIM23, respectively (Sirrenberg et al., 1996, Demishtein-Zohary et al., 2017).

Modern imaging techniques have revealed that mitochondria, once believed to exist individually throughout the cytosol, are instead dynamic organelles that form a highly-connected network (Tilokani et al., 2018). Such mitochondrial network is a reflection of the opposing processes of fission, division of one organelle into two, and fusion, the combination of two organelles into one (Koshiba et al., 2004). The constant interplay between fusion and fission is tightly controlled by a specialised family of dynamin-like GTPases (Hoppins et al., 2007), that favour one or the other according to cellular energy needs, or to adjust to specific cellular signals. Fusion permits the equilibration of mtDNA, proteins or metabolites when resources are low and is often correlated with mechanisms of defence to increase cell survival. In turn, fission is associated normally with mitochondrial dysfunction and cell death but is also vital for regular cellular processes such as mitochondrial distribution/trafficking or to isolate damaged mitochondria from the network and target them for degradation through selective autophagy, known as mitophagy (Pickles et al., 2018).

Mitochondria exist in virtually all human cells (except for erythrocytes) with variations in average number, size and motility within cells differing largely between tissues (McCarron et al., 2013). A single somatic cell can have between 200 and 2000 mitochondria, this number being a reflection of the cellular energy requirements. Not surprisingly, the most metabolically active tissues, such as skeletal and cardiac muscle, liver and brain, have the highest mitochondrial content (Pieczenik and Neustadt, 2007).

1.1.3. Mitochondrial Functions

Early studies of bioenergetics between the 1950s and the 1970s, defined mitochondria at the centre of energy production of the cell (Pagliarini and Rutter, 2013). As a result, mitochondria are still today commonly known as the "powerhouses" of the cell, a term first used in 1957, by Philip Siekevitz (Siekevitz, 1957).

Mitochondria produce more than 90% of cellular energy in the form of ATP (Pieczenik and Neustadt, 2007). Energy is released and used by almost all biochemical machineries by de-phosphorylation of an ATP molecule to an adenosine diphosphate (ADP) molecule. To be sustainable, this process requires that ATP is regenerated from nutrients in a process known as cellular respiration. This process involves the gradual oxidation of glucose into carbon dioxide, where the final electron acceptor of the chain, oxygen, is converted into water (Yoshikawa et al., 2011). A preceding bioenergetic step eventually linked to but independent from cellular respiration occurs outside mitochondria in the cytoplasm, in a sequential set of anaerobic reactions know as glycolysis. During the glycolytic pathway, glucose is oxidised to pyruvate, producing 2 molecules of ATP per molecule of glucose. To increase the net of ATP per molecule of glucose, glycolysis is linked to a second pathway, known as the tricarboxylic acid cycle (TCA, or Krebs cycle) (Figure 1.2). The pyruvate originated from glycolysis is transported into mitochondria, where the acetyl groups are transferred onto Coenzyme A (CoA), forming acetyl-CoA and nicotinamide adenine dinucleotide (NADH). The acetyl-CoA enters the TCA cycle undergoing a sequence of nine different enzymatic reactions, with the goal of stripping out reducing equivalents (electrons and protons) from the substrates by reducing the cofactors NAD+ and FAD to NADH and reduced flavine adenine dinucleotide ($FADH_2$), respectively. Each round generates 3 NADH molecules, 1 FADH2, and 1 guanosine triphosphate (GTP) and each molecule of glucose leads to two cycles. In the last step of cellular respiration, the electrons present in NADH and $FADH_2$ will be unloaded in a multi-protein complex embedded into the IMM, the electron transport chain (ETC), which carries out a set of essential redox reactions during respiration, a process which

provides energy to perform the condensation of ADP and inorganic phosphate (Pi) into ATP; the whole process is known as oxidative phosphorylation (OXPHOS) (Figure 1.2).The ETC is composed by four protein complexes (Complex I (CI), NADH:ubiquinone oxidoreductase; Complex II (CII), succinate:ubiquinone oxidoreductase; Complex III (CIII), ubiquinone:cytochrome c oxidoreductase; and Complex IV (CIV or COX), cytochrome c oxidase) that, by sequential redox reactions, transfer electrons from NADH and FADH2 to the final acceptor, oxygen, forming water (Hatefi, 1985). NADH enters the respiratory chain at CI (Hirst, 2013), while $FADH_2$ is the cofactor of CII (which is also part of the TCA cycle) (Cecchini, 2003). These electrons are used by both CI and CII to reduce ubiquinone (coenzyme Q) to ubiquinol (coenzyme QH_2). QH_2 is soluble in the IMM, and moves to CIII, which transfers electrons from QH_2 to another soluble electron-carrier, the cytochrome c (Berry et al., 2000). In turn, cytochrome c transfers the electrons to CIV, which finally delivers them to oxygen, producing water (Yoshikawa and Shimada, 2015). This process is termed as cellular respiration.

During this energetically favourable transfer of electrons down the ETC complexes, CI, CIII and CIV pump protons from the mitochondrial matrix, across the IMM, into the IMS creating a proton-motive force (PMF). The PMF results from the higher concentration of protons present in the IMS than in the mitochondrial matrix (ΔpH), as well as an unequal distribution of electrical charges across the IMM, designated the mitochondrial membrane potential ($\Delta\psi_M$) (Mitchell and Moyle, 1969, Dzbek and Korzeniewski, 2008). This PMF is exploited by another protein complex, Complex V (CV) or ATP synthase, to generate ATP by phosphorylating ADP, through the energy provided by the backflow of protons from the IMS to the mitochondrial matrix (Walker, 2013). The newly synthesised ATP present in the mitochondrial matrix can pass to the IMS, through the IMM, with the assistance of the ADP/ATP carrier (Kunji et al., 2016). From the IMS, ATP can cross freely through the OMM via VDAC and be distributed to the whole cell (Bonora et al., 2012).

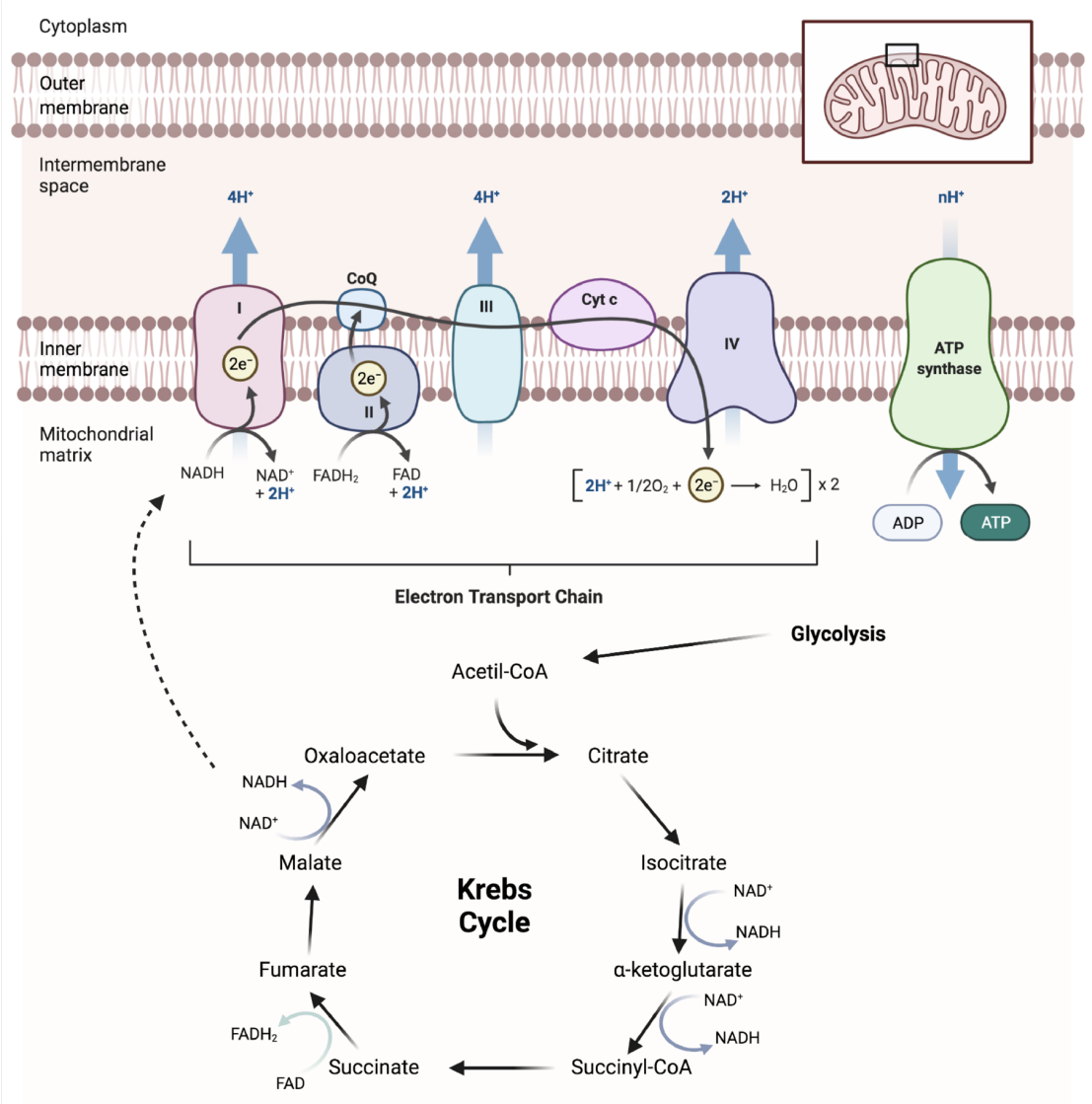

Figure 1.2. Bioenergetics of the electron transport chain and the Krebs cycle.
NADH and FADH2 are generated by the Krebs cycle enzymes. NADH is shuttled to complex I of the ETC where is converted to NAD^+ driving oxidative phosphorylation. In turn, $FADH_2$ enter the ETC through complex II. Transfer of electrons through the chain maintains the membrane potential via proton pumping into the IMS. In this final step, ADP is phosphorylated to form ATP via complex V (ATP synthase) (Osellame et al., 2012). Created with BioRender.com.

Mitochondria are also the main hub of Fatty Acid β-Oxidation (FAO), in which fatty acids are broken down in a cyclic process to produce cellular energy. To enter mitochondria, long-chain fatty acids are converted to fatty acyl-CoA, then to acyl carnitine and later, inside the mitochondrial matrix, reconverted to acyl-CoA by a specialised set of proteins from the carnitine palmitoyltransferases (CPTs) family. Once inside the mitochondria, the long-chain acyl-CoA is broken down to acetyl-CoA, producing NADH and $FADH_2$. The electrons from NADH and $FADH_2$ fuel

mitochondrial ETC for ATP production, while acetyl-CoA can feed the TCA cycle to generate more NADH and FADH2 (Carracedo et al., 2013, Phan et al., 2014).

Despite their central role in energy production, mitochondria are involved in numerous metabolic and homeostatic functions. Mitochondria are involved in heat production not associated with shivering activity, known as non-shivering thermogenesis (Burton and Edholm, 1956, Himms-Hagen, 1984). Heat production is a consequence of protons in the IMS that return to the mitochondrial matrix independently of ATP synthase in a process known as proton leak (Jastroch et al., 2010). Such thermogenesis is mediated by the actions of uncoupler proteins (UCPs) and are especially important in the brown adipose tissue found in newborn or hibernating mammals (Nedergaard et al., 2001, Cannon and Nedergaard, 2011). Mitochondria are also the sites for reactions involved in heme and iron-sulphur (Fe/S) clusters biosynthesis, and in the production and regulation of reactive oxygen species (ROS). Heme is an iron-containing porphyrin, incorporated, in addition to haemoglobin, into some subunits of the ETC, where it is necessary for cellular respiration (Lodish, 2000). It is also crucial in biological processes, for example: oxygen transport and storage, drug and steroid metabolism, signal transduction, and microRNA processing (Chiabrando et al., 2014). Fe/S clusters are prosthetic redox groups with a variety of biological roles in the activity of several enzymes, such as glycosylases, helicases, and primases. In addition, incorporation of Fe/S clusters is necessary for the correct function of the ETC complexes, CI, CII and CIII (Maio and Rouault, 2015). The major source of ROS production in mammalian cells is the electron leak that occurs in mitochondria during ETC, mostly in certain sites of CI, CII and CIII (Martinez-Cayuela, 1995). These highly reactive chemicals can damage biological molecules including DNA, lipids and proteins (Halliwell and Cross, 1994). Nonetheless, ROS contribute to normal cellular and organismal senescence (Starkov, 2008), by acting as signals in the regulation of biological and physiological processes (Murphy, 2009). ROS regulation is vital, as excessive production can induce mitochondrial dysfunction and be harmful to the cell (Droge, 2002). However, lack of ROS was also shown to

have detrimental effects, highlighting their physiological role in mitochondriogenesis (Dogan et al., 2018).

Mitochondria also play a key role in apoptosis, a process of programmed cell death (Ding and Yin, 2012). Apoptosis is required for embryonic development and numerous physiological functions and can be triggered by diverse stressors, such as irreparable DNA damage, growth factor inhibition and oxidative stressors (for example, ROS) (Kanduc et al., 2002). Once initiated, apoptosis consists of the mitochondrial outer membrane permeabilisation (MOMP), ultimately leading to the release of cytochrome c from the IMM to the cytosol. In the cytosol, cytochrome c forms the apoptosome, which determines the proteolytic activation of caspase enzymes, the effectors of programmed cell death (Tait and Green, 2010).

1.2. Mitochondrial Genome Maintenance and Expression

During evolution, most of the ancient genes from the mitochondrial ancestor were transferred to the nuclear genome (nDNA) of the host, eliminating autonomy of the mitochondrion and consequently, reinforcing their symbiotic relationship (Ku et al., 2015). Several of these genes are essential for mitochondrial homeostasis, while others were littered in the nDNA as mitochondrial pseudogenes, termed nuclear mitochondrial DNAs (NUMTs) (Bensasson et al., 2001). Nevertheless, mitochondria preserved a small genome of essential genes for ATP production and protein synthesis, the mitochondrial DNA (mtDNA).

The reason why mitochondria maintained their own reduced genome is not yet fully elucidated. One long-standing hypothesis suggests that highly hydrophobic proteins, as the ones currently encoded in the mtDNA, are difficult to import into mitochondria. Therefore, selective pressures might have been put in place to retain these hydrophobic proteins within the organelle to overcome any difficulties in their transport (von Heijne, 1986). Another theory is that the mtDNA-encoded proteins exist to maintain optimum electron flow through the respiratory chain by modulating the levels of individual complexes *in situ* (Allen, 2017). If key components of each complex in the ETC are encoded in mtDNA, each

mitochondrion can respond independently to its needs by expressing what is required and where, avoiding a possible delayed feedback if these proteins were to be encoded in the nucleus (Allen, 2017). A third hypothesis is that mtDNA genetic code differs slightly from nuclear DNA, presenting different codons encoding for methionine and tryptophan and only two stop codons (Osawa et al., 1992). Such differences might have led to incompatibility and limited any further gene transfer from mitochondria to the nucleus.

1.2.1. Mitochondrial Genome organisation

The mammalian mtDNA is a multi-copy, circular, double-stranded DNA (dsDNA) molecule encoding 13 essential protein subunits of the respiratory chain complexes (7 from CI, 1 from CIII, 3 from CIV, and 2 from CV), together with 22 tRNAs, and two ribosomal RNAs (rRNAs), necessary to translate them (Chinnery and Hudson, 2013) (Figure 1.3). CII is the only respiratory protein complex to be completely encoded by the nDNA (Bezawork-Geleta et al., 2017).

The human and mouse mtDNA were fully sequenced for the first time in 1981 (Anderson et al., 1981, Bibb et al., 1981). Based on the sequence, at that time, researchers were able to identify the genes for the 12S and 16S ribosomal RNAs, 22 tRNAs, cytochrome c oxidase subunits I, II and III, ATPase subunit 6 and cytochrome b. However, 8 unidentified proteins have been detected, dubbed unidentified reading frames (URFs). These URFs were later identified as the 7 subunits of NADH dehydrogenase (CI) and the remaining subunit of ATP synthase (CV), ATPase subunit 8 (Bibb et al., 1981, Chomyn et al., 1985, Macreadie et al., 1983). The mammalian mtDNA sequence reveals extreme economy and does not contain introns. With the exception of a major non-coding region (NCR), each gene is delimited by the next one, while two pairs of protein-coding regions even overlap (ND4/ND4L and ATP6/ATP8) (Chinnery and Hudson, 2013). The two strands are identified as heavy (H) or light (L) strand by their varying G+T contents causing differential densities in alkaline CsCl gradients. In alkaline conditions, G and T become ionised and can interact with Cs^+ ions, conferring a higher density to the strand with higher content of these bases, the H-strand (Alexeyev, 2020, Wells and Larson, 1972).

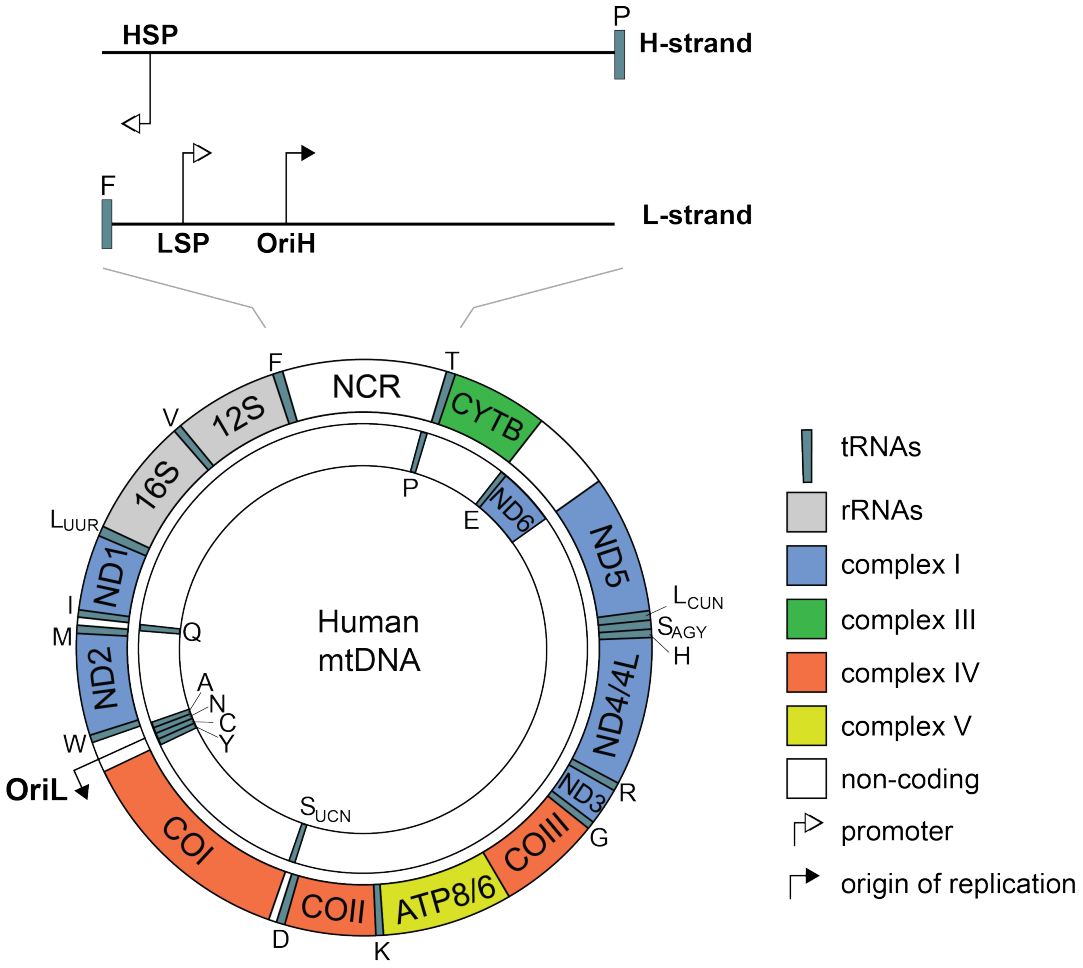

Figure 1.3. Organisation of the human mitochondrial genome.
Human mtDNA is a circular molecule of 16,569 bp, and encodes 13 polypeptides, as well as the 22 tRNAs and 2 rRNAs necessary for their translation. Most of the cis-elements required for mitochondrial transcription (H-strand promoter, HSP and L-strand promoter, LSP) and replication (Origin of replication of H-strand, OriH) are contained within the non-coding region (NCR). The Origin of replication of L-strand (OriL) is present about 11 kb downstream of OriH, between COI and ND2.

The NCR houses dedicated promoters for the transcription of both H- and L-strands of mtDNA, the H-strand promoter (HSP) and the L-strand promoter (LSP), respectively (Gustafsson et al., 2016). The NCR also harbours regulatory sequences controlling mtDNA replication, such as the origin of H-strand replication (OriH) (Gustafsson et al., 2016). A second origin of replication dedicated to L-strand synthesis (OriL) is situated approximately 11kb away from OriH (Nicholls and Minczuk, 2014) (Figure 1.3). The positions of the origins of replication splits the mtDNA in two sections, where the region between OriH and OriL is termed major arc, while the smaller remaining region is denoted minor arc (Nicholls and Minczuk, 2014).

Within the NCR, between LSP and OriH, three "conserved sequence blocks" (CSBs) can be found, referred to as CSB1, CSB2 and CSB3 (Walberg and Clayton, 1981). These "blocks" were identified by sequence comparisons between human and mouse mtDNA and later extended to include many other vertebrates (Walberg and Clayton, 1981, Saccone et al., 1991, Sbisa et al., 1997). In addition, the NCR harbours another element downstream of OriH, the termination-associated sequences (TAS) (Doda et al., 1981). The relevance of these sequences will be discussed in detail on Section 1.2.5.

The NCR also integrates a region where a third strand of DNA is synthesized holding apart the dsDNA and creating a structure named displacement-loop (D-loop) (discussed in the Section 1.2.5) (Nicholls and Minczuk, 2014). Often, the terms "NCR" and "D-loop" are used interchangeably in the literature. However, the D-loop is just present in a fraction of the NCR, since the third strand is not always present (Nicholls and Minczuk, 2014).

The mtDNA only encodes 13 proteins from over 1000 proteins present in mitochondria (Pearce et al., 2017). Therefore, the remaining components of the respiratory chain and other proteins necessary to ensure accurate mitochondrial physiology are synthesised from nuclear genes on cytosolic ribosomes (Pfanner et al., 2019) and later delivered to mitochondria using dedicated importers (see Section 1.2.2). This includes, but is not limited to, the proteins involved in mtDNA replication and transcription, which will be discussed with more detail in Section 1.2.3 and Section 1.2.4.

1.2.2. The mitochondrial nucleoid

The mtDNA is present in the mitochondrial matrix, often anchored to the IMM, in protein–DNA structures termed nucleoids (Kukat et al., 2011). Mammalian mitochondria usually have a width of approximately 0.5 μm, while mtDNA has a contour length of 5 μm (Nass, 1966). Such observation demonstrates why mtDNA must be packaged to fit inside mitochondria. Indeed, similarly to bacterial chromosomes, mtDNA is organised in the mitochondrial matrix into tightly-packed protein–DNA structures called nucleoids (Bogenhagen, 2012). Mitochondrial nucleoids can be often found anchored to the IMM at cristae junctions as scattered punctate foci (Satoh and Kuroiwa, 1991). However, these structures can also be seen freely diffusing through the mitochondrial network (Satoh and Kuroiwa, 1991). Initial predictions stated that a single nucleoid contained between 2 and 8 molecules of mtDNA (Legros et al., 2004). However, with the advances of super-resolution microscopy, the number of mtDNA molecules per nucleoid has now been estimated to be around 1.4 in human cells and around 1.1–1.5 in mouse cells, suggesting that mtDNA molecules are individually sheltered into single nucleoids (Kukat et al., 2011, Kukat et al., 2015). In support of this observation, an increase in mtDNA copy number in mouse cells results in a higher number of nucleoids per cell, while the nucleoid size and shape remains unaltered (Kukat et al., 2011).

Mitochondrial nucleoids are wrapped predominantly with the mitochondrial transcription factor A (TFAM) (Bogenhagen, 2012). TFAM belongs to the high-mobility group domain proteins and non-selectively binds DNA to induce a dramatic U-turn with an overall bend of 180° (Hallberg and Larsson, 2011). This enables TFAM to bind randomly at single DNA duplex structures, inducing bending. In addition, TFAM molecules may also link neighbouring DNA duplexes, resulting in cross-strand binding and looping of mtDNA (Kukat et al., 2015). This build-up of duplex bending and cross-strand binding leads to a gradual compaction of mtDNA. *In vitro* studies show that addition of increasing amounts of TFAM alone is sufficient to complete nucleoid compaction of mtDNA (Kukat et al., 2015). In mammalian cells, TFAM is abundant enough to coat the entire

mitochondrial genome, at a ratio of 1 subunit per 16–17 bp of mtDNA or about 1000 molecules per mtDNA molecule. TFAM is therefore, considered the core component of the nucleoid (Bogenhagen, 2012).

In vitro-reconstituted, compaction of nucleoids by TFAM blocks mtDNA replication and transcription (Farge et al., 2014). This observation suggests that nucleoid compaction by TFAM may play an important mechanistic role in the control of mtDNA expression. In addition, different degrees of nucleoid compaction are observed at physiological TFAM/mtDNA ratios, where fully compacted nucleoids can co-exist with poorly compacted ones (Kaufman et al., 2007, Farge et al., 2014). This infers that nucleoid compaction may dictate which nucleoids are in active mtDNA transcription or replication, where compaction favours blockage, while decompression favours access to mtDNA. In support of this notion, replication of mtDNA in cells only occurs in a fraction of nucleoids (Kukat et al., 2011).

Together with TFAM, other central components of mtDNA replication (catalytic and accessory subunits of POLγ, Twinkle, mtSSB) and transcription (POLRMT, TFB2M, TEFM, TFAM) also localize to the nucleoids (Bogenhagen, 2012).

1.2.3. Transcription of mtDNA

Mammalian mitochondrial transcription initiated at HSP and LSP, both located in the NCR, produces two near-genome length polycistronic RNAs (Figure 1.4 - A) (Gustafsson et al., 2016). Full-length LSP transcripts are terminated just downstream of the 16S rRNA, while full-length HSP transcripts are terminated at the 3′ end of the D-loop region (TAS) (Gustafsson et al., 2016). Transcription from LSP produces the mRNA encoding the CI subunit Nd6 and 8 tRNAs, while transcription from HSP yields the remaining 10 mRNAs (translated to 12 proteins), 14 tRNAs, and 2 rRNAs (Figure 1.4 - B) (Gustafsson et al., 2016). After being generated by the transcription machinery, these long polycistronic RNAs are later excised and processed into individual mRNAs by a dedicated machinery, before

being translated in mitochondrial ribosomes (D'Souza and Minczuk, 2018, Rebelo-Guiomar et al., 2019).

Transcription of the mtDNA is carried out by a single-subunit DNA-dependent RNA polymerase (POLRMT) (Ringel et al., 2011). POLRMT binds in a sequence-specific way to promoter elements, but it is unable to initiate transcription on its own and requires the coordinated action of mitochondrial transcription factor A (TFAM) and mitochondrial transcription factor B2 (TFB2M) (Gustafsson et al., 2016).

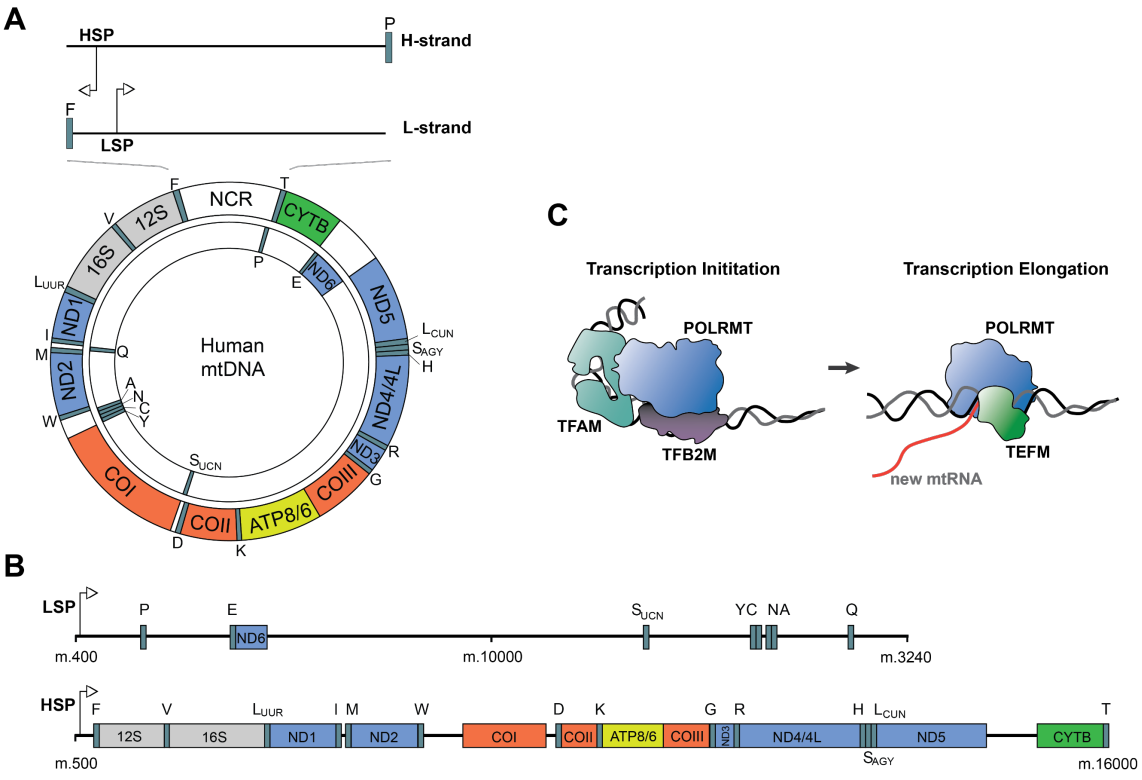

Figure 1.4. Transcription of the human mitochondrial genome.
A. Transcription of mtDNA initiates from H-strand promoter (HSP) and L-strand promoter (LSP), producing two long polycistronic transcripts. **B.** Transcription from LSP produces the mRNA encoding the CI subunit Nd6 and 8 tRNAs, while transcription from HSP yields the remaining 10 mRNAs (translated to 12 proteins), 14 tRNAs, and 2 rRNAs. **C.** Transcription initiation in mitochondria requires the RNA polymerase POLRMT and two transcription factors TFAM and TFB2M. Transcription elongation is stimulated by TEFM, which enhances processivity of POLRMT to produce long stretches of RNA.

The initiation of transcription begins with sequence-specific binding of TFAM to the promoter, upstream of the transcription start site, inducing a stable U-bend in the mtDNA (Figure 1.4 - C) (Fisher et al., 1987, Dairaghi et al., 1995, Gaspari et al., 2004, Shi et al., 2012). Subsequently, POLRMT is recruited to the promoters by concerted binding to TFAM creating a closed preinitiation complex (Hillen et al., 2017a). The formation of such complex leads to recruitment of TFB2M which induces structural changes in POLRMT. This interaction results in melting of the DNA duplex and formation of the open initiation complex, where RNA synthesis can initiate (Hillen et al., 2017a). The transition from transcription initiation to elongation involves the release of TFB2M and recruitment of the mitochondrial transcription elongation factor (TEFM)(Agaronyan et al., 2015, Posse et al., 2015). During elongation, interaction between TEFM and POLRMT, is thought to enhance the processivity of POLRMT allowing production of longer stretches of RNA (Figure 1.4 - C). It also assists in bypassing premature termination or stalling caused by secondary structured RNA regions (such as the G-quadruplex sequence of the CSB2) or oxidative lesions (such as 8-Oxo-2′-deoxyguanosine) (Posse et al., 2015, Hillen et al., 2017b).

The molecular mechanisms elucidating the termination of HSP transcription is still under debate. Previously, it was believed that transcription of the H-strand is initiated from two different sites, HSP1 and HSP2 (Montoya et al., 1982). Transcription initiated from HSP1 was supposedly terminated at a position immediately downstream of the 16S rRNA gene within the tRNALeu(UUR) gene, creating a smaller transcript with 12S and 16S rRNAs, while transcription initiation from HSP2 continued past the termination site and would create a near-genome length transcript (Christianson and Clayton, 1988, Camasamudram et al., 2003). This idea was originally proposed to explain the observed 50-fold higher abundance of mitochondrial rRNAs (Martin et al., 2005). The termination of this HSP1-derived transcript was believed to be governed by the mitochondrial termination factor 1 (MTERF1), which would induce transcription termination through base flipping and DNA unwinding (Jimenez-Menendez et al., 2010). However, the theory has been challenged by studies in MTERF1 knockout mice, in

which the relative levels of rRNA and mRNA remained unaffected (Terzioglu et al., 2013). Therefore, the increase in abundance of rRNAs is likely a consequence of increased stability rather than due to the existence of a different promoter (D'Souza and Minczuk, 2018).

1.2.4. Replication of mtDNA

Maintenance of mtDNA is a highly-regulated process essential for life and, therefore, requires a set of factors that warrant its faithful replication. In mammals, replication of mtDNA is carried out by a single polymerase, the DNA polymerase γ (POLγ), which is responsible for replication of both H- and L-strand (Falkenberg and Gustafsson, 2020). POLγ was first identified in the 1970s, as an RNA-dependent DNA polymerase in human HeLa cells and WI-38 cells (Fridlender et al., 1972). Early studies showed that POLγ has different chemical characteristics in comparison with other cellular DNA polymerases, such as high activity using synthetic RNA templates *in vitro* and resistance to aphidicolin, a reversible inhibitor of eukaryotic nuclear DNA polymerases (Kornberg and Baker, 1972).

POLγ is a heterotrimer with one catalytic POLγA subunit and two POLγB accessory subunits. The human catalytic subunit POLγA has a molecular mass of 140 kDa that harbours DNA 5′-3′polymerase, 3′-5′exonuclease, and 5′-deoxyribose phosphate lyase activities (Longley et al., 1998). The 3′-5′exonuclease activity is essential for proofreading and repair during DNA synthesis (Gray and Wong, 1992), turning POLγA in a highly accurate polymerase, with an error frequency of less than 1×10^{-6} per nucleotide (Longley et al., 2001). Disruption of POLγA 3′-5′exonuclease activity in mice leads to an accelerated accumulation rate of mutations in the mtDNA (Trifunovic et al., 2004). Structurally, the N-terminal exonuclease and C-terminal polymerase domains of POLγA are separated by a linker domain, which has a relevant function for interaction with accessory subunit POLγB (Lee et al., 2009).

The accessory subunit POLγB has a molecular mass of 55kDa, which acts to stabilize interactions with template-DNA, thereby increasing processivity of POLγ to generate long stretches of DNA (Lim et al., 1999). Both POLγA and POLγB are required for mtDNA replication in mammalian mitochondria. Not surprisingly, genetic elimination of POLγA and POLγB in mice results in early developmental arrest of embryos between embryonic days 7.5 and 8.5 associated with severe mtDNA depletion (Hance et al., 2005, Humble et al., 2013).

As mentioned previously, POLγ is the only DNA polymerase required for mtDNA replication in mammalian mitochondria. However, POLγ requires the presence of other replication factors to accomplish faithful replication of full-length mtDNA molecules. *In vitro*, the minimal replication machinery for mtDNA synthesis is composed of POLγ together with the TWINKLE DNA helicase (previously known as C10orf2) and the mitochondrial single-stranded DNA-binding protein (mtSSB) (Korhonen et al., 2004) (Figure 1.5 - A).

The TWINKLE protein works as a homohexameric DNA helicase that unwinds double-stranded DNA in a 5′ to 3′ direction using nucleotide triphosphate hydrolysis as a source of energy (Korhonen et al., 2004). During mtDNA replication, TWINKLE works in concert with POLγ by unwinding the dsDNA template in front of the DNA polymerase, which uses the resulting ssDNA strand as a template for the synthesis of the complementary DNA strand (Korhonen et al., 2004).

The mtSSB protein binds to ssDNA as a tetramer. During mtDNA replication, mtSSB coats the displaced ssDNA to protect it against nucleases, preventing secondary structure formation and unwanted primer formation (Miralles Fuste et al., 2014). In addition, mtSSB stimulates mtDNA synthesis by increasing the helicase activity of TWINKLE and the DNA synthesis activity of POLγ (Korhonen et al., 2003, Korhonen et al., 2004).

Initiation of mtDNA synthesis by POLγ requires prior priming of DNA at the origins of replication. This primase activity is performed by POLRMT, which in addition to its role in mtDNA transcription, also synthesises the RNA primers

required for initiation from the two mitochondrial origins of replication, OriH and OriL (Fuste et al., 2010). During mtDNA transcription, POLRMT presents robust processivity on dsDNA templates, allowing the formation of genomic length transcripts. However, on ssDNA templates POLRMT displays low processivity allowing the synthesis of short primers between 25–75 nt, which can be used by POLγ (Wanrooij et al., 2008). These mechanisms involved in primer formation will be discussed in section 1.2.4.2.

1.2.4.1. Models of mtDNA replication

The way mtDNA is replicated has raised many questions and led, over the years, to the development of several models. In 1972, Vinograd and co-workers presented a model for mtDNA replication by which mtDNA proceeds in an asynchronous manner through a strand-displacement model (Robberson et al., 1972, Clayton, 1991). Currently, this is the model that gathered more experimental evidence in its support and therefore, the most widely accepted (Falkenberg and Gustafsson, 2020).

The strand-displacement model implies replication is initiated from OriH by the replicative mitochondrial DNA polymerase γ (POLγ) which begins the synthesis of the nascent H-strand using the RNA primer transcribed by POLRMT from the LSP (Robberson and Clayton, 1972, Gillum and Clayton, 1979). Using the L-strand as a template, POLγ continues the synthesis of the new H-strand assisted by the helicase TWINKLE, which unwinds the dsDNA allowing the progression of the replication fork (Korhonen et al., 2003). As the replication fork advances, the non-template displaced H-strand is rapidly protected by the mitochondrial single-stranded binding protein (mtSSB), preventing the formation of secondary structures and blocking unwanted primer synthesis (Miralles Fuste et al., 2014). The replication machinery proceeds unidirectionally until it reaches OriL, where POLRMT synthesises a RNA primer. This primer is used by POLγ to initiate synthesis of the nascent L-strand (Fuste et al., 2010). Synthesis of the nascent H- and L-strands proceeds unidirectionally until two full-length, double-stranded mtDNA molecules are formed (Figure 1.5 - B).

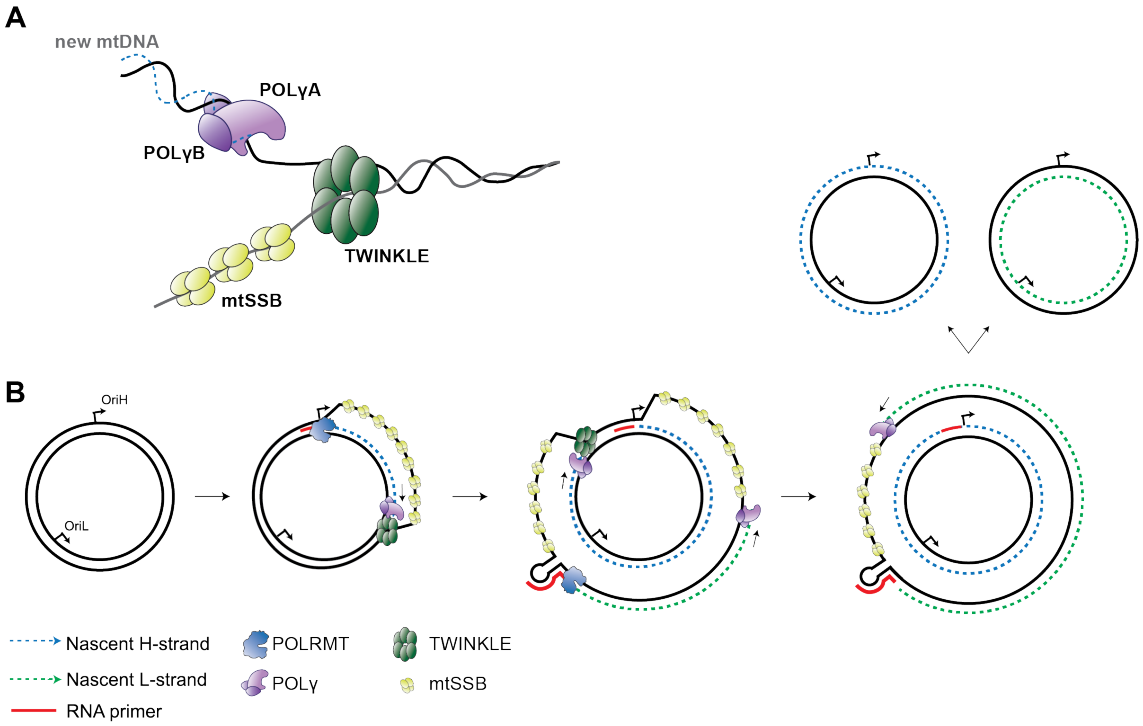

Figure 1.5. Replication of the human mitochondrial genome.
A. The minimal mtDNA replisome is composed by the DNA polymerase POLγ (composed by one catalytic subunit, POLγA and two accessory subunits POLγB), the TWINKLE helicase and the mitochondrial single-stand binding protein, mtSSB. **B.** Schematic representation of the strand-displacement model (SDM) of mtDNA replication. POLγ starts mtDNA replication on the origin of replication of the H-strand (OriH) using a RNA primer synthesised by POLRMT to synthesise the nascent H-strand using the L-strand as template. The helicase TWINKLE unwinds the dsDNA allowing the progression of the replication fork, while mtSSB rapidly coats the non-template displaced H-strand. Synthesis of the nascent L-strand is initiated when synthesis of the H-strand reaches the origin of replication of the L-strand (OriL). At OriL a formation of a stem loop enables POLRMT to synthesise a RNA primer, which is used by POLγ to initiate replication of the L-strand. Synthesis of the nascent H- and L-strands proceeds unidirectionally until two full-length, double-stranded mtDNA molecules are formed. At the end of replication, the RNA primers are degraded and the gaps filled by POLγ.

In addition to the strand-displacement model, two alternative models for mtDNA replication have been reported: the ribonucleotide incorporation throughout the lagging strand model (RITOLS) (Yasukawa et al., 2006), and the strand-coupled model (Holt et al., 2000). The RITOLS model is similar to the strand-displacement model, except that it suggests that during replication the parental H-strand is protected by RNA species, while the strand-displacement model attributes this function to mtSSB. However, the presence of RNase H1 mitochondria, a nuclease which actively degrades RNA molecules hybridized to ssDNA (RNA: DNA hybrids), argues against the use of RNA to stabilize ssDNA regions (Posse et al., 2019, Al-

Behadili et al., 2018). In addition, the high abundance of mtSSB in mitochondria disfavours the need of alternative modes of ssDNA protection (Miralles Fuste et al., 2014).

The strand-coupled model suggests that mtDNA replication starts bidirectionally at multiple places and that the nascent L-strand is synthesized as shorter, Okazaki-like fragments that are ligated to generate a continuous strand (Holt et al., 2000). This model was originated based on the findings, in some type of cells, of Okazaki-like fragments using neutral two-dimensional agarose gel electrophoresis (2D-AGE) and evidence for alternative origins of L-strand mtDNA synthesis by atomic force microscopy (Brown et al., 1986, Holt et al., 2000). However, these Okazaki-like fragments have not been detected in *in organello* labelling experiments performed in purified mitochondria, questioning their existence (Gustafsson et al., 2016). In addition, mtSSB normally restricts primer formation by POLRMT to OriL. However, in certain conditions, POLRMT might be able to access the parental H-strand and prime DNA synthesis from sites outside OriL, giving rise to alternative origins of L-strand mtDNA synthesis (Falkenberg and Gustafsson, 2020).

1.2.4.2. MtDNA replication initiation

Transcription initiated by POLRMT from LSP not only produces genomic-length transcripts, but also the RNA molecules used as primers for initiation of H-strand DNA synthesis, at OriH (Falkenberg et al., 2007). A considerable fraction of the transcription initiation events from LSP are believed to terminate prematurely downstream from the promoter, around the CSBs (Wanrooij and Falkenberg, 2010). These nascent RNAs can form a stable hybrid with the non-template DNA, thereby creating a triple-stranded structure, termed R-loop (Xu and Clayton, 1995). Among the CSBs present downstream of LSP, at least CSB2 was shown to be required for R-loop formation. During transcription, the guanine-rich nature of CSB2, is believed to favour the creation of R-loops, by folding the G-quadruplex structure together with non-template DNA (Wanrooij et al., 2012). Nevertheless, terminated 3' ends of RNA have been mapped also to CSB1 And CSB3 in human cells (Chang and Clayton, 1985). Since their discovery, the R-loops were associated

with the formation of primers required for replication initiation (Chang and Clayton, 1985). However, without subsequent processing, the R-loop cannot prime mtDNA synthesis, because the 3′-OH end of the RNA molecule is inaccessible by POLγ (Posse et al., 2019). Such processing is now believed to be mediated by the nuclease RNase H1. Cleavage of the R-loop by RNase H1 creates 3′-OH ends which can be used to prime synthesis of the nascent H-strand by POLγ (Posse et al., 2019). Nevertheless, primer formation at OriH and the mechanisms that regulate the switch to genomic length transcription are still under intense investigation. However, replication initiation at CSB2 has not yet been reconstituted *in vitro*, despite substantial efforts. Therefore, there may be missing factors that are essential for primer maturation (Falkenberg and Gustafsson, 2020).

POLRMT is also responsible for the generation of the primers required for initiation of replication at OriL, although the mechanism differs significantly from primer generation at OriH. According to the strand-displacement model, replication is initiated from OriH by the replication machinery and proceeds unidirectionally until it reaches OriL (Robberson and Clayton, 1972, Gillum and Clayton, 1979). When the single-stranded OriL is exposed, it forms a characteristic stem-loop structure with a poly-dT stretch. These ssDNA short dT-stretch can be used by POLRMT to initiate primer synthesis (Fuste et al., 2010). In normal conditions, mtSSB coats ssDNA to prevent unspecific primer formation across the mtDNA (Miralles Fuste et al., 2014). However, the presence of the stem-loop at OriL prevents mtSSB binding and leaves the region accessible to POLRMT, which then initiates primer synthesis from the poly-dT stretch (Fuste et al., 2010, Miralles Fuste et al., 2014). Replacement of the poly-dT stretch with a poly-dA sequence results in a total loss of primer synthesis, supporting the importance of this sequence (Fuste et al., 2010). Once POLRMT initiates primer formation, it produces a RNA primer of about 25 nt, after which is replaced by POLγ to initiate synthesis of the nascent L-strand (Fuste et al., 2010).

1.2.4.3. MtDNA replication termination

Once both strands have completed the replicative cycle, the RNA primers need to be removed and the newly synthesised mtDNA molecules must be properly ligated. The mechanism underlying termination of replication in mitochondria has been recently a focus of intense research, in which much of the information was brought to light in the last 10 to 15 years (Falkenberg and Gustafsson, 2020).

Primer removal at OriL seems to be mediated by the nuclease RNase H1. This nuclease removes the RNA primer from the poly-dT stretch in the loop region to the transition point between RNA and DNA at the base of the stem-loop, leaving 1 to 3 ribonucleotides at the transition between RNA and DNA (Lima et al., 2007). These remaining ribonucleotides impede ligation by mitochondrial Ligase 3, suggesting that on its own, RNase H1 cannot fully remove the RNA primer (Al-Behadili et al., 2018). An additional enzyme is, therefore required to remove the remaining ribonucleotides. The nuclear flap endonuclease 1 (FEN1) and EXOG have been suggested to be responsible for such function, however, current data do not support their involvement (Uhler and Falkenberg, 2015, Falkenberg and Gustafsson, 2020, Al-Behadili et al., 2018).

Primer removal at OriH also seems to be partially performed by the RNase H1. Similar to OriL, RNase H1 removes the initial RNA primer, from LSP to CSB2, where transition from RNA to DNA occurs (Holmes et al., 2015). However, a second nuclease capable of removing the remaining ribonucleotides is necessary. Such nuclease was proposed to be mitochondrial genome maintenance exonuclease 1 (MGME1) (Uhler et al., 2016, Nicholls et al., 2014, Kornblum et al., 2013). MGME1 was shown to be able to remove the section, from the CSB2 through OriH, including a portion of the newly synthesised H-strand (Uhler et al., 2016). The gap left by MGME1 is later filled by POLγ and finally ligated by mitochondrial Ligase 3 (Uhler et al., 2016).

1.2.5. The mtDNA D-loop

As mentioned above, transcription initiated from the LSP can also be utilised to prime mtDNA synthesis. During transcription, the transcript can fold together with the non-template strand to generate R-loops, promoted by the guanine-rich nature of CSB2. Processing of the R-loop by RNase H1 generates the primer to initiate synthesis of DNA (Falkenberg and Gustafsson, 2020). Nevertheless, not all replication events lead to full length molecules. Indeed, about 95% of the mammalian mtDNA replication events initiated at the leading strand terminate prematurely after ~650 nt downstream of OriH, in a region with conserved secondary elements, known as the termination associated sequences (TAS) (Nicholls and Minczuk, 2014, Jemt et al., 2015). The abortive mtDNA replication product is named 7S DNA. The 7S DNA often remains bound to the template L strand and displaces the non-template H strand, creating a triple-stranded structure called the displacement-loop (D-loop) (Figure 1.6) (Nicholls and Minczuk, 2014).

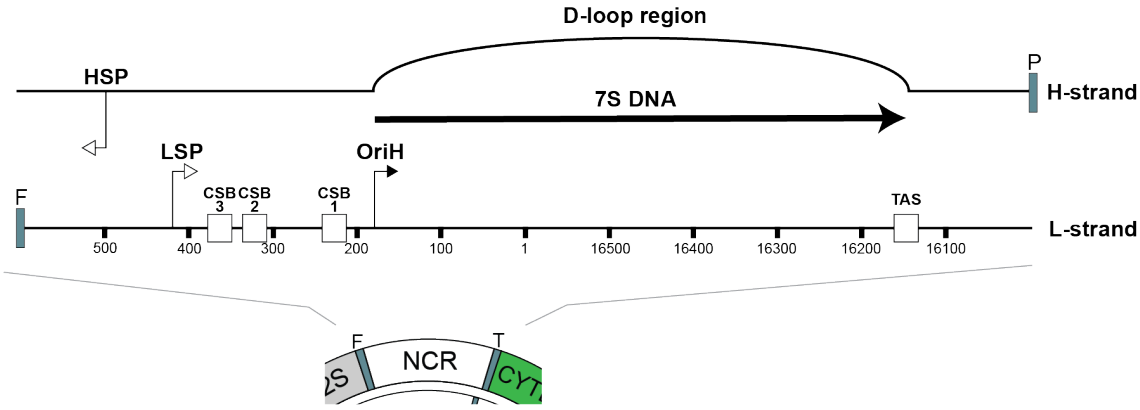

Figure 1.6. The mitochondrial D-loop region within the NCR.
Schematic representation of the non-coding region of human mtDNA highlighting the D-loop. The three conserved sequence blocks (CSB 1, CSB 2, and CSB 3) are located just downstream of light-strand promoter (LSP). Most mammalian mtDNA replication events initiated at origin of replication of the H-strand (OriH) terminate prematurely originating the 7S DNA. The termination occurs after synthesis of ~650 nt, in a region with conserved secondary elements, known as the termination associated sequences (TAS). The 7S DNA often remains bound to the template L strand and displaces the non-template H strand, creating a triple-stranded structure known as D-loop.

The D-loop was first identified in the 1970s, in electron micrograph images of mouse and chicken mtDNA (Arnberg et al., 1971, Kasamatsu et al., 1971). However, the physiological relevance of the D-loop in mtDNA maintenance and the reason why 7S DNA is synthesised and turned over at considerable energetic expense is still not well understood.

The 5′ and 3′ borders of the D-loop each contain an evolutionary conserved 15 nt palindromic sequence motif (ATGN9CAT). The element at the 5′-end coincides with CSB1, while the one in the 3′-border of 7S DNA is referred to as core-TAS, since it is located within the TAS region (Jemt et al., 2015). The significance of such motifs is still unknown. However, their presence suggests that the TAS territory at the 3′ of the D-loop may be involved in controlling the fate of replication initiation events between abortive (7S DNA) versus full-length mtDNA replication (Jemt et al., 2015, Pereira et al., 2008). Such hypothesis was further supported by the finding that POLγ and TWINKLE are enriched in the D-loop region, consistent with the synthesis of 7S DNA being more frequent than full length molecules (Jemt et al., 2015). In normal conditions, POLγ stalls at the 3′ end of the D-loop, while TWINKLE occupancy is decreased at this site. However, TWINKLE occupancy at 3′ end of the D-loop increases as response to mtDNA depletion, and correlates with a decrease in 7S DNA levels. This suggests a preference for full-length mtDNA replication vs. abortive events to restore the mtDNA levels. In addition, it suggests TAS acting as a control site where increased occupancy of TWINKLE promotes POLγ processivity to generate full-length mtDNA replication (Jemt et al., 2015). Furthermore, TWINKLE levels have been shown to correlate with the amount of mtDNA. TWINKLE depletion promotes a decrease in mtDNA levels, while its overexpression results in their increase (Tyynismaa et al., 2004, Milenkovic et al., 2013). Interestingly, TWINKLE depletion leads to a decrease in 7S DNA steady state levels, suggesting that it is also essential for 7S DNA synthesis (Milenkovic et al., 2013).

Besides TWINKLE, other elements of the replication machinery have been shown to influence the synthesis of 7S DNA. Depletion of mtSSB in human cells impairs generation of 7S DNA (Ruhanen et al., 2010). In addition, the *de novo* formation of

7S DNA was much reduced in mtSSB knockout mice (Jiang et al., 2021). Such observation came to support the role of mtSSB in primer formation, by possibly stabilising the R-loops for being processed by RNase H1 (Jiang et al., 2021). This further confirms that 7S DNA synthesis is dependent on replication initiation events. Another component of the replisome, POLγB has also been shown to influence 7S, since both its overexpression or depletion cause loss of 7S DNA (Di Re et al., 2009). However, the exact role of POLγB in D-loop maintenance remains to be elucidated.

Elements of the transcription apparatus have also been shown to influence the synthesis of 7S DNA. For example, adding TFAM to isolated mitochondria increased the rate of 7S DNA formation (Gensler et al., 2001). The formation of 7S DNA was much reduced in the absence of POLRMT, TFB2M and TEFM, consistent with 7S DNA being produced downstream of a transcription event (Kuhl et al., 2016, Qu et al., 2016, Jiang et al., 2019). Interaction between TEFM and POLRMT was reported to prevent the generation of replication primers and was thus suggested to serve as a molecular switch between replication and transcription (Agaronyan et al., 2015). However, *in vivo* data revealed that transcription events in Tefm knockout mice terminate before OriH and thus, cannot support primer formation, which is necessary for synthesis of both 7S DNA and full-length replication Therefore, TEFM is unlikely to be regulating the transcription/replication switch and instead seems to act as a general transcription elongation factor necessary for transcription and primer synthesis (Jiang et al., 2019).

The 7S DNA is turned over rapidly, with a half-life of around 45 minutes to one hour in mouse and rat cells (Bogenhagen and Clayton, 1978, Gensler et al., 2001). However, the reason why 7S is turned over so rapidly is still undetermined (Nicholls and Minczuk, 2014). Degradation of 7S DNA is believed to be regulated by nuclease activity. MGME1 can cut ssDNA and, thus, was indicated as a promising candidate (Kornblum et al., 2013). Abolishment of MGME1 activity has been shown to elevate the levels of 7S DNA, supporting the role of MGME1 in degrading this mtDNA species (Kornblum et al., 2013, Nicholls et al., 2014).

Similarly, loss of MGME1 in mice causes an increase in the steady-state levels of 7S DNA, which in turn was linked to an increased stability of these molecules rather than augmented synthesis (Matic et al., 2018). In fact, the *de novo* formation of 7S DNA was decreased suggesting that MGME1 might have additional roles in the D-loop (Matic et al., 2018). The role of MGME1 and possibly other factors in 7S DNA biology is therefore, not completely elucidated and requires further studies.

1.2.6. Control of mtDNA copy number

The mammalian mtDNA is a multi-copy genome. Typically, each cell contains hundreds to thousands of mtDNA molecules (Stewart and Chinnery, 2021). In contrast with the nuclear genome, mtDNA replication does not coincide with cell cycle and is replicated continuously even in post-mitotic cells (Gross et al., 1969, Magnusson et al., 2003).

The mtDNA encodes subunits of the OXPHOS system which are essential for cellular energy. Therefore, it is not surprising that mtDNA copy number is subject of tight control in a tissue- and developmental stage-specific manner and often correlates with the specific energetic demand of each cell type (Fuke et al., 2011, Wai et al., 2010, D'Erchia et al., 2015). For example, endothelial and spleen cells have very few mtDNA copies, while muscle cells and cardiomyocytes have high numbers (Moyes et al., 1998, Kelly et al., 2012). Depletion of mtDNA in cultured cells either chemically by 2',3'-dideoxycytidine (ddC) treatment or genetically with inducible dominant negative variants of POLγA, is generally reversible and restoration to normal levels occurs in a matter of days, further suggesting that mtDNA levels are tightly regulated (Brown and Clayton, 2002, Jazayeri et al., 2003).

Our knowledge on how mtDNA is replicated and transcribed has substantially increased in the last years. However, how exactly mtDNA copy number is sensed and regulated has remained an unanswered question for several decades, and still is (Moraes, 2001, Clay Montier et al., 2009). A hypothesis is that mtDNA content is governed by a balance between synthesis and degradation of mtDNA (Clay

Montier et al., 2009). However, the exact mechanism dictating the predominance of one over the other remains elusive.

Replication of mtDNA is coupled with mitochondrial transcription due to the dual role of POLRMT that not only generates the long RNA transcripts, but also synthesises the primers necessary for replication initiation (Gustafsson et al., 2016). Therefore, mtDNA replication can be regulated at different stages, anywhere between initiation of transcription at LSP, processing of this transcript in the CSB2 region to generate replication primers, or even by regulating the balance of abortive (7S DNA) vs. full length replication events (Falkenberg and Gustafsson, 2020). The weight of these events individually or together and the coordination of both replication and transcription machineries in regulating mtDNA replication is still undetermined. This has been exemplified in the previous section by the way 7S DNA is synthesised and turned over.

Another factor that might be regulating the initiation of DNA replication is the degree of mtDNA compaction influenced by TFAM levels (Falkenberg and Gustafsson, 2020). This hypothesis was prompted by the findings that *in vitro*, high levels of TFAM can block the replication and transcription machineries and that fully compacted nucleoids can co-exist with poorly compacted ones at physiological TFAM/mtDNA ratios (Kaufman et al., 2007, Farge et al., 2014). Interestingly, only a fraction of the cellular nucleoids is engaged in active replication of mtDNA (Kukat et al., 2011). In cultured cells, the TFAM:mtDNA ratio determines the active and non-active nucleoid populations, in which lower levels of TFAM are associated with less compact, active nucleoids (Bruser et al., 2021). In addition, the levels of mtDNA have been shown to be directly proportional to total TFAM levels. In mouse models, TFAM knockout severely depletes mtDNA while TFAM overexpression increases mtDNA content (Larsson et al., 1998, Ekstrand et al., 2004). In addition, TFAM is degraded when not bound to mtDNA by mitochondrial matrix proteases, suggesting that TFAM levels within mitochondria are controlled by a regulated process (Larsson et al., 1994, Lu et al., 2013).

Beside the possible regulation mediated by elements of the replication and transcription machineries, mtDNA copy number has been suggested to be

influenced by the availability of its building blocks, the nucleotides. Like nuclear DNA, mtDNA needs nucleotides for replication and specifically in post-mitotic cells in which the nuclear DNA in not actively replicated, the cellular nucleotide pools are mainly used for mtDNA replication (Bourdon et al., 2007). Not surprisingly, pathogenic mutations in the genes encoding enzymes involved in nucleotide supply for mtDNA synthesis (TP, TK2, DGUOK, RRM2B, SUCLA2, SUCLG1) are associated with depletion and deletions of mtDNA (Viscomi and Zeviani, 2017). Interestingly, imbalance of dNTPs is found in mice with mtDNA replication defects due to mutant variants of TWINKLE (Nikkanen et al., 2016). In yeast, nucleotide availability has also been shown to influence the balance between mtDNA synthesis and degradation by MIP1 (yeast homolog of *POLG*), where nucleotide insufficiency favoured degradation of mtDNA (Medeiros et al., 2018).

1.2.7. Role of Mitochondrial Matrix proteases in mtDNA maintenance

Mitochondria have established a quality control system composed of chaperones and proteases that regulate the folding, assembly, and turnover of proteins, as well as the removal of damaged proteins (Tatsuta, 2009). Chaperones certify that mitochondrial proteins are imported into the proper compartment and folded into their correct structure to support their functions. Proteins failing to fold correctly or that have been damaged are degraded by specialised proteases, described below (Tatsuta and Langer, 2008).

Inside the mammalian mitochondrial matrix there are two major soluble mitochondrial AAA+ proteases, the caseinolytic peptidase XP (ClpXP) and the Lon peptidase 1 (LONP1) (Szczepanowska and Trifunovic, 2021). AAA+ proteases belong to a heterogeneous group of proteins able to induce conformational changes in a wide range of substrate proteins, sharing a conserved ATP domain of around 230 amino acids, that assembles into oligomeric rings and undergoes conformational changes during cycles of nucleotide binding and hydrolysis (Hanson and Whiteheart, 2005).

The human ClpXP protease is a complex formed of two proteins, CLPP and CLPX (Kang et al., 2002). CLPP contains a serine protease domain with a catalytic triad, conferring proteolytic activity, while CLPX contains an AAA+ ATPase domain functioning as chaperone. Processive proteolytic activity by CLPP is ATP-dependent and requires interaction with CLPX. In addition, substrate recognition is mediated by CLPX (Kang et al., 2002).

ClpXP is the least studied of all mammalian mitochondrial proteases. The precise function of the human ClpXP protease remains elusive, partly due to absence of a homologous CLPP protease in *Saccharomyces cerevisiae* and *Schizosaccharomyces pombe*, despite the CLPX chaperone component being highly conserved (Yu and Houry, 2007). Recombinant human ClpXP is capable of degrading model peptides and proteins such as casein, and along with comparisons with the function of bacteria homologs, ClpXP is predicted to be involved in protein quality control (Kang et al., 2002). In support to this notion, ClpXP was shown to mediate the surveillance and repair of mitochondrial CI in mammals (Szczepanowska et al., 2020). A portion of CI exposed to the mitochondrial matrix, known as NADH-oxidizing-N-module, is turned over at a higher rate and independently of the rest of the complex by ClpXP, which selectively removes and degrades damaged subunits (Szczepanowska et al., 2020). Nevertheless, there is currently no evidence of direct role of ClpXP in the regulation of mtDNA maintenance.

In contrast with ClpXP, LONP1 homologs are highly conserved, these are present as soluble cytoplasmic proteins in eubacteria and bound to the cell membrane in archaea. In eukaryotes, a similar protease also exists in peroxisomes and dubbed LONP2 (Pomatto et al., 2017). In the 1990s, LONP1 was the first human mitochondrial matrix AAA+ protease to be identified based on its similarity to the bacterial Lon (Wang et al., 1993, Wang et al., 1994). Also, in contrast to the CLPP/CLPX pair, LONP1 not only has proteolytic activity but also retained the chaperone activity as an intrinsic part of the protease (Cha et al., 2010, Venkatesh et al., 2012). Thus, structurally LONP1 contains an AAA+ ATPase module on its N-terminal domain, which carries out the substrate recognition and unfolding, and a C-terminal serine protease domain (P-domain) containing a catalytic serine-lysine

dyad (Cha et al., 2010, Venkatesh et al., 2012). The LONP1 protease functions as a ring-like homo-oligomeric complex of six subunits of about 600 kDa (100 kDa for individual LONP1 subunits).

Although LONP1 functions and substrates have not yet been fully characterized, it has been associated with mitochondrial matrix protein quality by degrading misfolded and oxidised protein (Bezawork-Geleta et al., 2015, Bota and Davies, 2002). For example, LONP1 has been shown to be involved in the degradation of a folding-incompetent form of the human mitochondrial protein, ornithine transcarbamylase (OTC) (Bezawork-Geleta et al., 2015). LONP1 also selectively recognises and degrades the oxidized, hydrophobic form of aconitase after mild oxidative modification (Bota and Davies, 2002). These examples demonstrate the variety of substrates that LONP1 may have.

In addition to protecting mitochondria from the accumulation of misfolded and oxidized proteins, LONP1 was suggested to play a role in regulating mtDNA and nucleoid function. Studies in both *Drosophila melanogaster* and mammals showed that LONP1 regulates the degradation of TFAM (Lu et al., 2013, Matsushima et al., 2010). In fruit fly, LONP1 knockdown leads to the accumulation of TFAM, while overexpression results in a decrease in TFAM levels, supporting the idea that TFAM is degraded by LONP1 (Matsushima et al., 2010). However, in mammalian cells, knockdown of LONP1 alone does not lead to TFAM accumulation (Lu et al., 2013). Instead, it was demonstrated that in human cells, TFAM is only degraded by LONP1 when it is not bound to mtDNA. Furthermore, phosphorylation of TFAM by a cAMP-dependent protein kinase (PKA) impairs its binding to mtDNA, prevents initiation of transcription and promotes LONP1-dependent degradation (Lu et al., 2013). Given the role of TFAM in nucleoid packaging and the correlation between TFAM and mtDNA levels, LONP1-dependent degradation of TFAM can be a regulated mechanism influencing the abundance and accessibility of mtDNA through the balance of the mtDNA: TFAM ratio (Lu et al., 2013, Kaufman et al., 2007, Farge et al., 2014). Beside TFAM, mtSSB has also been suggested to be a substrate for LONP1. Such notion was based on the finding that mtSSB, and many

other proteins, accumulate upon expression of a catalytically dead version of LONP1 (amino acid substitution S855A) (Zurita Rendon and Shoubridge, 2018).

Interestingly, LONP1 alone can bind mtDNA in a sequence-specific and strand-specific manner. The mammalian LONP1 binds specifically to the ssDNA in guanine-rich parts of the mtDNA, preferentially in the NCR region which contains the HSP and LSP, as well as the OriH (Lu et al., 2007, Chen et al., 2008). However, the physiological relevance of this feature is thus far unclear. Even though LONP1 was the first human mitochondrial matrix AAA+ protease to be identified, our knowledge on its functions is still limited and most probably many substrates are yet to be identified.

1.3. Mitochondrial Diseases

In 1959, Swedish endocrinologist Rolf Luft and his colleagues reported the first case of a biochemically proven mitochondrial disease. The report described a young patient with euthyroid hypermetabolism, which was characterized by abundant sweating and weight loss despite high-calorie food intake. Subsequent muscle biopsy and enzyme analysis revealed uncoupling of mitochondria in the patient (Ernster et al., 1959). This landmark report set the beginning of the field of mitochondrial medicine. Since then, more than 150 distinct genetic mitochondrial syndromes have been defined and more than 300 individual human genes have been identified as the cause of mitochondrial diseases (Stenton and Prokisch, 2018).

Mitochondrial diseases are a group of genetic disorders traditionally characterized by impaired oxidative phosphorylation (OXPHOS), reducing ATP production below a critical threshold, which leads to cellular dysfunction and disease (Gorman et al., 2016). In addition to suboptimal ATP generation, other aspects of OXPHOS dysfunction, such as failure to restore the cellular pools of NAD^+, can also contribute to the pathogenesis of mitochondrial disease (Pirinen et al., 2020, Grange et al., 2021). While extremely rare if taken individually, altogether mitochondrial diseases are among the most prevalent groups of inherited

neurological disorders with a prevalence of ~1 in 4,300 (22.9 in 100,000) in the adult population (Gorman et al., 2015).

Mitochondrial diseases have the potential to affect any tissue harbouring mitochondria (Ghezzi and Zeviani, 2018). Typically, patients present with multi-organ involvement, especially organs with high energetic demand, such as the central nervous system (with associated pathologies termed encephalopathies), the skeletal muscle (myopathies), a combination of the two (encephalomyopathies), the heart (cardiomyopathies) or the liver (hepatopathies), amongst others (Figure 1.7) (Ghezzi and Zeviani, 2018). Rarely, patients can present single organ involvement, with the most prominent example being isolated optic nerve atrophy seen in Leber's hereditary optic neuropathy (LHON) (McFarland et al., 2010).

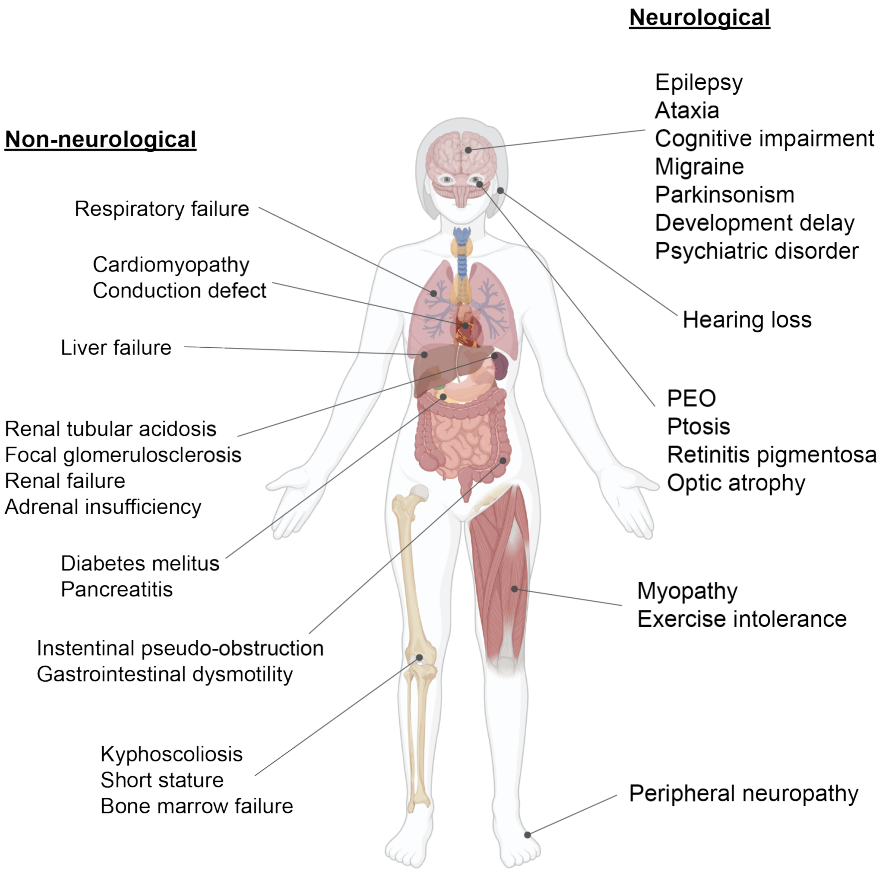

Figure 1.7. The clinical presentation of mitochondrial diseases.
Mitochondrial disease patients can present single or multi-organ involvement, especially those with high energetic demand and. The clinical presentations are highly variable among different patients. Generally, the clinical presentations can be divided in non-neurological or neurological symptoms. Created with BioRender.com and adapted from (Russell et al., 2020).

Mitochondrial diseases can also manifest at any age ranging from severe early childhood-onset syndromes to milder late-onset conditions. Patients with adult-onset mitochondrial disease usually display myopathies associated with CNS abnormalities (Gorman et al., 2016), whilst infantile or childhood presentations are characterized by increased severity impacting development, including cognitive impairment and muscular tone and coordination, and can be further characterised by cerebellar atrophy, dystonia, seizures, and respiratory abnormalities (Gorman et al., 2016).

Mitochondria maintenance and homeostasis are under a unique double genetic control of both nuclear and mtDNA. As consequence, mutations in these two genomes leading to mitochondrial dysfunction are relevant for human pathology and disease. Indeed, mitochondrial disorders can arise from inherited or de novo mutations in either the mtDNA or the nDNA (Zeviani et al., 2003, Gorman et al., 2015). Unlike nDNA, mtDNA is exclusively inherited through the maternal germ line (Wei and Chinnery, 2020). Therefore, mitochondrial diseases can be transmitted by any mode of inheritance (Mendelian (autosomal or X-linked dominant or recessive), or non-Mendelian, i.e. maternal, in nature), and, in some cases arise from *de novo* mutations (in particular, all the macrodeletions in mtDNA arise *de novo*). This complex genetic mode of inheritance further complicates the molecular diagnosis of these conditions (Ghezzi and Zeviani, 2018, Zeviani et al., 2003).

1.3.1. Mutations on mtDNA

Currently, more than 250 pathogenic mtDNA mutations have been identified (Mito-MAP database, www.mitomap.org). It is estimated that ~80% of adult-onset and 20–25% childhood-onset mitochondrial diseases are caused by mtDNA mutations (Thorburn, 2004, Lebon et al., 2003). Pathogenic mtDNA mutations can directly or indirectly affect proteins involved in OXPHOS. Mutations in mtDNA-encoded protein-coding genes can directly affect their function, while mutations

in mitochondrial tRNA- or rRNA-coding regions perturb the synthesis of these proteins. Additionally, rearrangements of mtDNA, such as large-scale mtDNA deletions, often disrupt several protein coding genes together with multiple tRNAs (Gorman et al., 2016).

The complexity of many mitochondrial diseases is further complicated by the presence of multiple copies of mtDNA within a cell. Frequently, pathogenic mtDNA mutations co-exist with unaffected mtDNA molecules, a condition known as heteroplasmy (Stewart and Chinnery, 2021). Both the presence of a germline bottleneck and the unequal distribution of mutant mtDNA in various tissues during development, can lead to significant fluctuations in the heteroplasmic levels (Stewart and Larsson, 2014, Stewart and Chinnery, 2021). The germline bottleneck implies a combination of a decrease in total mtDNA copy number as well as asymmetrical segregation of mutant and wild-type mtDNA into the mother's oocyte during gametogenesis, resulting in a variable distribution of a mtDNA mutation in newly generated gamete cells (Stewart and Larsson, 2014). Also, over lifespan certain mtDNA genotypes can accumulate in postmitotic tissues, leading to mutant mtDNA prevailing over wild-type, a phenomenon known as clonal expansion (Stewart and Chinnery, 2021). Clonal expansion of mutant mtDNA can occur even without cell division through a process of relaxed replication, in which mtDNA is replicated independently of the nuclear DNA (van den Ameele et al., 2020). Mathematical models have shown that even if co-existing mutated and WT mtDNAs undergo non-selective replication, this can lead over time to accumulation of mutant mtDNAs through random genetic drift (Chinnery and Samuels, 1999). However, there is indication that some mutant mtDNAs can undergo preferential replication, for instance, because they replicate faster such as mtDNA molecules with large-scale deletions (Diaz et al., 2002).

Clinical manifestations resulting from biochemical OXPHOS defects often require heteroplasmic mutant mtDNA to be present above a certain pathogenicity threshold (typically >60-70%, but variably dependent on the intrinsic pathogenicity of the mtDNA mutation), with the level of heteroplasmy correlated with the risk of developing severe disease (van den Ameele et al., 2020). For

example, individuals with the m.8993T>G mutation are often asymptomatic when heteroplasmy levels are <60%, those with heteroplasmy levels of 60–80% manifest clinically with adult-onset NARP phenotype, whereas those with heteroplasmy levels of >80% manifest clinically as early-onset Leigh syndrome (Tatuch et al., 1992). Nevertheless, the same mtDNA mutation at similar levels of heteroplasmy can result in different clinical outcomes. For example, one of the most common mtDNA mutations (m.3243A>G) has been associated with numerous different syndromes (Pickett et al., 2018). Occasionally, cells can contain only mutant mtDNA (absence of WT mtDNA), a condition termed homoplasmy. Even in such cases, clinical manifestation may be variable suggesting the influence of other factors. For example, LHON-associated mtDNA mutations are frequently homoplasmic but not every individual manifest the disease (Bianco et al., 2017). In fact, a higher risk of developing LHON has been associated with male gender and lifestyle factors, such as smoking and drinking (Kirkman et al., 2009, Matthews et al., 2015). However, increased mitochondrial biogenesis has been reported to be a protective factor in LHON penetrance (Giordano et al., 2014, Bianco et al., 2016). This suggests that the onset of clinical outcomes caused by mtDNA mutations might also be influenced by other genetic, environmental and epigenetic factors. This is not surprising giving the dual dependence of mitochondria on both nDNA and mtDNA, and the potential crosstalk between them (Chinnery et al., 2012).

1.3.2. Mutations in nuclear-encoded genes

In 1989, Zeviani and colleagues described an Italian family with adult-onset mitochondrial myopathy characterised by chronic progressive external ophthalmoplegia (CPEO) associated with multiple deletions of the mtDNA (Zeviani et al., 1989). Intriguingly, male patients also transmitted the disease to their offspring, excluding maternal inheritance and suggesting that the underlying genetic factors were not encoded in the mtDNA. Instead, the genetic trait was inherited in an autosomal dominant fashion. Such finding, argued for the first time that a mutation of a nDNA-coded protein could affect the integrity of the mtDNA in a specific, heritable way (Zeviani et al., 1989). However, at the time the precise

genetic mutation was not identified due to lack of proper untargeted diagnosis techniques. It was only almost 10 years later that the first nDNA mutations were identified causing mitochondrial disease (Nishino et al., 1999). These mutations were in the thymidine phosphorylase gene (*TP*) and were associated with multiple deletions of mtDNA in patients with mitochondrial neuro-gastro-intestinal leukoencephalopathy (MNGIE) (Nishino et al., 1999). Since then, with the advent of whole exome sequencing (WES) for molecular diagnosis, more than 150 nuclear genes were identified to cause mitochondrial diseases (Stenton and Prokisch, 2020). It is estimated that ~20% of adult-onset and 75–80% childhood-onset mitochondrial diseases are caused by nDNA mutations (Thorburn, 2004, Lebon et al., 2003), in which autosomal recessive mutations are the underlying cause of most of the severe childhood-onset syndromes (Skladal et al., 2003).

In principle, pathogenic mutations in the genes encoding any of the more than 1000 proteins imported into mitochondria can potentially lead to mitochondrial dysfunction and thereby, mitochondrial disease. Such mutations can directly or indirectly affect proteins involved in OXPHOS (Ghezzi and Zeviani, 2018). Apart from the mtDNA-encoded OXPHOS proteins, mitochondria import several nuclear-encoded components for accurate function and assembly (including all subunits of CII). Therefore, mutations in any of the structural subunits and assembly factors can result in loss of core components or complications in assembling them, directly affecting OXPHOS (Ghezzi and Zeviani, 2018). In addition, mutations in nuclear-encoded genes can affect OXPHOS indirectly by impairing processes related to the proper formation of OXPHOS. These include, but not restricted to, proteins involved in mtDNA maintenance and gene expression (mtDNA replication, transcription and translation), dNTP supply for mtDNA synthesis, protein quality control in mitochondria and mitochondrial dynamics (fusion and fission) (Viscomi and Zeviani, 2017). For example, genetic mutations have been identified and associated with mitochondrial diseases in all components of the minimal *in vitro* mtDNA replisome: POLγA (Naviaux and Nguyen, 2005), POLγB (Longley et al., 2006), TWINKLE (Van Goethem et al., 2003) and mtSSB (Del Dotto et al., 2020). Pathogenic mutations in such genes can lead

to truncated or defective variants which can affect the quality of mtDNA by introducing mtDNA mutations or deletions or affecting mtDNA quantity by decreasing mtDNA copy number. In either way, production of mtDNA encoded proteins can be compromised and thus, indirectly affect OXPHOS triggering the pathogenesis of mitochondrial diseases (Viscomi and Zeviani, 2017).

1.3.2.1. *POLG*-related disorders

Mutations in *POLG*, encoding POLγA, the catalytic subunit of the mitochondrial DNA polymerase, are a major cause of human disease causing a spectrum of mitochondrial disorders characterized by mtDNA instability (Viscomi and Zeviani, 2017). Pathogenic *POLG* mutations were first identified in 1991, while studying the underlying genetic cause of autosomal dominant and recessive forms of PEO (adPEO or arPEO) in 3 Belgian families (Van Goethem et al., 2001). The study led to the association of a *POLG* mutation substituting Tyrosine with Cysteine at codon 955 (Y955C) with adPEO and 2 compound heterozygote missense mutations with arPEO, predicting a substitution of Alanine with Threonine at codon 467 (A467T) in one allele, substitution of Leucine with Arginine at codon 304 (L304R) (Van Goethem et al., 2001). After this report, over the years, more than 300 mutations have been described in *POLG* (Figure 1.8). (Human DNA Polymerase Gamma Mutation Database: https://tools.niehs.nih.gov/polg/).

Four mutations (A467T, W748S, G848S and the T251I–P587L allelic pair) account for ~50% of all mutations identified in patients with *POLG*-related diseases, with ~75% of patients carrying at least one of these mutant alleles (Uusimaa et al., 2013). The A467T is the most frequent POLγA mutation in Scandinavian and Northern European Countries, together with another change, the W748S mutation, which belongs to the Finnish disease heritage (Ferrari et al., 2005, de Vries et al., 2007, Horvath et al., 2006, Nguyen et al., 2006).

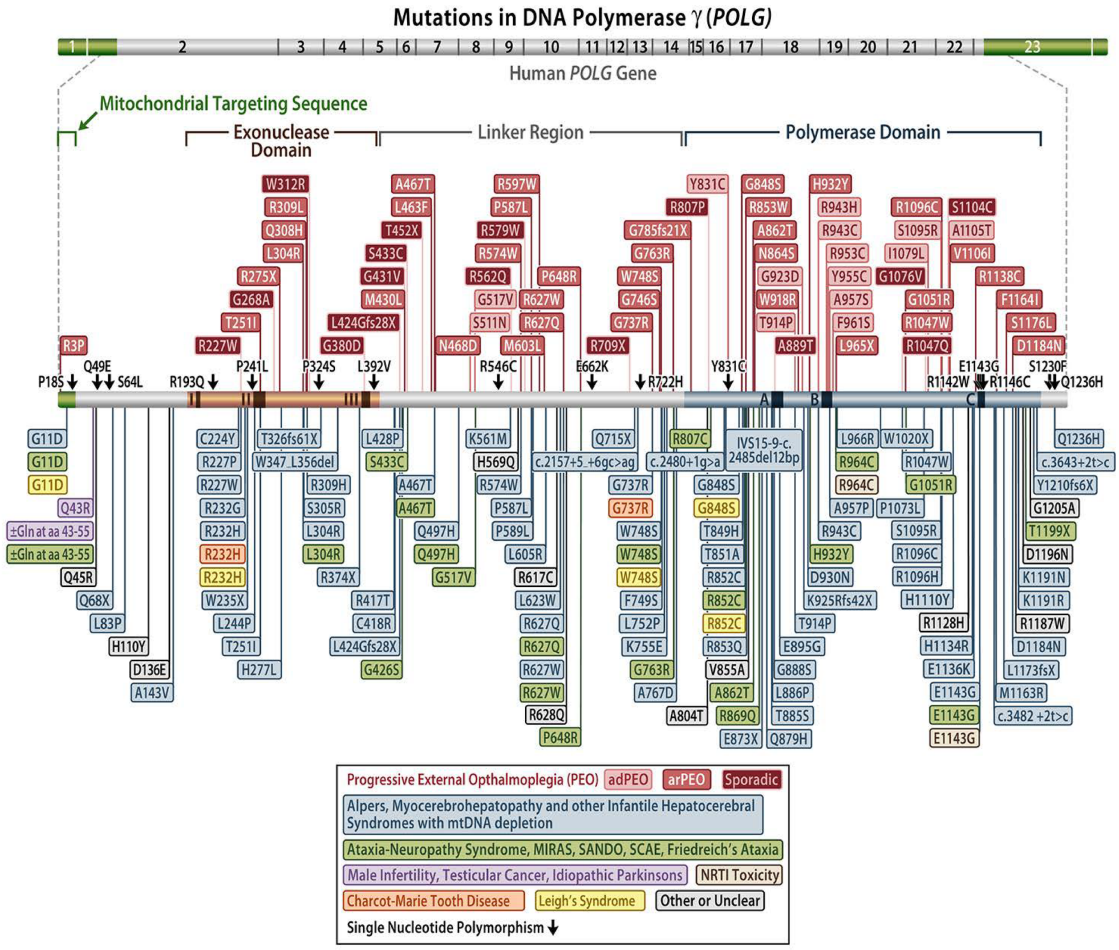

Figure 1.8. Pathogenic mutations on human *POLG* gene.
Schematic representation of the pathogenic mutations identified in the coding region of the *POLG* gene and respective location in the different domains of the POLγA protein. Figure retrieved from the Human Polymerase Gamma Database (https://tools.niehs.nih.gov/polg/index.cfm) on 19/08/2021.

POLG mutations may lead to mtDNA instability, and depending on the nature of the mutation, they can cause either multiple deletions or depletion of mtDNA copy number. Overall, depletion of mtDNA is normally associated with early-onset more severe paediatric syndromes, while mtDNA deletions are associated with later-onset more benign diseases, such as PEO. However, there is not always an obvious genotype–phenotype correlation, as in various occasions the same mutation can often lead to mtDNA deletions, mtDNA depletion or both (Figure 1.9). As an example, the A467T mutation is often associated with depletion of mtDNA, however in rare occasions, large-scale rearrangements such as deletions are found in critical tissues, particularly in specific regions of the brain (Van Goethem et al., 2001, Tzoulis et al., 2014). Consequently, it is difficult to firmly

classify *POLG*-associated diseases as often symptoms overlap, the same mutation can be associated to more than one syndrome, and each phenotype can be the consequence of the combination of different allelic mutations (for example A467T in one allele and W748S in the other). The wide spectrum of *POLG*-diseases, has been tentatively classified in the following categories with decreasing level of severity: (i) the severe early-onset Alpers-Huttenlocher syndrome (AHS), (often associated with the A467T mutation in compound heterozygosity with a truncating allele), characterised by refractory epilepsy due to severe spongiotic atrophy of the brain, and hepatic failure (ii) myocerebrohepatopathy spectrum (MCHS), which presents with developmental delay, lactic acidosis, myopathy and hepatic impairment; (iii) the typical spectrum of the A467T and W748S mutations (in either homozygosity or in combination), including myoclonic epilepsy myopathy sensory ataxia (MEMSA), comprising spinocerebellar ataxia with epilepsy (SCAE), frequently associated with sensory ataxia neuropathy with dysarthria and ophthalmoplegia (SANDO), and, (iv) finally, the late-onset autosomal dominant and recessive progressive external ophthalmoplegia (ad and arPEO) (Rahman and Copeland, 2019). A prototypical example is highlighted by the homozygous mutation A467T mutation, which has been associated with a range of phenotypes, from childhood-onset fatal AHS to MEMSA, ANS, SANDO and arPEO (Rahman and Copeland, 2019, Tzoulis et al., 2006).

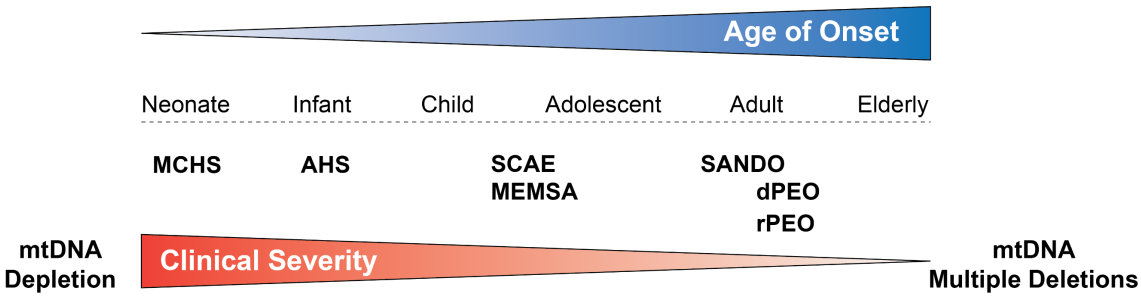

Figure 1.9. Continuous clinical spectrum of *POLG*-related disease.
Clinical syndromes of *POLG*-related disease according to age of onset and clinical severity. Broadly speaking, earlier onset syndromes manifest more severe clinical presentations. MtDNA depletion is often associated with earlier onset, more severe syndromes, while mtDNA multiple deletions are associated with the other end of the spectrum with later onset, milder manifestations. MCHS, myocerebrohepatopathy spectrum; AHS, Alpers–Huttenlocher syndrome; SCAE, spinocerebellar ataxia with epilepsy; MEMSA, myoclonic epilepsy myopathy sensory ataxia; SANDO, sensory ataxia neuropathy dysarthria and ophthalmoplegia; dPEO, dominant progressive external ophthalmoplegia; rPEO, recessive progressive external ophthalmoplegia.

In addition, the age of onset and the progression of *POLG*-related disease in patients with the same *POLG* mutations is amazingly variable and can span several decades. For instance, the onset of disease spans >70 years in compound heterozygous patients carrying the T251I/P587L mutations on one allele and the G848S mutation on the other (DeBalsi et al., 2017), and it spans at least four decades of life in most of the homozygous A467T patients (Tzoulis et al., 2006, Rajakulendran et al., 2016).

As mentioned, *POLG* mutations can be transmitted to offspring either as autosomal dominant or recessive mutations, and among the recessive ones, by far the most common is the A467T mutation associated with mtDNA depletion, whereas the Y955C is the most common variant within dominant traits, usually associated with the accumulation of mtDNA multiple deletions (Nurminen et al., 2017).

The A467T mutation affects the intermediate region between the proofreading and the polymerase domain of POLγA, generically defined as the "linker" region. The linker region seems to be the structural part where POLγA interacts with the accessory subunit POLγB, which is crucial for the processivity of the holoenzyme (Lee et al., 2009). Thus, the proposed pathogenic mechanisms, based on *in vitro* evidence, include lowering of the catalytic activity and reduction of the affinity for POLγB (Chan et al., 2005). All this would lead to stalling of the replication fork and depletion or instability of mtDNA.

In turn, the Y955C mutation sits in the polymerase domain of POLγA in a region that directly interact with the incoming dNTP (Graziewicz et al., 2004). *In vitro* characterization, revealed severely reduced catalytic activity and lower processivity due to decreased capacity to utilize dNTPs, in particularly when incorporating dATP (Atanassova et al., 2011). This decrease in polymerase activity is therefore the probable cause of mtDNA instability seen in patients with the Y955C mutation.

1.3.2.1.1. Drug-induced toxicity in *POLG* disorders

POLG-related disorders as well as other mitochondrial diseases are particularly sensitive to medicines well recognised to affect mitochondrial functions such as some antibiotics, statins, anaesthetics and chemotherapeutics (Nadanaciva and Will, 2011). Such substances normally do not present side effects in "healthy" individuals, but because *POLG*-patients already present some degree of mitochondrial dysfunction, these drugs can precipitate the disease (Rahman and Copeland, 2019).

Valproic acid (VPA) is a widely-used treatment for epilepsy, a symptom present in many *POLG* patients, as discussed in the previous section. VPA is normally well tolerated with little side effects. However, VPA administration induces a profound toxic reaction in several patients carrying *POLG* mutations, culminating in fatal liver failure (Tzoulis et al., 2006, Stewart et al., 2010). For this reason, VPA is contraindicated in patients with *POLG*-related disease and sequencing of *POLG* is recommended prior to administration of VPA to treat epilepsy (Saneto et al., 2010). VPA is a histone deacetylase inhibitor but is also known to inhibit fatty acid β-oxidation, which primarily occurs in the liver. However, the exact mechanism of action of VPA in the treatment of epilepsy remains poorly understood, similar to the reason why VPA triggers toxicity in *POLG* patients (Johannessen, 2000).

Nucleoside reverse transcriptase inhibitors (NRTIs) are antiviral drugs that are used worldwide to treat HIV infection (Holec et al., 2017). This class of drugs act by inhibiting the reverse transcriptase of the HIV virus, stalling its life cycle. However, NRTIs have also been shown to inhibit POLγ and consequently to trigger a reduction in mtDNA copy number in several patients (Lewis et al., 2003, Young, 2017, Dalakas et al., 1990). About 20% of the patients undergoing NRTI therapy present clinical symptoms resembling the ones of mitochondrial disease patients (Dalakas et al., 1990, Arnaudo et al., 1991). Although most cases of NRTI-induced mitochondrial toxicity were reported in non-*POLG* patients, caution should be taken when prescribing NRTI to these patients.

1.3.3. Emerging Mitochondrial Disease Therapies

Recent years have witnessed a transformation in the diagnostic and understanding of mitochondrial diseases. In most cases, mitochondrial diseases are highly disabling, complex conditions characterized by multisystem dysfunction, with a prevalence of neurological impairment. Currently, no curative therapies for mitochondrial disorders are available and interventions are based on management of the complications (such as epilepsy) and supportive care to the patient. Therefore, the identification of therapeutic options for mitochondrial disorders has been a major focus of mitochondrial research. Potential therapeutic strategies have been evaluated in pre-clinical models, including, but not restricted to, supplementation of dNTPs to bypass mtDNA replication defects (Garone et al., 2014), administration of the compound AICAR to favour mitochondrial biogenesis (Viscomi et al., 2011) and supplementation with antioxidants to reduce ROS (de Haas et al., 2017). In addition to these, gene therapy has been suggested as a promising therapeutic option for mitochondrial patients, particularly due to the encouraging advances of this field in the treatment of other non-mitochondrial disorders (Garone and Viscomi, 2018, Wang et al., 2019).

1.3.3.1. Gene Therapy

The concept of "gene therapy" was introduced in the 1970s, as a gene replacement therapy (Aposhian, 1970, Rogers, 1971, Osterman et al., 1970, Fox and Littlefield, 1971). Gene replacement therapy comprises the possibility of re-expressing the WT form of a missing or mutated gene, hopefully ameliorating the patients´ symptoms by restoring the original function of the "sick" gene. Such strategy is very attractive for all genetic diseases, including mitochondrial diseases, especially those with underlying mutations behaving as monogenic recessive traits, in which a WT copy is enough to avoid disease (Gillet et al., 2009).

The first gene therapy clinical trial was launched in 1990. In this trial, two young girls were treated for severe combined immunodeficiency, caused by mutations in the adenosine deaminase (*ADA*) gene. Functional copies of the gene encoding the ADA enzyme were introduced into peripheral blood T lymphocytes using a

retrovirus as vector. Such intervention improved patients´ immune system and allowed them to live a normal life (Blaese et al., 1995). The report of this trial constituted evidence that gene therapy can be a safe and effective treatment for several patients with monogenic disorders. Since then, many other clinical trials of gene therapy have been performed for a broad array of conditions (cancer, cardiovascular disease, AIDS, cystic fibrosis, Gaucher disease) (Bulaklak and Gersbach, 2020).

The major challenge of gene therapy is the development of safe and effective delivery vectors. Over the years, two types of vectors have been explored for systemic gene delivery in clinical trials, divided in viral vectors and non-viral vectors (Yin et al., 2014). Most gene therapy clinical trials have used attenuated recombinant viruses such as retroviruses, lentiviruses, adenoviruses and adeno-associated viruses (AAVs) by substituting elements of the original virulent genetic material with therapeutic genes (Yin et al., 2014). These viral vectors allowed an unprecedented progress in the field of gene therapy, but have also unravelled several limitations, particularly in terms of safety, as they have been association with carcinogenesis and adverse immune response (Baum et al., 2006, Bessis et al., 2004). To overcome these problems, non-viral gene therapy has been developed by exploiting synthetic molecules, such as liposomes and polymers, that aid delivery of DNA to the cell (Mintzer and Simanek, 2009). These vectors have lower immunogenicity than viral vectors and bypass the potential problem of pre-existing immunity against the capsid proteins of the virus (Pack et al., 2005, Mintzer and Simanek, 2009). Nevertheless, non-viral vectors present low systemic delivery efficiency compared to viruses, which underwent evolution to deliver their genomes efficiently into the cells (Yin et al., 2014).

1.3.3.1.1. Adeno-associated viral vectors (AAVs)

Adeno-associated viral vectors (AAVs) are currently the leading platform for *in vivo* delivery in gene therapy (Naso et al., 2017). AAVs are particularly attractive as delivery method because of their favourable safety profile and the availability of several tissue-specific serotypes. The main limitations concern the limited cloning

capacity (~4.7 kb total or half of this in self-complementary AAVs) and the difficulty in achieving therapeutic expression levels in certain tissues (Naso et al., 2017).

AAVs were first discovered in the 1960s, in laboratory preparations of adenovirus, hence its name and taxonomy (Atchison et al., 1965). After their discovery, AAV biology became an intense area of research, which collectively culminated in the development of AAVs as a delivery vector and the generation of the recombinant AAVs used today in gene therapy (Wang et al., 2019).

The AAVs found in nature are composed of an icosahedral protein capsid of ~26 nm in diameter encapsidating a ssDNA genome of ~4.7 kb that can either be the plus (sense) or minus (anti-sense) strand. This relatively small and simple genome is flanked by two T-shaped inverted terminal repeats (ITRs) at each end, which serve as the viral origins of replication and the packaging signal. Furthermore, it encodes three genes, the *rep* gene encoding proteins required for viral replication (Rep78, Rep68, Rep52 and Rep40), the *cap* gene encoding the three subunits of the capsid (VP1, VP2 and VP3), and a third gene encoding the assembly activating protein (AAP), shown to promote virion assembly (Wang et al., 2019). In turn, the genomes of recombinant AAVs are manipulated to replace all the viral protein-coding sequences by therapeutic transgene sequences and the regulatory elements necessary to sustain gene expression, such as promoters and polyadenylation signals (Wang et al., 2019). The removal of the viral elements turns the resulting AAV in a replication-incompetent virus ameliorating safety issues and reducing immune response, while maximizing the packaging capacity for therapeutic sequences (~4.7 kb total) (Wang et al., 2019). The only retained viral sequence are the ITRs which are strictly necessary to guide genome replication and packaging during recombinant vector production (Wang et al., 2019).

AAVs differ in their tropism for various target tissues, i.e. different AAVs selectively target with more efficiency one organ than others. The tropism is mainly determined by the molecular interactions between the capsid and target cell surface receptors such as glycoproteins. Therefore, AAVs are classified into serotypes based on the surface antigens presented in the capsids, which often

reflects their different tissue-type and cell-type tropism profiles (Nonnenmacher and Weber, 2012, Agbandje-McKenna and Kleinschmidt, 2011). Over the years, numerous natural AAV serotypes were identified from humans and other species (Gao et al., 2002), while others were engineered by rational design and/or directed evolution to obtain recombinant AAVs with a desired tropism profile (Chen et al., 2009, Warrington et al., 2004, Maheshri et al., 2006). For example, the AAV serotype 9 (AAV9) is a natural serotype first isolated from human liver tissue with widespread tropism but presenting a preference for liver (Gao et al., 2004). However, a screening of randomly mutagenized capsids of AAV9, led to a generation of a subtype AAV9.45 which has liver-detargeted tropism (Pulicherla et al., 2011). This and similar strategies, led to an ever-growing collection of natural and engineered tissue-specific AAV serotypes with desired therapeutic and tissue-targeting features, which allow the development of gene therapies for an array of specific diseases.

Several gene therapy approaches using AAV vectors are currently being developed for neuromuscular diseases, with some having gained regulatory approval, for example, voretigene neparvovec (Luxturna) to treat Leber congenital amaurosis (Russell et al., 2017) or onasemnogene abeparvovec (Zolgensma) to treat paediatric spinal muscular atrophy (Mendell et al., 2017). Nevertheless, the only AAV-based therapy currently under clinical trial for mitochondrial diseases is based on re-expression of the mtDNA-encoded *MT-ND4* gene, mutated in patients with Leber hereditary optic neuropathy (LHON). Favourable results of a phase 3 trial reported improved visual function in AAV-treated LHON subjects (Yu-Wai-Man et al., 2020).

These studies serve as examples for the potential of AAV-based gene replacement to achieve curative therapy of mitochondrial disorders. However, several mitochondriopathies, including those related to *POLG*-mutations, have a strong neurological involvement, particularly the paediatric cases. Gene delivery to the central nervous system (CNS), however, is still very challenging mainly because of the presence of the blood-brain barrier (BBB). The BBB is formed by endothelial cells, astrocytes and pericytes, creating a semipermeable physiological barrier that

separates the circulating blood from the central nervous system (Daneman and Prat, 2015). The BBB allows the passage of some molecules by passive diffusion, as well as the selective transport of molecules such as glucose, water, and amino acids that are crucial to neural function. However, this barrier restricts the diffusion of many solutes in the blood, and large or hydrophilic molecules into the cerebrospinal fluid (CSF), but importantly, it also hampers the passage of pathogens, including AAVs (Daneman and Prat, 2015). Several strategies have been exploited to bypass the BBB and deliver AAVs to the brain in both preclinical models and humans (Hudry and Vandenberghe, 2019). One of these strategies involves injecting AAVs directly in the brain (intracranial injections). However, this approach is not only invasive but also leads to localised therapeutic gene expression around the injection area, thereby not constituting a solution for most patients in which a widespread CNS expression is required (Hudry and Vandenberghe, 2019). Therefore, the development of AAV serotypes enabling widespread CNS transduction via systemic delivery is a major focus of gene therapy research (Li and Samulski, 2020).

The natural AAV9 was further engineered with the aim of being used in gene transfer into the CNS, since it appears to have modest ability to cross the BBB (Foust et al., 2009). However, therapeutic levels of expression in the brain are only achieved when using higher titers of the virus. This raises concern about the risk of toxicity in other tissues where AAV9 has a higher tropism as well as undesirable immune response (Inagaki et al., 2006, Hinderer et al., 2018). Recently, an engineered AAV9 subtype, called AAV-PHP.B, has demonstrated a remarkable capacity to cross the BBB when intravenously injected in adult C57BL/6 mice, leading to widespread CNS transduction and targeting both neurons and glial cells (Deverman et al., 2016). The AAV-PHP.B was developed by screening a library of AAV variants subject to selective pressure for increased capacity to cross the BBB (Deverman et al., 2016). This exceptional property was subsequently found to be mediated by a membrane glycoprotein of the brain endothelia, the lymphocyte antigen 6 complex, locus A (LY6A) receptor whose function had been thought to be limited to the biology of haematopoiesis (Batista et al., 2020).

1.4. Project Aims

Mutations in *POLG*, encoding POLγA, the catalytic subunit of the mitochondrial DNA polymerase, are a major cause of human mitochondrial disease (Viscomi and Zeviani, 2017). *POLG*-related syndromes are clinically heterogeneous in which the same mutation can be associated to more than one presentation, affecting different tissues and with variable age of onset among patients. The reasons for such complexity, tissue specificity and the exact molecular pathogenic mechanism of *POLG* mutations is still poorly understood. In addition, the substantial lack of relevant *in vivo* models has hampered our understanding of the pathogenesis of *POLG*-related disorders, which in turn delays the development of therapies. Currently, no curative therapies for mitochondrial disorders are available.

<u>The three main aims of this work are:</u>

1) to generate mouse models expressing common pathogenic *POLG* mutations found in human patients;

2) to elucidate the molecular pathogenic mechanisms of common *POLG* mutations using *in vivo* models complemented with *in vitro* techniques;

3) to explore AAV-mediated gene therapy as a therapeutic option for mitochondrial disease patients.

In **Chapter 3**, I describe the generation of two *POLG* knockin mouse models, corresponding to the human A467T and Y955C mutations.

In **Chapter 4**, I provide a systematic *in vivo* and *in vitro* mechanistic characterisation of the *POLG* A467T mutation, and insights on the impact of this mutation in mtDNA replication and POLγA stability.

In **Chapter 5**, I explore the use of a novel AAV-PHP.B capsid as a gene therapy platform to ameliorate the neurological symptoms of a mouse model of mitochondrial disease.

Chapter 2 Material and Methods

2. Material and Methods

2.1. Mouse Models and Associated Procedures

All animal experiments were carried out in accordance with the UK Animals (Scientific Procedures) Act 1986 (PPL: P6C20975A) and EU Directive 2010/63/EU. The *Polg*$^{A449T/A449T}$ and *Polg*$^{A449T/KO}$ mice were kept on FVB/NJ background, and WT littermates were used as controls. The *Ndufs4*$^{-/-}$ mice were kept on C57BL/6J background, and WT littermates were used as controls. The animals were maintained in a temperature- and humidity-controlled animal care facility with a 12-h light/12-h dark cycle and free access to water and food, and they were monitored weekly to examine body condition, weight and general health. The mice were sacrificed by cervical dislocation at the indicated age for subsequent analysis.

The data related to the *Lonp1* knockout mouse was courtesy of Dr. Aleksandra Trifunovic and the experiment carried by Dieu-Hien Rozsivalova.

Lonp1 gene targeting (*Lonp1*$^{+/tm1a(EUCOMM)Hmgu/Ieg}$, project number HEPD0936_3_B11) was carried out as part of the The European Conditional Mouse Mutagenesis Program (EUCOMM), on the C57BL/6NTac genetic background. We generated the heart and skeletal muscle (SKM)-specific *Lonp1* knockout mice by mating *Lonp1*$^{fl/fl}$ animals with transgenic mice expressing cre recombinase under the control of muscle creatine kinase promoter (*Ckmm*-cre) (Larsson et al., 1998), after removal of a gene-trap DNA cassette. Experiments were performed on 12-week-old mice. All experiments on *Lonp1*$^{fl/fl}$; Ckmm-Cre animals were approved and permitted by the Animal Ethics Committee of North-Rhein Westphalia (Landesamt für Natur, Umwelt und Verbraucherschutz Nordrhein-Westfalen; LANUV) following the German and European Union regulations.

2.1.1. Generation of the *Polg*$^{A449T/A449T}$ and *Polg*$^{A449T/KO}$ mice

The *Polg*^{A449T} mice were generated using the double nickase CRISPR/Cas9 D10A approach, with all the components of the system (Cas9-D10A, gRNAs and HDR template) injected directly in fertilised one-celled oocytes. A detailed explanation of the strategy is described in Section 3.3.

The Cas9 D10A mRNA (Sigma-Aldrich, CAS9D10AMRNA-1EA), IVT gRNAs (GeneArt) and HDR donor (IDT) were sent to the 'Core Facility for Conditional Mutagenesis' at the IRCCS Ospedale San Raffaele, (Milan, Italy) for microinjection into fertilised mouse one-celled zygotes. Genotyping of the resulting pups allowed the identification of founder mice (F0), heterozygous for the A449T allele, *Polg*$^{WT/A449T}$. The *Polg*$^{WT/A449T}$ mouse was then bred with a WT FVB/NJ mouse. Genotyping of the originated pups (F1) showed the presence of the A449T allele and confirmed germline transmission and successful generation of a *Polg*^{A449T} mouse line. *Polg*$^{A449T/A449T}$ mice were obtained by breeding two heterozygous *Polg*$^{WT/A449T}$. Genotyping of the *Polg* A449T allele is described in Section 2.3.3.3.

The *Polg*$^{A449T/KO}$ mouse was generated by crossing the *Polg*$^{A449T/A449T}$ mice with a *Polg*$^{WT/KO}$ mouse, obtained from Trifunovic´s lab (Hance et al., 2005). Because the *Polg*$^{WT/KO}$ mouse was previously kept in a C57BL/6 background, the *Polg*$^{A449T/KO}$ mice were crossed back with FVB/NJ mice for at least 8 generation to allow direct comparison with *Polg*$^{A449T/A449T}$ mice.

2.1.2. Generation of the *Polg*$^{WT/Y933C}$ mouse

The *Polg*^{Y933C} mice were generated using the single nuclease CRISPR/Cas9 WT approach, with all the components of the system (Cas9-WT, gRNAs and HDR template) electroporated first in embryonic stem (ES) cells, followed by a screening of positive clones, and generation of chimeric mice harbouring the *Polg* Y933C allele. A detailed explanation of all the different strategies applied to generate the *Polg*^{Y933C} mice are described in Section 3.4.

The Cas9 WT mRNA (Sigma-Aldrich, CAS9MRNA), the IVT gRNA-Fw1 (5´- ATG GCC GCA TCT ATG GGG CT – 3´) (GeneArt) and the HDR template (IDT) were sent to the "Core Facility for Conditional Mutagenesis" at the IRCCS Ospedale San Raffaele, (Milan, Italy), where they were delivered to mouse ES cells by electroporation. The cells were then seeded as single clones in 96-well plates and allowed to grow for DNA extraction as described in Section 2.3.1.1. One of the identified positive clones (3B2p20L2) was expanded and microinjected into

blastocysts, originating one female mouse with ~40% chimerism. The chimera was then bred with a WT male to verify germline transmission. Genotyping of the resulting pups allowed the identification of founder mice (Fo), heterozygous for the Y933C allele, *Polg*$^{WT/Y933C}$, and confirmed generation of a *Polg*^{Y933C} mouse line. The genotyping protocol either by PCR or Sanger sequencing are described in Section 2.3.3.5 and Section 2.3.6, respectively.

2.1.3. Metabolic and Phenotypic Analysis

2.1.3.1. CLAMS™

A Comprehensive Lab Animal Monitoring System (CLAMS) apparatus (Columbus Instruments), was used to measure the total spontaneous movements for a period of 48h, taking in account the 12h light/dark cycle, according to the manufacturer's instructions. Data for each mouse were collected every 10-minutes. The following parameters were recorded: VO2 (volume of oxygen consumed, ml/Kg/hr), VCO2 (volume of carbon dioxide produced, ml/Kg/hr) and locomotor activity in the xyz axis (measured as infrared beam interruptions, termed 'counts'). The respiratory exchange ratio (RER) was calculated as ratio between the amount of carbon dioxide produced and oxygen consumed.

2.1.3.2. Treadmill

A standard treadmill apparatus (Panlab) was used to measure motor endurance according to the number of falls in the motivational air puff during a gradually accelerating program with speed initially at 6.5 m/min and increasing by 0.5 m/min every 3 min. The test was terminated by exhaustion, defined as >10 air puffs activations/min.

2.1.3.3. Rotarod

A rotarod apparatus (Ugo Basile, Varese, Italy) was used to assess motor performance and coordination. During the test, mice had to maintain themselves on a rod turning at accelerating speeds. The latency to fall was recorded. Three trials were completed setting the apparatus to accelerate from 2 to 40 rpm in 300 seconds.

2.1.4. Pharmacological Treatments

2.1.4.1. Valproic Acid (VPA)

In VPA-treated *Polg*$^{A449T/A449T}$ and WT mice, VPA (Sigma) was administrated by daily oral gavage (300 mg/kg in water) for 2 weeks or added to a standard diet at 1.5% (1.5 g VPA/1 kg food) and administered for 60 days, starting at 8 weeks of age. VPA-treated mice were observed twice daily during the experiment. The weights were registered daily for the first 10 days of the experiment and then twice weekly until sacrifice. At sacrifice livers were collected for histological and molecular analysis as described in Section 2.1.6.2 and Section 2.3.3.9.1, respectively. A sample of blood was also collected for evaluation of Alanine Aminotransferase (ALT) levels. ALT values were determined in serum isolated from total blood samples. Briefly, blood was centrifuged for 5min at 4000 x rpm and serum was collected as supernatant. Serum analysis were carried out by the Core Biochemical Assay Laboratory of the Addenbrookes´s Hospital (Cambridge, UK).

2.1.4.2. Carbon Tetrachloride (CCl_4)

Polg$^{A449T/A449T}$ and control mice received a single intra-peritoneal injection of CCl_4, 1 mL per kg of body weight diluted 1/10 in olive oil (Sigma). Mice were weighted before injection to adjust the volume accordingly. Half of the mice were sacrificed at day 2 post-injection and the other half at day 4 post-injection. An untreated group was used as day 0 (pre-treatment). Livers were collected for histological analysis and processed as described in Section 2.1.6.2.

2.1.5. *In vivo* Adeno-Associated Virus (AAVs) Transduction

The plasmid encoding the AAV-PHP.B capsid was kindly provided by Dr. B.E. Deverman. The AAV2-CMV (cytomegalovirus)-h*NDUFS4* vector was generated by Dr. Carlo Viscomi and previously described (Di Meo et al., 2017). Both plasmids were used to generate the AAV particles. The AAV-PHP.B-h*NDUFS4* particles were synthesized by the AAV Vector Core of the Telethon Institute of Genetics and Medicine (TIGEM, Naples, Italy) and suspended in storage buffer (1 X PBS with 350 mM NaCl + 5% D-Sorbitol) until use at -80 ^{o}C.

A single injection of 1-2 x 10^{12} viral genomes of AAV-PHP.B-h*NDUFS4* was achieved in adult *Ndufs4*$^{-/-}$ mice (between P26-28) by tail-vein intravenous injection. Injections of 1 x 10^{12} viral genomes of AAV-PHP.B-h*NDUFS4* in newborn *Ndufs4*$^{-/-}$ mice (P1) was achieved via the temporal vein. All injections were carried with a 30G, 30° bevelled needle syringe (SOL-VET). Injected mice were observed twice daily during the experiment. The weights were registered daily up to 90 days of the experiment and then weekly.

2.1.6. Histological Analysis

2.1.6.1. Tissue preparation and processing

Mice were sacrificed at the indicated age by cervical dislocation. The organs were quickly dissected and samples for histology analysis were taken. Liver, brain, kidney and heart samples were placed in formaldehyde, in the form of 10% neutral buffered formalin (NBF). The NBF guarantees preservation of tissue and cell morphology, hardening of the samples for posterior processing, inactivation of proteolytic enzymes and protection of the samples against contamination and decomposition. After several days of fixation, samples were processed and infiltrated in paraffin (Leica). The paraffin block containing the samples were then sectioned on a Leica RM2245 semi-automated rotary microtome to a thickness of 4 µm. These sections were then stained with H&E and PathoGreen, or were subjected to immunohistochemistry as detailed below. In turn, gastrocnemius (skeletal muscle) samples for histology were frozen by immersion in isopentane

pre-cooled with liquid nitrogen and stored at -80 °C until analysis. This method is commonly used to preserve enzymes and their enzymatic activity, which is particularly important when performing COX and SDH staining. For histological preparation, each sample was mounted into a specimen disk with optimal cutting temperature compound (OCT), and sectioned on cryostat at -20 °C to a thickness of 8 µm, fixed with alcohol and washed with deionised water. These sections were then stained with H&E or subjected to COX and SHD staining, as detailed below. All histological preparations of tissues and analyses described in this work were performed by Raffaele Cerutti (Zeviani´s lab).

2.1.6.2. Haematoxylin and Eosin (H&E) staining

H&E staining was performed in 4-mm-thick paraffin sections. It is one of the most common methods used to show overall structure of the tissue, with nuclei stained blue, muscle fibres pink and the connective tissues a lighter pink. Sections were placed in Mayer's haematoxylin for 5 mins, rinsed with tap water for 3 mins, and then transferred in 1 % eosin-Y solution for 15 secs. Sections were then washed with tap water, and dehydrated with a series of ascending alcohol concentrations (70 – 100 %). Finally, stained sections were cleared in xylene and mounted with dibutylphthalate polystyrene xylene (DPX) mountant.

2.1.6.2.1. Necrotic area quantification

Quantification of necrotic areas was done in H&E stained 4-mm-thick paraffin sections from liver samples of CCl_4 treated mice. Quantification was performed with digitally captured images using ImageJ software by dividing the necrotic areas around the central veins by total area of the section. Five different regions of the slide were analysed and average value obtained.

2.1.6.3. Cytochrome C Oxidase (COX) and Succinate dehydrogenase (SDH) staining

Histological analysis of COX activity was performed in 8-mm-thick cryostat sections of skeletal muscle, using diaminobenzidine (DAB) as an electron acceptor to produce a brown end-product. Each section was incubated for 40 minutes at 37 °C with 10 ml of COX activity solution [5 µM DAB and 100 µM cytochrome c in 100 mM sodium phosphate buffer (pH = 7.4)].

Histological analysis of SDH activity was performed in 8-mm-thick cryostat sections of skeletal muscle, using nitroblue tetrazolium (NBT) as an electron acceptor to produce a deep blue colour. Each section was incubated for 30 minutes at 37 °C with 10 ml of SHD activity solution [35.2 mg/ml succinate, 1.22 mg/ml NBT, 61 µg/ml PMS and 65 µg/ml sodium azide in 100 mM sodium phosphate buffer (pH = 7.0)].

At the end of incubation, both COX and SDH sections were rinsed in tap water, dehydrated with a series of ascending alcohol concentrations, cleared with xylene and mounted with DPX.

2.1.6.4. Immunohistochemistry (IHC)

Immunohistochemistry was performed in 4-mm-thick paraffin sections of the indicated brain regions, using the Novolink Polymer Detection System (Leica, RE7140-K), following manufacturer´s recommendations. Slides were deparaffinised with xylene and rehydrated with graded alcohols. Antigen retrieval was then performed to expose the antigenic sites and allow binding of the primary antibodies. The slides were washed twice with deionised water and endogenous peroxidase was neutralised with Peroxidase Block for 5 mins. Then, the slides were washed twice with 1 X TBS (tris-buffered saline buffer) and incubated in Protein Block for 5 mins. The slides were washed again twice with 1 X TBS and incubated with the primary antibody ON at 4 ^{o}C. List of primary antibodies and dilutions are presented in Table 2.1. The next day, slides were washed twice with 1 X TBS and incubated with Post Primary for 30 mins. The slides were washed again twice with

1 X TBS and incubated with the "secondary" NovoLink™ polymer for 30 mins at RT. After the secondary, slides were washed twice with 1 X TBS for 5 mins with gentle rocking. The slides were then incubated with DAB working solution for 5 mins to develop peroxidase activity, which produces a brown precipitate at the antigen site. The slides were finally rinsed in deionised water, dehydrated, cleared and mounted.

Table 2.1 Antibodies used for immunohistochemistry.

Antigen	Host	Dilution	Manufacturer (CN)
NDUFS4	Rabbit	1:100	Novus Biologicals (NBP1-31465)
CD68	Rabbit	1:100	Abcam (ab125212)
GFAP	Mouse	1:1000	Sigma-Aldrich (G3893)

2.1.6.5. PathoGreen (PG) staining

PathoGreen stain™ (Biotium, 80027) was performed in 4-mm-thick paraffin sections of the indicated brain regions. PathoGreen is a green fluorescent dye that stains degenerating neurons by an unknown mechanism. Slides were deparaffinised with ethanol and rehydrated. Sections were then incubated in a 0.06 % potassium permanganate solution for 10 mins, rinsed twice with distilled water and further incubated in distilled water for 2 mins. Slides were then incubated for 10 mins in 1 X PathoGreen™ staining solution (1:1000 stock in 0.1 % acetic acid), rinsed three times for 1 min each with distilled water and then air-dried on a slide warmer at 50-60 ^{o}C for at least 5 mins. At the end of incubation, sections were cleared in xylene and mounted with DPX.

2.2. Cellular models and Associated Procedures

2.2.1. Mouse Embryonic Fibroblasts (MEFs) isolation

MEFs were isolated from embryos at embryonic stage of 12.5 to 13.5 days. A breeding pair of mice (male and female) was set in the morning. The next day the

vaginal plug was checked, and the male was removed from positive females. After 12 days the pregnant female was sacrificed, the abdominal wall and uterus were cut through and embryos retrieved from the uterus and placed in a 50 ml falcon filled with ice-cold PBS without Ca^{2+} and Mg^{2+} (Life Technologies, Gibco®). In a tissue culture hood, the embryos were individually placed in 6-well plates containing PBS. Each embryo was then dissected with sterilised surgical instruments. The yolk sack was removed, all the red tissue (heart and liver), limbs, tail and head were removed. The head was kept for further DNA extraction (Section 2.3.1.1) and genotyping of the individual MEFs lines (Section 2.3.3.3).

The rest of the embryo was minced with scissors into 1–2 mm pieces and washed with PBS. The resulting homogenate was then transferred to a 15 ml falcon and centrifuged (200 g for 5 minutes at RT). The wash with PBS was repeated and the final pellet was re-suspended in 1 ml of digestion solution [40 mg of collagenase dissolved in 20 ml of culture medium (DMEM containing 4.5 g/L D-glucose, sodium pyruvate and GlutaMAX™, supplemented with 10 % foetal bovine serum and 100 units/ml penicillin, 0.1 mg/ml streptomycin and 25 µg/ml amphotericin B (Fungizone) (all from Life Technologies, Gibco®)]. Tubes were placed at 37 °C in a water bath (Grant instruments, UK) for 30-90 minutes until the embryo pieces were fully dissociated. The cell homogenate was then washed with PBS and centrifuged (200 g for 5 minutes at RT) to pellet the cells. The solution was then re-suspended in 12-14 ml of culture medium and left 10 minutes to allow undigested pieces to sediment at the bottom. The clean solution was plated in a 100 mm Petri dish and cultured under 5 % (vol/vol) CO_2 and 37 °C to stablish the MEF culture. After a couple of passages, amphotericin B (Fungizone) was removed from the culture media.

2.2.2. Culturing Conditions

Polg$^{A449T/A449T}$ and control MEFs were cultured under 5 % (vol/vol) CO_2 and 37 °C in complete Dulbecco's Modified Eagle Medium (DMEM) (4.5 g/L glucose 2 mM glutamine, 110 mg/ml sodium pyruvate), supplemented with 10% fetal bovine serum (FBS) and 5% penicillin/streptomycin. The same culturing conditions were

used for C2C12 mouse cells. Human HeLa cells were grown under 5 % (vol/vol) CO_2 and 37 °C in DMEM (4.5 g/L glucose, 2 mM glutamine, 110 mg/ml sodium pyruvate) supplemented with 10% FBS and 5% penicillin/streptomycin.

2.2.3. T7 endonuclease assay

C2C12 mouse cells plated in a 100 mm Petri dish at a confluency of 80% were transfected with the pX458 plasmid encoding Cas9 WT and the individual gRNA to be accessed. Cloning of individual gRNAs are described in Section 2.3.5.1. Briefly, 20 ng of each plasmid was diluted in 800 µl of Optim-MEM (ThermoFisher), following addition of 60 µl of FuGENE-HD (Promega). The mix was incubated for 15 min at room temperature and then added drop-by-drop to the cells. After 48 h, cells were collected for Fluorescence-activated cell sorting (FACS) and sorted for GFP (marker encoded in pX458). FACS was carried by the Flow Cytometry facility at Cambridge Institute for Medical Research (CIMR). The collected GFP-positive cells were allowed to recover for another 72 h and then were collected for DNA extraction as described in Section 2.3.1.1. The purified genomic DNA was used to PCR-amplify the *Polg* Y933C region of interest as described in Section 2.3.3.5. The PCR products were then processed for the T7 endonuclease assay. First, the 500 ng of PCR product were set in reaction of 20 µl (500 ng of PCR product, 2 µl 10 X NEB buffer 2, H_2O to 20 µl) and were denatured and reannealed with program indicated in Table 2.2.

Table 2.2 Denaturation and reannealing program of PCR products.

Temperature	Ramp Rate	Time
95 °C		5 mins
95-25 °C	- 0.5 °C / sec	
4 °C		∞

After the denaturing and reannealing step, 1 µl of T7 endonuclease I (NEB, M0302) was added to the reaction and incubated for 30 mins at 37 °C. Finally, reactions were loaded in a 1.5% agarose gel and run at constant 90 V for about 1 h and visualised as described in Section 2.3.3.2. Bands of interest (fractions cleaved) were quantified using ImageLab™ (BioRad) software. Calculation of the estimated gene modification was performed applying the formula:

$$\% \text{ gene modification} = 100 \times (1-(1-\text{fraction cleaved})^{1/2})$$

2.2.4. Ethidium Bromide (EtBr) treatments

Polg$^{A449T/A449T}$ and control MEFs were seeded in six-well plates at 20% confluence. Cells were incubated with or without 100 ng/mL EtBr for 5 days and DNA samples were collected every 24h. At day 5, new medium without EtBr was added and cells were allowed to recover for an additional 8 days. Again, DNA samples were collected every 24h. MtDNA quantification were normalised to MEFs cultured without EtBr and performed as described in Section 2.3.3.9.1.

2.2.5. Bromodeoxyuridine (BrdU) and Immunocytochemistry (ICC)

Polg$^{A449T/A449T}$ and control MEFs were seeded in 24-well plate and incubated for 1 h with 50 µM BrdU (Invitrogen). After the incubation, cells were fixed in 5% paraformaldehyde (PFA) in PBS at 37 °C for 15 min and incubated with 50 mM ammonium chloride in PBS for 10 min at room temperature (RT). After three washes in PBS, cells were permeabilised using 0.1% Triton X- 100 in PBS for 10 min, washed three times with PBS, and then blocked in 10% FBS in PBS for 20 min at RT. Cells were then incubated with indicated primary antibodies for 2 h in 5% FBS in PBS, washed in 5% FBS in PBS and incubated with secondary Alexa Fluor conjugated antibodies in 5% FBS/PBS for 1 h at RT. List of antibodies used for immunocytochemistry is presented in Table 2.3.

Table 2.3 Antibodies used for immunocytochemistry.

Antigen	Host	Dilution	Manufacturer (CN)
TOM20	Rabbit	1:1000	Abcam (ab232589)
DNA	Mouse	1:1500	Millipore (CBL186)
Rabbit IgG (Alexa Fluor 594)	Goat	1:1000	Invitrogen (A-11012)
Mouse IgG (Alexa Fluor 488)	Donkey	1:1000	Invitrogen (A-21202)

EdU incorporation was detected using Invitrogen Click-iT EdU AlexaFluor 647 (Invitrogen, C10340) labelling kit according to manufacturer's instructions. Coverslips were mounted onto slides using Dako fluorescence mounting medium (Dako). Images were then acquired as 7 stacks of 0.2 µm each, using a 100× objective lense (NA1.4) on a Nikon Eclipse TiE inverted microscope using an Andor Dragonfly 500 confocal spinning disk system, equipped with a Zyla 4.2 PLUS sCMOS camera, exciting with 488 nm, 594 nm or 633 nm lasers, and coupled with Fusion software (Andor). For quantification of EdU or mtDNA foci, max projection images were processed once with the 'smooth' function in Fiji and nucleus was removed. Images were then manually thresholded, 'smoothed' and number of particles were obtained using the 'Analyse particles' plugin in Fiji with a minimum area of 0.1 µm^2. The representative images were processed once with the 'smooth' function in Fiji.

2.2.6. siRNA Knockdown

For siRNA transfections, 0.3 × 10^6 HeLa cells were reverse transfected with 5 nM of siRNA using Lipofectamine RNAiMAX (ThermoFisher), according to manufacturer´s instructions. The siRNAs used in this are presented in Table 2.4. Three days after transfection, cells were harvested, washed with PBS and used for western blotting as described in Sections 2.4.2 and 2.4.4.

Table 2.4 siRNA used to knockdown human *LONP1*, *POLG* and *POLG2*.

Target	Sequence (5′- 3′)
LONP1	GGUGCUGUUCAUCUGCACGtt
POLG	CGGUGCCUUGGAACACUAUtt
POLG2	CCCAUUGGACAUCCAGAUGtt

2.3. Nuclei Acid-based Methods

2.3.1. DNA extraction

2.3.1.1. From Cells and Mouse Tissues

Genomic DNA was extracted by re-suspending either cultured cells (≥ 5 x 10^5 cells) or frozen mouse tissues (~20 mg) samples in 400 µl of DNA lysis buffer [0.5% sodium dodecyl sulfate (SDS), 0.1 M NaCl, 50 mM Tris–HCl (pH 8.0), 2.5 mM EDTA]. Samples were then incubated ON at 56°C, shaking at 300RPM after addition of Proteinase K (final concentration: 20 ng/µL). The next day, 1 volume of chloroform + 0.6 M potassium acetate were added to the tube and mixed vigorously by inversion. The resulting solution was spin down (21000 g for 10 min at 4 °C). The upper aqueous phase was then transferred to a new tube, followed by ethanol precipitation with 1 ml of 95% ethanol. The tubes were spin down (21000 g for 10 min at 4 °C) and the supernatant discarded. The pellet was washed with 70% ethanol and spin down again (21000 g for 5 min at RT). Next, the supernatant was discarded, the pellet air-dried and finally eluted in nuclease-free water. DNA concentrations were measured by NanoDrop™ 8000 Spectrophotometer (Thermo Scientific™, Thermo Fisher Scientific, UK) at λ = 260/280.

2.3.1.2. From Liver-isolated Mitochondria

DNA extraction from purified mitochondria obtained for *in organello* (Section 2.3.8) and 2D-AGE (Section 2.3.9) experiments was carried by addition of Proteinase K (final concentration of 0.1 mg/ml) to the mitochondrial suspension in lysis buffer, followed by an incubation of 30 mins on ice. After incubation, sodium N-lauroylsarcosinate was added to a final concentration of 1% (v/v), followed by

addition of Phenol Chloroform Isoamyl alcohol in a 1:1 (v/v) ratio. The resulting solution was mixed by inversion and spin down (16000 g for 5 min at 4 °C). The upper aqueous phase was then transferred to a new tube, followed isopropanol precipitation (100 mM NaCl, 5 µl Glycogen and 1 Volume of isopropanol). The tubes were stored at -20 °C for at least 1 h and then spin down (21000 g for 20 min at 4 °C). The supernatant was discarded, the pellet air-dried and finally eluted in nuclease-free water. DNA concentrations were measured by NanoDrop™ 8000 Spectrophotometer (Thermo Scientific™, Thermo Fisher Scientific, UK) at λ = 260/280.

2.3.2. RNA extraction and cDNA Retrotranscription

Total RNA was extracted from the indicated tissues using the TRIzol Reagent (Thermofisher) following the manufacturer´s protocol. Frozen mouse tissues (~50 mg) were suspended in 1 ml of TRIzol Reagent and homogenised with a gentleMACS™ Dissociator (Miltenyi Biotec, Bergisch Gladbach, Germany) with the recommended setting per tissue type. An initial spin (500 g for 5 min at 4 °C) was performed to remove larger debris and the resulting supernatant was transferred to a new 1.5 ml Eppendorf. A volume of 200 µl chloroform was added per 1 ml of TRIzol, followed by vigorous shaking of the tube. Samples were then centrifuged (15000 x g for 15 min at 4 ºC). The upper aqueous phase was then transferred to a new tube, followed isopropanol precipitation (100 mM NaCl, 5 µl Glycogen and 0.5 Volumes of isopropanol). The tubes were spin down (12000 g for 10 min at 4 °C) and the supernatant discarded. The pellet was washed with 70% ethanol and spin down again (7500 g for 10 min at 4 ºC). Next, the supernatant was discarded, the RNA pellet air-dried and finally eluted in nuclease-free water. RNA concentrations were measured by NanoDrop™ 8000 Spectrophotometer (Thermo Scientific™, Thermo Fisher Scientific, UK) at λ = 260/280.

For cDNA synthesis, extracted RNA was treated with 1 µl TURBO™ DNase (Ambion®, Life Technologies™) for 30 mins at 37 °C to remove any trace DNA. Next, cDNA synthesis was performed using the Omniscript Reverse Transcription (RT) Kit (Qiagen) following manufacturer's recommendations. Retrotranscription

reactions were performed with 2 µg template RNA in a final volume of 20 µl, with the following mixture: 1 X Buffer RT, 0.5 mM of each dNTPs, 1 µM of oligo dT primer, 10 µM of random hexamers, 0.2 U/µl of reverse transcriptase, 10 U/µl of RNAsin® RNase inhibitor, nuclease-free H_2O. The final mixtures were incubated for 1 h at 37 °C, and further incubated for 5 mins at 95 °C. The resulting cDNA were diluted to 50 µl with nuclease-free H_20 and used for Real-time Reverse Transcription quantitative PCR in Section 2.3.3.10.

2.3.3. Polymerase Chain Reaction (PCR) Associated Procedures

The PCR reactions were performed using a ProFlex PCR system (Applied BioSciences) with *Taq* polymerase to amplify a DNA sequence of interest by multiple cycles of three temperature-mediated steps: 1) denaturation of the double-stranded template DNA, 2) annealing of specific forward (Fw) and reverse (Rv) primers to the region of interest on both denatured strands and 3) extension of the primer-annealed DNA sequences by the *Taq* polymerase. The primer sequences and respective cycling programs are indicated in the following individual sections.

2.3.3.1. Design and synthesis of Oligonucleotide Primers

The PCR primers used in this study were designed using the web-based software Primer3Plus (www.bioinformatics.nl/cgi-bin/primer3plus/primer3plus.cgi).

The general settings applied included:

- Primer Size between 18 and 27 nt, with 20 nt as optimal;

- Primer T_m between 57 and 63 °C, with 60 °C as optimal;

- Primer GC% between 20 and 80 %.

Each selected primer pair was accessed for non-specifically amplified off-targets using the web-based tool NCBI Primer-Blast:

www.ncbi.nlm.nih.gov/tools/primer-blast/index.cgi

All nucleotide primers were ordered from Merck, Sigma-Aldrich®, delivered dry and desalted and re-suspended to a stock concentration of 100 µM with nuclease-free H_2O.

2.3.3.2. Agarose Gel Electrophoresis

Analysis of the DNA products of PCR amplification was performed by separating the DNA fragments by agarose gel electrophoresis according to their size. Gels of 1% agarose were used for general application unless otherwise stated. Gels were cast with appropriate weight per volume (w/v), typically 1% gels: 0.75 g of agarose (Invitrogen) dissolved in 75 ml of 1 x TBE [89 mM tris base, 89 mM boric acid, 2 mM EDTA (pH 8.0)]. To the gel solution, 7.5 µl 10,000 X SYBR Safe dye (Invitrogen™) was added to allow visualisation with an ultraviolet (UV) light transilluminator (Gel Doc™ Imaging System, Bio-Rad, UK) after the run. A 1kb Plus DNA ladder (Invitrogen™) was used as standard for fragment size determination, and samples were electrophoresed at 90 V (EM100, Mini Gel Unit, Engineering & Design Plastics, UK) for approximately 40-50 mins with 1 x TBE as the running buffer.

2.3.3.3. Genotyping of the *Polg* A449T allele

Genomic DNA extracted from cells or mouse tissues was used to genotype individual mice and MEFs. PCR was performed in 25 µl containing: 25-50 ng of DNA, 0.2 mM of each dNTP, 1.25 U of GoTaq polymerase (Promega), 1 X Green GoTaq Buffer and 0.25 µM of each primer. Primer sequences and PCR conditions are in Table 2.5.

Table 2.5 Primers and PCR conditions of the *Polg* A449T allele.

Temperature	Duration	
95°C	3 min	
95°C	30 sec	X 35 cycles
63.7°C	30 sec	
72°C	1 min	
72°C	5 min	
4°C	∞	

Primer	Sequence (5′- 3′)
Polg_A449T_Fw	GTTGTCCCTGTCTTCCTCCA
Polg_A449T_Rv	AAGCTTCCCACCTTCCTGAT

At the end of the PCR reaction, 1 U of PvuII (restriction site next to the Knockin allele) was added together with 1 X restriction digest buffer suggested by the manufacturer. The restriction reaction was incubated for at least 3 h at 37 °C. At the end of the reaction, samples (5 µl) were loaded directly into 1 % agarose gel (thanks to the loading dye incorporated in the GoTaq buffer) and run as described in Section 2.3.2.2.

Expected products:

- Two WT alleles: 769 bp
- One WT allele and one *Polg* A449T allele: 769 bp + 490 bp + 279 bp
- Two *Polg* A449T alleles: 490 bp + 279 bp

2.3.3.4. Genotyping of the *Polg* KO allele

Genomic DNA extracted from mouse tissues was used to genotype individual mice. PCR was performed in 25 µl containing: 25-50 ng of DNA, 0.2 mM of each dNTP, 1.25 U of GoTaq polymerase (Promega), 1 X Green GoTaq Buffer and 0.25 µM of each of the 3 primers. Primer sequences and PCR conditions are in Table 2.6.

Table 2.6 Primers and PCR conditions of the *Polg* KO allele.

Temperature	Duration	
95°C	3 min	
95°C	30 sec	X 35 cycles
55°C	30 sec	
72°C	1 min	
72°C	5 min	
4°C	∞	

Primer	Sequence (5′- 3′)
Polg_KO_Fw1	CTTCGTCGATCGACCTCGAATAAC
Polg_KO_Rv	CTGCCATTCACCTTACCC
Polg_KO_Rv2	GGATGGGCAGGAACAGTTAG

At the end of the PCR reaction, samples (5 µl) were loaded directly into 1 % agarose gel (thanks to the loading dye incorporated in the GoTaq buffer) and run as described in Section 2.3.2.2.

Expected products:

- Two WT alleles: 700 bp
- One WT allele and one *Polg* KO allele: 700 bp + 399 bp

2.3.3.5. Screening and Genotyping of the *Polg* Y933C allele

Genomic DNA extracted from cells or mouse tissues was used to genotype individual mice and ES clones. PCR was performed in 25 µl containing: 25-50 ng of DNA, 0.2 mM of each dNTP, 1.25 U of GoTaq polymerase (Promega), 1 X Green GoTaq Buffer and 0.25 µM of each primer. Primer sequences and PCR conditions are in Table 2.7.

Table 2.7 Primers and PCR conditions of the *Polg* Y933C allele.

Temperature	Duration	
95°C	3 min	
95°C	30 sec	X 35 cycles
62°C	30 sec	
72°C	1 min	
72°C	5 min	
4°C	∞	

Primer	Sequence (5′- 3′)
Polg_Y933C_Fw	GGGGTCTGGTGTACAGTTTCAT
Polg_Y933C_Rv	AGGTTTAGAGGGACAGCACTCA

At the end of the PCR reaction, 1 U of MscI (restriction site next to the Knockin allele) was added together with 1 X restriction digest buffer suggested by the manufacturer. The restriction reaction was incubated for at least 3 h at 37 °C. At the end of the reaction, samples (5 µl) were loaded directly into 1 % agarose gel (thanks to the loading dye incorporated in the GoTaq buffer) and run as described in Section 2.3.2.2.

Expected products:

- Two WT alleles: 404 bp + 349 bp
- One WT allele and one *Polg* Y933C allele: 404 bp + 349 bp + 213 bp + 191 bp
- Two *Polg* Y933C alleles: 349 bp + 213 bp + 191 bp

2.3.3.6. Genotyping of the *Ndufs4* KO allele

Genomic DNA extracted from mouse tissues was used to genotype individual mice. PCR was performed according to JAX protocol 27899, in 25 µl containing: 25-50 ng of DNA, 0.2 mM of each dNTP, 1.25 U of GoTaq polymerase (Promega), 1 X Green GoTaq Buffer and 0.25 µM of each of the 3 primers. Primer sequences and PCR conditions are in Table 2.8.

Table 2.8 Primers and PCR conditions of the *Ndufs4* KO allele.

Temperature	Duration	
95°C	3 min	
95°C	30 sec	X 35 cycles
62°C	30 sec	
72°C	30 sec	
72°C	5 min	
4°C	∞	

Primer	Sequence (5′- 3′)
Ndufs4_WT	AGTCAGCAACATTTTGGCAGT
Ndufs4_common	GAGCTTGCCTAGGAGGAGGT
Ndufs4_KO	AGGGGACTGGACTAACAGCA

At the end of the PCR reaction, samples (5 µl) were loaded directly into 1 % agarose gel (thanks to the loading dye incorporated in the GoTaq buffer) and run as described in Section 2.3.2.2.

Expected products:

- Two WT alleles: 201 bp
- One WT allele and one *Ndufs4* KO allele: 400 bp + 201 bp
- Two *Ndufs4* KO alleles: 400 bp

2.3.3.7. Long-Range PCR for mtDNA deletions detection

Genomic DNA extracted from cells or mouse tissues was used to genotype individual mice and ES clones. PCR was performed in 25 µl containing: 50 ng of DNA, 0.2 mM of each dNTP, 1 U of PrimeSTAR GXL DNA polymerase (TAKARA, Japan), 1 X GXL Buffer and 0.25 µM of each primer. Primer sequences and PCR conditions are in Table 2.9.

Table 2.9 Primers and PCR conditions of the Long-Range PCR.

Temperature	Duration	
98°C	3 min	
98°C	10 sec	X 35 cycles
68°C	13 min	
72°C	5 min	
4°C	∞	

Primer	Sequence (5′- 3′)
LongR_mtDNA_Fw	GAGGTGATGTTTTTGGTAAACAGGCGGGGT
LongR_mtDNA_Rv	GGTTCGTTTGTTCAACGATTAAAGTCCTACGTG

At the end of the PCR reaction, samples (10 µl) were mixed with 6 X DNA loading dye (Promega) and loaded into 0.8 % agarose gel and run in 1 X TBE buffer at constant 60 V for 3 h. This set of primers anneal tail-to-tail in the mouse 16S gene producing an expected band of 15781 bp that spans almost the entire mouse mtDNA.

2.3.3.8. PCR amplification of a 7S DNA probe

Genomic DNA extracted from C2C12 mouse cells was generate the probe annealing the region of the 7S DNA. PCR was performed in 25 µl containing: 25-50 ng of DNA, 0.2 mM of each dNTP, 1.25 U of GoTaq polymerase (Promega), 1 X Green GoTaq Buffer and 0.25 µM of each primer. Primer sequences and PCR conditions are in Table 2.10.

Table 2.10 Primers and qPCR conditions for 7S DNA probe.

Temperature	Duration	
95°C	10 min	
95°C	30 sec	X 35 cycles
62°C	30 sec	
72°C	30 sec	
72°C	5 min	
4°C	∞	

Primer	Sequence (5′- 3′)
7S_probe_Fw	ATCAATGGTTCAGGTCATAAAATAATCATCAAC
7S_probe_Rv	GCCTTAGGTGATTGGGTTTTGC

This pair of primers produce an expected fragment of 524 bp spanning the 7S region of mouse mtDNA. At the end of the PCR cycling, the reactions were purified as described in Section 2.3.4 and later used to generate a radiolabelled probe as described in Section 2.3.10.2.

2.3.3.9. Real-time quantitative PCR (qPCR)

All Real-time qPCR reactions were performed in individual wells of a 96-well plate, which was sealed and loaded into a 7900HT RT-QPCR System (Applied Biosystems, Thermo Fisher Scientific, USA).

2.3.3.9.1. MtDNA copy number

Real-time qPCR was used to determine the relative mtDNA copy number in the different mouse tissues and MEFs during mtDNA depletion/recovery experiments. For mtDNA relative quantification, SYBR Green technology was used. SYBR Green emits fluorescence when bound to dsDNA, thus after each PCR cycle the amount

of SYBR green fluorescence is correlated with the amount of DNA. The amplification cycle at which the fluorescence crosses the background threshold is called the cycle of threshold (Ct) and is used for the calculation of the relative gene copy number or gene expression, using the ΔΔCt analysis.

MtDNA relative quantification in this work was performed using primers specific to a mouse mtDNA region in the *CoI* gene and primers specific to *RNaseP*, a single copy gene taken as a nuclear gene reference.

Each sample was run in technical replicates and each reaction was performed in 25 µl containing: 25ng of DNA, 1 X SYBR™ Green PCR Master Mix (ThermoFisher) and 0.25 µM of each primer (either *CoI* or *RNaseP)*. Primer sequences and PCR conditions are in Table 2.11.

Table 2.11 Primers and qPCR conditions of mtDNA relative quantification.

Temperature	**Duration**	
95°C	10 min	
95°C	15 sec	X 40 cycles
60°C	1 min	

Primer	**Sequence (5′- 3′)**
qPCR_mCoI_Fw	TGCTAGCCGCAGGCATTACT
qPCR_mCoI_Rv	CGGGATCAAAGAAAGTTGTGTTT
qPCR_RnaseP_Fw	GCCTACACTGGAGTCGTGCTACT
qPCR_ RnaseP _Rv	CTGACCACACGAGCTGGTAGAA

In the end of the assay, the Ct values for each sample were transferred into excel and used to calculate relative mtDNA copy number using the ΔΔCt analysis, as detailed in (Livak and Schmittgen, 2001).

2.3.3.9.2. Viral Genome copies

Real-time qPCR was used to determine the viral genomes copies of AAV-PHP.B-h*NDUFS4* in the different tissues of injected mice. The SYBR Green technology was used as described above in Section 2.3.3.9.1. However, final analysis was performed differently.

Quantification of viral genome copies was performed using a pair of *NDUFS4* primers that anneal to both human *NDUFS4* and mouse *Ndufs4*. Primers specific to *RNaseP*, was taken as reference of single copy gene to normalise the values.

Each sample was run in technical replicates and each reaction was performed in 25 µl containing: 25ng of DNA, 1 X SYBR™ Green PCR Master Mix (ThermoFisher) and 0.25 µM of each primer (either *NDUFS4* or *RNaseP)*. Primer sequences and PCR conditions are in Table 2.12.

Table 2.12 Primers and qPCR conditions of viral genomes quantification.

Temperature	**Duration**	
95°C	10 min	
95°C	15 sec	X 40 cycles
60°C	1 min	

Primer	**Sequence (5′- 3′)**
qhm_NDUFS4_Fw	CTTTGTTCCTGCTCGCAATA
qhm_NDUFS4_Rv	ATGCCCAACCCATCAAAG
qPCR_RnaseP_Fw	GCCTACACTGGAGTCGTGCTACT
qPCR_ RnaseP _Rv	CTGACCACACGAGCTGGTAGAA

In the end of the assay, the Ct values for each sample were transferred into excel for analysis. The *NDUFS4* Ct values were first normalised using the RnaseP Ct values to account for variations in the input of DNA. Given that the *NDUFS4* primers anneal to both AAV vector and mice, untreated mice were used to extrapolate the value of Ct corresponding to 2 copies of *NDUFS4* per nucleus. Thus, the viral genome copies were calculated as $2 \times 2^{-\Delta Ct}$, in which ΔCt corresponds to the difference between the Ct values of injected mice minus Ct values of untreated mice.

2.3.3.10. Real-time Reverse Transcription quantitative PCR (RT-qPCR)

All Real-time RT-qPCR reactions were performed in individual wells of a 96-well plate, which was sealed and loaded into a 7900HT RT-QPCR System (Applied Biosystems, Thermo Fisher Scientific, USA).

2.3.3.10.1. MtDNA transcripts

Real-time RT-qPCR was used to determine the relative levels of the mitochondrial transcripts *CoI* and *Nd4* in the different mouse tissues. Procedure with the SYBR Green technology and respective analysis was performed as described above in Section 2.3.3.9.1, except that in this case cDNA is used instead of genomic DNA.

MtDNA transcripts relative quantification in this work was performed using primers specific to mouse mtDNA transcripts of *CoI* and *Nd4* genes and primers specific to *RNaseP*, taken as housekeeping gene to normalise the values.

Each sample was run in technical replicates and each reaction was performed in 25 µl containing: 5 µl of cDNA, 1 X SYBR™ Green PCR Master Mix (ThermoFisher) and 0.25 µM of each primer (either *CoI*, *Nd4* or *Gapdh)*. Primer sequences and PCR conditions are in Table 2.13.

Table 2.13 Primers and qPCR conditions of mtDNA transcripts relative quantification.

Temperature	Duration	
95°C	10 min	
95°C	15 sec	X 40 cycles
60°C	1 min	

Primer	Sequence (5′- 3′)
qPCR_mCoI_Fw	TGCTAGCCGCAGGCATTACT
qPCR_mCoI_Rv	CGGGATCAAAGAAAGTTGTGTTT
qPCR_mNd4_Fw	TCGCCTACTCCTCAGTTAGCCA
qPCR_mND4_Rv	GATGTGAGGCCATGTGCGATT
qPCR_Gapdh_Fw	CACCATCTTCCAGGAGCGAG
qPCR_Gapdh _Rv	CCTTCTCCATGGTGGTGAAGAC

In the end of the assay, the Ct values for each sample were transferred into excel and used to calculate relative mtDNA copy number using the ΔΔCt analysis.

2.3.3.10.2. *Polg* and *polg2* transcripts

Real-time RT-qPCR was also used to determine the relative levels of the nuclear transcripts *Polg* and *Polg2* in the different mouse tissues. However, in this case pre-tested and validated specific Gene Expression TaqMan assays (ThermoFisher Scientific) were used. The TaqMan technology uses an oligonucleotide probe annealing within the amplified region of interest. The probe contains a fluorophore at the 5′-end which is normally neutralised by a quencher at the 3′-end. When the probe binds the region of interest during PCR cycling, the Taq polymerase synthesises a new strand and degrades the probe, separating the quencher from the fluorophore generating a fluorescent signal. Like the SYBR Green technology, the emitted fluorescence is correlated with the amount of DNA allowing to calculate the Ct values. The availability of compatible fluorophores with different excitation wavelengths and emission allows for the identification of multiple targets in the same assay.

Relative gene expression of *Polg* and *Polg2* was performed using the Taqman Assay IDs: *Polg* (Mm00450527_m1) and *Polg2* (Mm00045166_m1). The *B2m* transcript assay (Mm00437762_m1) was used as housekeeping gene to normalise the values. The reactions were performed in multiplex, in which either *Polg* or *Polg2* (fluorophore FAM) were paired in the same reaction with *B2m* (fluorophore VIC).

Each sample was run in technical replicates and each reaction was performed in 20 µl containing: 5 µl of cDNA, 10 µl of 2 X TaqMan™ Gene Expression Master Mix (ThermoFisher), 1 µl *B2m* TaqMan™ Gene Expression assay (VIC) and 1 µl of either *Polg* or *Polg2* TaqMan™ Gene Expression assay (FAM). Primer and probe sequences are not disclosed by the supplier. PCR conditions are the same as described above in Table 2.13.

In the end of the assay, the Ct values for each sample were transferred into excel and used to calculate relative mtDNA copy number using the ΔΔCt analysis.

2.3.4. Purification of PCR products

The PCR products were purified from other reaction mixture components using the QIAquick PCR Purification kit (Qiagen), following the manufacturer´s protocol. The PCR reaction was mixed with 5 Volumes of high-salt binding buffer (PB buffer), which facilitates binding of DNA to the QIAquick spin column, a silica-based membrane. After DNA binding to the column, impurities were eliminated with an ethanol-based washing step. Once dried, the DNA was eluted in pre-warmed nuclease-free water. DNA concentrations were measured by NanoDrop™ 8000 Spectrophotometer (Thermo Scientific™, Thermo Fisher Scientific, UK) at λ = 260/280.

2.3.5. Molecular cloning

2.3.5.1. Cloning of gRNAs into pX458

The gRNAs targeting the *Polg* Y933C locus were cloned individually into the pX458 backbone (Addgene plasmid # 48138, was a gift from Feng Zhang) to access their targeting efficiency with a T7 endonuclease assay (Section 2.3.3). For each gRNA to be cloned, two oligonucleotides were ordered so that the forward oligo has a 5'CACC tail overhang and the reverse oligo has a 5'AAAC tail overhang. When the oligo pair is annealed, the generated overhangs can be readily ligated into the BbsI-digested pX458 backbone.

All nucleotide primers were ordered from Merck, Sigma-Aldrich®, and a list is presented in Table 2.14.

Table 2.14 Oligos used to clone gRNAs into pX458.

Target	Sequence (5´- 3´)
gRNA_F1_Fw	caccGATGGCCGCATCTATGGGGCT
gRNA_F1_Rv	aaacAGCCCCATAGATGCGGCCATC
gRNA_F2_Fw	caccGTTCAACTATGGCCGCATCTA
gRNA_F2_Rv	aaacTAGATGCGGCCATAGTTGAAC
gRNA_R1_Fw	caccGCGGCCATAGTTGAAGATTT
gRNA_R1_Rv	aaacAAATCTTCAACTATGGCCGC
gRNA_R2_Fw	caccGCTCTCGGCTGATGCCCACAG
gRNA_R2_Rv	aaacCTGTGGGCATCAGCCGAGAGC

The oligos (Fw + Rv) of each gRNA were annealed in reactions of 10 µl [1 µl of 100 µM Fw oligo, 1 µl of 100 µM Rv oligo, 1 µl of T4 DNA ligase Buffer (NEB), 1 µl of T4 Polynuclease Kinase (NEB), 6 µl H_2O]. The mixture was first incubated at 37 °C for 30 mins to allow the kinase to phosphorylate the 5′-end of the oligos for subsequent ligation. Then the phosphorylated oligos were annealed using the annealing program described in Table 2.15.

Table 2.15 Reannealing program of oligonucleotides.

Temperature	Ramp Rate	Time
95 °C		2 mins
95-25 °C	- 0.5 °C / sec	
4 °C		∞

The pX458 vector (2 µg) was restriction digested with 2 U of BbsI, for at least 2 h at 37 °C. At the end, 1 µl of Alkaline Phosphatase from Calf Intestine (NEB) was added to the reaction and incubated for an extra 1 h to dephosphorylate the BbsI-digested end of the backbone, avoiding re-ligation. The reaction was then purified with a commercial kit described in Section 2.3.4.

For ligation, 50 ng of digested pX458 were mixed with 1 µl annealed gRNAs (1:100 dilution of the annealing mix) using a T4 DNA ligase (NEB). The ligation reaction was incubated ON at 16 °C. The next day, 5 µl of the ligation reaction was used for transformation of E. coli competent cells (Section 2.3.5.3).

The resulting plasmids from individual colonies were confirmed for correct insertion of the gRNA by Sanger sequencing using a U6-promoter plasmid (5′-GAG GGC CTA TTT CCC ATG ATT -3′). The validated gRNA containing pX458 vectors were then used for the T7 endonuclease assay (Section 2.3.3).

2.3.5.2. TOPO TA cloning

The purified PCR products were cloned in the pCR2.1 TOPO TA cloning kit (Invitrogen). *Taq*-based polymerases introduce a non-templated nucleotide to the 3' end of a PCR product, typically an Adenine (A). This feature is explored by the TOPO vectors provided in the kit that are linearized and have 3′-T overhangs that are complementary with the A-tail of the PCR products. The enzyme DNA topoisomerase I also provided in the kit, functions both as a restriction enzyme and as a ligase and is covalently bound to the 3′ phosphate on each end of the vector. The topoisomerase activity enables the vectors to readily ligate to A-tailed PCR products with compatible ends. A 10 min incubation at RT is normally sufficient to provide ligated products, ready for transformation.

2.3.5.3. Transformation of *E. coli* chemically competent cells

Transformation of DNA plasmids (TOPO vectors with ligated PCR fragments) were performed using Subcloning Efficiency DH5α™ competent *E. coli* cells (Thermo Fisher Scientific). Five µl of ligation reaction was added to 50 µl competent cells with an initial incubation on ice for 30 mins, followed by a heat shock at 42 ^{o}C in the water batch and then another 5 mins incubation on ice. Recovery was performed by addition of 200 µl of SOC media (2 % tryptone, 0.5 % yeast extract, 10 mM NaCl, 2.5 mM KCl, 10 mM $MgCl_2$, 10 mM $MgSO_4$, and 20 mM glucose) to the transformed bacteria, and subsequent growth for 1 h at 37 ^{o}C with shaking at 225 rpm. The transformed competent cells (100 µl) were then plated in agar plates made with LB media (1 % tryptone, 0.5 % yeast extract, and 10 mM NaCl), containing 100 µg/ml ampicillin, and allowed to form colonies ON at 37 ^{o}C. The next day, several colonies were picked and cultured in 2 ml LB, containing 100 µg/ml amp, in a shaking incubator (225 rpm) at 37 ^{o}C ON. The resulting cultures were then used to extract plasmid DNA.

2.3.5.4. Plasmid DNA preparation

The plasmid DNA were prepared using the QIAprep Spin Miniprep Kit(Qiagen), following the manufacturer´s protocol using 2 ml of an ON bacterial culture. The bacterial culture is pelleted with a quick centrifugation (5000g for 5 mins). The resulting bacterial pellet is then lysed under alkaline conditions, subsequently neutralized and adjusted to high-salt–binding conditions allowing binding of the plasmid DNA to the QIAquick spin column. After DNA binding to the column, impurities were eliminated with an ethanol-based washing step. Once dried, the plasmid DNA was eluted in pre-warmed nuclease-free water. DNA concentrations were measured by NanoDrop™ 8000 Spectrophotometer (Thermo Scientific™, Thermo Fisher Scientific, UK) at λ = 260/280.

2.3.6. DNA sequencing and analysis

Sequencing of PCR products and cloned plasmids was carried out using the dideoxy-chain termination method "Sanger sequencing" (Sanger et al., 1977) by a commercial service (Source Bioscience Ltd, Cambridge, UK). Sequencing of PCR products related to the *Polg* Y933C was performed using the primer Polg_Y933C_Fw (5´- GGG TCT GGT GTA CAG TTT CAT – 3´). Sequencing of individual alleles of *Polg* Y933C in TOPO vectors was performed with either Polg_Y933C_Fw or M13_Fw (5´- TGT AAA ACG ACG GCC AGT – 3´). Resulting sequences were aligned with the modified *Polg* Y933C allele sequence using SnapGene® software.

2.3.7. Analysis of 7S DNA steady-state levels (1-Dimensional electrophoresis)

For one-dimensional Southern blotting, 3 μg of total DNA isolated from each tissue were linearized using 10 U of the restriction enzyme BlpI in a final volume of 20 μl for 3 h at 37 °C. The entire digested product was then mixed with 6 X DNA loading dye (provided with the restriction enzyme, NEB), and loaded in 0.8% agarose gels [0.8 g ultrapure agarose (Invitrogen), 100 ml 1 x TBE]. The gel was run with 1 x TBE

[89 mM tris base, 89 mM boric acid, 2 mM EDTA (pH 8.0)] at constant 25 V for 18 h. After the run, the gel was processed, dry-blotted onto nylon membranes, hybridised and visualised as described in Section 2.3.10.

2.3.8. In Organelo de novo DNA synthesis

2.3.8.1. Mitochondrial Isolation from Fresh Mouse Livers for *In Organello* assays

Freshly-collected mouse whole livers were placed individually in 50 ml falcon tubes containing 25 ml of ice-cold STE-BSA buffer [320 mM sucrose, 1 mM EDTA, 10 mM Tris-HCl (pH 7.4), 1 mg/ml BSA]. All steps were carried on ice or in the cold room at 4°C. The liver was placed in a beaker on ice with 20 ml of STE-BSA and minced finely with sharp scissors, changing the solution at least 3 times to get rid of blood and fat. The pieces of liver were then homogenised in a glass Dounce-type homogeniser using a manually-driven glass pestle (~15 strokes) with 4 volumes of STE-BSA buffer (ml) per gram of liver. The homogenate was transferred to a 50 ml falcon and an initial spin (1000 g for 5 min at 4 °C) was performed to remove larger debris. The supernatant was then split into individual 1.5 ml Eppendorf tubes in aliquots of 1 ml each (e.g. 16 ml of supernatant split into 16 tubes) and spin down (10000 g for 2 min at 4 °C). The supernatants were removed and the resulting mitochondrial pellets re-suspended gently in 800 µl of STE-BSA buffer. At this stage, half of the mitochondrial suspensions were transferred to the other half of the tubes (e.g. 8 tubes were transferred to the other 8, halving the number of tubes) and spin down again (10000 g for 2 min at 4 °C). This process was repeated until all the mitochondrial pellets related to one genotype were in a single 1.5 ml Eppendorf tube. The final mitochondrial pellet was re-suspended in 800 µl Incubation Buffer [10 mM Tris-HCl (pH 8.0), 20 mM sucrose, 20 mM glucose, 65 mM D-sorbitol, 100 mM KCl, 0.05 mM EDTA (pH 8.0), 5 mM $MgCl_2$, 1 mg/ml FA-free BSA, 1 mM ADP, 5 mM glutamate, 5 mM malate]. Mitochondria protein concentrations were then estimated by NanoDrop™ 8000 Spectrophotometer (λ = 280 nm). The mitochondrial suspension was once again spin down (10000 g for 2 min at 4 °C) and re-suspended in Incubation Buffer with a final concentration of 1

mg/ml. Mitochondria were then transferred to tubes to be "pulsed" in 250 µl aliquots.

2.3.8.2. Pulse labelling of newly synthesised DNA

Following purification, to each of the 250 µl aliquots of mitochondria was added 1.75 µl of Pulse mix (50 µM of each cold dTTP, dCTP, dGTP and 6.6 nM of [α-^{32}P] dATP). Tubes were then pulsed labelled for 5; 15; 30; 60 and 90 min (as indicated in the figures) in a hybridization oven at 37 °C with rotation. At the end of the incubation period, mitochondria were pelleted (10000 g for 2 min at 4 °C) and re-suspended in 475 µl of lysis buffer [75mM NaCl, 50mM EDTA, 20mM HEPES (pH 7.8)] and DNA extracted as described in Section 2.3.1.2. The resulting DNA was linearized with BlpI restriction digest and run in 1% agarose gel at constant 80 V for 3 h, followed by southern blotting and visualisation as described in Section 2.3.10.

2.3.9. Two-Dimensional Agarose Gel electrophoresis (2D-AGE)

2.3.9.1. Mitochondrial Isolation from Fresh Mouse Livers for 2D-AGE

Freshly-collected mouse whole livers (2 per genotype) were placed in 50 ml falcon tubes containing 25 ml of ice-cold extraction buffer (EB) [for 1 l of EB: 41 g Mannitol, 25.6 g Sucrose, 2.4 g HEPES, 20 ml of 0.5M EDTA, 1 g BSA, 25 µl ß-mercaptoethanol, deionised H_2O to 1l and adjust pH=7.8 with NaOH]. All steps were carried on ice or in the cold room at 4°C. The livers were washed once with 25 ml of EB to remove excess blood. The livers were then placed in a beaker on ice with 20 ml of EB and minced finely with sharp scissors, changing the solution at least 3 times to get rid of blood and fat. The pieces of liver were then homogenised in a glass Dounce-type homogeniser using a manually-driven glass pestle (~15 strokes) with 9 volumes of EB (ml) per gram of liver. The homogenate was transferred to a 50 ml falcon and an initial spin (600 g for 10 min at 4 °C) was performed to remove larger debris. The supernatants were transferred to a new 50 ml falcon and a spin (5000 g for 10 min) was performed to pellet mitochondria,

discarding the supernatant and the fluffy layer. The resulting pellet was then re-suspended in 5 ml of EB, homogenised with a glass homogeniser and spin down (5000 g for 10 min) in a 15 ml falcon. The supernatant was discarded and the pellet re-suspended in 2.5 ml of EB, homogenised and spin down as in the previous step. The resulting crude mitochondrial pellet was finally re-suspended in 0.5 volumes of EB (ml) per gram of initial liver. The re-suspended mitochondria were then transferred into centrifuge tubes containing a sucrose gradient [17.5 ml of 1.5 M and 1 M each, prepared in gradient buffer (10 mM HEPES, pH 7.8, 10 mM EDTA, pH 8.0)] and spin down (40000 g for 1 h, using a SW32 rotor). The mitochondria pelleted in the interface of the two gradients were transferred to a 15 ml falcon, gently homogenised in 5 ml of gradient buffer and spin down (5000 g for 10 min). The final mitochondrial pellet was then re-suspended in 4 ml of lysis buffer [75mM NaCl, 50mM EDTA, 20mM HEPES (pH 7.8)] and DNA extracted as described in Section 2.3.1.2.

2.3.9.2. Analysis of replication intermediates with 2D-AGE

The 2D-AGE consists of a restriction enzyme digestion, followed by separation of DNA in two dimensions (Reyes et al., 2009). The first-dimension agarose gel separation is carried out at low field strength (lower % of agarose) in the absence of ethidium bromide, thus DNA molecules are separated only based on mass. In turn, the second-dimension is carried out at high field strength (higher % of agarose), in the presence of ethidium bromide. Because ethidium bromide intercalates between DNA bases and rigidifies non-linear DNA structures (such as replication forks or bubbles) the DNA molecules are separated by both mass and shape in the second dimension (Reyes et al., 2009).

The 2D-AGE were performed as previously described (Reyes et al., 2009). For 2D-AGE, 5 g of DNA extracted from fresh liver-isolated mitochondria (Section 2.3.1.2) were digested using 20 U of the restriction enzyme BclI in a final volume of 20 µl for 3 h at 37 °C. For the first dimension, the entire digested product was mixed with 10 X DNA loading dye [0.25 % (w/v) bromophenol blue, 0.25 % (w/v) xylene cyanol, 40 % (v/v) glycerol], and loaded in 0.4% agarose gels [0.4 g ultrapure agarose

(Invitrogen), 100 ml 1 x TBE] without Ethidium Bromide. The gel was run with 1 x TBE [89 mM tris base, 89 mM boric acid, 2 mM EDTA (pH 8.0)] at constant 28 V for 18 hours. After the first-dimensional run, sample-containing lanes were excised individually from the gel using a scalpel blade (and the top 4 cm removed), rotated 90 ^{o} contraclockwise and transferred to the top part of the second-dimension tank. The slices were then covered with the second-dimension 1% agarose gels [4 g ultrapure agarose (Invitrogen), 400 ml 1 x TBE, with 500 ng/ml of Ethidium Bromide]. The second-dimension gel was run with 1 x TBE also containing 500 ng/ml of Ethidium Bromide, at constant 260 mA for 6 h in the 4 ^{o}C cold room. At the end of the second-dimension run, the gel was processed, dry-blotted onto nylon membranes, hybridised and visualised as described in Section 2.3.10.

2.3.10. Southern Blotting

2.3.10.1. Southern Transfer

Following DNA electrophoresis through 1 Dimensional or 2D-AGE, gels were depurinated to aid transfer of large molecules by incubation in 0.25 N HCl for 20 min with gentle rocking. Gels were then denatured by incubation in Southern denaturation buffer (0.5 M NaOH, 1.5 M NaCl) twice for 10 minutes, followed by incubation in Southern neutralisation buffer (0.5 M Tris-HCl, pH 7.4, 1.5 M NaCl) twice for 10 minutes. Gels were then dry blotted onto a charged nylon membrane overnight, and cross-linked by exposure to 254 nm UV light, 120 mJ/cm^{2} in a CL-1000 UV Crosslinker (UVP).

2.3.10.2. Preparation of radiolabelled dsDNA probes

Probes annealing in the 7S DNA region were initially amplified by PCR from total DNA of C2C12 mouse cells as described in Section 2.3.3.8 and purified as in Section 2.3.4. For radiolabelling, OLB Buffer A [1.25 M tris-HCl (pH 8), 125 mM $MgCl_2$, 250 mM b-mercaptoethanol, 0.5 mM each dATP, dGTP and dTTP] and OLB Buffer B [2 M HEPES (pH 6.6)] were mixed in a 2:5 ratio to create the final OLB Buffer. The PCR product (50 ng) in a total volume of 20 µl was denatured at 95 ^{o}C for 5 mins

and then placed on ice for 2 mins. The labelling was carried at 37 °C for 1 h after adding 10 µl of OLB Buffer, 2 µl of 1 mg/ml BSA, 5 U Klenow polymerase (NEB), 1 µl of 3 µg/µl Random hexamers, 13 µl nuclease-free water and 3 µl of [α-^{32}P] dCTP (111 TBq/mmol). The resulting labelled probe was then denatured again at 95 °C for 5 minutes, before being added to the membrane-containing hybridisation tube.

2.3.10.3. Southern Blotting Hybridization and Imaging

The UV cross-linked nylon membranes were blocked by incubation in 25 ml Church's buffer [0.25 M phosphate buffer, 7 % (w/v) SDS] for 1 hour at 65 °C in a hybridisation oven. The blocking buffer was then replaced with another 15 ml of Church's buffer, and the labelled probe added. Probe hybridisation was performed ON in an oven at 65 °C. After hybridization, the probe was discarded and the membrane washed three times with 50 ml 1 x SSC [150 mM NaCl, 15 mM sodium citrate (pH 7.0)] for 20 mins each, followed by an additional three washes with 1 x SSC containing 0.1 % SDS, for 20 mins each. The membranes were then wrapped in cling film and exposed to storage phosphor screens for various periods of time. The phosphor screens were then imaged digitally using an Amersham Typhoon 5 scanner. Bands or regions of interest were quantified using ImageLab™ (BioRad) software.

2.4. Protein-based Methods

2.4.1. Determination of Protein Concentration

Protein concentrations of whole cell lysates derived from cultured cells and from mouse tissues were estimated with a modified version of the Lowry protein assay, the DC™ Protein Assay (Bio-Rad), following manufacturer's instructions. The absorbance of the protein samples with unknown concentration and of seven BSA standards in a concentration range from 0 to 2 mg/ml were measured at λ= 750 nm and at RT with a SpectraMax Plus384 plate reader (Molecular Devices, Sunnyvale, CA, USA). The known BSA standards were used to elaborate a calibration curve, which was used to extrapolate the unknown protein concentrations using of their absorbance values.

2.4.2. Sodium Dodecyl Sulfate Polyacrilamide Gel Electrophoresis (SDS-PAGE)

Cultured cells (≥ 1 x 10^6 cells) were harvested by trypsinisation (Trypsin-0.5 % EDTA), washed twice with ice-cold PBS and pelleted by centrifugation at 4 °C (300 g x 5 min). Cell pellets were re-suspended and lysed with RIPA buffer (150 mM NaCl, 1.0% NP-40, 0.5% sodium deoxycholate, 0.1% SDS, 50 mM Tris, pH 8.0) containing 1X cOmplete™ mini EDTA-free Protease Inhibitor Cocktail (Roche, UK) and incubated on ice for 20 mins. Samples were then centrifuged (20,000 x g for 20 min at 4 ºC). Supernatants, containing solubilised cellular proteins, were transferred to a new 1.5 ml Eppendorf tubes and protein concentration determined as described in Section 2.4.1. Samples were stored at -20 °C until use.

Frozen mouse tissues (~50 mg) were suspended in 500 µl of ice-cold RIPA buffer and homogenised with a gentleMACS™ Dissociator (Miltenyi Biotec, Bergisch Gladbach, Germany) with the recommended setting per tissue type. An initial spin (500 g for 5 min at 4 °C) was performed to remove larger debris and the resulting supernatant was transferred to a new 1.5 ml Eppendorf. Samples were then centrifuged (20,000 x g for 20 min at 4 ºC). The final supernatants were then transferred to a new 1.5 ml Eppendorf tubes and protein concentration determined as described in Section 2.4.1. Samples were stored at -20 °C until use.

Protein lysates (10 – 40 µg) were mixed with 10 X NuPAGE™ sample reducing agent and 4X NuPAGE™ LDS sample buffer (Invitrogen™), and incubated for 5 min at 95 °C (or 10 min at RT when analysing proteins of the MRC). Protein samples were loaded and separated under denaturing conditions by SDS-PAGE using either 12% or 4-12% gradient precast polyacrylamide NuPAGE® Bis-Tris gels (Invitrogen™). The NuPAGE® MES SDS Running Buffer (1X: 50 mM MES, 50 mM Tris Base, 0.1 % SDS, 1 mM EDTA, pH 7.3) was used in all applications (Invitrogen™). Gels were run at 150V for 1-2 h at RT, with 3 µl Precision Plus Protein™ Dual-color Standard (Bio-Rad, UK) in one of the lanes for size comparison.

2.4.3. Blue Native Gel Electrophoresis (BNGE)

Frozen mouse tissues (~50 mg) were homogenised in 10 volumes of Medium A (320 mM sucrose, 1mM EDTA, 10mM Tris-Hcl, pH 7.4) in a glass Dounce-type homogeniser using a manually-driven glass pestle (~15 strokes). Homogenates were centrifuged (800 x g for 5 min at 4 °C) to remove nuclei and debris. The resulting supernatant was collected and centrifuged (9,000 x g for 10 minutes at 4 ºC) to obtain an enriched mitochondrial fraction. The obtained pellet was then re-suspended in 1 ml of Medium A and an aliquot of 5 µl was taken for determination of protein concentration (Section 2.4.1). The samples were then centrifuged (9,000 x g for 5 minutes at 4 ºC) and the pellet was re-suspended in an appropriated amount of solubilisation buffer (1.5 M aminocaproic acid, 50 mM Bis-Tris/HCl, pH 7) to obtain a protein concentration of 10 mg/ml. Samples were solubilised with 4 mg Digitonin/mg protein, incubated on ice for 5 minutes and centrifuged (20,000 x g for 30 minutes at 4 ºC). The resulting cleared supernatants were mixed with sample buffer (750 mM aminocaproic acid, 50 mM Bis-Tris, 0,5 mM EDTA and 5 % Serva Blue G-250).

BNGE protein samples (50 – 100 µg) were loaded and separated under non-denaturing conditions and run through a 3-12 % Native-PAGE gel (NativePAGE™ Novex™ Bis-Tris Gels, Thermo Fisher Scientific). Initially the gel was run for 1 h at 150 V in Cathode Buffer A (50 mM tricine, 15 mM Bis-Tris, pH = 7.0), and 0.02% Coomassie® G 250), and further run for 1-2 h at 200V (~8mA) in Cathode Buffer B (50 mM Tricine, 15 mM Bis-Tris, pH = 7.0, and 0.002% Coomassie® G 250). The Anode Buffer (50 mM tricine, 15 mM Bis-Tris pH = 7.0) was used in all applications.

2.4.4. Western Blotting

Proteins separated both through SDS-PAGE and BNGE gels were electroblotted to methanol activated PVDF membranes (Immobilon-P Membrane, Merck Millipore) using a wet transfer system (Mini-PROTEAN® Tetra Cell, Mini Trans-Blot® Module, Bio-Rad, UK). Transfer of SDS-PAGE was performed at 4 ºC and 100 V for 1 h in transfer buffer (25 mM Tris-HCl, 192 mM Glycine, 20 % methanol (v/v) and 0.025 % SDS). Blotting of BN-PAGE was done at 4 ºC and 300 mA for 1 h in bicarbonate transfer buffer (10 mM $NaHCO_3$, 3 mM $NaCO_3$).

2.4.5. Coomassie staining

Coomassie staining was used as a loading control in some experiments. After transfer of the proteins to PVDF membranes, the residual proteins that remained in the gel were detected using SimpleBlue SafeStain (ThermoFisher), according to manufacturer's instructions. After transfer, the gel was briefly rinsed with water and then embedded in SimpleBlue SafeStain solution for 1 h at RT. The staining solution was then substituted with water and incubated ON. Gels were digitally scanned with a professional scanner (EPSON Expression 1680 Pro, EPSON, UK).

2.4.6. Immunodetection

PVDF membranes were blocked with 5% milk in PBS with 0.1% Tween 20 (PBS-T) for 1 h at RT while shaking and then incubated overnight with specific primary antibodies in 5% milk in PBS-T at 4°C (see Table 2.16). After incubation with the primary antibody, membranes were washes three with PBS-T (10 min at RT) while shaking. Then membranes were incubated with horseradish peroxidase (HRP)-conjugated anti-rabbit, anti-mouse or anti-goat (Promega, catalogue number: W4011 [rabbit], W4021 [mouse] and V8051 [goat]) IgG secondary antibodies at a dilution of 1:3000, respective to the used primary antibody. Three additional washes in PBS-T were performed (10 min at RT) and then membranes were developed by incubating with Amersham ECL™ Western Blotting Detection Reagents (GEHealthcare, Chalfont St Giles, UK), according to manufacturer's

instructions. Developed membranes were imaged digitally with an Amersham Imager 680 blot and gel imager (GE Healthcare, Bio-Sciences, Pittsburgh, Pennsylvania, USA). Bands were quantified using the Fiji software.

Table 2.16 Primary antibodies used for immunodetection.

Antigen	Host	Dilution	Manufacturer (CN)
POLγA	Goat	1:500	Santa Cruz Biotechnology (sc-5931)
POLγB	Rabbit	1:1000	LSBio (LS-C334882)
GAPDH	Mouse	1:3000	Abcam (ab53098)
LONP1	Rabbit	1:1000	ProteinTech (15440–1-AP)
HSC70	Mouse	1:1000	Santa Cruz Biotechnology (sc-7298)
NDUFS4	Rabbit	1:1000	Novus Biologicals (NBP1-31465)
ß-Tubulin	Rabbit	1:3000	ProteinTech (100094-1-AP)
NDUFA9	Mouse	1:1000	Abcam (ab14713)
SDHB	Mouse	1:2000	Abcam (ab14714)
LY6A	Rabbit	1:1000	Abcam (ab109211)

2.5. Mitochondrial Respiratory Chain Functional Assays

2.5.1. Mitochondrial Respiratory Chain complex enzymatic activity

The activities of respiratory chain complexes and citrate synthase (CS) were measured spectrophotometrically in mouse tissue samples. Frozen murine tissues (~50 mg) were minced into small pieces with sterilised surgical scissors and then homogenised in 15 volumes of Medium A (320 mM sucrose, 1mM EDTA, 10mM Tris-Hcl, pH 7.4) in a glass Dounce-type homogeniser using a manually-driven glass pestle (~15 strokes). Homogenates were centrifuged (800 x g for 5 min at 4 °C) and the crude mitochondria-enriched supernatants were snap frozen immediately in liquid nitrogen. Samples were stored at -80°C until use. On the day of the experiment, the mitochondria-enriched homogenates were thawed on ice initially and then snap frozen and quickly thawed between liquid nitrogen and a 37°C water bath for three consecutive freeze-thaw cycles. Protein concentration

was determined as described in Section 2.4.1, and samples were loaded into individual wells of a 96-well plate and placed on ice.

The spectrophotometric activity of CI, CII, CIII, CIV, and CS, was measured as described in (Bugiani et al., 2004). The protein concentration and pathlength per each 200 µl reaction were used to calculate the specific biochemical activities of each sample using the Beer-Lambert law: A=εlc (A=absorbance, ε=molar absorption coefficient, l=optical pathlength, c=molar concentration).

$$Specific\ activity = \frac{\Delta Abs \text{ x total reaction volume (ml)}}{\varepsilon \text{ x sample volume (ml)x [prot]} \left(\frac{mg}{ml}\right) \text{x l (cm)}}$$

The specific activities of CI, CII, CIII, CIV were each normalised against the relative activity of CS. Technical replicates (n ≥ 3) were performed per sample using the same reaction buffer.

2.5.1.1. Complex I

CI activities were performed in tissue homogenates by following NADH oxidation over 2 mins. Oxidised NADH (NAD^+) is not detectable at this wavelength so the 'disappearance' of NADH following the addition of CoQ was measured as the change in absorvance (λ = 340 nm) at 30 °C. Tissue homogenate samples were incubated in CI buffer (Table 2.17) for 10 mins. The CI-inhibitor rotenone was then added and incubated for at least 1 min, and a second measurement under the same conditions was taken as background for all non-CI linked NADH oxidation. The difference between these values was calculated relative to the extinction coefficient of the reaction ($\varepsilon_{NADH_{340nm}}$ = 6.81 ($mlnmol^{-1}cm$), volume and concentration of the sample, and pathlength through each well.

Table 2.17 Complex I enzymatic activity assay mixture and substrates.

Reagent	Reagent Manufacturer | CN	Final Concentration
PK buffer (pH = 8.0)	-	20 mM
NADH (in dH_20)	Roche | 10107735	0.2 mM
Sodium azide (NaN_3) (in dH_20)	Sigma-Aldrich® | S8032	1 mM
BSA (in dH_20 + EDTA 10 mM pH 7.4)	Sigma-Aldrich® | A6003	1 mg/ml
CoQ (in 10 % EtOH)	Sigma-Aldrich® | C7956	50 µM
Rotenone (in 25 % EtOH)	Sigma-Aldrich® | R8875	5 µM

2.5.1.2. Complex II

CII activities were performed in tissue homogenates using the mixture detailed in Table 2.18. Measurement was performed at 30 °C by following the reduction rate of DCPIP (an electron acceptor); λ= 600 nm for 2 mins. $\varepsilon_{DCPIP600nm}$ = 19 $mlnmol^{-1}cm$. Addition of CoQ followed to measure specific MRC-linked CII activity.

Table 2.18 Complex II enzymatic activity assay mixture and substrates.

Reagent	Reagent Manufacturer | CN	Final Concentration
PK buffer (pH = 7)	-	50 mM
Potassium cyanide (KCN) (in dH_20)	Sigma-Aldrich® | 31252	1.5 mM
2,6-Dichlorophenolindophenol (DCPIP)	Sigma-Aldrich® | D1878	0.1 mM
Sodium succinate (in dH_20)	Sigma-Aldrich® | S2378	16 µM
CoQ (in 10 % EtOH)	Sigma-Aldrich® | C7956	50 µM

2.5.1.3. Complex III

CIII activities were performed in tissue homogenates using the mixture detailed in Table 2.19. Measurement was performed at 30 °C by following the reduction of cytochrome *c* (electron acceptor); λ= 550 nm for 2 mins. $\varepsilon_{NADH340nm}$ = 21 mlnmol^{-1}cm.

Table 2.19 Complex III enzymatic activity assay mixture and substrates.

Reagent	Reagent Manufacturer | CN	Final Concentration
PK buffer (pH = 7.4)	-	50 mM
NaN_3 (in dH_20)	Sigma-Aldrich® | S8032	1.5 mM
BSA (in dH_20 + EDTA 10 mM pH 7.4)	Sigma-Aldrich® | A6003	0.1 mM
Cytochrome c (in dH_20)	Sigma-Aldrich® | C7752	16 µM
Reduced decylubiquinone (DBH_2)	Sigma-Aldrich® | D7911	50 µM

2.5.1.4. Complex IV

CIV activities were performed in tissue homogenates using the mixture detailed in Table 2.20. Measurement was performed at 37 °C by following oxidation of cytochrome *c* (electron donor); λ= 550 nm for 2 mins. $\varepsilon_{Cytc550nm}$ = 18.5 mlnmol^{-1}cm.

Table 2.20 Complex IV enzymatic activity assay mixture and substrates.

Reagent	Reagent Manufacturer | CN	Final Concentration
90-95 % reduced cytochrome c (1.3 mg/ml) (in 50 mM KP buffer (pH = 7))	Sigma-Aldrich® | C7752	50 mM

2.5.1.5. Citrate Synthase

CS activities were performed in tissue homogenates using the mixture detailed in Table 2.21. CS catalyses the reaction between acetyl-CoA and oxaloacetate. In this assay, measurement was performed at 30 °C following the of absorbance of thionitrobenzoic acid (TNB), the main reaction product from CoA with 5-dithio-bis-(2)-nitrobenzoic acid (DTNB). The increase in absorbance due to generation of TNB is proportional to the amount of liberated CoA and indicates the relative activity of CS; λ= 412 nm for 2 mins. $\varepsilon_{TNB412nm}$ = 13.8 mlnmol^{-1}cm.

Table 2.21 CS enzymatic activity assay mixture and substrates.

Reagent	Reagent Manufacturer | CN	Final Concentration
Tris-HCl buffer (pH = 8)	-	75 mM
DTNB (in 187.5 mM Tris-HCl (pH = 8))	Sigma-Aldrich® | D8130	0.1 mM
Triton X-100	Roche | 11332481001	0.1 %
Acetyl-CoA	Sigma-Aldrich® | A2181	0.4 mM
Oxalacetic acid	Sigma-Aldrich® | O4126	0.5 mM

2.5.2. In-Gel Activity (IGA)

In-gel activity was performed on BNGE samples, prepared as described in Section 2.4.3. Gels were briefly rinsed in water and then incubated 2 hr at RT while gently shaking in 10 ml of CI detection solution [0.1 M Tris-HCl pH 7.4, 0.14 mM NADH, 1 mg/ml Nitro blue tetrazolium (NBT, Sigma-Aldrich)]. After incubation, gels were washed with water and digitally scanned with a professional scanner (EPSON Expression 1680 Pro, EPSON, UK).

2.6. *In vitro* Assays with Recombinant Proteins

The set of *in vitro* assays with purified recombinant proteins presented in this work were carried at Maria Falkenberg´s lab at the Department of Medical Biochemistry and Cell Biology at the University of Gothenburg as part of a secondment of the Marie Sklodowska-Curie ITN-REMIX. Some of the assays were performed in collaboration with members of Falkenberg´s lab and acknowledged in the respective figure legends.

2.6.1. Expression and Purification of Recombinant Proteins

Expression and purification of all the recombinant proteins used in this work was carried by members of Falkenberg´s lab.

LONP1 (WT and *LONP1*^{S855A}) gene lacking the mitochondrial targeting sequence (aa 1–67) was cloned into a pNic28-BSA4 vector with a cleavable 6×HisTag in the N-terminus. Rosetta™(DE3) pLysS competent cells (Novagen) were transformed with the plasmid and grown in Terrific Broth media with 50 mg/l Ampicillin and 34 mg/l Chloramphenicol at 37°C until OD_{600} = 3. Protein expression was induced with 1 mM IPTG at 16 °C for 4 h.

Cells were harvested by centrifugation, frozen in liquid nitrogen, thawed and lysed at 4 °C in lysis buffer (25 mM Tris-HCl pH 8.0, 0.8 M NaCl and 10 mM β-mercaptoethanol). The suspension was homogenized using an Ultra-Turrax T3 homogenizer (IKA) and centrifuged at 20 000 × *g* for 45 min in a JA-25.50 rotor (Beckman Coulter). The supernatant was loaded onto His-Select Nickel Affinity Gel (Sigma-Aldrich) equilibrated with buffer A (25 mM Tris–HCl, pH 8.0, 0.4 M NaCl, 10% glycerol and 10 mM β-mercaptoethanol). The protein was eluted with buffer A containing 250 mM imidazole. Removal of the 6×HisTag was achieved by overnight dialysis in presence of ≈0.5 mg TEV in buffer A. An additional Nickel purification step was performed to get rid of uncut His tagged protein and TEV. The protein was subsequently purified over a 5-ml HiTrap Heparin HP column (GE Healthcare) and a 1-ml HiTrap Q HP column (GE Healthcare), both equilibrated in buffer B (25 mM Tris–HCl pH 8.0, 10% glycerol and 1 mM DTT) containing 0.2

M NaCl, followed by elution driven by a linear gradient (50 and 10 ml, respectively) of buffer B containing 1.2 M NaCl (0.2–1.2 M NaCl). Protein purity was checked on a precast 4–20% gradient SDS-PAGE gel (BioRad, 567–8094) and pure fractions were aliquoted and stored at –80 °C.

Human and mouse POLγA versions (lacking the mitochondrial targeting sequence aa 1–25) and human and mouse POLγB (lacking the mitochondrial targeting sequence aa 1–24 and aa 1–16, respectively) were expressed in Sf9 cells and purified as described above for LONP1, with the following modifications. For POLγA, an additional step of purification with 1 ml HiTrap SP HP column was added after the HiTrap Q HP column purification. The column was equilibrated with buffer B containing 0.1 M NaCl and eluted with a linear gradient (10 ml) of buffer B containing 1.2 M NaCl (0.1–1.2 M NaCl). For POLγB, an additional step of purification with a 1-ml HiTrap Talon column (GE Healthcare) was used in between HiTrap Heparin HP (GE Healthcare) and HiTrap SP HP (GE Healthcare). This column was equilibrated with buffer C (25 mM Hepes pH 6.8, 10% glycerol, 0.4 M NaCl, 1 mM β-mercaptoethanol) containing 5 mM imidazole and elution driven by a linear gradient (10 ml) of buffer C containing 150 mM imidazole (5–150 mM imidazole).

2.6.2. Electrophoresis Mobility Shift Assay (EMSA)

DNA binding affinity of POLγA and POLγA-B2 to a primer-template was assayed using a 36-nucleotide (nt) oligonucleotide [5′-TTT TTT TTT TAT CCG GGC TCC TCT AGA CTC GAC CGC-3′] annealed to a ^{32}P 5′-labeled 21-nt complementary oligonucleotide (5′-GCG GTC GAG TCT AGA GGA GCC-3′). This produces a primed-template with a 15-base single-stranded 5′-tail. Reactions were carried out in 15 µl volumes containing 10 fmol DNA template, 20 mM Tris–HCl [pH 7.8], 1 mM DTT, 0.1 mg/ml bovine serum albumin, 10 mM $MgCl_2$, 10% glycerol, 2 mM ATP, 0.3 mM ddGTP and 3 mM dCTP. POLγA and POLγB were added as indicated in the figures and reactions were incubated at RT for 10 min before separation on a 6% Native PAGE gel in 0.5 × TBE for 35 min at 180 V. Bands were visualized by autoradiography.

For K_d analysis, band intensities representing unbound and bound DNA were quantified using Multi Gauge V3.0 software (Fujifilm Life Sciences). The fraction of bound DNA was determined from the background-subtracted signal intensities using the expression: bound/(bound+unbound). The fraction of DNA bound in each reaction was plotted versus the concentration of POLγA or POLγA-B2. Data were fit using the 'one site – specific binding' algorithm in Prism 8 (Graphpad Software) to obtain values for K_d.

2.6.3. Coupled Exonuclease-Polymerase Assay

DNA polymerization and 3′-5′ exonuclease activity were assayed using the same primer-template as described above for electrophoresis mobility shift assay (EMSA). The reaction mixture contained 10 fmol of the DNA template, 25 mM Tris-HCl [pH 7.8], 10% glycerol, 1 mM DTT, 10 mM $MgCl_2$, 100 µg/ml BSA, 60 fmol of POLγA, 120 fmol of POLγB and the indicated concentrations of the four dNTPs. The reaction was incubated at 37 °C for 15 min and stopped by the addition of 10 µl of TBE-UREA-sample buffer (BioRad). The samples were analysed on a 15% denaturing polyacrylamide gel in 1 × TBE buffer.

2.6.4. Exonuclease Assay

A ^{32}P 5′-labeled 32-mer oligonucleotide [5′-CTA TCT CAG CGA TCT GTC TAT TTC GTT CAT CG-3′] was hybridized at the 5′-end to single-stranded pBluescript SK(+), creating a 31-bp dsDNA region with a one-nucleotide mismatch at the 3′-end of the pBluescript SK(+). Reactions were carried out in 20 µl volumes containing 10 fmol template DNA, 25 mM Tris–HCl (pH 7.8), 1 mM DTT, 10 mM $MgCl_2$, 0.1 mg/ml BSA, 150 fmol POLγA and 300 fmol POLγB (without dNTPs). Reactions were incubated at 37 °C for the indicated times and stopped by the addition of 6 µl of stop buffer (90 mM EDTA, 6% SDS, 30% glycerol, 0.25% bromophenol blue and 0.25% xylene cyanol) and separated on a 7 M urea/20% denaturing polyacrylamide gel in 1 × TBE.

2.6.5. DNA Synthesis on ssDNA Templates

A ^{32}P 5′-labeled 70-mer oligonucleotide [5′-42(T)-ATC TCA GCG ATC TGT CTA TTT CGT TCA T-3′] was hybridized to a single-stranded pBluescript SK(+). The template formed consists of a 42 nt single-stranded 5′-tail and a 28 bp duplex region. Reactions were carried out in 20 µl volumes containing 10 fmol template DNA, 25 mM Tris–HCl (pH 7.8), 1 mM DTT, 10 mM $MgCl_2$, 0.1 mg/ml BSA, 100 µM dATP, 100 of the four dNTPs, 2.5 pmol mtSSB, 150 fmol POLγA and 300 fmol POLγB. Reactions were incubated at 37 °C for the indicated times and stopped by the addition of 6 µl of stop buffer (90 mM EDTA, 6% SDS, 30% glycerol, 0.25% bromophenol blue and 0.25% xylene cyanol) and separated on a 0.9% agarose gel at 130V in 1 × TBE for 4 h.

2.6.6. Rolling Circle *in vitro* Replication Assay

A 70-mer oligonucleotide [5′-42(T)-ATC TCAG CGA TCT GTC TAT TTC GTT CAT-3′] was hybridized to a single-stranded pBluescript SK(+) followed by one cycle of polymerization using KOD polymerase (Novagen) to produce a ~3-kb double-stranded template with a preformed replication fork. Reactions of 20 µl were carried out containing 10 fmol template DNA, 25 mM Tris–HCl (pH 7.8), 1 mM DTT, 10 mM $MgCl_2$, 0.1 mg/ml BSA, 4 mM ATP, 100 µM dATP, 100 µM dTTP, 100 µM dGTP, 10 µM dCTP, 2 µCi [α-^{32}P] dCTP, 2 pmol mtSSB, 200 fmol TWINKLE, 200 fmol POLγA and 500 fmol POLγB (or as indicated in the figure). Reactions were incubated at 37 °C for 60 min (or as indicated in the figure) and stopped with 6 µl alkaline stop buffer (18% [wt/vol] Ficoll, 300 mM NaOH, 60 mM EDTA [pH8], 0.15% [wt/vol] Bromocresol green and 0.35% [wt/vol] xylene cyanol). Products were run in 0.8% alkaline agarose gels and visualized by autoradiography.

Incorporation of [α-^{32}P]-dCTP was measured by spotting 5 µl aliquots of the reaction mixture (after the indicated time points at 37°C) on Hybond N+ membrane strips (GE Healthcare Lifesciences). The membranes were washed (3 × with 2 × SSC and 1 × with 95% EtOH) and the remaining activity was quantified using Multi Gauge V3.0 software (Fujifilm Life Sciences). A dilution series of known specific activity of [α-^{32}P]-dCTP was used as a standard.

2.6.7. Thermofluor Assay

The fluorescent dye Sypro Orange (Invitrogen) was used to monitor the temperature-induced unfolding of WT and mutant POLγA as previously described (Al-Behadili et al., 2018). The WT and mutant POLγA (with or without POLγB) were set up in 96-well PCR plates at a final concentration of 1.6 μM protein and 5 × dye in assay buffer (50 mM Tris–HCl pH 7.8, 10 mM DTT, 50 mM MgCl2 and 5 mM ATP). Differential scanning fluorimetry was performed in a C1000 Thermal Cycler using the CFX96 real time software (BioRad). Scans were recorded using the HEX emission filter (560–580 nm) between 4 and 95 °C in 0.5 °C increments with a 5 s equilibration time. The melting temperature (Tm) was determined from the first derivative of a plot of fluorescence intensity versus temperature. Three independent measurements were performed.

2.6.8. Gel Filtration

Complex formation between POLγA and POLγB was tested by size-exclusion chromatography using a Superose 6 Increase 10/300 column (GE Healthcare) connected to an ÄKTA Purifier (GE Healthcare). The column was equilibrated in buffer D (25 mM Tris–HCl, pH 7.8, 10% glycerol, 1 mM DTT, 0.5 M NaCl, 10 mM $MgCl_2$). Equal amounts (1 nmol) of POLγA and POLγB (calculated as a dimer) were pre-incubated in buffer D for 10 min on ice before injection. Samples (200 μl) were injected onto the column through a 200 μl loop and run at 1 ml/min. Fractions of 250 μl were collected and analysed on a precast 4–20% gradient SDS-PAGE gel and visualized using ImageLab™ (BioRad). A size calibration curve was previously prepared using thyroglobulin (670 kDa), c-globulin (158 kDa), ovalbumin (44 kDa), myoglobin (17 kDa) and vitamin B12 (1.35 kDa) according to the manufacturer's instructions (BioRad, 151–1901).

To analyse the $LONP1^{S855A}$-POLγA interaction, a home-made gel filtration column (0.5 cm x 30 cm) was prepared using Bio-Gel agarose with a bead size of 75–150 μm (BioRad, 151–0440) and calibrated using a gel filtration standard (BioRad, 151–1901). Preincubation of the proteolytic mutant of LONP1 with POLγA in the presence of

2 mM ATP and 10 mM MgCl2 at 37 °C for 10 min allowed the formation of the complex that was later injected into the column and eluted in 1 CV of buffer D. Fractions of 200 µl were collected and analysed in a precast 4–20% gradient SDS-PAGE gel and visualized using ImageLab™ (BioRad).

2.6.9. LONP1 Proteolysis Assay

Protease activity of purified LONP1 on POLγA was measured in a 15 µl reaction volumes containing 0.5 µg of LONP1 WT and 0.55 µg of POLγA (in presence or absence of 0.22 µg of POLγB). When having both POLγA and POLγB in the same reaction, a pre-incubation in ice for 10 min was made before adding LONP1 to the reaction. Samples were incubated at 37 °C for 0–90 min (as indicated in the figures) in a buffer containing 50 mM Tris–HCl pH 8.0, 10 mM $MgCl_2$, 0.1 mg/ml BSA, 2 mM ATP and 1 mM DTT and the reactions were stopped by addition of Laemli sample buffer (BioRad, 16107447). Samples were run on precast 4–20% gradient SDS-PAGE gels (BioRad, 567–8094) and visualized using ImageLab™ (BioRad) to detect proteolytic activity on POLγA. Band intensities were measured with ImageLab™ (BioRad) and calculations were made to provide % of remaining POLγA-values compared to time (min) = 0. Reactions and calculations were made in triplicate and SD was calculated.

2.7. Statistics

Graphical visualisation of data and all statistical analyses were performed with GraphPad Prism software (version 8.0). All numerical data are expressed as mean ± standard error of mean (SEM) or mean ± standard deviation (SD), as labelled in each corresponding figure legend. Pre-test analyses on sample distribution were not performed and all data was assumed to have a normal distribution. A two tailed Student's t-test was used to assess statistical significance (see figure legends for details) in two groups comparisons. One-way or two-way analysis of variance ANOVA with Tukey's correction were used for multiple comparisons. Kaplan-Meier distribution and a log rank test were used for survival analysis. The statistical procedure used for each set of results will be mentioned either in-text and/or in the corresponding figure legends. Differences were considered statistically significant for $P < 0.05$., with the following system used:

$p < 0.05$ = *, $p < 0.01$ = **, $p < 0.005$ = *** and $p < 0.001$ = ****.

Animals were randomized in treated and untreated groups. No blinding to the operator was used.

Chapter 3 Results

Generation of *POLG* A449T and Y933C knockin mouse models

3. Generation of *POLG* A449T and Y933C knockin mouse models

3.1. Introduction

Mutations in *POLG*, encoding POLγA, the catalytic subunit of the mitochondrial DNA polymerase, are a major cause of human disease causing a spectrum of clinical manifestations characterized by either mtDNA multiple deletions or depletion of mtDNA copy number (Viscomi and Zeviani, 2017).

POLG-related syndromes are clinically heterogeneous and the same mutation can be associated to more than one presentation, affecting different tissues and with variable age of onset among patients. There is a correlation between the age of onset and the severity of the syndrome and the range of symptoms that are detectable, in which earlier onsets lead to more severe symptoms. The reasons for such complexity, tissue specificity and peculiar genetic transmission remain largely unclear.

More than 300 mutations have been described in *POLG*. Of these, a substitution of Alanine with Threonine at codon 467 (A467T) is the most common autosomal recessive mutation. Patients homozygous for *POLG* A467T are often presented with more severe early-onset mtDNA depletion syndromes, representing one extreme end of the clinical spectrum. In turn, the substitution of Tyrosine with Cysteine at codon 955 (Y955C) is the most frequent dominant mutation. Patients heterozygous for *POLG* Y955C normally represent the other extreme end of the clinical spectrum with milder later-onset syndromes, associated with multiple deletions of the mtDNA (Nurminen et al., 2017).

In this chapter, I describe the generation of two *POLG* knockin mouse models, corresponding to the human A467T and Y955C mutations, using different CRISPR/Cas9-based approaches. These models are envisioned to modulate in mice the most common recessive and dominant *POLG* mutations in humans, representing the two extreme ends of the clinical spectrum of manifestations of *POLG* patients.

3.1.1. Brief overview of the CRISPR/Cas technology to generate Knockins

The CRISPR/Cas system was originally identified as an RNA-based immunological defence mechanism present in bacteria that recognises and degrades foreign DNA from invading viruses and plasmids (Garneau et al., 2010). Insights of such bacterial defence mechanism served as a foundation to engineer the current technology used for targeted genome editing (Cong et al., 2013). The current CRISPR/Cas editing tool was based on the type II CRISPR locus of *Streptococcus pyogenes* and includes two elements, the Cas9 nuclease and a guide RNA (gRNA) (Cong et al., 2013). The gRNA is a short synthetic RNA that contains a scaffold structure, necessary for Cas9 binding, and a spacer, which is a user-defined short synthetic RNA of 20-nucleotides that guides the Cas9 nuclease to the genomic region of interest where it will cut the DNA. The system also requires the presence of a 3-nucleotide sequence immediately at the 3′ end of the targeted locus, the PAM sequence (Rath et al., 2015). The PAM sequence required by Cas9 is 5′-NGG-3′, however it differs between different Cas proteins isolated from other organisms (Rath et al., 2015). Once inside a cell, the Cas9 interacts with the scaffold of the gRNA forming a ribonucleoprotein complex. The Cas9:gRNA complex then screens the genome for the presence of PAM sequences until it finds a region where the spacer of the gRNA is complementary to the target DNA (Rath et al., 2015). Target binding and PAM detection induces a conformational change in the Cas9 nuclease, enabling a production of a double-strand break (DSB) ~3-4 nucleotides upstream of the PAM sequence, inside the spacer region. Breaks on the DNA can have harmful consequences; thus, cells will attempt to fix them using dedicated repair mechanisms (Rath et al., 2015). Frequently, DSBs are repaired by the non-homologous end joining (NHEJ) pathway. However, this pathway is error-prone and recurrently causes small nucleotide insertions or deletions (indels), resulting in amino acid deletions, insertions or frameshift mutations, many of them likely to result in loss-of-function mutations (Rath et al., 2015). This is particularly convenient and the underlying mechanism of the CRISPR/Cas9 strategy to generate knockout cells or animal models.

Less often, DSBs can be repaired by the homology directed repair (HDR) pathway. In contrast with NHEJ that does not use a DNA template to perform repair, HDR uses another DNA fragment with homology to the damaged allele, normally a sister chromatid (Rath et al., 2015). However, provision of a user-designed synthetic DNA template can be exploited to precisely install insertions, deletions or point mutations in the DNA sequence (Cong et al., 2013). This strategy can be used to introduce point mutations and to generate knockin cells and animal models, in which the precise gene editing is accomplished by repairing an accurate CRISPR/Cas9-mediated DSB by HDR using a DNA template with the intended modification (Figure 3.1 - A) (Cong et al., 2013).

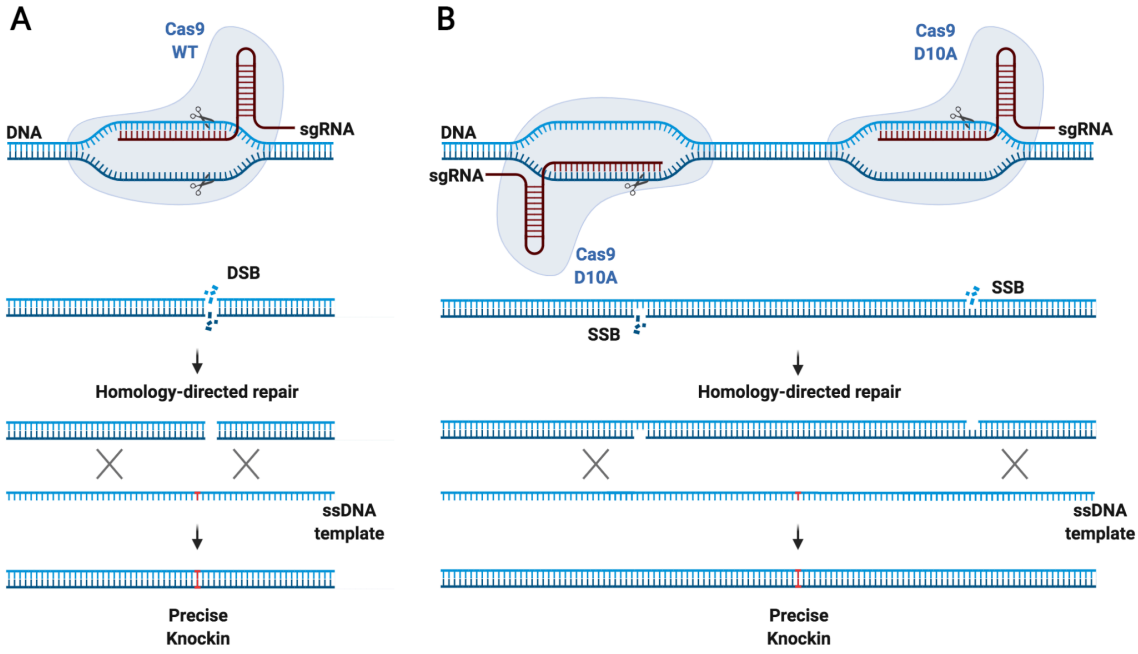

Figure 3.1. Comparison between CRISPR/Cas9 technologies to generate targeted knockins. **(A)** Schematics of the single nuclease CRISPR/Cas9 WT approach. The WT version of Cas9 is used with a single gRNA, which as a complex creates a DSB in the targeted DNA region. The DBS can be repaired by the HDR pathway, which exploits the presence of a user-designed ssDNA with the intended knockin modification as template to repair the endogenous DNA. The end product is a precise knockin in the intended region of the genome. **(B)** Schematics of the double-nickase CRISPR/Cas9 D10A approach. A nickase version of Cas9 (created by introducing a D10A modification) is used with a pair of gRNAs each creating a SSB in opposite strands in the targeted DNA region. Similar to DSB, these SSBs can trigger the HDR pathway which uses a user-designed ssDNA with the intended knockin modification as template. The use of two gRNAs is used as a strategy to reduce off-targets across the genome, but compromises HDR frequency. DBS- double strand break; SSB- single strand break; ssDNA- single stranded DNA; HDR- homology-directed repair.

DBS are preferentially repaired by NHEJ, rather than HDR, resulting mainly in the formation of indels. Notwithstanding, single-strand breaks (SSBs) are preferentially repaired through HDR. Therefore, a nickase version of Cas9 was created yielding SSBs and thus enhancing HDR efficiencies. This was accomplished by introducing an aspartate-to-alanine (D10A) mutation in the RuvC catalytic domain, allowing the Cas9-D10A to cleave only the strand complementary to the gRNA (Cong et al., 2013).

One major concern related to the use of CRISPR/Cas9 for genome editing and model generation is the possibility of the spacer sequence from the gRNA to anneal to similar sequences that are not the intended target. DSBs or SSBs in these off-targets can lead to undesired indels elsewhere in the genome, confounding the effects of the edits made in the region of interest. To overcome this, a double nickase approach was developed (Ran et al., 2013). Such strategy uses the Cas9-D10A nickase together with two gRNAs with a small offset around the targeted area, creating two nearby SSBs in each strand, which are treated as a DSB. Given that individual nicks in the genome are repaired with high fidelity by HDR, the use of two gRNAs effectively extends the number of specifically recognized bases in the target site, greatly reducing off-targets (Figure 3.1 - B) (Ran et al., 2013). Nevertheless, while reducing off-targets, in this strategy the two SSB are processed as a DSB, favouring NHEJ over HDR and therefore, precise on-target editing efficiency is reduced. Thus, a balance between off-targets and precise editing efficiencies has to be weighted when selecting the strategy to generate cells and animal models.

3.2. Human *POLG* residues A467 and Y955 are evolutionary conserved in mice and other species

To model the human *POLG* A467T and Y955C in mice, the equivalent residues need to be mapped in mouse POLγA. The protein sequences of human and mouse POLγA were retrieved from the UniProt database (https://www.uniprot.org/) and aligned using the web tool Clustal Omega (https://www.ebi.ac.uk/Tools/msa/clustalo/). Analysis of the aligned sequences revealed that both human A467 and Y955 are conserved in mice, at positions A449 and Y933, respectively. In addition, these residues were conserved in the POLγA sequences of other organisms: chimpanzee (*Pan troglodytes*), pig (*Sus scrofa*) and fruit fly (*Drosophila melanogaster*) (Figure 3.2). Such evolutionary conservation further supports the critical role of A449 and Y933 in the function of human POLγA, and thus the pathogenicity of mutations affecting them.

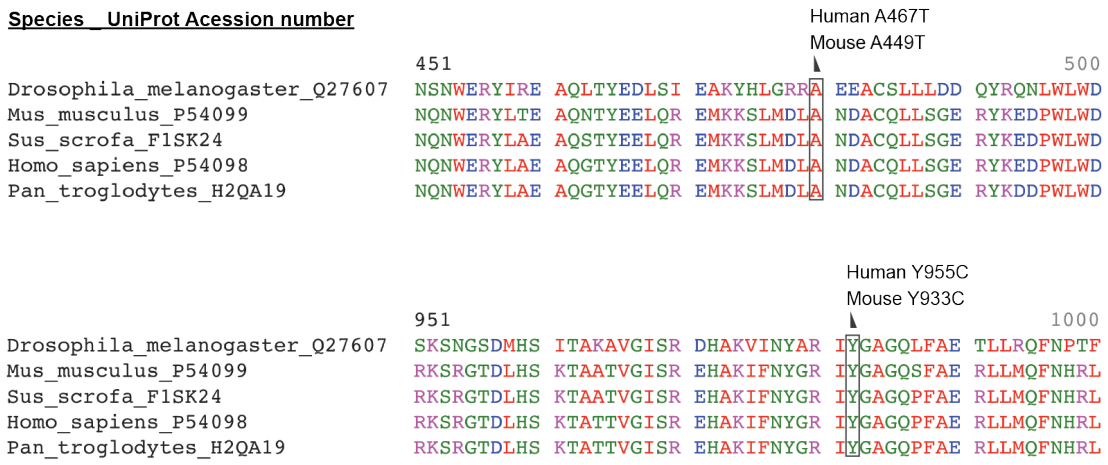

Figure 3.2. Protein sequence alignment of POLγA between different species. The POLγA sequences of human (*Homo sapiens*), mouse (*Mus musculus*), chimpanzee (*Pan troglodytes*), pig (*Sus scrofa*) and fruit fly (*Drosophila melanogaster*) were retrieved from UniProt and aligned using Clustal Omega. Note the evolutionary conservation of human A467 and Y955 in the different species. The human A467 and Y955 correspond in mice to PolγA residues A449 and Y933, respectively. Colour legend: blue = hydrophobic, red = positive charge, magenta = negative charge, green = polar, pink = cysteines, orange = glycines, yellow = prolines, cyan = aromatic.

3.3. Generation of the *Polg*^{A449T} mouse model

3.3.1. Generation of *Polg*^{A449T} mice by the double-nickase CRISPR/Cas9 D10A approach

The *Polg*^{A449T} was previously established in Zeviani´s lab, therefore the strategy presented here is used as comparison to the generation of the *Polg*^{Y933C} mice.

The *Polg*^{A449T} mice were generated using the double nickase CRISPR/Cas9 D10A approach, with all the components of the system (Cas9-D10A, gRNAs and HDR template) injected directly in fertilised one-celled oocytes. Delivery of the CRISPR/Cas9 system directly into oocytes enhances the probability of obtaining full-body edited mice already in the first litter (Figure 3.3). In addition, the double nickase CRISPR/Cas9 D10A strategy was used to reduce the risk of creating off-targets. Such strategy comes with reduced HDR frequency, thereby reducing the probability of obtaining a A449T knockin. However, in this occasion, because the born mice are screened for the presence of the A449T allele and only one mouse is needed to start a colony, reduced off-targets were preferred over knockin efficiency.

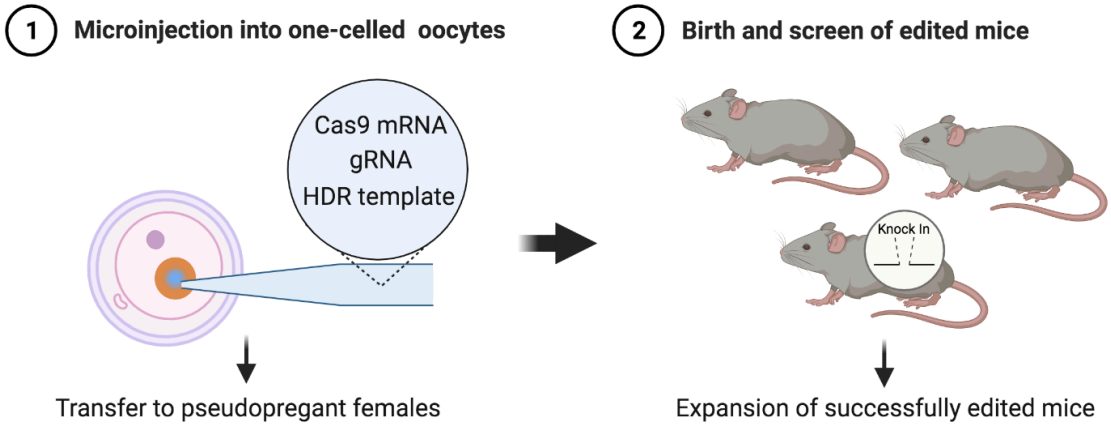

Figure 3.3. CRISPR/Cas9 editing of fertilized oocytes. (1) In this strategy, the CRISPR/Cas9 components are microinjected directly into the zygote before the fusion of the two pronuclei. Activity of CRISPR/Cas9 in early one-celled embryos before the first cell division increases the chance of introducing the knockin in every cell. The modified oocytes are cultured until the blastocyst stage, when they are transferred pseudo-pregnant females. **(2)** The pups originated from the edited blastocyst are screening for a full-body knockin. The positive mice constitute founder mice (Fo) and can be used immediately to expand a colony for characterization. In addition, the mice are generated in the same pure background strain as the oocyte-donors.

The two gRNAs necessary for the double nickase strategy were selected to target the mouse *Polg* gene in exon 7 with an offset of 17 nucleotides, each gRNA targeting opposite strands around the region to be edited (c.1345G). A 140 bp synthetic ssDNA was designed to serve as HDR template. The HDR template contained a G>A modification, changing the amino acid from Alanine to Threonine generating the desired knockin mutation (c.1345G>A/p.A449T). To guarantee that CRISPR/Cas9 does not cut the DNA repetitively once the knockin was created, the HDR also contained a silent C>A mutation to disrupt the PAM site of one of the gRNAs (gRNA-Rv) and a silent T>C modification to abolish the recognition sequence of the other gRNA (gRNA-Fw). The latter modification also creates a PvuII restriction site useful for screening and genotyping of the A449T allele (Figure 3.4).

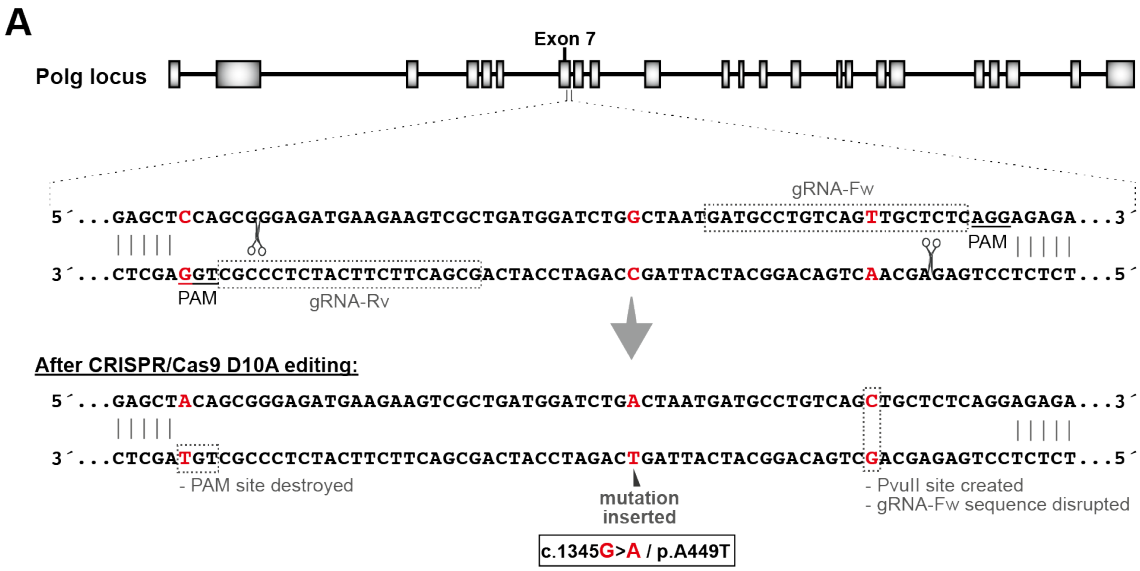

Figure 3.4. Strategy for double-nickase CRISPR/Cas9 D10A mediated gene editing of mouse *Polg* gene in exon 7. Modified nucleotides are presented in red letters. On the left side a silent C>A modification was inserted to abolish the PAM site of the sgRNA-Rv. On the right side, a silent T>C modification was inserted to disrupt the recognition sequence of the sgRNA-Fw and to create a PvuII restriction site for genotyping purposes. In the centre, a G>A modification was inserted changing the amino acid from Alanine to Threonine generating the desired knockin mutation (c.1345G>A / p.A449T).

The Cas9 D10A mRNA, gRNAs and HDR donor were sent to the 'Core Facility for Conditional Mutagenesis' at the IRCCS Ospedale San Raffaele, (Milan, Italy) for microinjection into fertilised mouse one-celled zygotes. FVB/NJ was the mouse strain of choice because the large size of the pronuclei in the fertilised oocytes facilitates the injection procedure. The injected embryos were then transferred into pseudo-pregnant females which gave birth to several pups after 3 weeks.

Genetic analyses of the resulting pups allowed the identification of founder mice (F0), heterozygous for the A449T allele, *Polg*$^{WT/A449T}$. To ensure germline transmission and allow allele segregation, the *Polg*$^{WT/A449T}$ mouse was bred with a WT FVB/NJ mouse. Genotyping of the originated pups (F1) showed the presence of the A449T allele and confirmed germline transmission and successful generation of a *Polg*^{A449T} mouse line.

The human *POLG* A467T mutation behaves as recessive trait. Therefore, to reproduce the human genotype, heterozygous *Polg*$^{WT/A449T}$ mice were interbred to generate homozygous *Polg*$^{A449T/A449T}$ mice. For the same reason, this work restricted the analysis to *Polg*$^{A449T/A449T}$ mice.

During the term of this work, breeding of heterozygous *Polg*$^{WT/A449T}$ mice resulted in all expected genotypes (WT/WT; WT/A449T; A449T/A449T) in the predicted Mendelian ratios (1:2:1, respectively). In addition, breeding between homozygous *Polg*$^{A449T/A449T}$ mice (*Polg*$^{A449T/A449T}$ male with *Polg*$^{A449T/A449T}$ female) resulted in normal sized litters (9.6 pups on average compared to 9.2 pups from WT pairs, n = 10 breeding pairs of each genotype). Thus, suggesting that the A449T mutation does not affect fertility.

3.4. Generation of the *Polg*^{Y933C} mouse model

3.4.1. Attempted generation of *Polg*^{Y933C} mice by the double-nickase CRISPR/Cas9 D10A approach

The generation of *Polg*^{Y933C} mice was attempted using the double nickase CRISPR/Cas9 D10A approach, with all the components of the system (Cas9-D10A, gRNAs and HDR template) injected directly in fertilised one-celled oocytes. As previously mentioned, this strategy reduces CRISPR/Cas9 off-targets and offers a rapid generation of full-body mutants in the first generation of pups (Figure 3.3). In addition, our lab had positive experience upon generation of the *Polg*^{A449T} mouse using this approach.

Pairs of gRNAs were designed *in silico* using the web tool benchling (https://www.benchling.com/) to target the region to be edited (c.2798A) on exon 18 of mouse *Polg*. Two pairs (gRNA-F1 + gRNA-Rv1 and gRNA-F2 + gRNA-Rv2) were selected based on their score which takes in account the prediction of on-target efficiency and number of possible off-target (Figure 3.5).

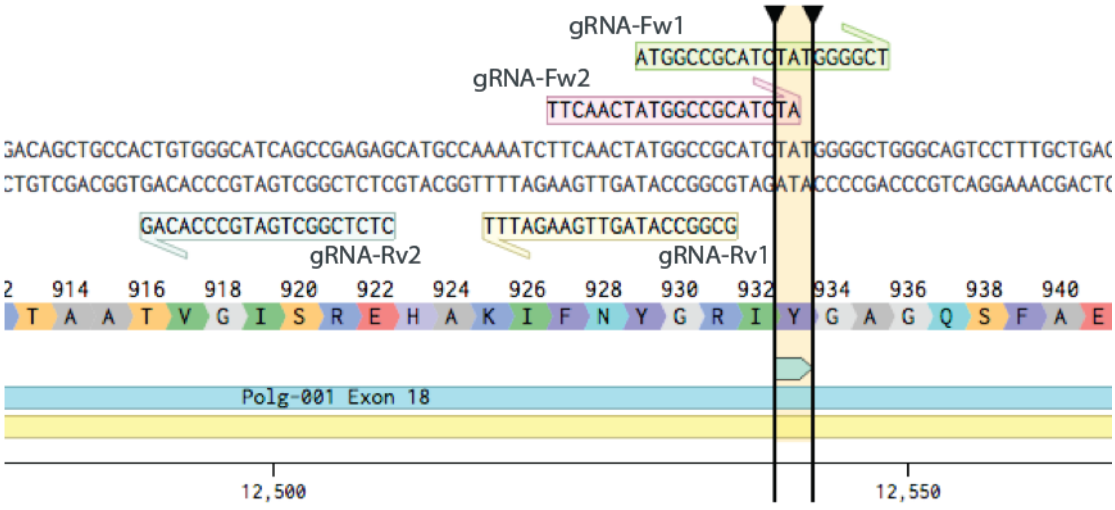

Figure 3.5. In silico design of selected gRNAs targeting the Y933C locus of *Polg*.
Schematic representation of the gRNAs targeting the Y933C locus (c.2798A) on exon 18 of mouse *Polg*. The two pairs of gRNAs were designed *in silico* using the web tool benchling (https://www.benchling.com/)

These pairs were further assessed for their efficiency in cultured C2C12 mouse cells using a T7 endonuclease assay, which reflects the capability of individual gRNAs to create indels (Figure 3.6 - A). The gRNA-F1 showed the highest efficiency of genome targeting of 28%, while gRNA-F2 presented an efficiency of 14%. In turn, gRNA-Rv1 and gRNA-Rv2 revealed efficiencies of 8% and 4%, respectively (Figure 3.6 - B). Since the pair gRNA-F1 + gRNA-Rv1 presented higher individual targeting efficiency, these were selected to proceed for microinjection of mouse embryos.

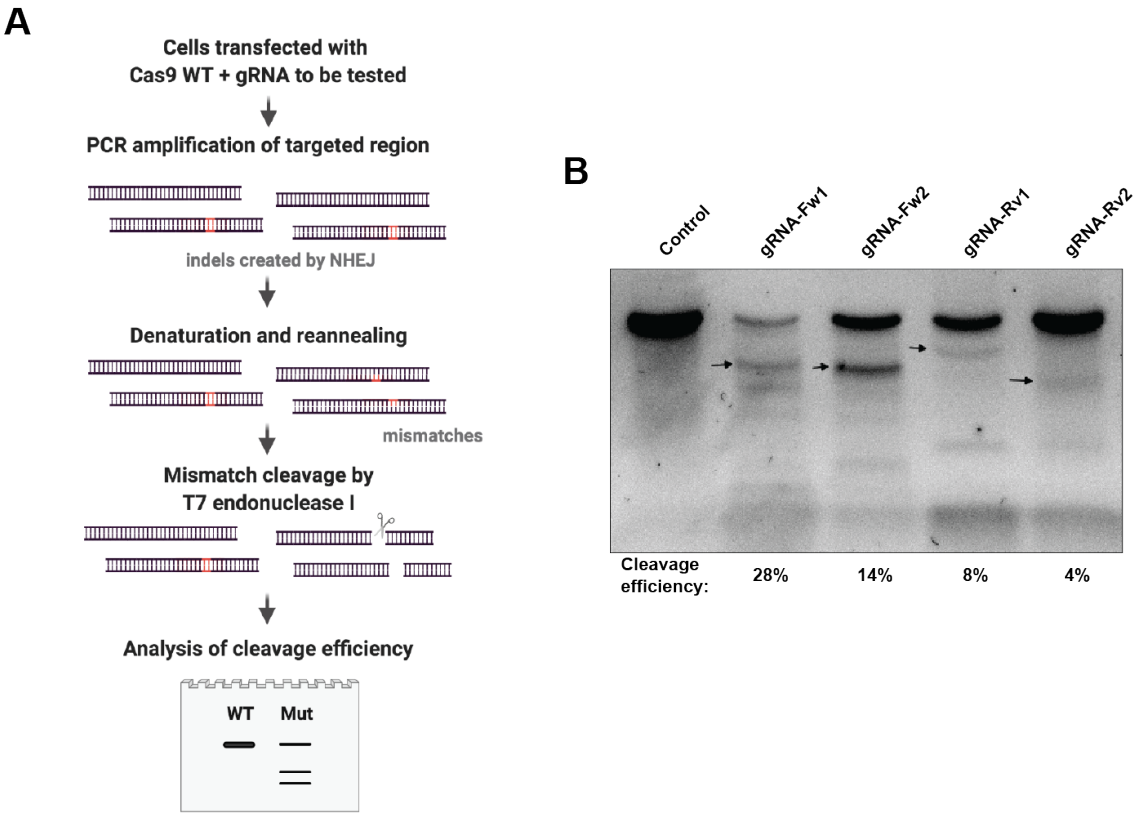

Figure 3.6. Genome targeting efficiency of in silico selected gRNAs in cells accessed by T7 endonuclease assay. (A) Schematic representation of the T7 endonuclease assay. In this assay, cells are transfected with a plasmid encoding the Cas9 WT and the gRNA to be accessed. Upon transfection, the Cas9+gRNA (without any donor template) will produce DSBs in the targeted region, which will result in indels after NHEJ-mediated repair. Genomic DNA is then extracted and the region of interest is amplified by PCR. The PCR products are subsequently denatured and reannealed creating hybrid duplex DNA with mismatches between WT and mutated sequences. Such mismatches are cleaved by the T7 endonuclease I, creating smaller DNA fragments which can be resolved by electrophoresis in agarose gels. **(B)** T7 endonuclease assay of the selected gRNAs to target the *Polg* Y933C site upon transfection of mouse C2C12 cells. Below the gel, the gRNA cleavage efficiency was calculated based on the percentage between the cleaved fragments and non-cleaved fragments, which is reflected by the number of indels created by individual gRNAs.

After gRNAs selection, a 146 bp synthetic ssDNA was designed to serve as HDR template and to accommodate modifications compatible with the gRNAs. The HDR template contained a A>G modification, changing the amino acid from Tyrosine to Cysteine generating the desired knockin mutation (c.2798A>G / p.Y933C). To guarantee that CRISPR/Cas9 does not cut the DNA repetitively once the knockin was created, the HDR also contained a silent G>C mutation to disrupt the PAM site of gRNA-Rv1 and created a XmnI restriction site useful for screening and genotyping of the Y933C allele (Figure 3.7).

Figure 3.7. Strategy for double-nickase CRISPR/Cas9 D10A mediated gene editing of mouse *Polg* gene in exon 18. Modified nucleotides are presented in red letters. On the left side a silent C>G modification was inserted to abolish the PAM site of the sgRNA-Rv1 and to create a XmnI restriction site for genotyping purposes. On the right side, a A>G modification was inserted changing the amino acid from Tyrosine to Cysteine generating the desired knockin mutation (c.2798A>G / p.Y933C).

The Cas9 D10A mRNA, gRNAs and ssDNA HDR donor were all outsourced and mixed in the requested concentrations (see Chapter 2- Methods) before sending to the "Transgenic Services" of the Central Biomedical Services at the University of Cambridge, (Cambridge, UK) for microinjection into mouse FVB/NJ zygotes. A total of 47 embryos were transferred into two pseudo-pregnant females which together gave birth to only 3 pups. Genotyping of the pups by RFLP using the XmnI restriction site failed to reveal the presence of the Y933C allele (data not shown).

To further confirm that the Y933C allele was not present, the region harbouring the Y933C site was sequenced, but the results confirmed a WT sequence in all 3 pups (data not shown). The low number of pups from the initial microinjections prompted us to repeat the procedure, resulting in an additional 8 pups. However, all 8 pups had a WT genotype, which was confirmed by XmnI restriction digest and Sanger sequencing (data not shown). Furthermore, there was no evidence of indels being formed in the targeted region. Despite the number of obtained pups remained low for this kind of procedure, the absence of indels suggested a low targeting efficiency using this strategy in the *Polg* Y933 locus. As mentioned, the use of a double-nickase CRISPR/Cas9 strategy reduces the number of off-targets, but it also reduces the on-target efficiency. Therefore, another approach using the Cas9 WT together with only one gRNA was attempted.

3.4.2. Generation of *Polg*^{Y933C} mice by the single nuclease CRISPR/Cas9 WT approach

The generation of a *Polg*^{Y933C} mouse using a double-nickase strategy was unsuccessful, possibly due to a lower genome targeting efficiency of this approach. Therefore, a different strategy was designed by using the original CRISPR/Cas9 technology, that uses only one gRNA. The downside of such strategy is the increased number of genome-wide off-targets. However, a suitable breeding program can eliminate any potential off-targets arisen from the DNA editing intervention.

The single nuclease CRISPR/Cas9 WT strategy uses only one gRNA, therefore we selected the gRNA-Fw1, since it showed the highest genome targeting efficiency in the T7 endonuclease assay (Figure 3.6). A new 169 bp synthetic ssDNA was designed to serve as HDR template and to suit the modifications compatible with gRNA-Fw1. The HDR template retained the A>G modification, changing the amino acid from Tyrosine to Cysteine generating the desired knockin mutation (c.2798A>G / p.Y933C). However, a different silent G>C mutation was introduced to disrupt the PAM site of gRNA-Fw1 and to create a MscI restriction site for genotyping of the Y933C allele (Figure 3.8).

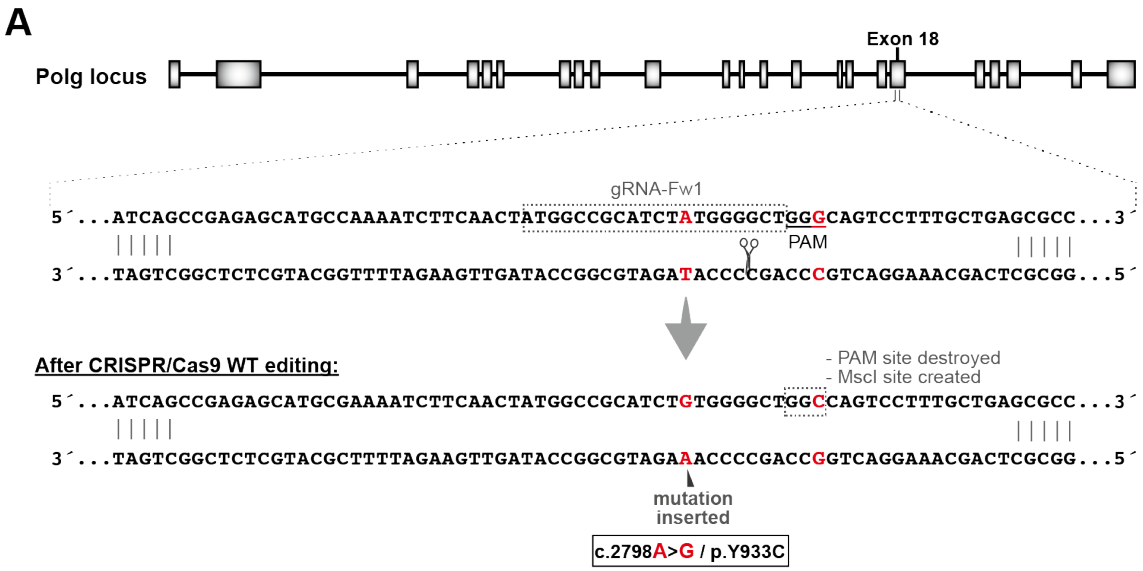

Figure 3.8. Strategy for single nuclease CRISPR/Cas9 D10A mediated gene editing of mouse *Polg* gene in exon 18. Modified nucleotides are presented in red letters. On the right side a silent G>C modification was inserted to abolish the PAM site of the sgRNA-Fw1 and to create a MscI restriction site for genotyping purposes. On the right side, a A>G modification was inserted changing the amino acid from Tyrosine to Cysteine generating the desired knockin mutation (c.2798A>G / p.Y933C).

A third round of microinjections was carried injecting the Cas9 WT mRNA, the gRNA-Fw1 and the new HDR template. This time, from a total of 5 pseudo-pregnant females, 20 pups were born. Genotyping was performed using the MscI restriction site and subsequently by Sanger sequencing, but all mice presented WT sequences with no evidence of indels (data not shown). Unfortunately, no recombinant *Polg* Y933C were detected, despite the fact that gRNA-Fw1 was clearly active in cultured cells.

Therefore, we decided to attempt a different approach by creating a *Polg*^{Y933C} knockin in mouse embryonic stem (ES) cells first. Positively edited ES cells are then microinjected in mouse blastocysts to create chimeric mice with both WT and edited cells. Such approach is more time consuming than zygote microinjections, as first chimeras need to be generated and later germ line transmission needs to be assessed by crossing with a WT mouse to generate founder mice (Fo) (Figure 3.9). However, the high recombinogenic properties of ES cells boosted by CRISPR/Cas9 technology ensures that a high number of edited ES clones are generated and screened, and only the validated cells are finally injected in the blastocysts.

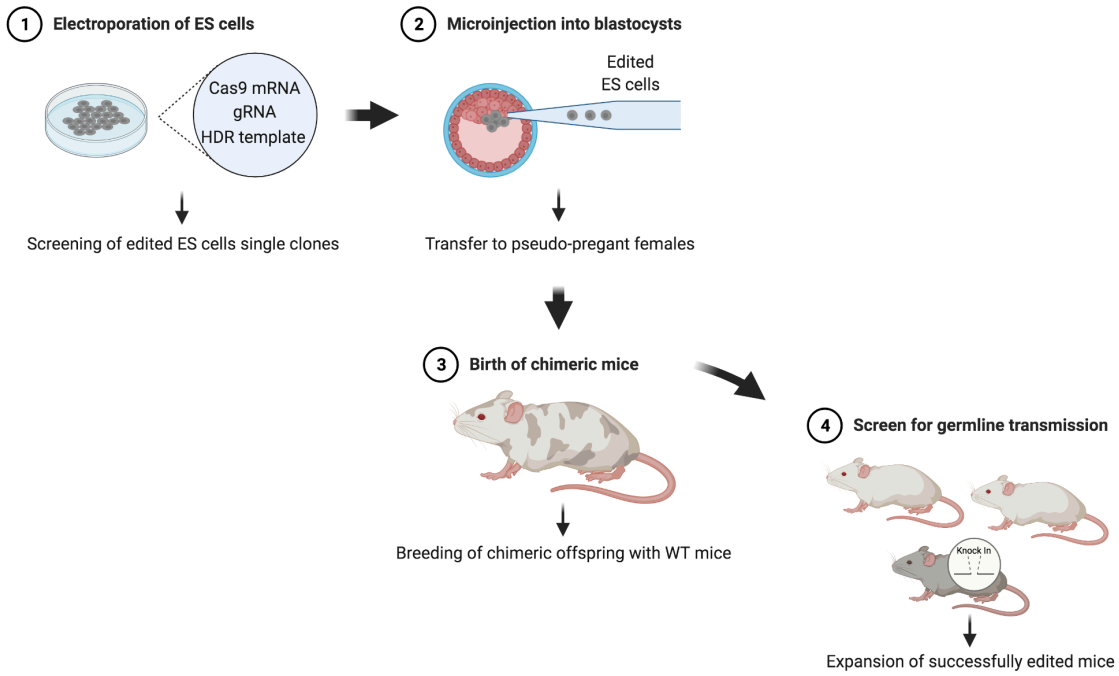

Figure 3.9. CRISPR/Cas9 editing of ES cells. **(1)** In this strategy, the CRISPR/Cas9 components are delivered to mouse ES cells by electroporation. The ES cells are screened for successfully edited clones. Notably, the high rate success of HDR due to CRISPR/Cas9 dsDNA cuts allow to skip a selection step with neomycin (or other antibiotics) **(2)** Selected ES clones are microinjected into blastocyst which are then transferred to pseudo-pregnant females. **(3)** The success of ES cells delivery into blastocyst is indicated by the presence of chimeric mice in the litters, since the ES cells are originated from a mouse strain with different fur colour from the blastocyst donors. Chimeras are mated with WT to evaluate germline transmission of the knockin. **(4)** The originated pups are screening for a full-body knockin. The positive mice constitute founder mice (Fo) and are then used to expand a colony for characterization. Founder mice are generated in a mixed strain background, between the donors of the ES cells and blastocysts.

The Cas9 WT mRNA, the gRNA-Fw1 and the HDR template were sent to the "Core Facility for Conditional Mutagenesis" at the IRCCS Ospedale San Raffaele, (Milan, Italy), where they were delivered to mouse ES cells by electroporation. The cells were then seeded as single clones in 96-well plates and allowed to grow to have enough material to send us for genotyping.

We screened a total of 384 ES clones (four 96-well plates) by RFLP using the MscI restriction site. Remarkably, a high number of clones were positive for the presence of the MscI site (96 out of 384), demonstrated by a smaller DNA fragment in the agarose gel (Figure 3.10 - A). Of these, 90 seemed to be heterozygous (e.g. clone A5), as the band corresponding to a WT allele coexisted with the smaller DNA fragment. In addition, 6 of these clones seemed to be homozygous (e.g. clone B3), as the band corresponding to a WT allele was completely digested (Figure 3.10 - A).

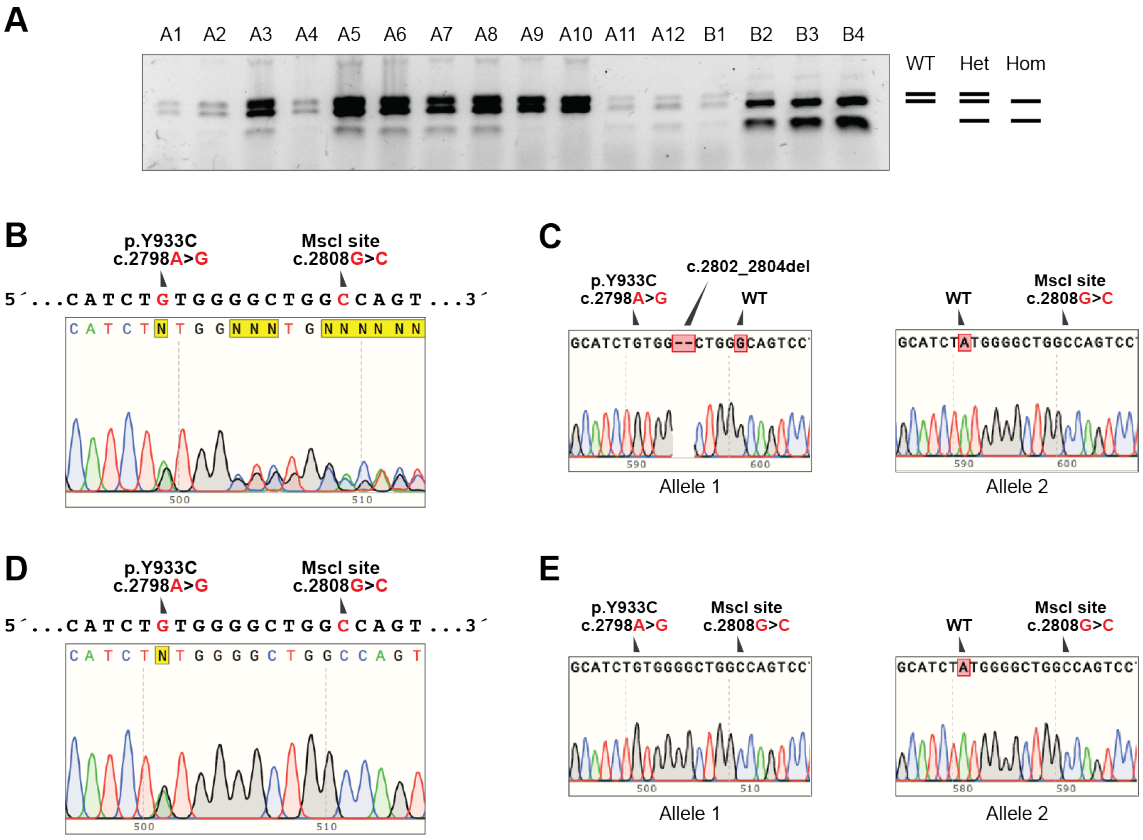

Figure 3.10. Screening of ES cells for CRISPR/Cas9-mediated knockin of *Polg* Y933C. (A) Representative image of the RFLP screening using the MscI site to identify positive ES clones, prior microinjection into blastocysts (plate 3 – clones A1 to B4). On the right, scheme of the expected DNA fragments in WT, heterozygous and homozygous clones. **(B)** Sanger sequencing of the heterozygous ES clones. Note the presence of the expected modification c.2798A>G together with a pattern characteristic of indels. **(C)** Sanger sequencing of the individual alleles of heterozygous ES clones. Note the segregation of c.2798A>G with a deletion of two Guanines. **(D)** Sanger sequencing of the homozygous ES clones. Note the presence of the expected modification c.2798A>G just in one allele, while the MscI site is present in both. **(E)** Sanger sequencing of the individual alleles of homozygous ES clones. Note in allele 1 the co-segregation of both c.2798A>G and the MscI site, validating these ES clones for transfer into blastocysts.

All clones positive for the existence of a MscI site were then sequenced to access the correct knockin of Y933C. Analyses of the sequences of the "heterozygous" clones revealed the presence of the c.2798A>G, corresponding to the p.Y933C modification, however it was also present a sequencing pattern indicative of a frameshift mutation (Figure 3.10 - B). To analyse in detail each allele, the PCR fragments were cloned in a TOPO vector and transformed in bacteria. Each bacterium only uptakes one vector containing one single PCR fragment, and therefore sequencing of single bacterial clones represents an individual allele. Alignment of the individual alleles of the heterozygous clones confirmed the presence of the p.Y933C modification in allele 1, however the required modification was always co-segregated with a deletion of two Gs (c.2802_2804del) while the

MscI site was absent. In turn, allele 2 lacked the p.Y933C modification but had the MscI site (Figure 3.10 - C). Thus, even if the heterozygous clones were positive by RFLP, the sequencing data showed that the p.Y933C mutation was in cis with a frameshift mutation, invalidating these ES clones.

Analysis of the sequences of the "homozygous" clones revealed the presence of the p.Y933C modification and the MscI site. However, the presence of two peaks at position c.2798, suggested that the p.Y933C mutation was actually in heterozygosity, while the MscI site was clearly homozygous (Figure 3.10 - D). These findings suggest that at least one of the alleles had the p.Y933C mutation co-segregating with the MscI site. Indeed, analysis of the individual alleles of the homozygous clones confirmed the presence of the p.Y933C modification together with the MscI site in allele 1, while allele 2 had the MscI site but lacked the p.Y933C modification (Figure 3.10 - E). Importantly, no frameshift mutations were detected in these clones. The homozygous clones were then good candidates to be injected in blastocysts, as the allele 2 could be later removed through breeding while retaining allele 1 which has the desired combination of modifications (p.Y933C + MscI site).

The ES clone B2 from plate #3 (3B2p20L2) was selected to proceed to microinjection into blastocyst, which were then transferred to pseudo-pregnant females. In one of the originated litters, one male mouse presented a chimerism of ~40%, indicative of successful transfer of mutant ES cells. This chimera was then bred with a WT female to verify germline transmission and allow segregation of alleles 1 and 2. Genotyping of the seven pups (F0) by sequencing showed the presence of the MscI site in all of them, as expected given the homozygous state of such site in the ES clone (Figure 3.11). Nevertheless, three of the F0 pups presented the Y933C site in heterozygosity, together with the MscI site (Figure 3.11 - middle). The remaining four were WT for the Y933C site and thus only presented the MscI site (Figure 3.11 - left). We further analysed individually the alleles of putative heteroplasmic F0 pups (#2, 4 and 6), and confirmed that the Y933C and MscI modifications were present in the same allele, while the other allele was WT (Figure 3.11 - right). Thus, these results confirmed successful germline of the Y933C allele and the F0 pup #4 was used to expand a colony *Polg*^{Y933C} mice.

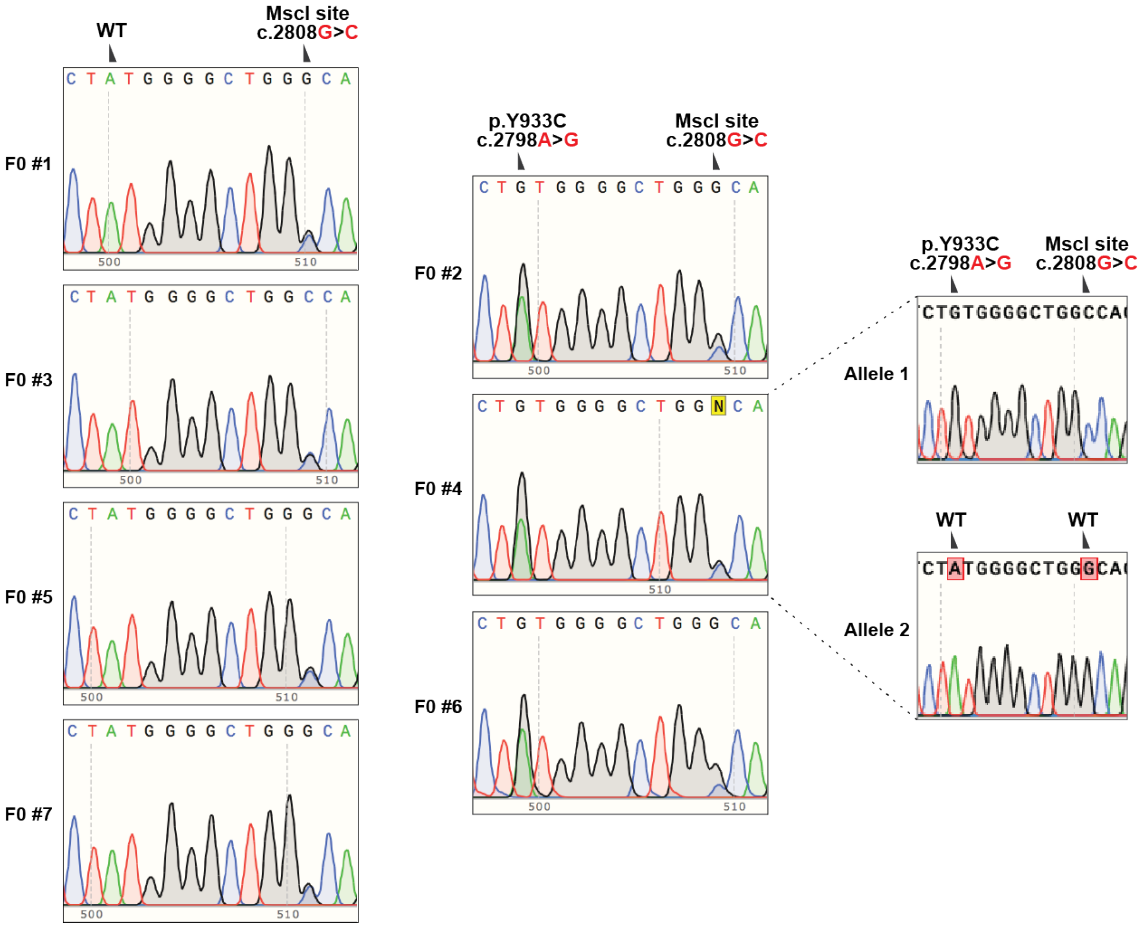

Figure 3.11. Screening of Fo pups for germline transmission of the *Polg* Y933C knockin. (A) On the left, Sanger sequencing of pups #1 ,3, 5 and 7, which were negative for the Y933C modification, but heterozygous for MscI site. In the middle, Sanger sequencing of positive pups (#2, 4 and 6), presenting with heterozygous Y933C and MscI modifications. On the left, Sanger sequencing of the individual alleles of pup #4, confirming the presence of the Y933C modification and the MscI site in the same allele.

Preliminary evidence by interbreeding heterozygous *Polg*$^{WT/Y933C}$ mice failed to produce homozygous *Polg*$^{Y933C/Y933C}$. From a total 63 mice, we obtained 25 WT/WT and 38 *Polg*$^{WT/Y933C}$, thus suggesting that Y933C is lethal in homozygosity. Such observation comes in line with the dominant behaviour of *POLG* Y955C in human disease, and that only heterozygous patients have been reported so far.

Given the challenges encountered and the need of several editing approaches to generate the *Polg*^{Y933C} mouse, the procedure took considerably more time than expected. Therefore, detailed characterization of this *Polg* mouse model became unattainable during the term of this work and thus, the following chapters will be mainly focused on the study of the *Polg*^{A449T} model.

Chapter 4 Results

In vivo and *in vitro* mechanistic characterization of the POLγA A449T mutation

4. *In vivo* and *in vitro* mechanistic characterization of the POLγA A449T mutation

4.1. Introduction

The *POLG* A467T mutation is by far the most frequent allele found in *POLG*-affected patients. Patients homozygous for *POLG* A467T are often presented with more severe early-onset mtDNA depletion syndromes. However, the A467T mutation, has been associated with a range of phenotypes, from childhood-onset fatal AHS to MEMSA, ANS, SANDO and arPEO (Rahman and Copeland, 2019, Tzoulis et al., 2006), with a clinical onset that can span at least four decades of life (Tzoulis et al., 2006, Rajakulendran et al., 2016). The reasons for such complexity and exact molecular pathogenesis mechanism of the A467T mutation is still poorly understood, which in turn delays the development of therapies for these patients.

In this chapter, I provide a systematic characterisation of the impact of the *Polg* A449T mutation (mouse homolog of A467T) in disease using a double approach: 1) *in vivo* characterisation of the homozygous *Polg*$^{A449T/A449T}$ and the double mutant *Polg*$^{A449T/KO}$ mouse models and 2) *in vitro* characterisation of the mouse A449T and human A467T mutations using purified recombinant protein versions of POLγA.

I describe the clinical phenotypes observed in *Polg*^{A449T} mouse mutants using a set of apparatuses including the CLAMS^{TM} system and an automated treadmill. I also describe molecular findings in mtDNA quantity and quality in the different tissues of mutant mice and effects of the A449T mutation in mtDNA replication. These findings are complemented with a set of *in vitro* assays characterising biochemical properties of the mutant POLγA^{A449T}, including DNA binding, exonuclease and polymerase activity and interaction with POLγB.

In the last part of this chapter, I describe the impact of the A449T mutation in POLγA stability and provide *in vivo* and *in vitro* mechanistic insights on how the mutant POLγA^{A449T} is susceptible for degradation by proteases present in the mitochondrial matrix, such as LONP1.

4.2. Phenotypic characterization of *Polg*$^{A449T/A449T}$ mice

4.2.1. *Polg*$^{A449T/A449T}$ mice did not show alterations on energy metabolism

To determine the impact of the A449T mutation on the energy metabolism of mice we used a CLAMS™ system. This system places individual mice in separate cages that measure metabolic parameters such as oxygen consumption (VO2) and carbon dioxide production (VO2). Three-month-old and 1-year-old *Polg*$^{A449T/A449T}$ homozygous animals did not show any differences of oxygen consumption and carbon dioxide production compared with their aged-matched WT littermates (Figure 4.1).

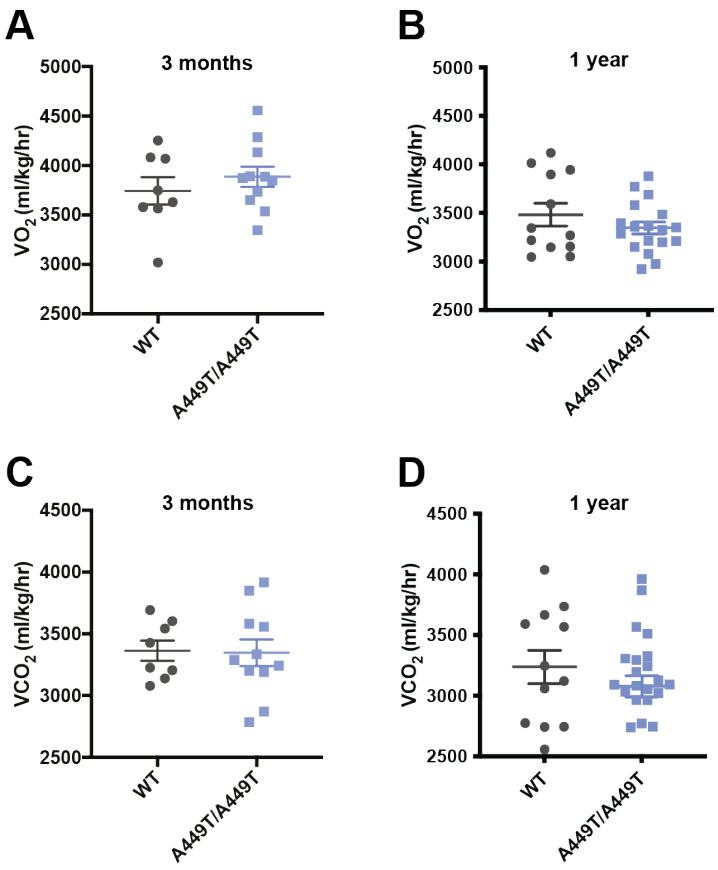

Figure 4.1. Energy metabolism parameters measured in the CLAMS™ system.
Volume of oxygen (ml/kg/hr) consumed by 3-month-old (**A**) and 1-year-old (**B**) WT and *Polg*$^{A449T/A449T}$ animals. Volume of carbon dioxide (ml/kg/hr) produced by 3-month-old (**C**) and 1-year-old (**D**) WT and *Polg*$^{A449T/A449T}$ animals. Data are presented as mean ± SEM. P value was calculated by two tailed unpaired Student's t-test. Each symbol represents a biological replicate.

In addition, the CLAMS™ software uses the oxygen consumption and carbon dioxide production variables to derive the respiratory exchange ratio (RER) and heat production, the latter being directly related to energy expenditure. RER is the ratio between the amount of carbon dioxide produced and oxygen consumed and is associated with the balance between glucose and fat as source of energy. Typically, a RER value of 0.7 indicates that the main fuel used is fat, a RER of 1.0 or above means that the source of energy is mainly carbohydrates and a RER of around 0.85 means that both fat and carbohydrates are being used.

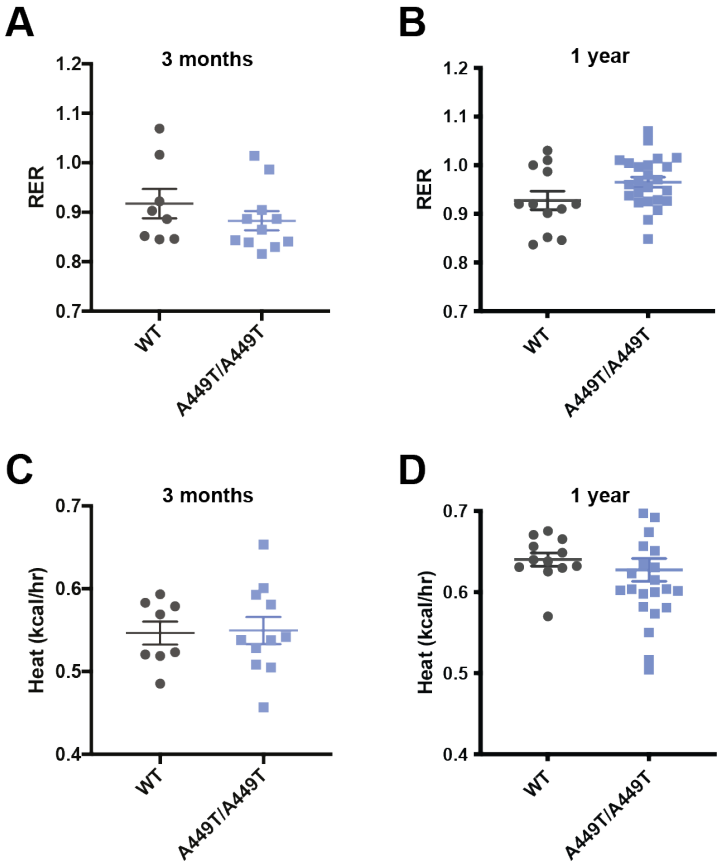

Figure 4.2. Energy metabolism parameters calculated in the CLAMS™ system.
Respiratory exchange ratio (RER) in 3-month-old (**A**) and 1-year-old (**B**) WT and *Polg*$^{A449T/A449T}$ animals. Heat (Kcal/hr) produced by 3-month-old (**C**) and 1-year-old (**D**) WT and *Polg*$^{A449T/A449T}$ animals. Data are presented as mean ± SEM. P value was calculated by two tailed unpaired Student's t-test. Each symbol represents a biological replicate.

Three-month-old and 1-year-old *Polg*$^{A449T/A449T}$ homozygous animals presented RER values similar to those obtained for age-matched control mice. Similarly, *Polg*$^{A449T/A449T}$ of both ages did not show significant differences of heat production (Figure 4.2). These results suggest that *Polg*$^{A449T/A449T}$ mice do not present

alterations of energy metabolism either in early adulthood nor in aged 1-year-old mice.

4.2.2. *Polg*$^{A449T/A449T}$ mice exhibit decreased spontaneous motility

The CLAMS™ system is also equipped with infrared beam sensors in each cage that allows the evaluation of spontaneous motility, including rear and ambulatory activities. Each time mice break the beams by standing on their hind-limbs to explore their environment, is registered as 1 count of rear activity. In turn, each time mice break the beams by moving horizontally in the cage, is registered as 1 count of ambulatory activity. In addition, night and day cycles are evaluated separately to account for the nocturnal behaviour of mice.

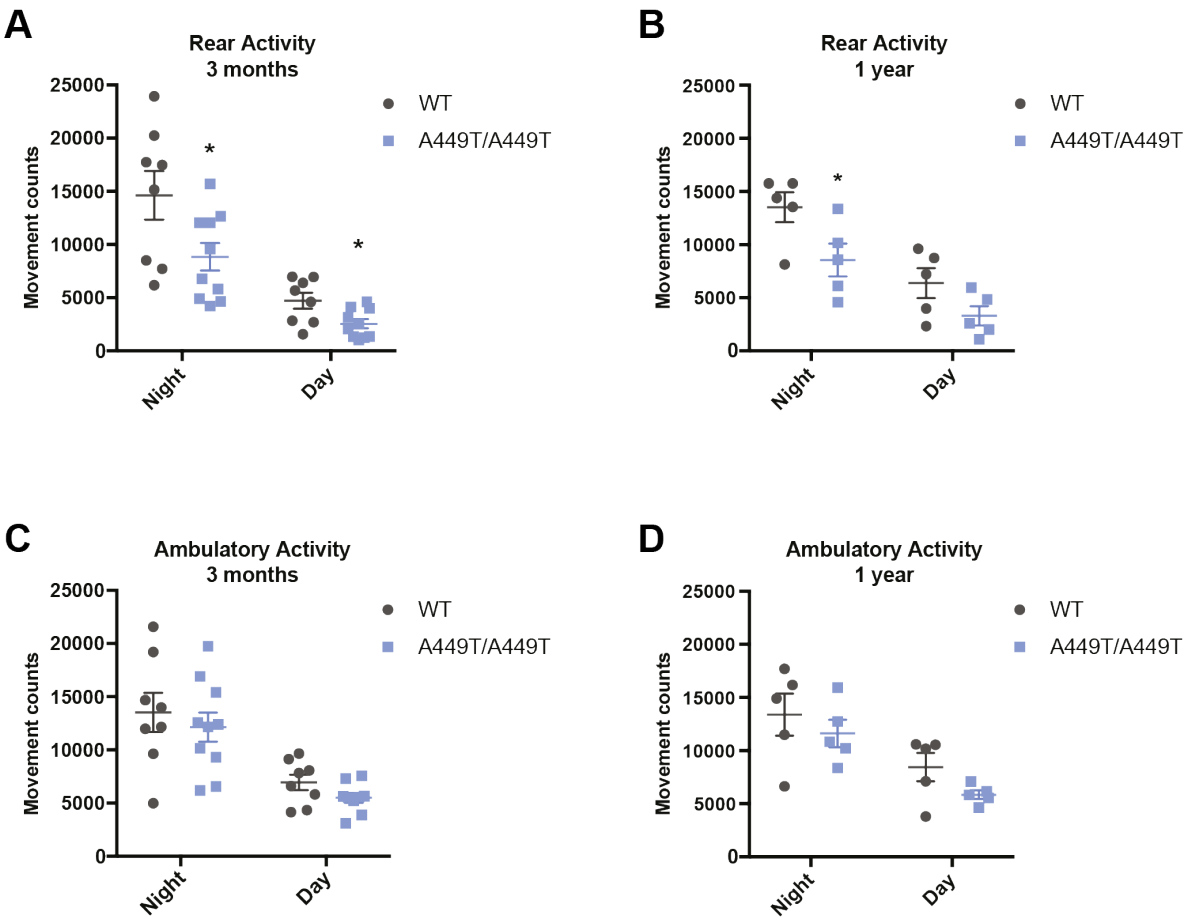

Figure 4.3. Spontaneous motor activity measured in the CLAMS™ system.
Spontaneous rear activity (vertical movement counts) of 3-month-old (**A**) and 1-year-old (**B**) WT and *Polg*$^{A449T/A449T}$ animals. Spontaneous ambulatory activity (horizontal movement counts) of 3-month-old (**C**) and 1-year-old (**D**) WT and *Polg*$^{A449T/A449T}$ animals. Data are presented as mean ± SEM. P value was calculated by two tailed unpaired Student's t-test: *P < 0.05. Each symbol represents a biological replicate.

Three-month-old *Polg*$^{A449T/A449T}$ homozygous mice displayed a 41% ($P < 0.05$) reduction in spontaneous rearing movements during the night and a 46% ($P < 0.05$) reduction during the day, compared with controls. One-year-old *Polg*$^{A449T/A449T}$ mutants showed a similar trend displaying a 37% ($P < 0.05$) reduction during the night and a 48% reduction during the day, however the later failed to reach statistical significance ($P = 0.1013$) (Figure 4.3 - A and B). In contrast, *Polg*$^{A449T/A449T}$ of both ages did not show significant differences of ambulatory activity compared with WT littermates (Figure 4.3 - C and D). These results support a predisposition of *Polg*$^{A449T/A449T}$ mutants to spontaneously move and explore less their environment, which is not aggravated by age.

4.2.3. *Polg*$^{A449T/A449T}$ mice display mild exercise intolerance

Mutations in the human *POLG* gene, including A467T, are associated with myopathy disorders, often characterised by fatigue and exercise intolerance (Rahman and Copeland, 2019) in addition to a number of other symptoms. Following the observation that *Polg*$^{A449T/A449T}$ have decreased spontaneous motility, we decided to evaluate whether the mutant mice presented compromised motor performance by running until exhaustion on a treadmill apparatus. The exhaustion trials consisted of an automated treadmill with standardised program to increase the belt speed by 0.3 m/min to a maximum speed of 75 m/min. The distance ran by each mouse until exhaustion was registered. Three-month-old *Polg*$^{A449T/A449T}$ mice displayed significant exercise intolerance compared with WT controls, with a 19.6% ($P < 0.05$) reduction in treadmill motor endurance (Figure 4.4). These results suggest that *Polg*$^{A449T/A449T}$ mice present mild exercise intolerance which is already present in early adulthood. We then thought to evaluate the exercise tolerance in older mice. However, one-year-old WT and *Polg*$^{A449T/A449T}$ resisted to run even at the beginning of the running program, and seemed to ignore the motivational air puff, and therefore, failed to produce functional data.

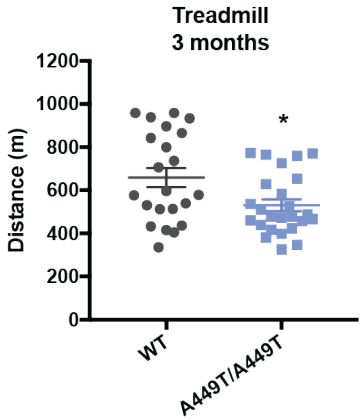

Figure 4.4. Evaluation of exercise endurance.
Distance run in metres by 3-month-old WT and *Polg*$^{A449T/A449T}$ animals on the treadmill. Data are presented as mean ± SEM. *$P < 0.05$; Student's *t*-test. Each symbol represents a biological replicate.

4.3. Histological Analyses of Tissues from *Polg*$^{A449T/A449T}$ mice

Post-mortem mouse tissues were subjected to histological examination to assess whether the *Polg* A449T mutation affected the normal architecture of various high-energy tissue types, and whether hallmarks of disease were visible.

Hematoxylin and eosin (H&E) staining was performed in skeletal muscle of 3-month-old and 1-year-old *Polg*$^{A449T/A449T}$ mice. H&E staining of gastrocnemius showed normal fibre morphology and size without present of centralised nuclei in *Polg*$^{A449T/A449T}$ of both ages (Figure 4.5). Centralised nuclei are a feature found in several myopathies, representing degenerative fibres (Folker and Baylies, 2013). In addition, muscle biopsies of *POLG* patients recurrently present cytochrome-c oxidase (COX) negative fibres. Three-month-old and 1-year-old *Polg*$^{A449T/A449T}$ muscle samples were submitted to COX and SDH staining, but COX negative fibres were not found in both ages (Figure 4.6).

Liver and kidney of 3-month-old and 1-year-old *Polg*$^{A449T/A449T}$ mice were also analysed by H&E staining, however no signs of morphological alterations were observed when compared with WT littermates (Figure 4.7). In addition, H&E staining was performed in brain sections of 1-year-old *Polg*$^{A449T/A449T}$. Evaluation of regions of the cerebral cortex and cerebellum showed absence of structural alterations, and no signs of neuronal loss (Figure 4.8). Together these results indicate that the *Polg* A449T mutation has little impact on histological morphology of mouse tissues and that these finding to not exacerbate with age.

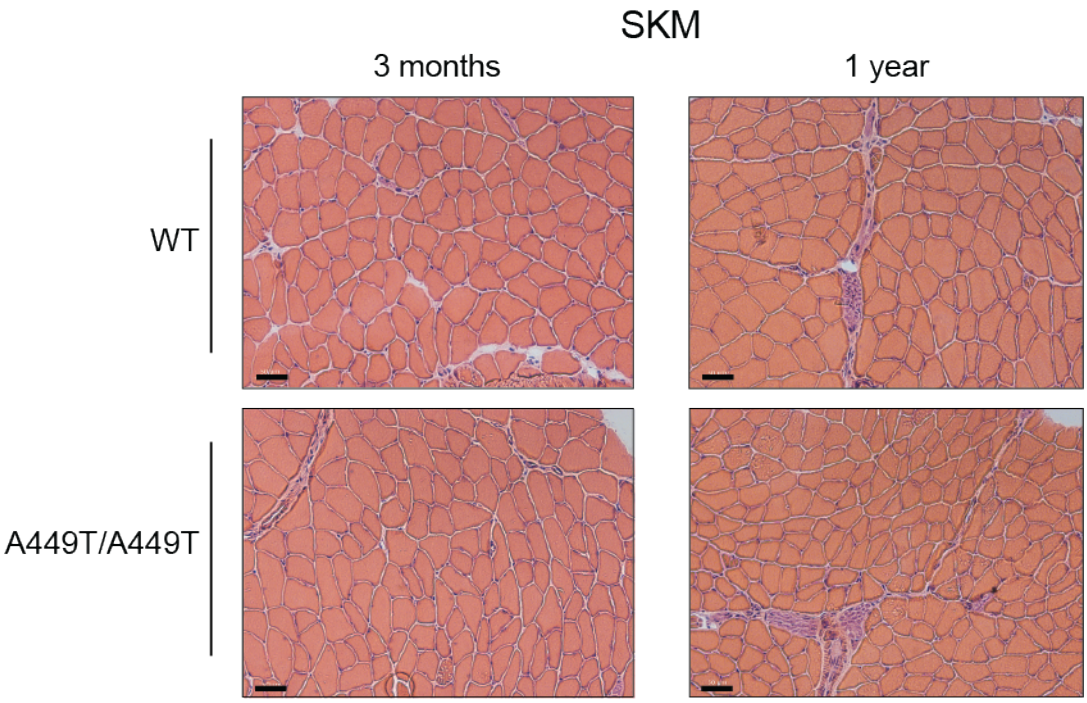

Figure 4.5. Histological analysis of skeletal muscle.
Representative H&E staining of liver and kidney sections of 3-month-old (**A**) and 1-year-old (**B**) WT and *Polg*$^{A449T/A449T}$ *animals*. Scale bars: 50 μm; SKM - skeletal muscle.

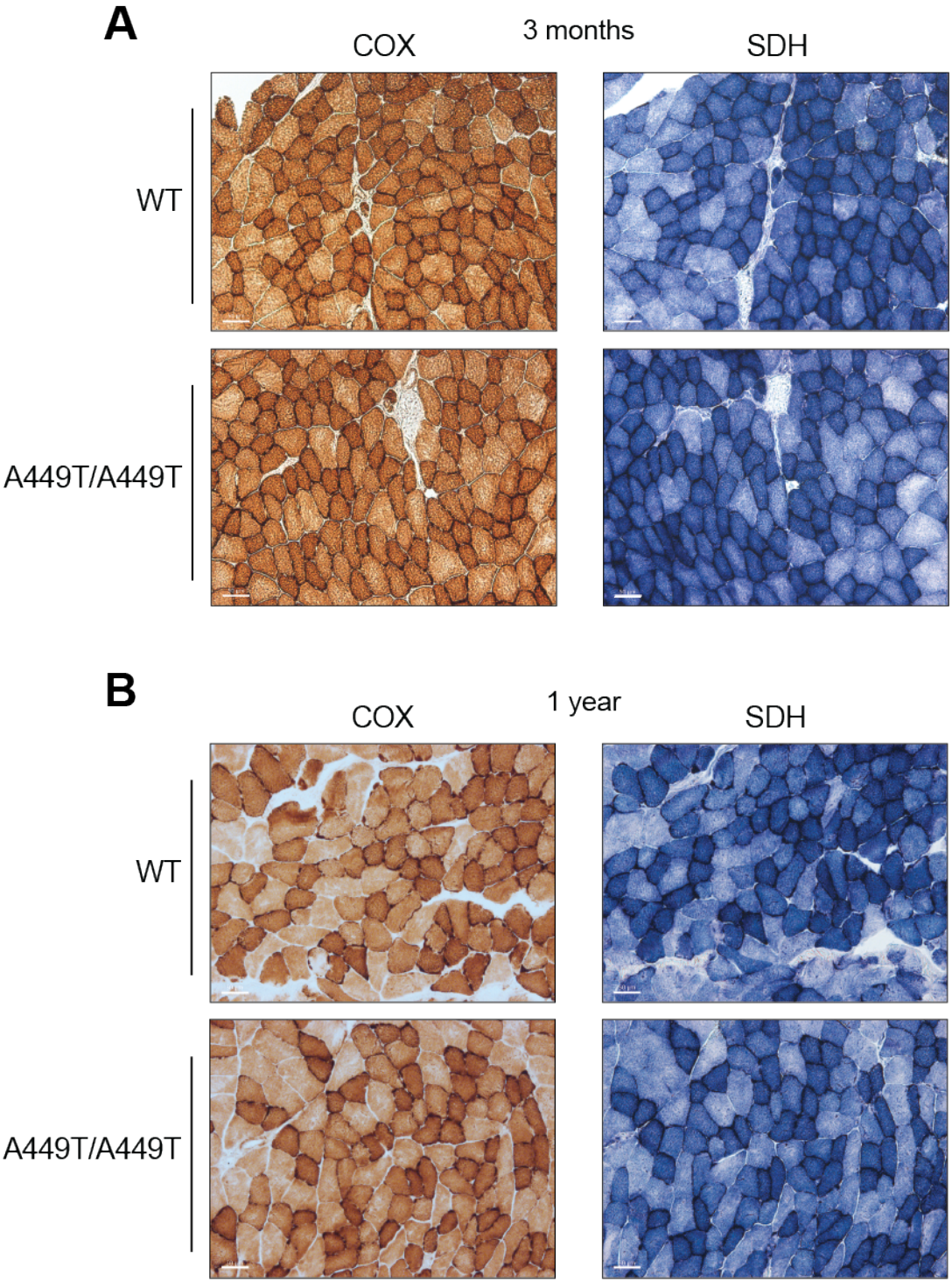

Figure 4.6. Histological analysis of skeletal muscle (2).
Representative staining for COX (left) and SDH (right) in skeletal muscle samples of 3-month-old (**A**) and 1-year-old (**B**) WT and *Polg*$^{A449T/A449T}$ animals. Scale bars: 50 µm.

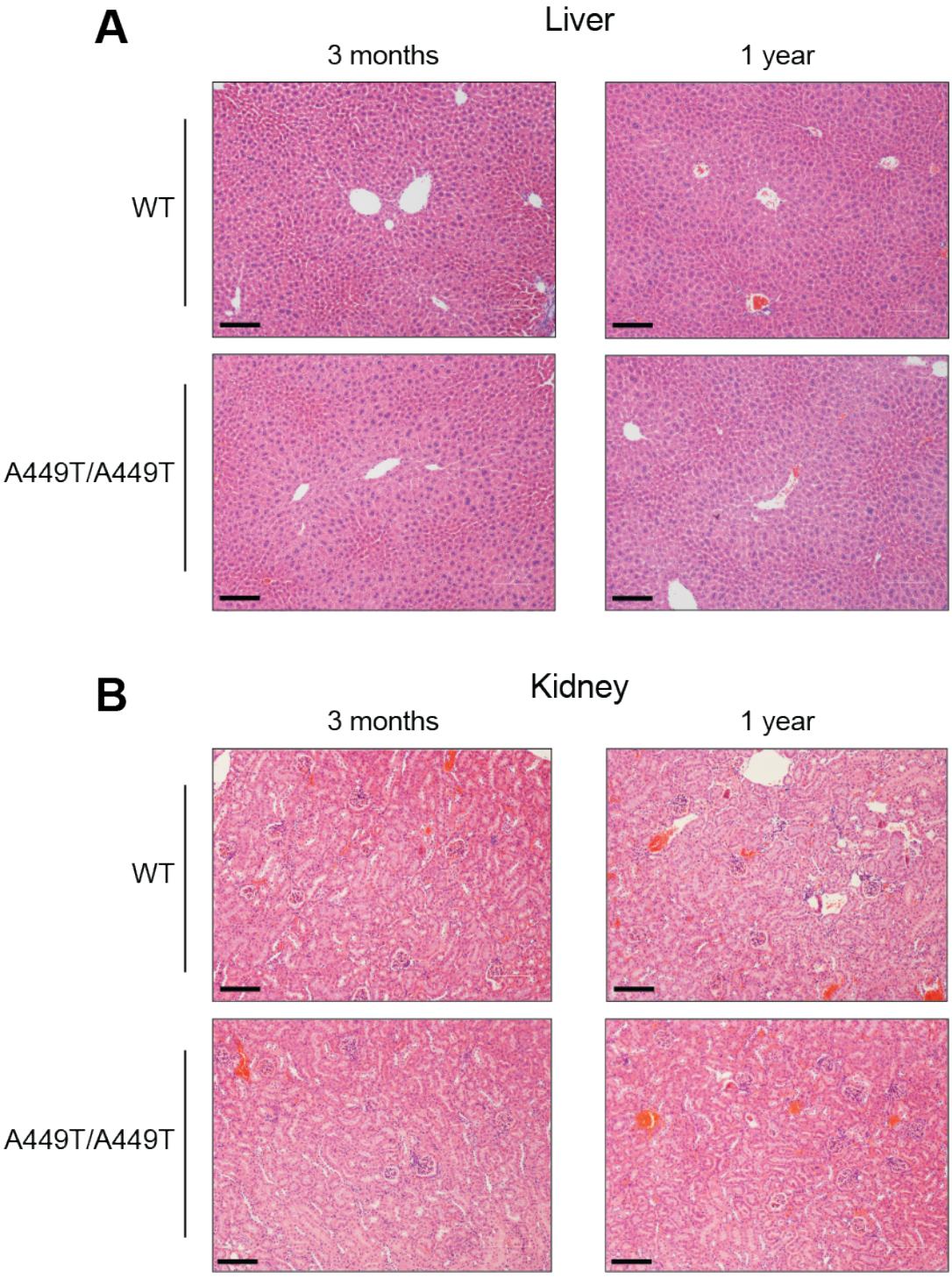

Figure 4.7. Histological analysis of liver and kidney.
Representative H&E staining of liver and kidney sections of 3-month-old (**A**) and 1-year-old (**B**) WT and *Polg*$^{A449T/A449T}$ animals. Scale bars: 100 µm.

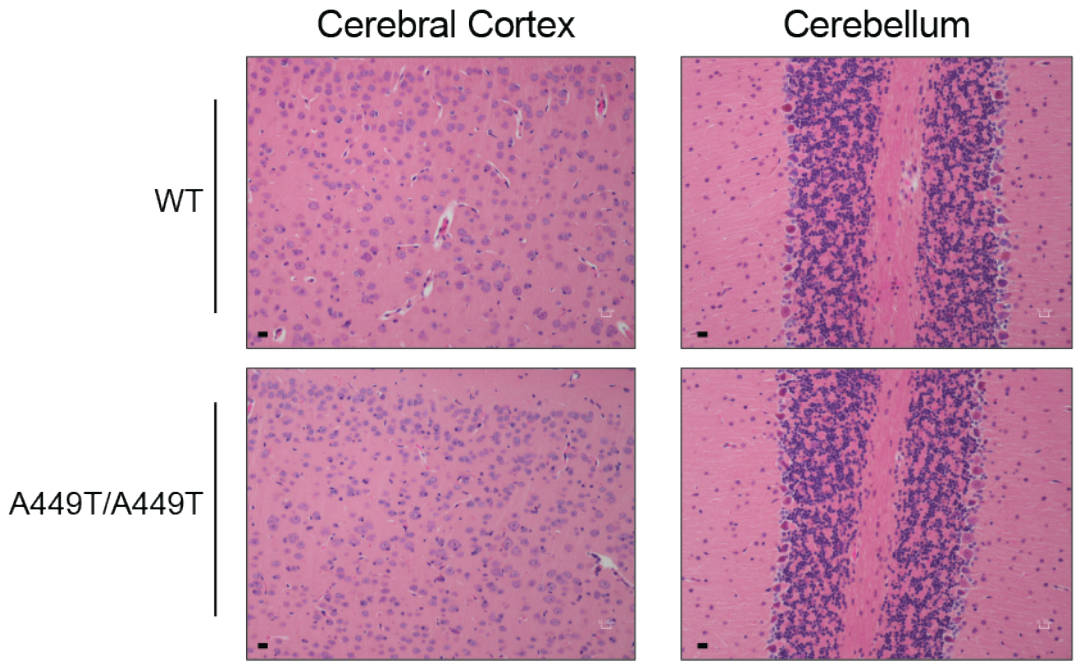

Figure 4.8. Histological analysis of brain.
Representative H&E staining of cerebral cortex and cerebellum sections of 1-year-old WT and *Polg*$^{A449T/A449T}$ animals. Scale bars: 10 μm.

4.4. Molecular and Biochemical Analyses of Tissues from *Polg*$^{A449T/A449T}$ mice

4.4.1. *Polg*$^{A449T/A449T}$ mice display mild mtDNA depletion

Since mutations in *POLG* are associated with reduction of mtDNA copy number in human patients, we next investigated the mtDNA content in several tissues, including liver, skeletal muscle, brain, kidney and heart from both *Polg*$^{A449T/A449T}$ versus WT littermates, at 3 months and 1 year of age. MtDNA copy number was significantly reduced in the skeletal muscle of 3-month-old (80 ± 4%, $P < 0.01$) *Polg*$^{A449T/A449T}$ mice, while the other tissues presented no significant differences (Figure 4.9 - A). Quantifications of mtDNA of aged 1-year-old were very similar to that of the 3-month-old mice, except that in addition to SKM (63 ± 7%, $P < 0.05$), a mild decrease in mtDNA copy number was also observed in kidney (79 ± 6%, $P < 0.01$) and heart (87 ± 3%, $P < 0.01$) (Figure 4.9 - B).

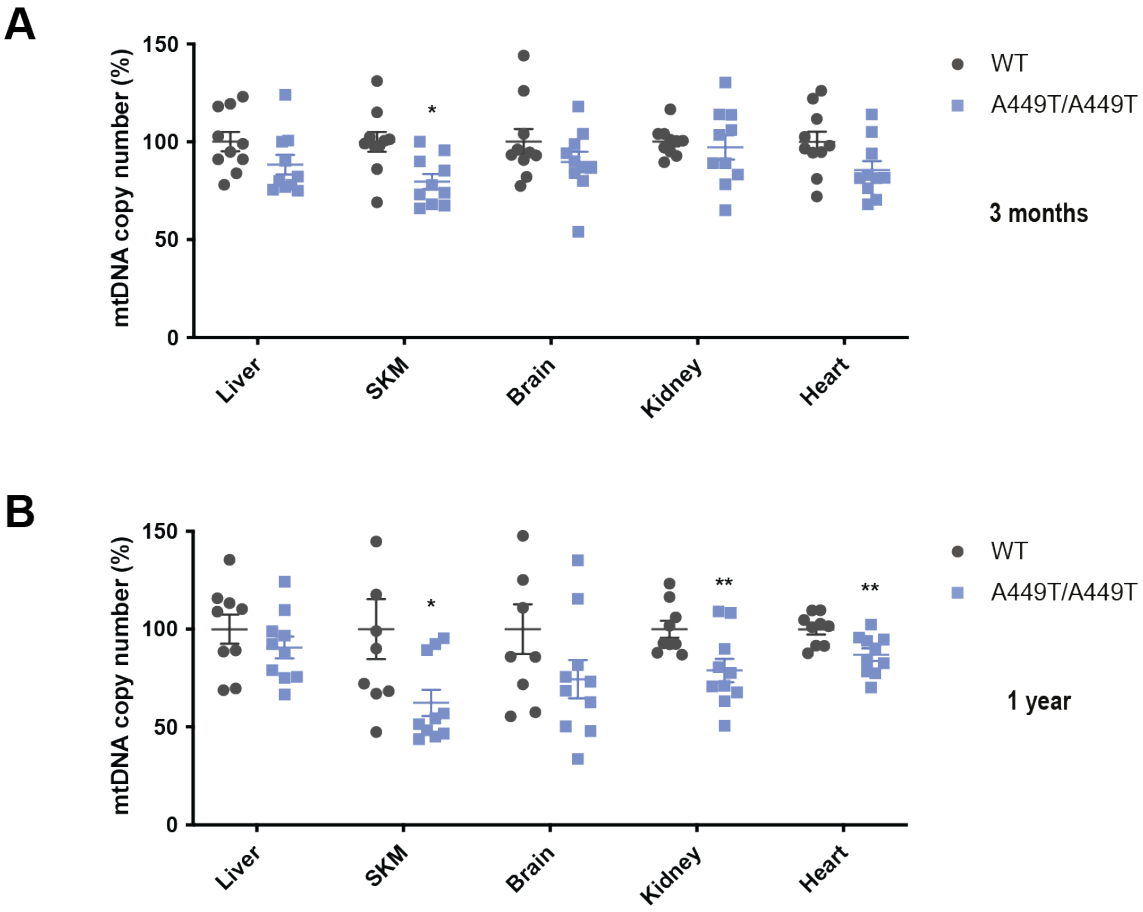

Figure 4.9. MtDNA levels in the different tissues of *Polg*$^{A449T/A449T}$ mice.
Real-Time qPCR quantification of mtDNA content in liver, skeletal muscle (SKM), kidney, brain and heart of 3-month-old (**A**) and 12-month-old (**B**) WT and *Polg*$^{A449T/A449T}$ animals. Data are presented as mean ± SEM. Unpaired two tailed Student's t-tests: *p<0.05; **p<0.01. Each symbol represents a biological replicate.

4.4.2. Multiple mtDNA deletions are not detected in *Polg*$^{A449T/A449T}$ mice

POLG mutations are also associated with multiple deletions of mtDNA copy number in human patients. We then examined by long range PCR the presence of such deletions in the several tissues of *Polg*$^{A449T/A449T}$ mice. Analysis of liver, skeletal muscle, brain, kidney and heart revealed absence of noticeable mtDNA deletion in samples from 3-month-old *Polg*$^{A449T/A449T}$ mice (Figure 4.10 – A to E). Deletions of mtDNA were also not detected in tissues of aged 1-year-old mice (Figure 4.10 – F to J), even if such deletions normally accumulate with age in human patients. These results imply that multiple mtDNA deletions do not accumulate in *Polg*$^{A449T/A449T}$ mice.

4.4.3. Mitochondrial transcripts and OXPHOS activities are not affected in *Polg*$^{A449T/A449T}$ mice

The phenotypes, histological analysis and molecular signatures present in 3-month-old *Polg*$^{A449T/A449T}$ mice, were similar in 3-months and 1-year-old mice. In addition, we monitored *Polg*$^{A449T/A449T}$ and WT littermates up to 2 years of age, but neither reduction of the lifespan nor the presence of obvious age-related phenotypes was observed. Thus, we decided to focus our analysis on 3-month-old animals.

Led by the observation of mtDNA depletion in skeletal muscle of *Polg*$^{A449T/A449T}$ mice, we evaluated the possible impact on the levels of mtDNA transcripts and OXPHOS activities in skeletal muscle and liver. Analysis of the transcript levels of *mt-Nd4* and *mt-CoI* revealed no differences between *Polg*$^{A449T/A449T}$ mice and WT controls (Figure 4.11). To quantify any alteration in the OXPHOS function of *Polg*$^{A449T/A449T}$ mice, kinetic measurements of CI, CII, CIII, and CIV specific enzymatic activities were performed spectrophotometrically with tissue homogenates. No alterations were observed in the activities of all complexes analysed between *Polg*$^{A449T/A449T}$ mice and WT littermates (Figure 4.12 – A and B). Variations were also not observed when analysing CI assembly and activity by Blue Native-PAGE (BNGE) followed by an in-gel reaction in the skeletal muscle and liver of mutant mice and controls (Figure 4.12 – C and D). Together these results suggest that the depletion of mtDNA observed in *Polg*$^{A449T/A449T}$ mice does not translate into effects on mtDNA transcripts levels and OXPHOS activities.

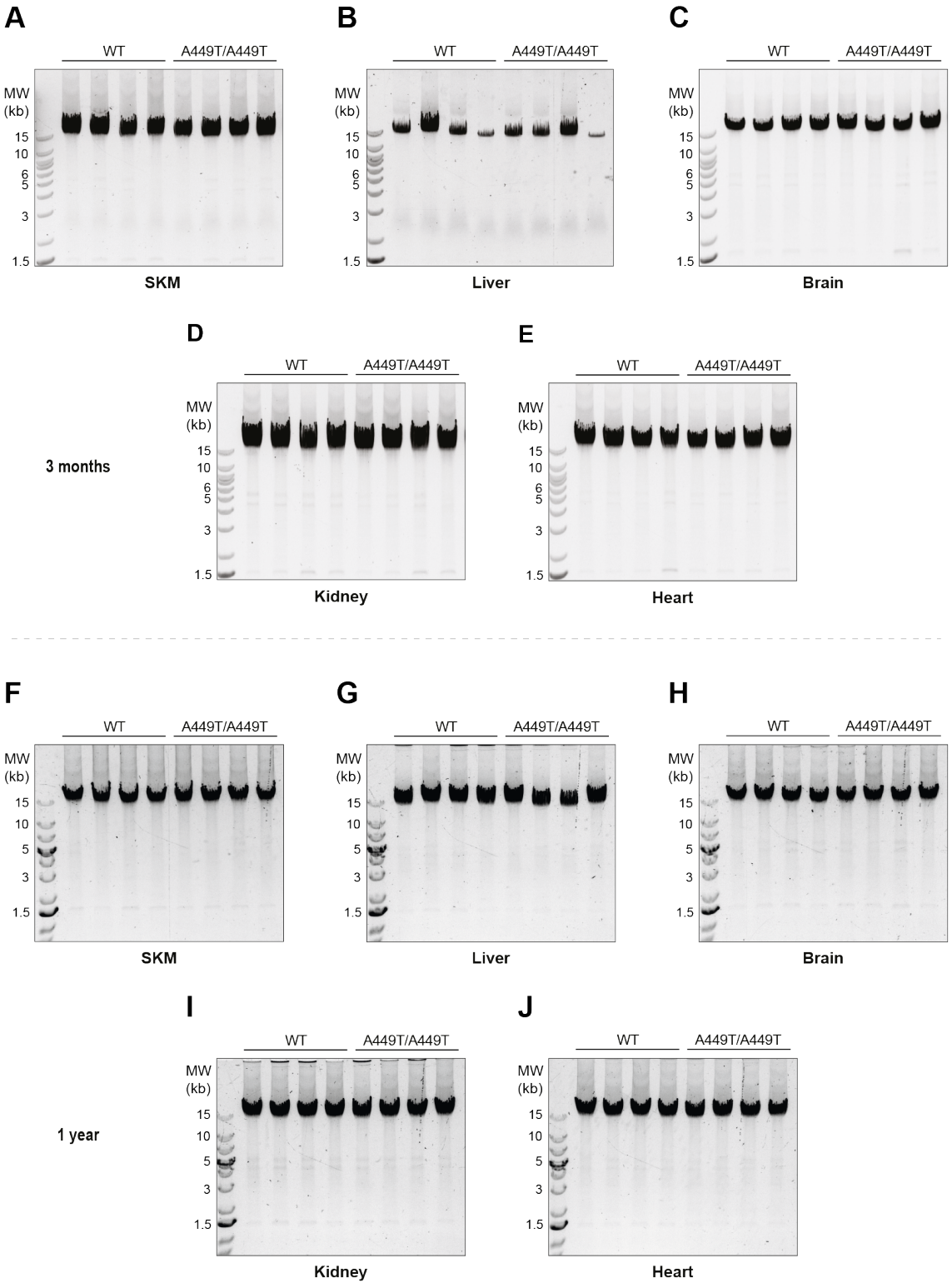

Figure 4.10. Investigation of mtDNA deletions in the different tissues of *Polg*$^{A449T/A449T}$ mice. Long-range PCR performed in DNA isolated from: Liver; SKM; brain; kidney and heart of 3-month-old (**A-E**) and 1-year-old (**F-J**) WT and *Polg*$^{A449T/A449T}$ animals. Primers amplifying a fragment of 15,781bp of the mtDNA. The bands were visualized by SYBR™ safe staining. SKM - skeletal muscle. Each lane represents a sample from an individual mouse.

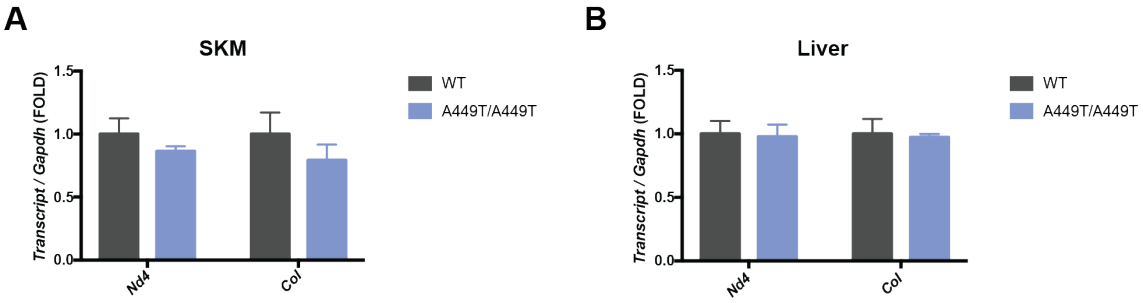

Figure 4.11. Mitochondrial transcripts levels in SKM and liver of *Polg*$^{A449T/A449T}$ mice.
Real-Time qRT-PCR quantification of mitochondrial transcripts *mt-Nd4* and *mt-CoI*, normalized to *Gapdh*, in (**A**) SKM and (**B**) Liver of WT and 3-months-old *Polg*$^{A449T/A449T}$ animals. Data are presented as mean ± SEM. P value were calculated by two tailed unpaired Student's t-test. (n = 5). SKM- Skeletal Muscle.

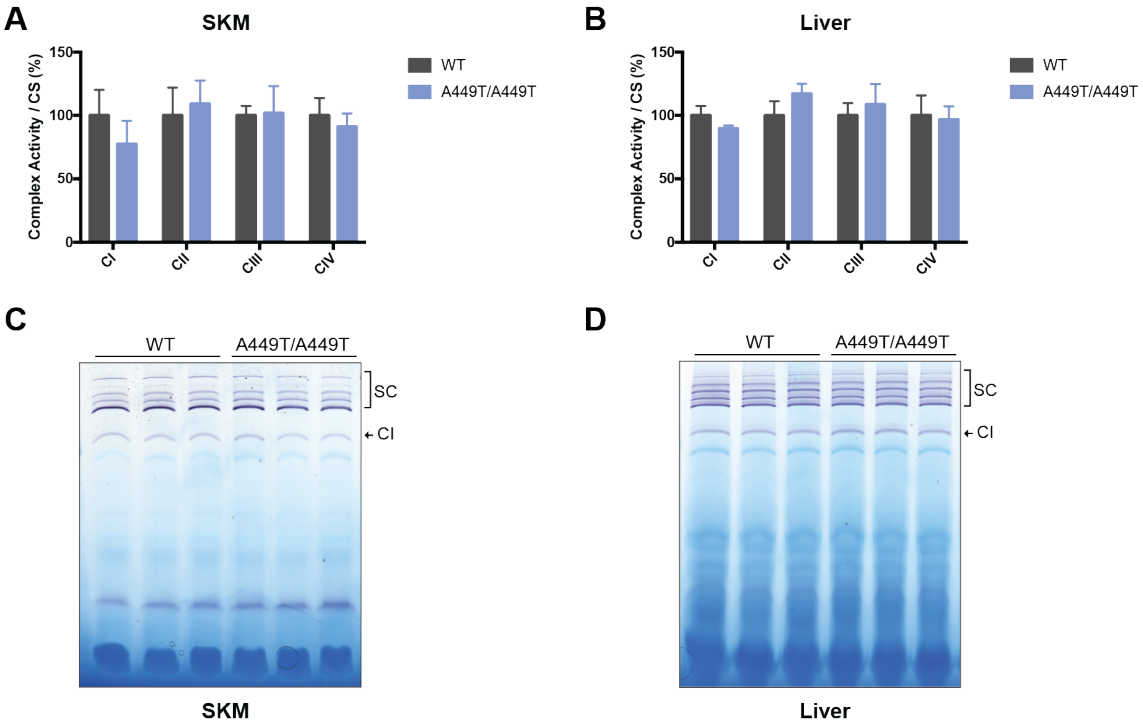

Figure 4.12. Analysis of OXPHOS activities and assembly in SKM and liver of *Polg*$^{A449T/A449T}$ mice.
A-B. Spectrophotometric activity of complex I (CI), complex II (CII), complex III (CIII) and complex IV (CIV), normalized to citrate synthase (CS), in (**A**) SKM and (**B**) Liver of WT and *Polg*$^{A449T/A449T}$ animals. Data are presented as mean ± SEM. P value were calculated by two tailed unpaired Student's t-test. (n = 4); **C-D.** In-gel activity of complex I (CI) on a first-dimension BNGE in mitochondrial protein isolated from (**C**) SKM and (**D**) liver from WT and *Polg*$^{A449T/A449T}$ animals. Each lane represents a sample from an individual mouse. SKM-Skeletal Muscle. SC- super complexes.

4.5. Effects of drug-induced toxicity in *Polg*$^{A449T/A449T}$ mice

4.5.1. Valproic acid does not trigger toxicity in *Polg*$^{A449T/A449T}$ mice

Valproic acid (VPA) is widely used around the world to treat epilepsy, a symptom present in many *POLG* mutant patients. However, VPA is contraindicated in patients carrying *POLG* mutations, as it results in a fulminant, fatal liver failure (Tzoulis et al., 2006, Stewart et al., 2010).

To understand if VPA could have a similar effect in *Polg*$^{A449T/A449T}$ mice, we treated our animals with VPA using two dosing regimens: by daily oral gavage (300mg/kg VPA) for one week or in food pellets (1.5% VPA) for two months. During the course of oral gavage administration, all experimental groups did not show any sign of illness and at sacrifice histological analyse of liver samples did not show any obvious pathological alterations (data not shown). Because the half-life of VPA is ~1 hour in mice comparing to ~10 hours in humans (Nau, 1985), we decided to supplement the diet with VPA of another cohort of WT and *Polg*$^{A449T/A449T}$ mice, to obtain a constant administration over time. During the period of two months, no differences were observed in body weight between *Polg*$^{A449T/A449T}$ and control mice (Figure 4.13 - A) and both did not show any sign of illness or behaviour alteration. At sacrifice, blood concentration of ALT, a biomarker of liver, was slightly elevated in the VPA-treated vs non-treated groups (37.5 ± 1.2 U/L, non-treated vs 67 ± 17 U/L, VPA-treated). However, no significant differences were observed between *Polg*$^{A449T/A449T}$ and WT-treated mice (64 ± 7 U/L, A449T-treated vs 70 ± 17 U/L, WT-treated) (Figure 4.13 - B). In addition, WT-treated mice presented a mild but significant increase in mtDNA copy number compared to non-treated WT mice, while *Polg*$^{A449T/A449T}$-treated mice did not show this increase compared with their non-treated controls, suggesting that POLγA mutants fail to expand mtDNA in response to VPA (Figure 4.13 - C). However, histological analysis of liver samples by H&E did not present any pathological alterations characteristic of VPA-induced toxicity in *POLG* patients (Figure 4.13 - D), such as microvesicular steatosis or evidence of hepatocellular necrosis (Fontana et al., 2009). Together these results indicate that VPA does not induce differential toxicity in *Polg*$^{A449T/A449T}$ when compared to WT mice.

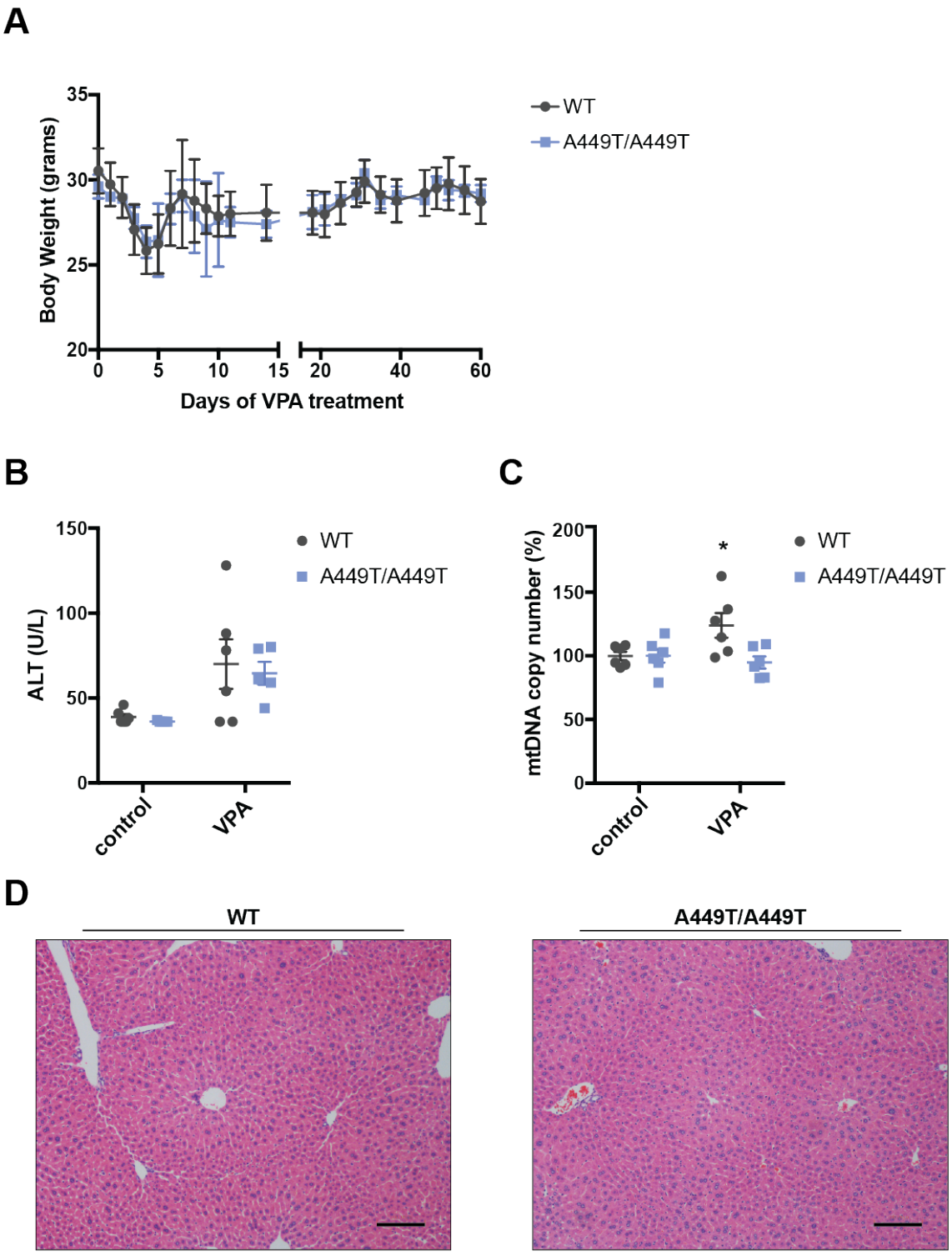

Figure 4.13. Effects of VPA-supplemented diet on *Polg*$^{A449T/A449T}$ mice.
A. Body weights of WT and *Polg*$^{A449T/A449T}$ treated animals during the course of 60 days under a VPA-supplemented diet. **B.** Blood levels of ALT (U/L) in non-treated WT and *Polg*$^{A449T/A449T}$ mice and in treated WT and *Polg*$^{A449T/A449T}$ after 60 days under a VPA-diet. **C.** Real-Time qPCR quantification of mtDNA content in liver of non-treated WT and *Polg*$^{A449T/A449T}$ and in VPA-treated WT and *Polg*$^{A449T/A449T}$ animals at sacrifice. Data are presented as mean ± SEM. Unpaired two tailed Student's t-tests: *p<0.05. Each symbol represents a biological replicate. **D.** Representative H&E staining of liver sections of VPA-treated WT and *Polg*$^{A449T/A449T}$ mice at the end of the 60-day treatment. Scale bars: 100 µm.

4.5.2. *Polg*$^{A449T/A449T}$ mice present impaired liver regeneration upon acute Carbon Tetrachloride exposure

In the previous section, we showed that VPA does not induce liver toxicity in *Polg* mutants. However, reports on VPA-induced liver failure in *POLG* patients suggests that liver failure occurs in these patients regardless of VPA dosing, and liver pathology cannot distinguish between the samples that were treated with valproic acid or not (Harding, 1990). Such findings suggest that VPA treatment is a catalyst of a pre-existent pathology rather than the underlying cause (Harding, 1990).

Because *Polg*$^{A449T/A449T}$ mice did not display a noticeable liver pathology, we decided to evaluate the liver regenerative capacity of POLγA mutant upon induced liver damage using carbon tetrachloride (CCl_4). CCl_4 is a potent hepatotoxin often used to study liver regeneration upon acute liver damage, triggering liver cell division to repopulate the necrotic areas. CCl_4 is metabolized in the liver to trichloromethyl radical (CCl_3*) by cytochrome P450 2E1 (CYP2E1), initiating free radical-mediated lipid peroxidation. Accumulation of such lipid-derived oxidative products results in liver injury (Manibusan et al., 2007).

We challenged a cohort of mice with a single injection of CCl_4 (day 0). We then analysed the extent of liver necrosis in half of the mice after 2 days, corresponding to the peak of liver damage, and the other half after 4 days, allowing a 2-day recovery. Two days after the injection, both WT and *Polg*$^{A449T/A449T}$ mice showed comparable extensive areas of necrosis (approximatively 35% of the liver), which was reduced to 6±0.46 % in WT mice after four days, but still above 10% in *Polg*$^{A449T/A449T}$ mutant (10±1.15 %, $p<0.05$) (Figure 4.14). These results suggest that liver regeneration is impaired in *Polg*$^{A449T/A449T}$ mice, possibly due to the incapacity of the surrounding hepatocytes to rapidly divide and repopulate the necrotic areas. Cell replication could be compromised in *Polg*$^{A449T/A449T}$ animals, likely due to the lack of bioenergetic supply by impaired mitochondria in stress conditions.

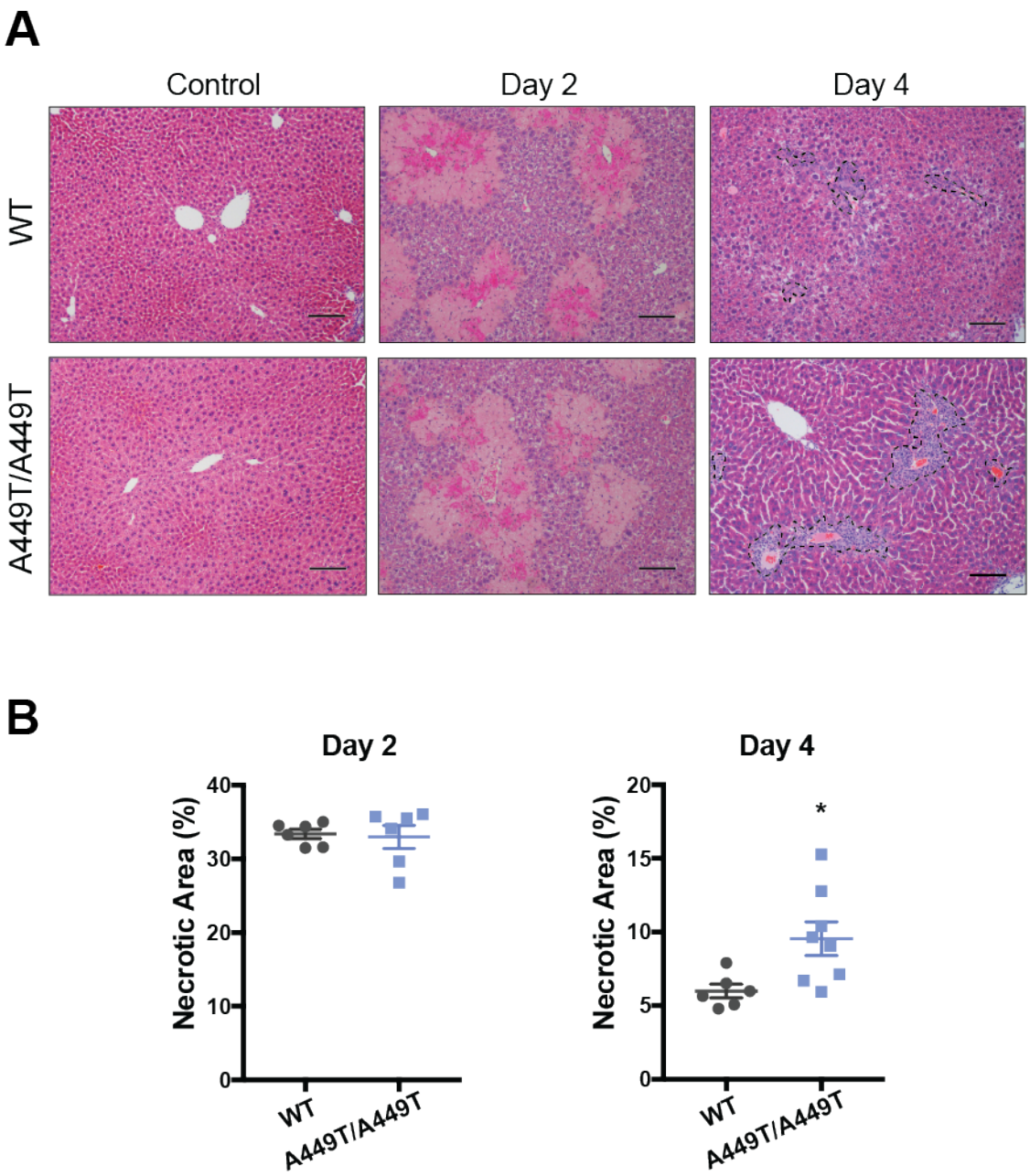

Figure 4.14. Effects of CCl_4 on liver regeneration of *Polg*$^{A449T/A449T}$ mice.
A. Representative H&E staining of liver tissue sections of WT (top) and *Polg*$^{A449T/A449T}$ (bottom) animals with a single injection of CCl_4. Two days after injection (middle), 4 days after injection (right) and control/non-injected mice (left). Note the necrotic areas around the central veins (highlighted with black lines at day 4). Scale bar 100 µm. **B.** Quantification of necrotic areas (H) as percentage (%) of the total section area, 2 and 4 days after a single injection of CCl_4. Data are presented as mean ± SEM. Two tailed unpaired Student's *t*-test: $^*P < 0.05$. Each symbol represents a biological replicate.

4.6. Characterization of mtDNA replication in *Polg*$^{A449T/A449T}$ MEFs

4.6.1. *Polg*$^{A449T/A449T}$ MEFs display impaired mtDNA copy number recovery upon EtBr-mediated depletion

To investigate in detail the effects on mtDNA replication, we generated mouse embryonic fibroblasts (MEFs) from *Polg*$^{A449T/A449T}$ and WT E8.5 embryos. Analysis of the mtDNA copy number in MEFs, revealed that the mtDNA content was similar in the two genotypes (Figure 4.15 - A). We then decided to evaluate if mtDNA replication was affected by the A449T mutation by depleting mtDNA and assessing the recovery of mtDNA content. We used ethidium bromide (EtBr) for 5 days to deplete mtDNA content to ~15%, and found that after removal of EtBr, mtDNA content recovered to pre-treatment values within 3 days in WT MEFs, whereas no recovery at all was observed in the mutant cells (Figure 4.15 - B), strongly indicating severely impaired mtDNA replication in stress conditions of *Polg*$^{A449T/A449T}$ mouse mitochondria.

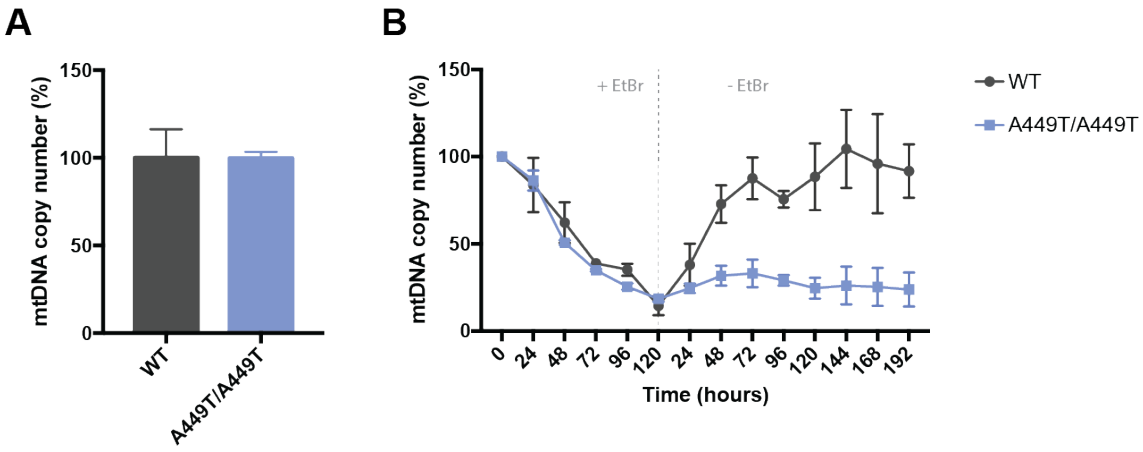

Figure 4.15. Evaluation of mtDNA recovery in *Polg*$^{A449T/A449T}$ MEFs.
A. Real-Time qPCR quantification of mtDNA content in WT and *Polg*$^{A449T/A449T}$ MEFs. Data are presented as mean ± SEM. P value were calculated by two tailed unpaired Student's t-test. (n = 4). **B.** Real-time qPCR quantification of mtDNA content in WT and *Polg*$^{A449T/A449T}$ MEFs during ethidium bromide-mediated depletion and then recovery of mtDNA. Data are presented as mtDNA percentage (%) of untreated cells of each genotype. Data are presented as mean ± SEM (n = 3).

4.6.2. *Polg*$^{A449T/A449T}$ MEFs present an increased number of replicating mtDNA foci

As presented in the previous section, *Polg*$^{A449T/A449T}$ MEFs had comparable mtDNA content to WT cells, despite presenting a clear replication defect upon chemical depletion of mtDNA. To further characterize mtDNA replication of *Polg*$^{A449T/A449T}$ in normal conditions, we investigated the fraction of mtDNA foci under active replication in individual cells by confocal microscopy. We used 5-ethynyl-2′-deoxyuridine (EdU) staining in conjunction with an anti-DNA antibody to label replicating and total mtDNA. In addition, we used an anti-TOM20 antibody to label the mitochondrial network. While the number of mtDNA foci was similar between *Polg*$^{A449T/A449T}$ and WT cells, mutant MEFs revealed a higher total number of replicating mtDNA foci per cell (Figure 4.16 – A to C). Normalizing the number of replicating mtDNA foci to the number of total mtDNA foci, revealed a significantly increased fraction of replicating mtDNA molecules in *Polg*$^{A449T/A449T}$ versus WT MEFs (Figure 4.16 - D), These results indicate that more mtDNA foci were engaged in replication of *Polg*$^{A449T/A449T}$, possible compensating for mtDNA replication defects displayed by mutant POLγA.

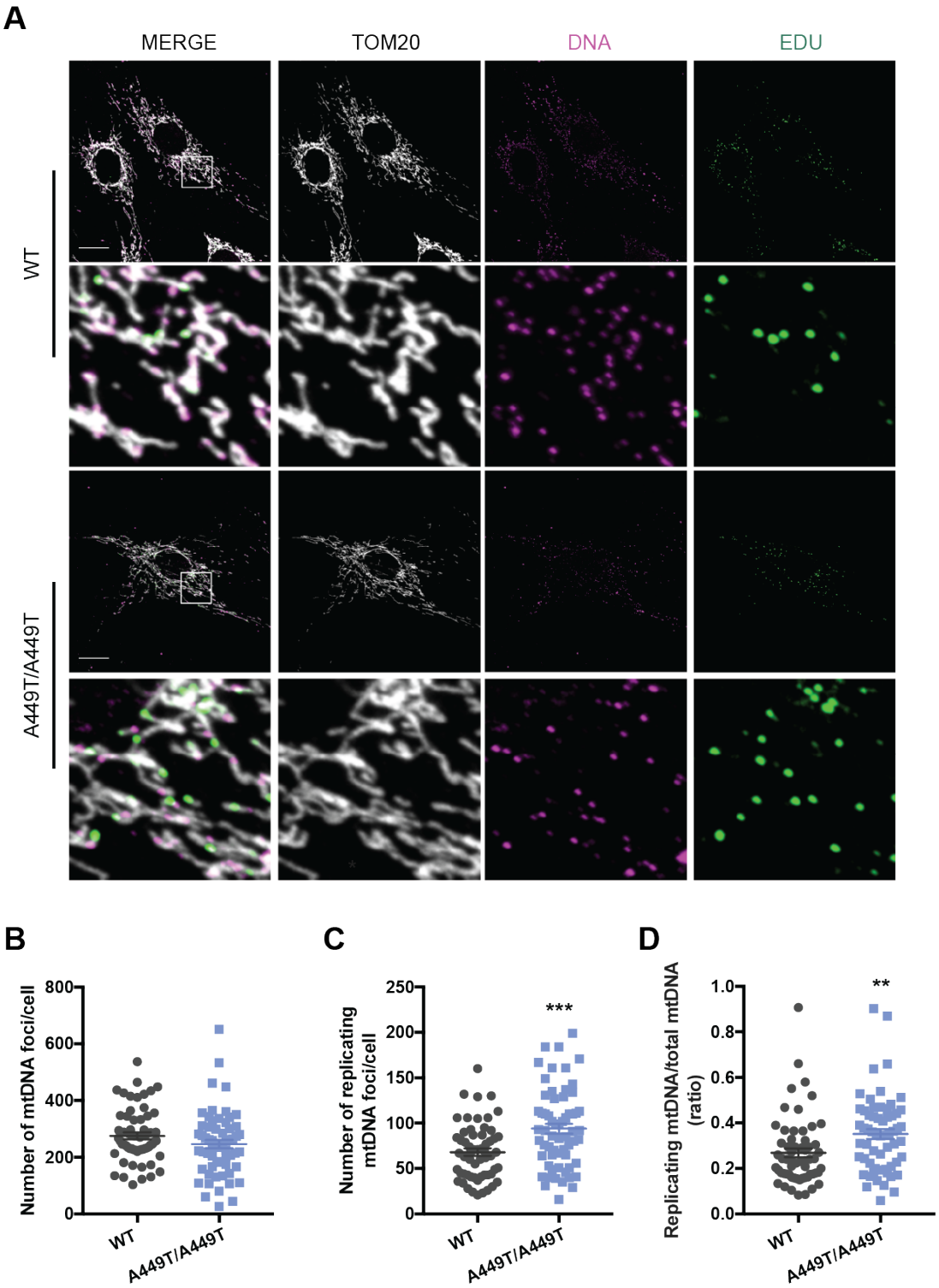

Figure 4.16. Microscopy characterization of mtDNA replication in *Polg*$^{A449T/A449T}$ MEFs.
A. Representative confocal images of mitochondria, DNA and replicating mtDNA (EdU) from WT and *Polg*$^{A449T/A449T}$ MEFs. Mitochondria and mtDNA were labeled using anti-TOM20 and anti-DNA antibodies, respectively. Replicating DNA was visualized in fixed cells after incubation with 50 µM EdU for 1 h. Scale bar 20 µm. Note: The EdU staining of the nucleus was computationally removed using Fiji. **B.** Quantification of total mtDNA from (A). **C.** Quantification of mitochondrial EdU positive foci from (A). **D.** Ratio of the mitochondrial replicating mtDNA/total mtDNA.
All data are presented as mean ± SEM. Two tailed unpaired Student's t-test: **P < 0.01; ***P < 0.001. Each symbol represents individual cells (n = 60) from three independent experiments. These experiments were performed in collaboration with Lisa Tilokani (Prudent´s lab).

4.7. Characterization of mtDNA replication in tissues of *Polg*$^{A449T/A449T}$ mice

4.7.1. *Polg*$^{A449T/A449T}$ mice present reduced 7S DNA levels in several tissues

Led by the findings obtained in *Polg*$^{A449T/A449T}$ MEFs, we decided to investigate mtDNA replication in mitochondria isolated from several tissues. Normally, about 95% of all replication events are prematurely terminated, generating a 650 nucleotide-long molecule, called 7S DNA (Bogenhagen and Clayton, 1978). Therefore, changes in 7S DNA levels could be indicative of the balance between successful vs aborted replication events (see introductory section 2.5). We thus investigated mtDNA replication in the tissues of the mutant and control mice by Southern blot to analyse 7S DNA levels. Compared with WT littermates, *Polg*$^{A449T/A449T}$ mice presented significantly reduced 7S levels in skeletal muscle and kidney, and a similar trend was also present in the other analysed tissues, except for the heart (Figure 4.17). The decreased levels of 7S DNA indicate that possibly less replication mtDNA events are aborted in knockin mice versus WT littermates, increasing the number of events leading to synthesis of full-length mtDNA.

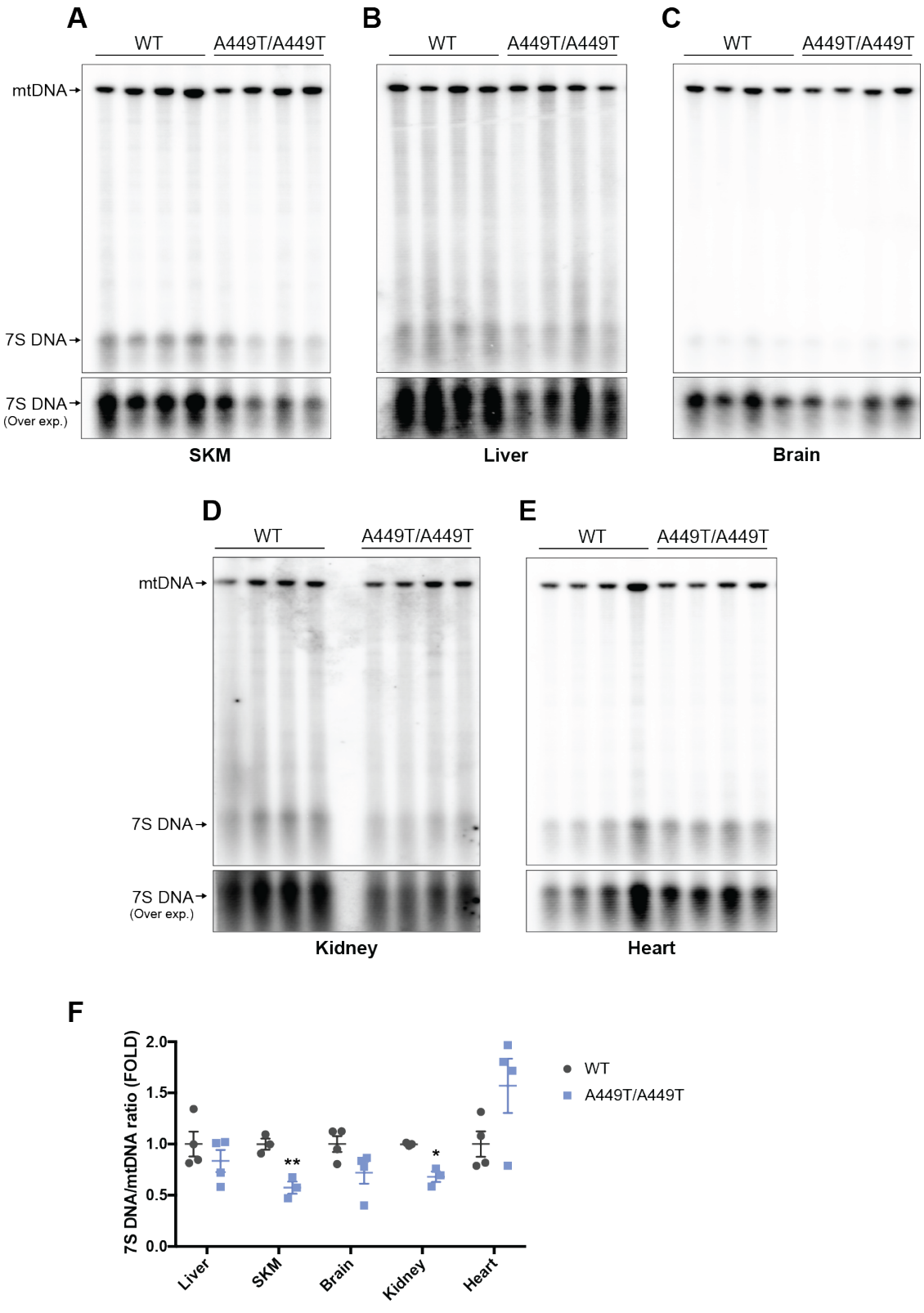

Figure 4.17. Mitochondrial 7S DNA levels in tissues of *Polg*$^{A449T/A449T}$ mice.
A-E. Southern blot analysis of BlpI-digested mtDNA and 7S DNA from SKM (**A**), Liver (**B**), brain (**C**), kidney (**D**) and heart (**E**) of WT and *Polg*$^{A449T/A449T}$ animals. **F.** Quantification of the Southern blots presented in panel (A-E). 7S DNA levels were normalized to linearized full length mtDNA and presented as FOLD change from WT animals. Data are presented as mean ± SEM. Two tailed unpaired Student's t-test: *P <0.05; **P <0.01. Each symbol represents a biological replicate.

4.7.2. *Polg*$^{A449T/A449T}$ mitochondria display normal mtDNA replication rates but present accumulation of replication intermediates

To investigate the mechanistic details of mtDNA replication, we then performed *in organello* replication experiments in liver-isolated mitochondria, by pulse-labelling with α-32P-dATP, allowing the evaluation of mtDNA replication rates (Figure 4.18). Analysis of newly synthesized full length mtDNA levels over time (5; 15; 30; 60 and 90 min), failed to reveal obvious differences in replication rates of mtDNA between WT and *Polg*$^{A449T/A449T}$ mice, in which we could observe an almost complete overlap of fitted regression lines (Figure 4.18 A and B). However, in *Polg*$^{A449T/A449T}$ samples, the levels of *de novo* synthesised 7S DNA required longer incubation periods to saturate compared with WT mitochondria (Figure 4.18 A), suggesting that a subset of newly synthesised 7S DNA may quickly proceed to full-length replication generating replication intermediates (RIs). MtDNA molecules in active replication remain bound to these newly synthesised RIs, leading to an increase in their molecular mass and resulting in a slower migration in electrophoretic gels (Figure 4.18 A). Interestingly, the signal due to long but incomplete mtDNA RIs molecules was much more intense in the POLγ mutants compared to WT samples, thus suggesting accumulation of replication intermediates (RIs) in the mutant versus controls. Detailed quantification of the ratio between RIs and newly synthesized mtDNA after a pulse of 60 minutes revealed a ~1.8x higher accumulation of RIs in *Polg*$^{A449T/A449T}$ samples compared with WT controls (Figure 4.18 C). We next applied two-dimension agarose gel electrophoresis (2D-AGE), which resolves DNA molecules based on size and shape, allowing a snapshot of the RIs. Notably, *Polg*$^{A449T/A449T}$ mice displayed an overall increase of the different types of RIs compared to WT animals (Figure 4.19 A to C). The observation that RIs accumulate equally across the mtDNA, suggests that RIs accumulate as a result of generalized replication fork stalling mainly due to abnormal replication present in *Polg*$^{A449T/A449T}$ mice. Together, these results support the idea that near-normal rates of replication mtDNA present in *Polg*$^{A449T/A449T}$ mice are possibly due to a compensatory mechanism, whereby a defect of mtDNA replication cause by mutant POLγA is neutralised by initiation of more successful replication events.

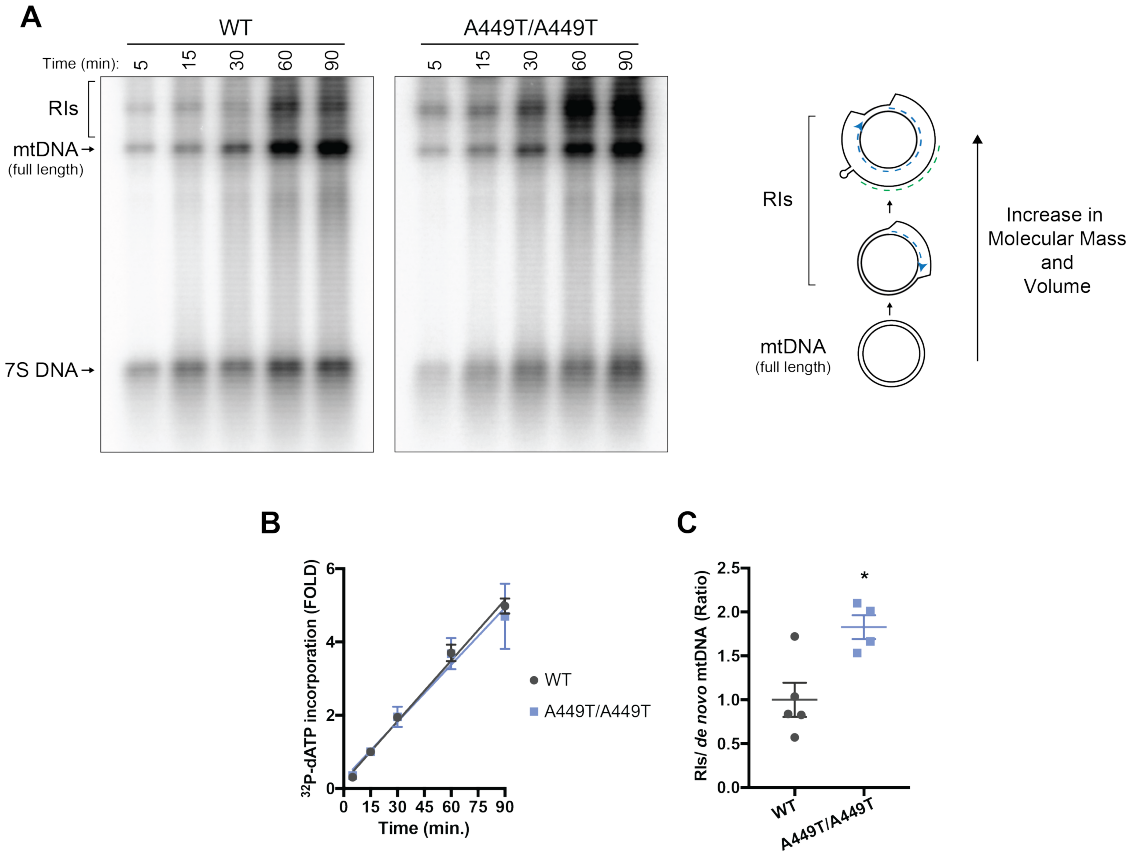

Figure 4.18. In organello mtDNA replication rates of *Polg*$^{A449T/A449T}$ mitochondria.
A. Time course of de novo DNA synthesis of mtDNA, 7S DNA and RIs in liver-isolated mitochondria of WT and *Polg*$^{A449T/A449T}$ animals. Brackets indicate mtDNA replication intermediates (RIs). Pulse-labelling time (min) is indicated on the top. On the right, schematics of how the synthesis of RIs contribute to an increase in the molecular mass and volume of mtDNA species, leading to a slower migration in the gel. **B.** Replication rate of mtDNA, measured as incorporation of [α 32 P]-dATP into linear BlpI- digested mtDNA (full length) over a time course (panel A). The resulting quantifications are presented as FOLD change to a pulse-labelling of 15 min. Data are presented as mean ± SEM. (WT: n=5; *Polg*$^{A449T/A449T}$: n=4). A linear regression line was calculated for each genotype. (WT: R2 = 0.993; *Polg*$^{A449T/A449T}$: R2 = 0.9853). **C.** Ratio between newly synthesized mitochondrial RIs and de novo mtDNA after a pulse-labelling of 60 min (panel A). Data are presented as mean ± SEM. *P<0.05; Student's t-test. Each symbol represents a biological replicate.

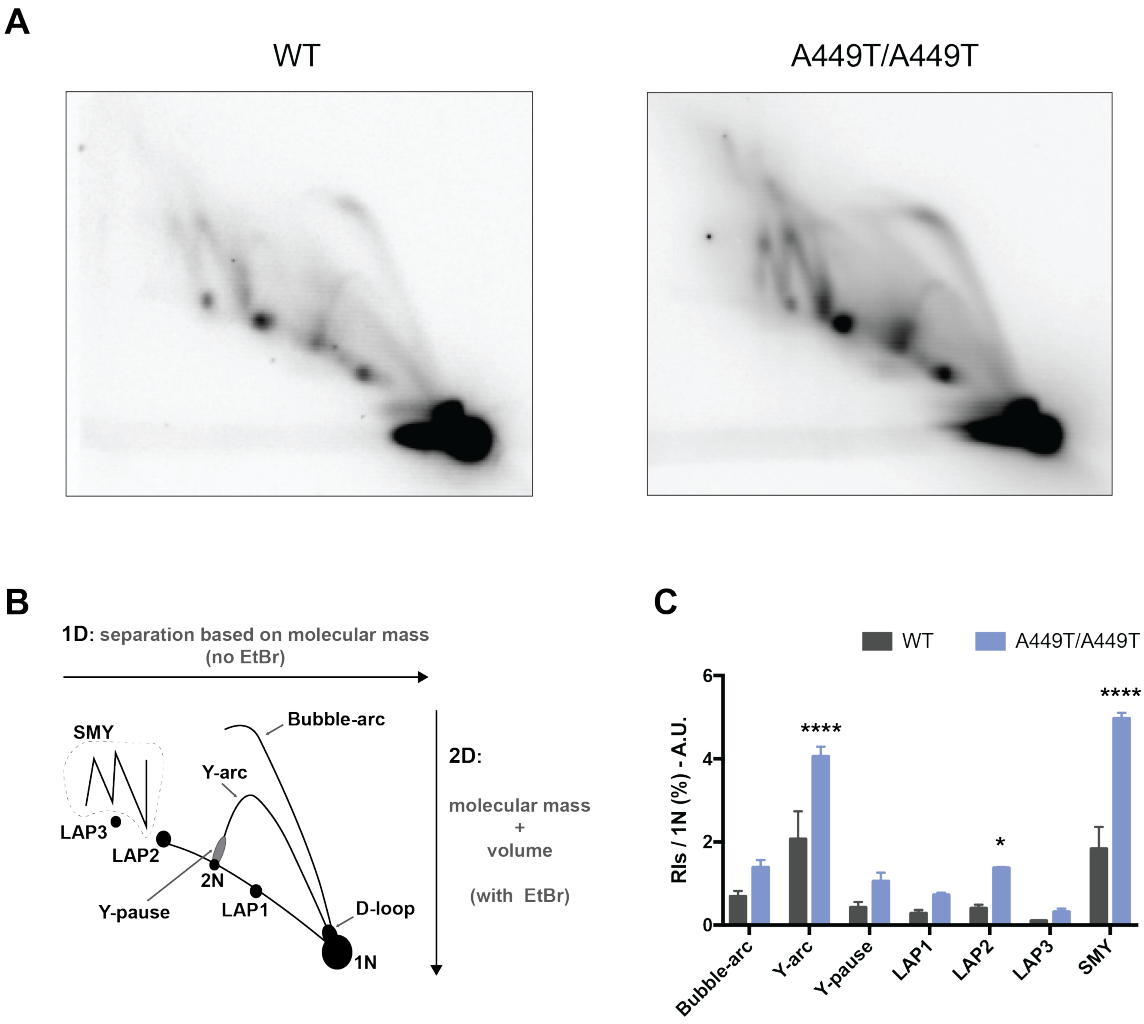

Figure 4.19. Analysis of mtDNA replication intermediates in *Polg*$^{A449T/A449T}$ mitochondria. **A.** Analysis of the mtDNA RIs in the liver-isolated mitochondria of WT and *Polg*$^{A449T/A449T}$ mice, resolved by 2D-AGE and followed by southern blot visualization. DNA was digested with the BclI restriction enzyme. **B.** Schematic representation of the different types of mtDNA replication intermediates (RIs), as resolved by 2D-AGE followed visualization by southern blot, where 1N corresponds to a full-length mtDNA molecule without any RIs attached to it. In the first dimension, the DNA is separated in the gel based on molecular mass. In the second dimension, the DNA is separated based on molecular mass and volume, the later enhanced by the intercalation of Ethidium Bromide (EtBr) into DNA strands. **C.** Quantification of mtDNA replication intermediates (RIs) from (panel A) as percentage (%) of non-replicating mtDNA (1N). Data are presented as mean ± SEM. One-way ANOVA test with Tukey's correction (n = 2): *p<0.05; ****p<0.0001.

4.8. Comparison of a *Polg*$^{A449T/KO}$ mouse with *Polg*$^{A449T/A449T}$ mice

Characterization of *Polg*$^{A449T/A449T}$ mice in the previous sections showed that these animals present a mild clinical phenotype. Despite a mild decrease in mtDNA copy numbers and near-normal *in organello* mtDNA replication rates, *Polg*$^{A449T/A449T}$ mice presented low levels of 7S DNA and accumulation of mtDNA replication intermediates, suggesting a compensatory mechanism. Therefore, we decided to knockout one of the *Polg* alleles, creating a double mutant *Polg*$^{A449T/KO}$ mouse, with the goal of driving additional constrains to mtDNA replication. This genotype reproduces the most common allelic situation in humans, which is associated with Alpers-Hunterlocher syndrome, an extremely severe hepato-encephalopathy. To create the double mutant *Polg*$^{A449T/KO}$ strain, we crossed the *Polg*$^{A449T/A449T}$ mice with a *Polg*$^{WT/KO}$ mouse (Hance et al., 2005). In the following sections, we compare the clinical and molecular phenotype of *Polg*$^{A449T/KO}$ to the key findings from *Polg*$^{A449T/A449T}$ and WT animals shown in previous sections.

4.8.1. *Polg*$^{A449T/KO}$ and Polg$^{A449T/A449T}$ mice have similar phenotype

To study the phenotype of *Polg*$^{A449T/KO}$ mice we evaluated their spontaneous motility using a CLAMS^{TM} system and their muscle endurance on a treadmill. In the same tests, *Polg*$^{A449T/A449T}$ mice performed slightly, but significantly, less than WT controls.

Polg$^{A449T/KO}$ mice displayed a 45% ($P < 0.01$) reduction in spontaneous rearing movements during the night and a 53% ($P < 0.05$) reduction during the day, compared with WT controls. No statistically significant differences were observed between *Polg*$^{A449T/KO}$ and *Polg*$^{A449T/A449T}$ mice (45 vs 41%, during the night and 53 vs 46% during the day) (Figure 4.20 A). In addition, *Polg*$^{A449T/KO}$ mice presented a 27% ($P < 0.05$) reduction in ambulatory activity during the day compared with WT controls. Also in this case, no statistically significant differences were observed between *Polg*$^{A449T/KO}$ and *Polg*$^{A449T/A449T}$ mice during the day (27 vs 19%), and both genotypes did not show significant differences of ambulatory activity during the night compared with WT littermates (Figure 4.20 B).

In the treadmill motor endurance test, *Polg*$^{A449T/KO}$ mice displayed significant exercise intolerance compared with WT controls, with a 25.5% ($P < 0.05$) reduction, similar to *Polg*$^{A449T/A449T}$ mice which presented a 19.6% ($P < 0.05$) reduction (Figure 4.20 C). No statistically significant differences were detected between *Polg*$^{A449T/KO}$ and *Polg*$^{A449T/A449T}$ mice.

Altogether these results indicate that *Polg*$^{A449T/KO}$ present a mild clinical phenotype very similar to *Polg*$^{A449T/A449T}$ mice and characterised by reduced spontaneous motor activity and exercise intolerance.

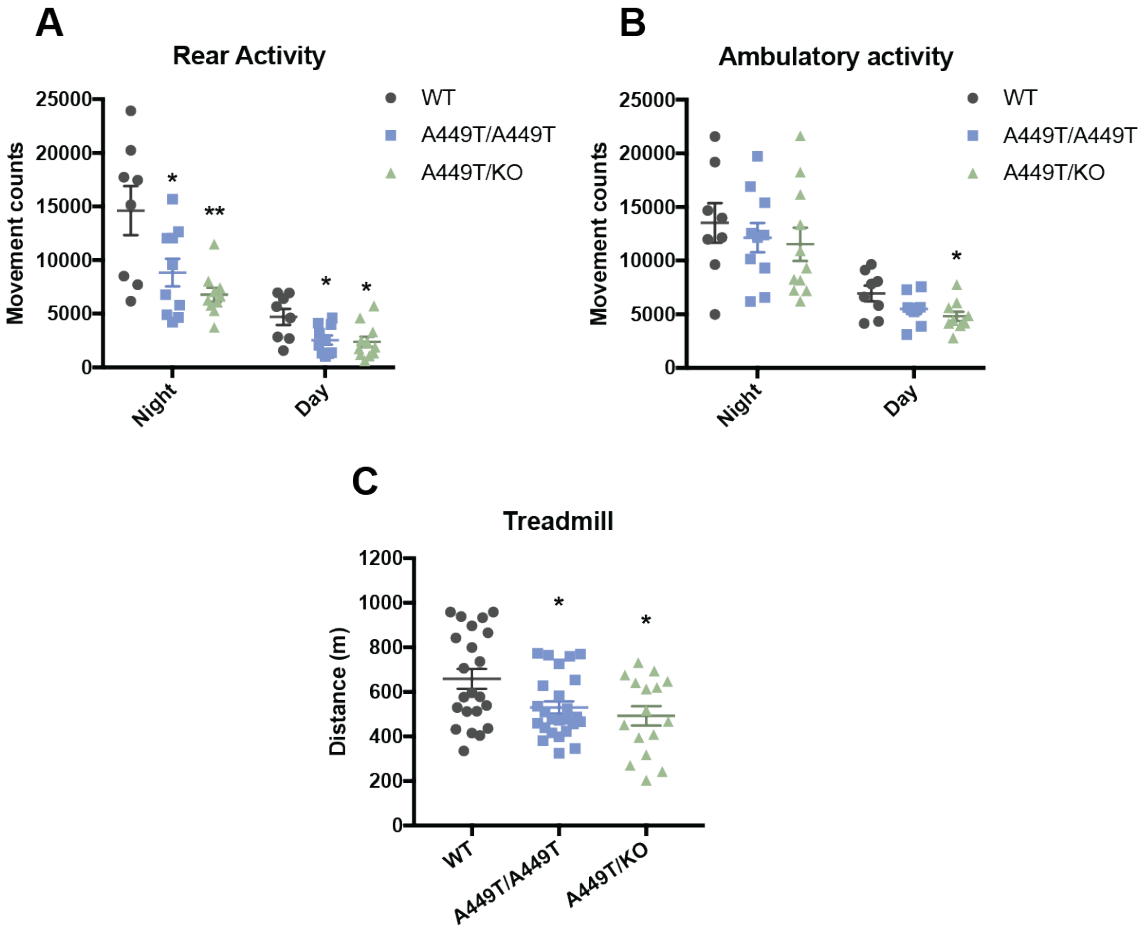

Figure 4.20. Phenotypic characterization of *Polg*$^{A449T/KO}$ mice.
A. Spontaneous rear activity (vertical movement counts) of 3-month-old WT, *Polg*$^{A449T/A449T}$ and *Polg*$^{A449T/KO}$ animals. **B.** Spontaneous ambulatory activity (horizontal movement counts) of 3-month-old WT, *Polg*$^{A449T/A449T}$ and *Polg*$^{A449T/KO}$ animals. Data are presented as mean ± SEM. One-way ANOVA: *P < 0.05, **P < 0.01. Each symbol represents a biological replicate. **C.** Distance run in metres by 3-month-old WT, *Polg*$^{A449T/A449T}$ and *Polg*$^{A449T/KO}$ animals on the treadmill. Data are presented as mean ± SEM. *$P < 0.05$; One-way ANOVA. Each symbol represents a biological replicate.

4.8.2. *Polg*$^{A449T/KO}$ mice display mild mtDNA depletion comparable to *Polg*$^{A449T/A449T}$ mice

To study the consequences of the *Polg*$^{A449T/KO}$ genotype in mtDNA copy numbers, we evaluated mtDNA content in several tissues, including liver, skeletal muscle, brain, kidney and heart, and compared them to *Polg*$^{A449T/A449T}$ and WT mice.

Like *Polg*$^{A449T/A449T}$ mice, *Polg*$^{A449T/KO}$ displayed a 21 ± 3% ($P < 0.01$) reduction in the skeletal muscle compared with WT controls. However, no statistically significant differences in skeletal muscle were observed between *Polg*$^{A449T/KO}$ and *Polg*$^{A449T/A449T}$ mice (21 ± 3% vs 20 ± 4%) (Figure 4.21). Apart from skeletal muscle, *Polg*$^{A449T/KO}$ mice presented a 30 ± 4% ($P < 0.001$) reduction in the kidney compared with WT controls, which was also significantly decreased compared to *Polg*$^{A449T/A449T}$ mice (70 ± 4% vs 98 ± 4% of total copy number, $P < 0.001$) (Figure 4.21). MtDNA quantification in liver, brain and heart did not reveal significant differences among the different genotypes (Figure 4.21).

These results suggest that *Polg*$^{A449T/KO}$ present a mild mtDNA depletion, which is comparable to *Polg*$^{A449T/A449T}$ mice.

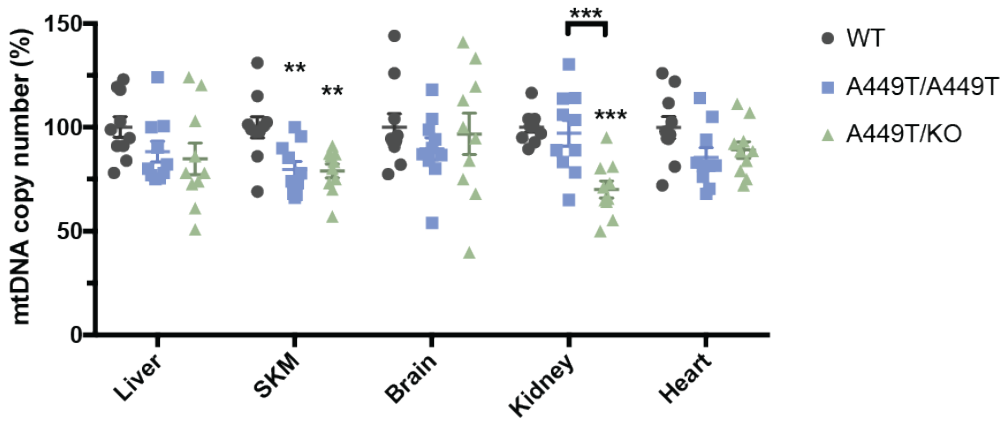

Figure 4.21. MtDNA levels in the different tissues of *Polg*$^{A449T/KO}$ mice.
Real-Time qPCR quantification of mtDNA content in liver, skeletal muscle (SKM), kidney, brain and heart of 3-month-old WT, *Polg*$^{A449T/A449T}$ and *Polg*$^{A449T/KO}$ animals. Data are presented as mean ± SEM. One-way ANOVA: *p<0.05; **p<0.01, ***p<0.001. Each symbol represents a biological replicate.

4.8.3. *Polg*$^{A449T/KO}$ mice present additional reduction of 7S DNA levels in several tissues

In previous sections, *Polg*$^{A449T/A449T}$ mice displayed a decrease in 7S DNA steady-state levels, thus suggesting an atypical balance between abortive vs full-length mtDNA replication that could underlie a compensatory mechanism. Given that *Polg*$^{A449T/KO}$ mice present mild clinical phenotypes and mild mtDNA depletion which are comparable with *Polg*$^{A449T/A449T}$, we thus evaluated if 7S DNA levels were also decreased in *Polg*$^{A449T/KO}$ mutants.

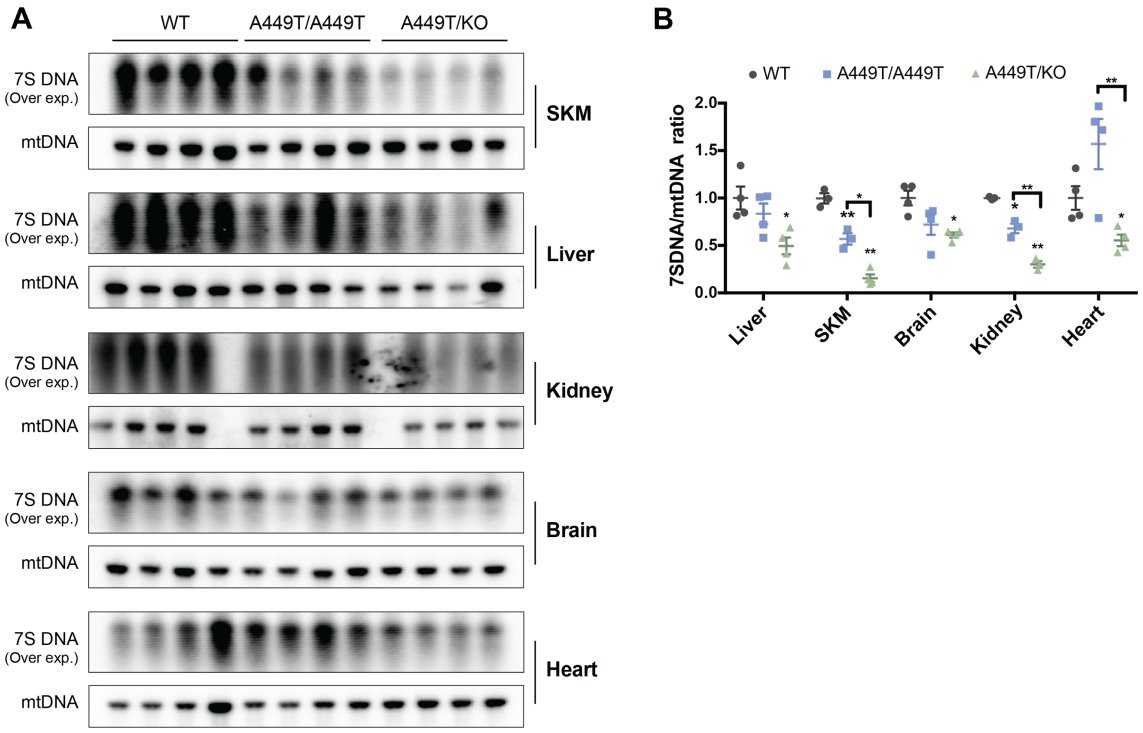

Figure 4.22. Mitochondrial 7S DNA levels in tissues of *Polg*$^{A449T/KO}$ mice.
A. Southern blot analysis of BlpI-digested mtDNA and 7S DNA from skeletal muscle (SKM), Liver, brain, kidney and heart of WT, *Polg*$^{A449T/A449T}$ and *Polg*$^{A449T/KO}$ animals. **B.** Quantification of the Southern blots presented in panel (A). 7S DNA levels were normalized to linearized full length mtDNA and presented as FOLD change from WT animals. Data are presented as mean ± SEM. One-way ANOVA: *P <0.05; **P <0.01. Each symbol represents a biological replicate.

Polg$^{A449T/KO}$ mice presented significantly reduced 7S DNA levels in all tissues analysed compared with WT littermates, in contrast with *Polg*$^{A449T/A449T}$ in which a significant decrease was only observed in skeletal muscle and kidney (Figure 4.22). In addition, 7S DNA levels in *Polg*$^{A449T/KO}$ mice were significantly further reduced in skeletal muscle and kidney when compared with *Polg*$^{A449T/A449T}$ (Figure 4.22). These results suggest that the mechanism behind the decreased levels of 7S

DNA observed in *Polg*$^{A449T/A449T}$ mice is further enhanced resulting in even lower levels of 7S DNA in *Polg*$^{A449T/KO}$ mice, possibly as consequence of higher degree of mtDNA replication defects.

4.8.4. *Polg*$^{A449T/KO}$ mitochondria present additional accumulation of replication intermediates

Next, we performed *in organello* replication and 2D-AGE experiments in liver-isolated mitochondria, to evaluate mtDNA replication rates and investigate if mtDNA RIs are also accumulated in *Polg*$^{A449T/KO}$ mice. *In organello* replication rates of newly synthesized mtDNA of *Polg*$^{A449T/KO}$ mitochondria were indistinguishable from WT and *Polg*$^{A449T/A449T}$ samples, suggesting that synthesis of full-length mtDNA is not affected in all genotypes (Figure 4.23 A and B). However, the levels of *de novo* synthesised 7S DNA of *Polg*$^{A449T/KO}$ samples required longer incubation periods to saturate compared with WT mitochondria, a finding also observed in *Polg*$^{A449T/A449T}$ samples (Figure 4.23 A). Analysis of the upper band corresponding to RIs, demonstrated that *Polg*$^{A449T/KO}$ samples accumulate over time more RIs compared with WT, and possibly compared to *Polg*$^{A449T/A449T}$. Indeed, detailed quantification of the ratio between RIs and newly synthesized mtDNA after a pulse of 60 minutes revealed a ~2.5x higher accumulation of RIs in *Polg*$^{A449T/KO}$ samples compared with WT controls, and a ~1.4x higher accumulation compared to *Polg*$^{A449T/A449T}$ (Figure 4.23 C).

To further validate our findings, we determined the steady-state levels of RIs by resolving them using a 2D-AGE. Remarkably, *Polg*$^{A449T/KO}$ mice exhibited an overall increase of the different types of RIs compared to WT animals. Furthermore, the observed accumulation of RIs was significantly greater in *Polg*$^{A449T/KO}$ compared to *Polg*$^{A449T/A449T}$ mice (Figure 4.24 A to C).

These results suggest that the abnormal mtDNA replication caused in *Polg*$^{A449T/A449T}$ by a mutant POLγA and further aggravate by a knockout of one *POLG* allele in *Polg*$^{A449T/KO}$ mice, could be compensated at the replication initiation level, as suggested by gradual decrease in 7S DNA levels and accumulation of RIs in correlation with the degree of mtDNA replication defect.

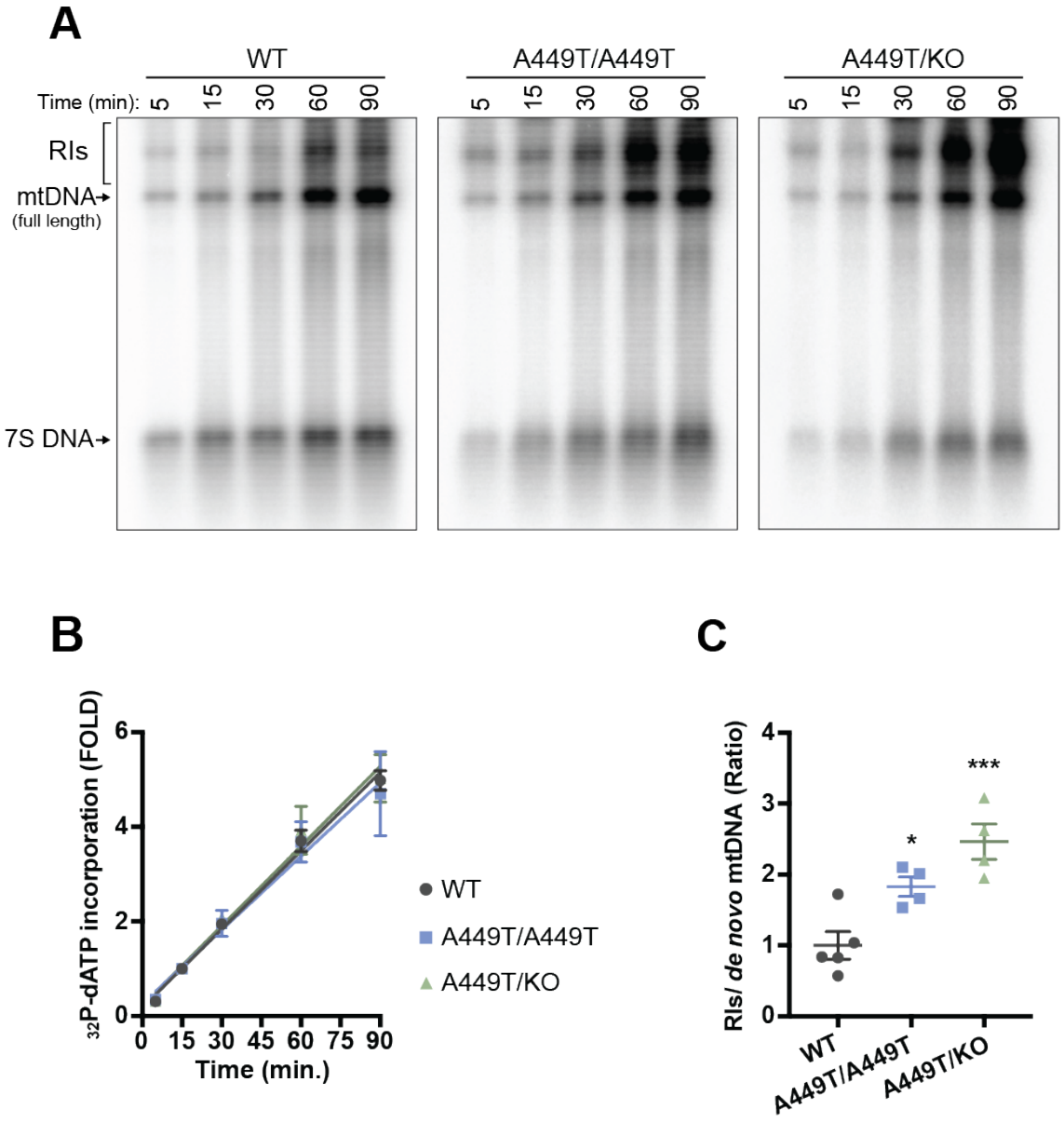

Figure 4.23. In organello mtDNA replication rates of *Polg*$^{A449T/KO}$ mitochondria.
A. Time course of de novo DNA synthesis of mtDNA, 7S DNA and RIs in liver-isolated mitochondria of WT, *Polg*$^{A449T/A449T}$ and *Polg*$^{A449T/KO}$ animals. Brackets indicate mtDNA replication intermediates (RIs). Pulse-labelling time (min) is indicated on the top. **B.** Replication rate of mtDNA, measured as incorporation of [α 32 P]-dATP into linear BlpI- digested mtDNA (full length) over a time course (panel A). The resulting quantifications are presented as FOLD change to a pulse-labelling of 15 min. Data are presented as mean ± SEM. (WT: n=5; *Polg*$^{A449T/A449T}$: n=4; *Polg*$^{A449T/KO}$: n=4). A linear regression line was calculated for each genotype. (WT: R^2 = 0.993; *Polg*$^{A449T/A449T}$: R^2 = 0.9853; *Polg*$^{A449T/KO}$: R^2 = 0.9844). **C.** Ratio between newly synthesized mitochondrial RIs and de novo mtDNA after a pulse-labelling of 60 min (panel A). Data are presented as mean ± SEM. *P<0.05; ***P<0.001; One-way ANOVA. Each symbol represents a biological replicate.

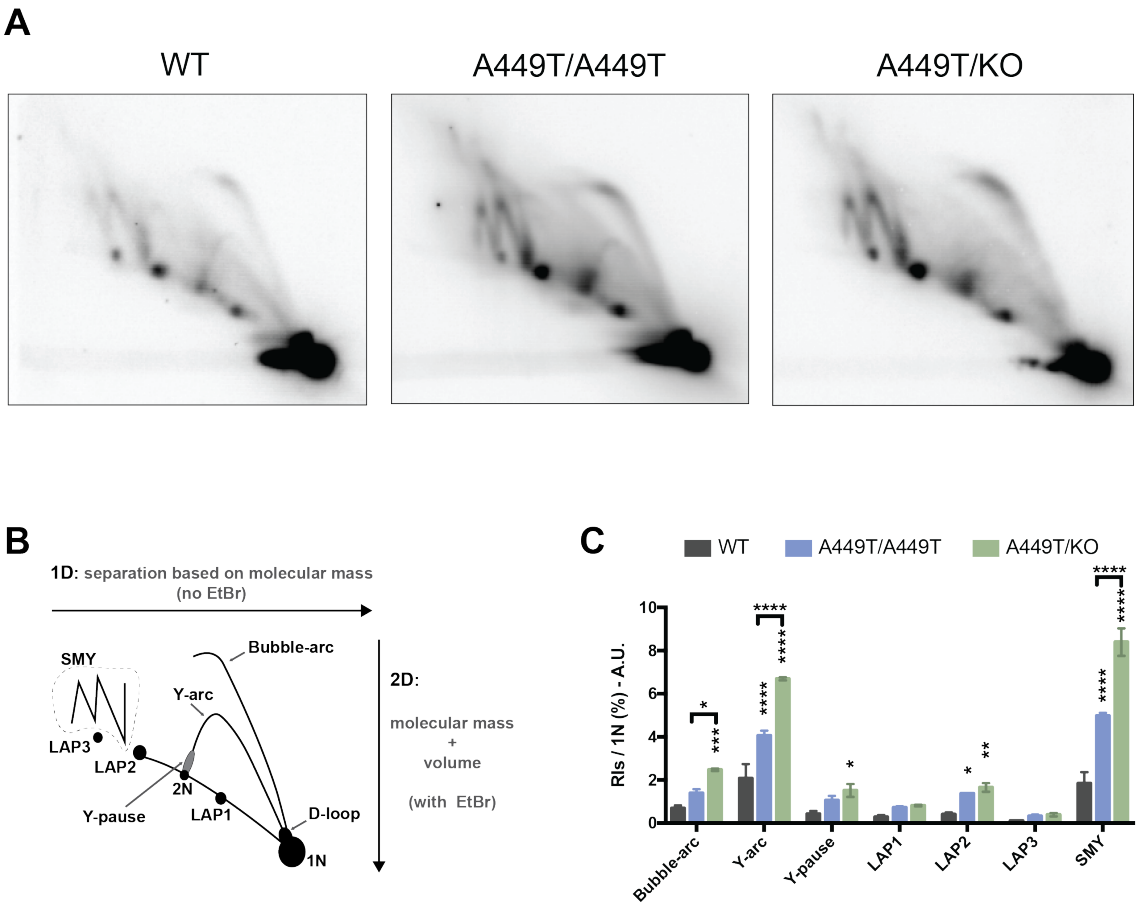

Figure 4.24. Analysis of mtDNA replication intermediates in *Polg*$^{A449T/KO}$ mitochondria. **A.** Analysis of the mtDNA RIs in the liver-isolated mitochondria of WT, *Polg*$^{A449T/A449T}$ and *Polg*$^{A449T/KO}$ mice, resolved by 2D-AGE and followed by southern blot visualization. DNA was digested with the BclI restriction enzyme. **B.** Schematic representation of the different types of mtDNA replication intermediates (RIs), as resolved by 2D-AGE followed visualization by southern blot, where 1N corresponds to a full-length mtDNA molecule without any RIs attached to it. In the first dimension, the DNA is separated in the gel based on molecular mass. In the second dimension, the DNA is separated based on molecular mass and volume, the later enhanced by the intercalation of Ethidium Bromide (EtBr) into DNA strands. **C.** Quantification of mtDNA replication intermediates (RIs) from (panel A) as percentage (%) of non-replicating mtDNA (1N). Data are presented as mean ± SEM. Two-way ANOVA test with Tukey's correction (n = 2): *p<0.05; **p<0.01; ***p<0.001; ****p<0.0001.

4.9. *In vitro* characterization of mPOLγA^{A449T} mutant protein on mtDNA replication

Characterization of *Polg*$^{A449T/A449T}$ and mice *Polg*$^{A449T/KO}$ in the previous sections showed that these animals clearly present anomalous mtDNA replication. However, *in vivo* systems are complex and normally present many variables that affect the readout of experimental procedures. To analyse in detail the mechanistic consequences of the mutant POLγA A449T on mtDNA replication and to compare it with the human counterpart, we expressed and purified both human (h) and mouse (m) WT (hPOLγA and mPOLγA) and mutant (hPOLγA^{A467T} and mPOLγA^{A449T}) as recombinant proteins. We then used such purified system to study specific functions of POLγ, including DNA binding, stimulation of POLγA by POLγB, polymerase and exonuclease activities.

4.9.1. mPOLγA^{A449T} displays less affinity to DNA template

First, we used an Electrophoresis Mobility Shift Assay (EMSA) to measure the binding of mPOLγA to a primed DNA template. Binding of mPOLγA to the template causes a shift during electrophoresis, allowing the quantification of the portion of mPOLγA that binds the template.

When alone (without POLγB), 300 fmol of mPOLγA^{A449T} was needed to fully shift the template, while this was accomplished by mPOLγA^{WT} at concentrations of 100 fmol (Figure 4.25 - A). Calculation of the dissociation constants for DNA binding Kd(DNA) revealed that when alone, mPOLγA^{A449T} bound DNA ≈ 3.4 times less than mPOLγA^{WT} [WT: Kd(DNA) = 1.7 nM ± 0.3 vs A449T: Kd(DNA) = 5.9 nM ± 0.8] (Figure 4.25 – B). We then performed similar experiments with addition of the accessory subunit POLγB, which enhances POLγ binding to DNA. Accordingly, inclusion of POLγB reduced the amount of holoenzyme (POLγA-B2) necessary to fully shift the template to ~30 fmol when using mPOLγA^{WT}, while a full shift was only seen using mPOLγA^{A449T} at concentrations of 100 fmol (Figure 4.25 – C). In addition, calculation of the dissociation constants for DNA binding Kd(DNA) showed that in the presence of POLγB, mPOLγA^{A449T} bound DNA ≈ 1.75 times less than mPOLγA^{WT} [WT+B: Kd(DNA) = 0.8 nM ± 0.1 vs A449T+B: Kd(DNA) = 1.4 nM ± 0.2] (Figure 4.25 – D). These results demonstrate that mPOLγA^{A449T} presents

lower affinity do DNA and that stimulation by POLγB improves DNA binding, but not to the same levels of mPOLγA^{WT}.

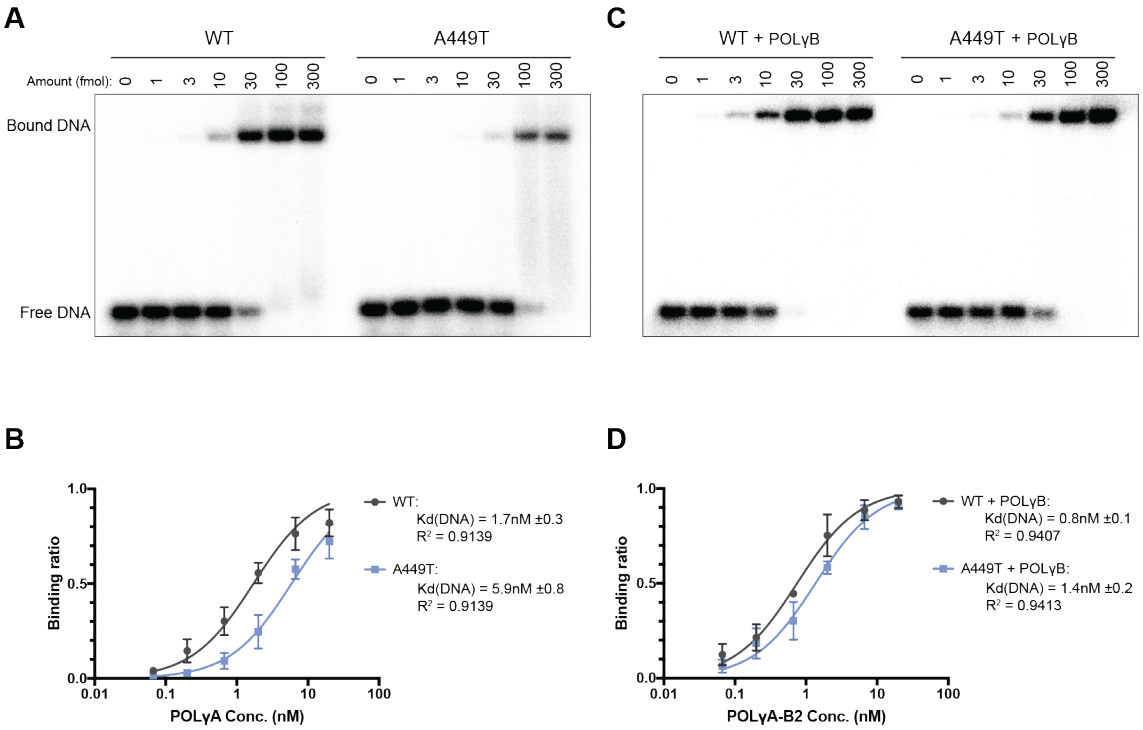

Figure 4.25. Analysis of POLγA^{A449T} binding affinity to DNA.
A. Electrophoretic mobility assays using mPOLγA^{WT} and mutant mPOLγA^{A449T} to estimate affinity to a DNA template. Each lane contains 10 fmol of DNA substrate and the indicated amounts of POLγA on the top. **B.** Binding ratio of mPOLγA^{WT} and mutant mPOLγA^{A449T} (without mPOLγB) across increasing concentrations of POLγA. Binding ratio was calculated as bound/(bound+unbound). Data are presented as mean ± SEM. (n = 3). A nonlinear regression line was calculated for WT and mutant mPOLγA^{A449T}. **C**. Electrophoretic mobility assays using mPOLγA^{WT} and mutant mPOLγA^{A449T} with addition of mPOLγB to estimate affinity to a DNA template. Each lane contains 10 fmol of DNA substrate and the indicated amounts of POLγ holoenzyme (1 mPOLγA: 2 mPOLγB) on the top. **D.** Binding ratio of mPOLγA^{WT} and mutant mPOLγA^{A449T} with addition of mPOLγB, across increasing concentrations of POLγA-B2. Binding ratio was calculated as bound/(bound+unbound). Data are presented as mean ± SEM. (n = 3). A nonlinear regression line was calculated for mPOLγA^{WT} and mPOLγA^{A449T} holoenzymes.

4.9.2. mPOLγA^{A449T} in isolation does neither present exonuclease nor polymerase activities

Next, we investigated mPOLγA activities using a short DNA template annealed to a radioactively labelled primer (coupled exonuclease-polymerase assay). By performing the experiment across a range of dNTP concentrations, we could analyse both polymerase and exonuclease function. The exonuclease activity is

favoured in the absence of dNTPs and can digest the labelled primer, whereas the polymerase activity can elongate the primer and synthesize an additional short, 15 nucleotide-stretch of DNA. As expected, at lower dNTP levels, mPOLγA^{WT} displayed 3′-5′ exonuclease activity, but at higher concentrations, it switched to polymerase activity (Figure 4.26 – A). Interestingly, the mutant mPOLγA^{A449T} was completely inactive in isolation, most likely due to its inability to efficiently bind primed DNA (Figure 4.26 – A). Addition of mPOLγB to mPOLγA^{WT} reduced exonuclease activity and favoured DNA synthesis even at lower dNTP concentrations because of the predominant polymerase activity observed *in vitro* (Figure 4.26 – B). Similarly, addition of mPOLγB restored the polymerase activities of mPOLγA^{A449T}, to levels like those observed with mPOLγA^{WT} (Figure 4.26 – B). These results indicate that mPOLγA^{A449T} is dysfunctional on its own, and effect that can be reverted by stimulation by POLγB, supporting its role in stabilizing the complex.

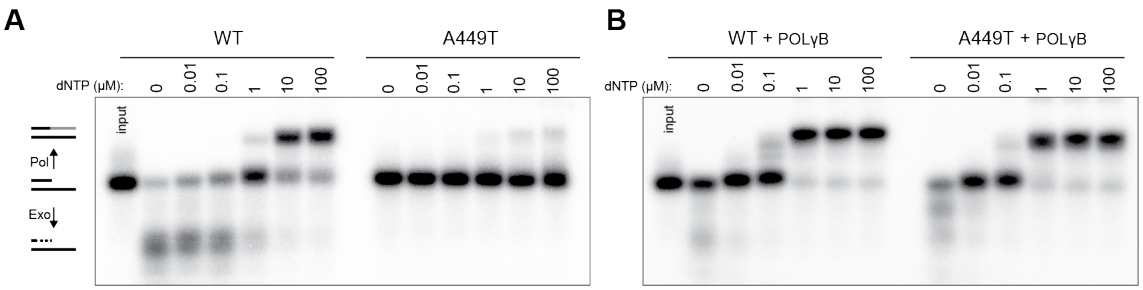

Figure 4.26. Simultaneous evaluation of exonuclease and polymerase activities of POLγA^{A449T} in short DNA templates.
A. Coupled exonuclease–polymerase assay using mPOLγA^{WT} and mutant mPOLγA^{A449T} (without mPOLγB) across increasing concentrations of dNTPs using a short DNA template. A schematic representation of the assay is presented on the left. **B.** Coupled exonuclease polymerase assay using mPOLγA^{WT} and mutant mPOLγA^{A449T} with addition of mPOLγB, across increasing concentrations of dNTPs using a short DNA template.

4.9.3. Exonuclease activity in not affected in mPOLγA^{A449T}

During the coupled exonuclease-polymerase experiments, there was an indication that exonuclease activity could be slightly affected in mPOLγA^{A449T}, revealed by an accumulation of a diffuse intermediate in the absence of dNTPs (see Figure 4.26 – B, at dNTP (μM) = 0, WT vs A449T). To further explore this possibility, we performed an *in vitro* exonuclease assay using a radiolabelled primer annealed to a circular ssDNA template and evaluated exonuclease activity of mPOLγA over time (Figure 4.27 – A). However, this assay failed to reveal major differences of exonuclease activity between mPOLγA^{A449T} and mPOLγA^{WT}, in which after 30 minutes of reaction both could digest the annealed primer (Figure 4.27 – B). Thus, mPOLγA^{A449T} does not display defects on exonuclease activity.

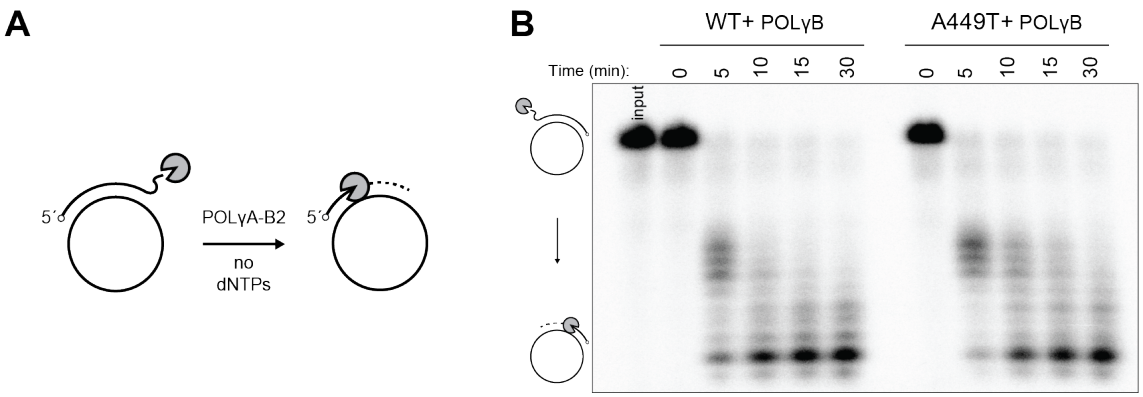

Figure 4.27. Evaluation of POLγA^{A449T} exonuclease activity in long stretches of DNA.
A. Schematic representation of the *in vitro* exonuclease assay. The template consists of a 32-bp oligonucleotide P^{32}-labelled at the 5′-end annealed to a single-strand template, creating a 31-bp dsDNA region with a 1-nucleotide mismatch at the 3′-end. Absence of dNTPs favours the exonuclease activity of the POLγA-B2 holoenzyme. **B.** Exonuclease assay using mPOLγA^{WT} and mutant mPOLγA^{A449T} to assess exonuclease activity in the absence of dNTPs. The reactions were incubated for the indicated times on top of the blot.

4.9.4. mPOLγA^{A449T} displays slower DNA synthesis rates in ssDNA templates

The mutant mPOLγA^{A449T} presented WT-like polymerase activity in the coupled exonuclease-polymerase assay. However, this assay uses a short DNA template that can be quickly filled even if DNA synthesis rates are compromised. To further challenge the system, we performed a DNA synthesis assay using a long circular ssDNA template of 3000 nt annealed with a short 5' radiolabelled primer and

evaluated polymerisation of the second strand over time (Figure 4.28 – A). In this assay, when using mPOLγA^{WT} the full circle was completed in 10 minutes, while 30 minutes were required by mPOLγA^{A449T}. Thus, mPOLγA^{A449T} clearly displayed a slower DNA synthesis rate compared to the mPOLγA^{WT}, even in the presence of the mPOLγB subunit. (Figure 4.28 – B).

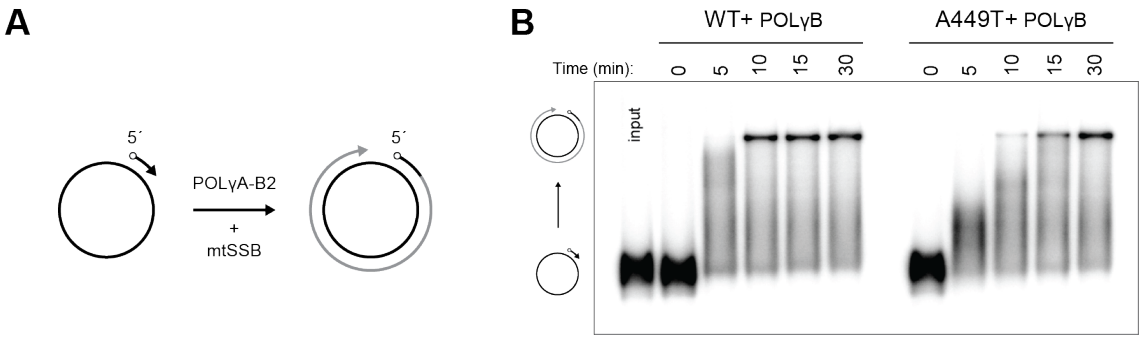

Figure 4.28. Analysis of POLγA^{A449T} polymerase activity in long single-stranded DNA templates.
A. Schematic representation of the second strand synthesis assay. This assay evaluates the ability of polymerise long stretches of DNA by synthesizing the second strand of a single-stranded template hybridized with a 5' radiolabeled primer. POLγB and mtSSB are added in the reaction. **B.** Second strand synthesis assay using mWT and mutant mPOLγA^{A449T} to assess polymerase activity using longer DNA templates. The reactions include POLγA-B2 and mtSSB and were incubated for the indicated times on top of the blot.

4.9.5. mPOLγA^{A449T} and hPOLγA^{A467T} displays slower DNA synthesis rates in dsDNA templates

Next, to monitor the effects of the A449T mutation on replication of dsDNA, we used a template containing a ~4 kb long dsDNA region with a free 3′-end acting as a primer. This rolling circle replication assay is performed in the context of the minimal *in vitro* replisome, with addition of the TWINKLE DNA helicase, required to unwind the DNA, and mtSSB to stimulate the reaction. This reaction is also dependent on POLγB and once initiated, very long stretches of DNA can be formed (Figure 4.29 – A). In this assay, when incubated for a fixed period of 60 minutes, mPOLγA^{A449T} showed reduced polymerase DNA synthesis compared to mPOLγA^{WT}, at all concentrations tested (Figure 4.29 – B), demonstrating that mPOLγA^{A449T} has reduced polymerase activity.

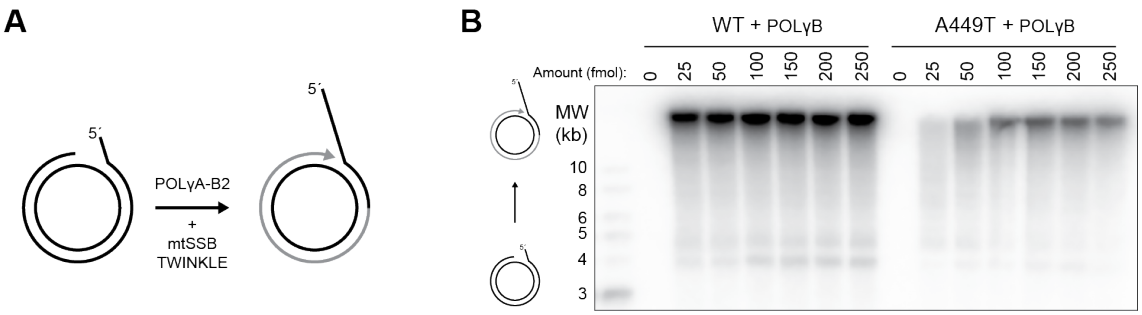

Figure 4.29. Effects of POLγA^{A449T} concentration on polymerase activity using long double-stranded DNA templates.
A. Schematic representation of the rolling circle *in vitro* replication assay. The template consists of an incomplete double stranded DNA template with a mismatch on the 5' of the incomplete strand. In the presence of TWINKLE and mtSSB, POLγA-B2 can polymerase long stretches of DNA using the 3'-end of the incomplete strand. **B.** Rolling circle in vitro replication assay using mPOLγA^{WT} and mutant mPOLγA^{A449T} to assess polymerase activity, across the indicated concentrations of POLγA-B2, in the context of the minimal mitochondrial replisome (POLγA-B2, TWINKLE and mtSSB). The reactions were incubated for 60min.

Using the same assay, synthesis rate of DNA was also evaluated over time with a fixed amount of POLγA, confirming that mPOLγA^{A449T} displays reduced polymerase DNA synthesis compared to mPOLγA^{WT} (Figure 4.30 – A). A similar effect was obtained with the hPOLγA^{A467T} (Figure 4.30 – B). Detailed analysis of incorporated radiolabelled nucleotides over time indicated that the *in vitro* replication rates with 10 μM dNTPs, were reduced to about 60% for mPOLγA^{A449T} compared to mPOLγA^{WT} (3.5 fmol/min versus 5.5 fmol/min) (Figure 4.30 – C and D). Interestingly, the reduction was more pronounced with hPOLγ^{AA467T} compared to hPOLγA^{WT} (1.4 versus 5.3 fmol/min), than for the mouse equivalents, which could explain the more severe phenotype observed in patients (Figure 4.30 – C and D). Together these data demonstrate that both mPOLγA^{A449T} and hPOLγ^{AA467T} display reduced polymerase activity in dsDNA templates in the context of the *in vitro* minimal replisome.

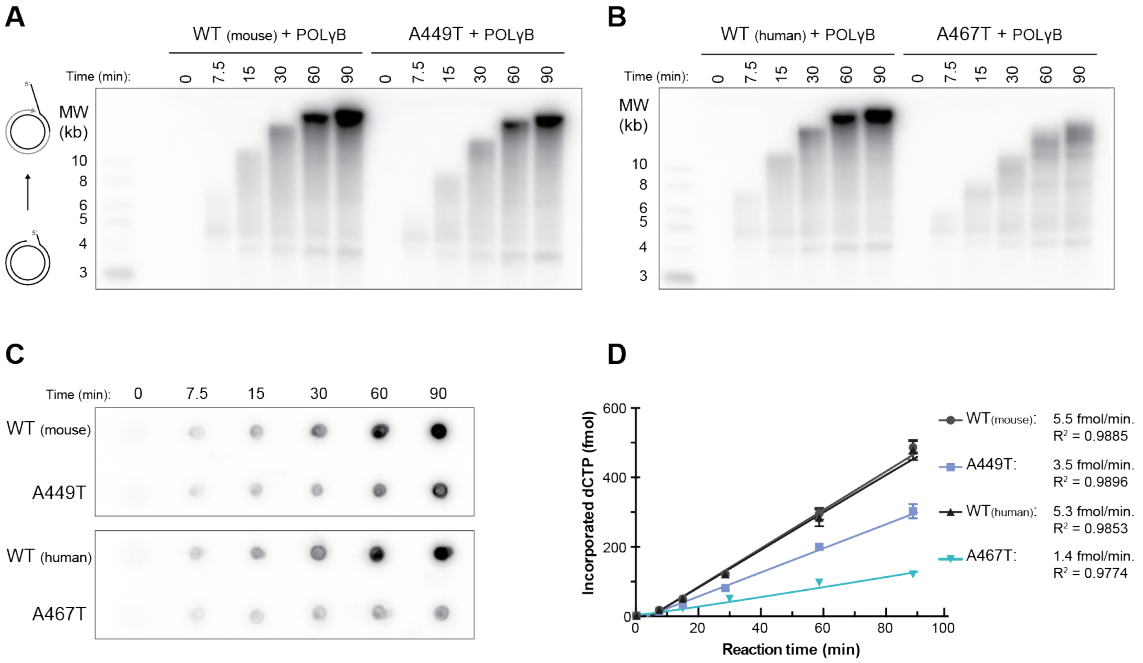

Figure 4.30. Analysis of POLγA^{A449T} polymerisation rates in double-stranded DNA templates.

A. Rolling circle *in vitro* replication assay using mPOLγA^{WT} and mutant mPOLγA^{A449T} to assess polymerase activity in the context of the minimal mitochondrial replisome, which includes POLγ holoenzyme WT or mutant, TWINKLE and mtSSB. The reactions were incubated for the indicated times (top). **B.** Rolling circle *in vitro* replication assay using human versions of hPOLγA^{WT} and mutant hPOLγA^{A467T} to assess polymerase activity in the context of the minimal mitochondrial replisome (POLγ holoenzyme WT or mutant, TWINKLE and mtSSB). The reactions were incubated for the indicated times (top). **C.** Rolling circle in vitro replication assay (aliquots from panel A and B) represented as a dot blot to compare mouse and human polymerase activities of mutant mPOLγA^{A449T} and hPOLγA^{A467T}. Mouse versions of POLγA were used in the upper panel. Human versions of POLγA were used in the lower panel. The reactions were incubated for the indicated times (top). **D.** In vitro replication efficiency of mutant mouse and human POLγA, measured as incorporation of [α32 P]-dCTP over a time course during a rolling circle assay. Data are presented as mean ± SEM. (n = 3). A linear regression line was calculated for each POLγA version.

4.10. Effects of the *Polg* A449T mutation in POLγA stability

4.10.1. POLγA protein levels are reduced in tissues of *Polg*$^{A449T/A449T}$ mice

During characterization of *Polg*$^{A449T/A449T}$ mice, we assessed the effects of the A449T mutation on POLγA and POLγB protein levels. Notably, immunoblotting revealed a strong reduction of POLγA^{A449T} amount, as low as 50%, in all tissues examined, including liver, skeletal muscle, brain, kidney and heart (Figure 4.31 – A and B). In contrast, POLγB levels were unchanged in most tissues, although a mild upregulation and downregulation in brain and heart, respectively, was observed (Figure 4.31 – A and C).

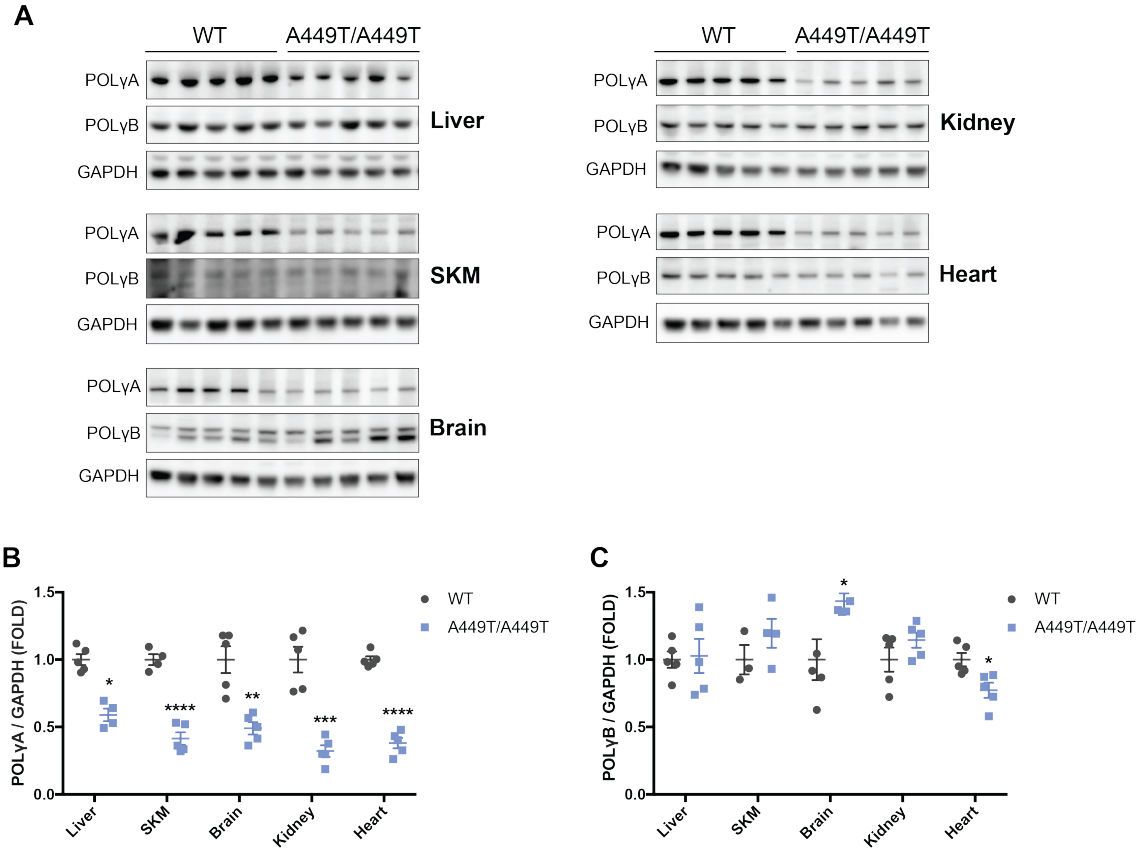

Figure 4.31. Analysis of POLγA and POLγB protein levels in tissues of *Polg*$^{A449T/A449T}$ mice
A. Western blot analysis of steady-state levels of POLγA and POLγB in liver, skeletal muscle, kidney, brain and heart of WT and *Polg*$^{A449T/A449T}$ animals. The lower band in the brain is unspecific. GAPDH was used as loading control. Each lane represents a biological replicate. **B** and **C**. Quantification of blots presented in (A): POLγA (**B**) and POLγB (**C**) levels were normalized to GAPDH and presented as FOLD change from WT animals. Data are presented as mean ± SEM. Two tailed unpaired Student's *t*-test: **P* < 0.05; ***P* < 0.01; ****P* < 0.001; *****P* < 0.0001. Each symbol represents a biological replicate.

To understand if the observed decrease of POLγA levels could be due to reduced transcription, *Polg* (POLγA) and *Polg2* (POLγB) mRNA levels were evaluated. However, both transcripts were similar to those of control littermates in both liver and skeletal muscle of *Polg*$^{A449T/A449T}$ mice (Figure 4.32), indicating that the decrease of POLγA levels was not related to defects at the transcriptional level.

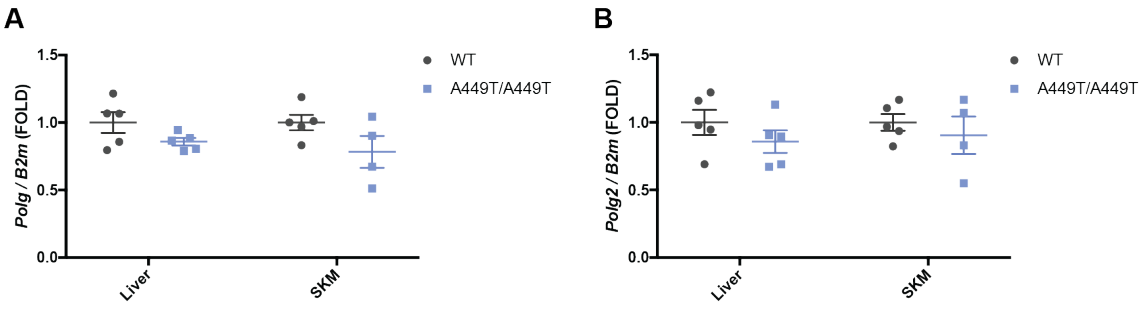

Figure 4.32. Evaluation of *Polg* and *Polg2* mRNA levels in tissues of *Polg*$^{A449T/A449T}$ mice
A and **B**. Real-time qRT-PCR quantification of the transcripts *Polg* (**A**) and *Polg2* (**B**), normalized to *B2m*, in liver and skeletal muscle of WT and *Polg*$^{A449T/A449T}$ animals. Data are presented as mean ± SEM. Two tailed unpaired Student's *t*-test: non-significant. Each symbol represents a biological replicate.

4.10.2. mPOLγA^{A449T} is unstable in absence of POLγB *in vitro*

We then decided to use *in vitro* purified proteins to better understand the impact of the A449T mutation on protein stability. Thus, we performed a thermofluor stability assay and monitored temperature-induced unfolding of mPOLγA^{WT} and mPOLγA^{A449T}, both in the absence and in the presence of mPOLγB (Figure 4.33). The stability assay revealed no major differences in the fluorescence profile between mPOLγA^{WT} and mPOLγA^{A449T} from 37 °C upwards, but the fluorescence signal of mPOLγA^{A449T} was already higher than the mPOLγA^{WT} at 25 °C, clearly indicating that the mutant protein was already partially unfolded even at <37 °C temperatures (Figure 4.33). Interestingly, the presence of the mPOLγB had a dramatic stabilizing effect, by increasing the unfolding temperature of about 10 °C for both proteins (Figure 4.33). These data suggest that mPOLγA^{WT} is also partially unstable in the absence of POLγB.

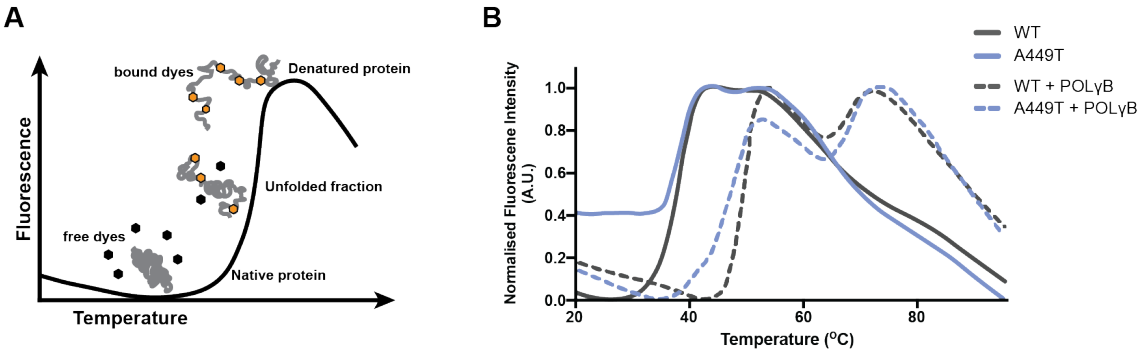

Figure 4.33. Evaluation of POLγA^{A449T} stability *in vitro*.
A. Schematic representation of a typical thermofluor stability assay. This assay uses a fluorescent dye, SYPRO Orange, to monitor the temperature-induced unfolding of proteins. When the temperature starts to rise and unfold the protein, the SYPRO Orange dye fluoresces by binding to exposed hydrophobic patches. **B**. Thermofluor stability assay to evaluate thermostability of mPOLγA^{WT} (black) and mPOLγA^{A449T} (blue), in absence (solid line) or presence (dashed line) of mPOLγB.

4.10.3. mPOLγA^{A449T} presents loss of interaction with POLγB

Previous *in vitro* studies have shown that hPOLγA^{A467T} compromises interaction with POLγB (Chan et al., 2005). We hypothesized that the A449T mutation could impair interactions with mPOLγB and thus be the underlying cause of mPOLγA^{A449T} instability. The A449 (mouse)/A467 (human) residue is in the thumb helix that forms contacts with POLγB. The mutation disrupts the local hydrophobic environment formed by L466 and L602. Consequently, there is a slight spatial shift of the thumb domain, which could potentially disturb binding to POLγB (Figure 4.34) (Lee et al., 2009). To address this possibility, we investigated mPOLγA^{A449T} interactions with mPOLγB by performing size-exclusion chromatography. At 1:1 molar ratio of mPOLγA and mPOLγB (calculated as a dimer), mPOLγ^{WT} and mPOLγB migrated as a single peak, corresponding to a stable complex between the two proteins (Figure 4.35 - A), as confirmed by SDS-PAGE (Figure 4.35 – B). In contrast, mPOLγA^{A449T} and mPOLγB showed an additional peak, corresponding to unbound mPOLγB (Figure 4.35 – A and C). The resolution of the chromatography cannot separate free POLγA from the POLγ holoenzyme. These results suggest that the A449T mutation significantly reduces the interaction between POLγA and POLγB subunits. Loss interaction with POLγB could possibly leave mPOLγA^{A449T} as a free, partially unfolded protein that can be targeted to degradation.

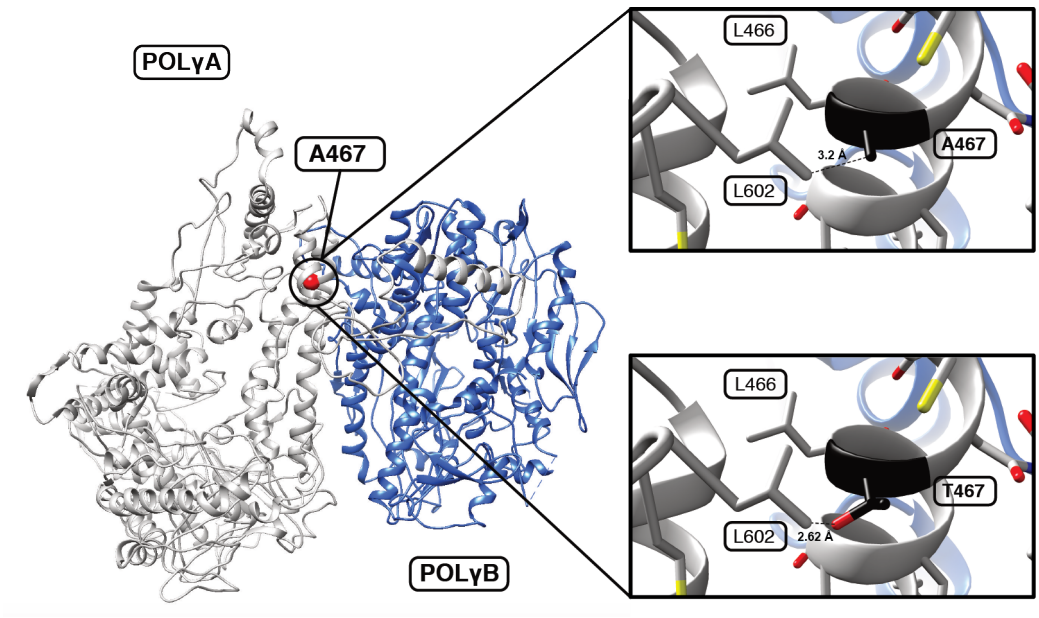

Figure 4.34. Scructural interactions of human POLγA and POLγB.
Overview of the human POLγ holoenzyme structure (PDB code: 3IKM) showing the POLγA A467 residue in an alpha-helix in the thumb domain and the changes occurring in the local environment when mutated to T467 (highlighting residues L466 and L602). Grey - hPOLγA; Blue - hPOLγB dimer

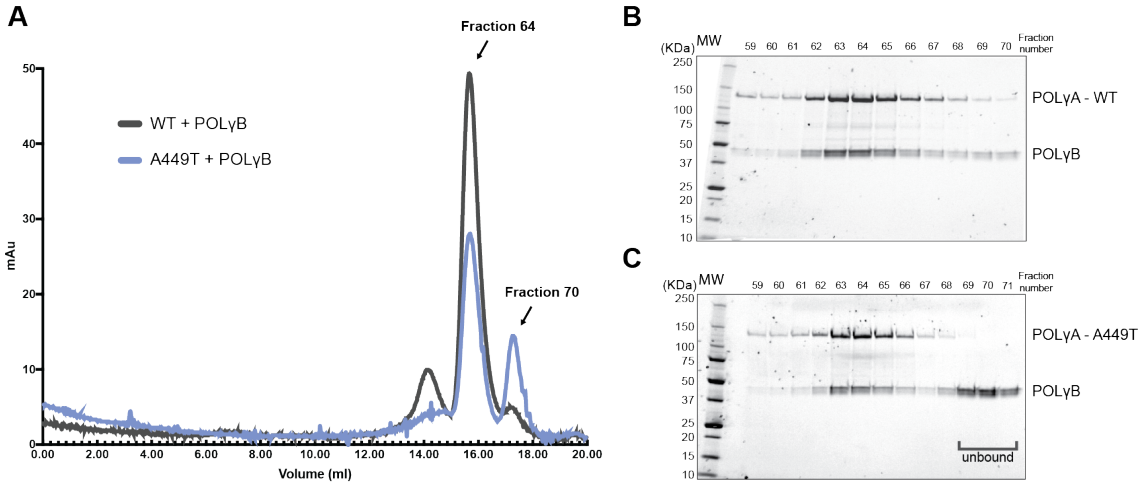

Figure 4.35. *In vitro* interaction between mPOLγA^{A449T} and POLγB.
A. Size-exclusion chromatogram of mPOLγA^{WT} (black line) and mPOLγA^{A449T} (blue line) in presence of mPOLγB, to evaluate interaction between POLγA and POLγB. **B.** SDS-PAGE of the selected peak fractions from (A) of mPOLγA^{WT} and mPOLγB. **C.** SDS-PAGE of the selected peak fractions from (A) of mPOLγA^{A449T} and mPOLγB. Note the brackets highlighting unbound POLγB (free from POLγA^{A449T}).

4.10.4. LONP1 knockdown leads to increased POLγA levels in cells and *in vivo*

Degradation of misfolded proteins is carried by proteases. In the mitochondrial matrix (where POLγA is present), a particularly relevant role is carried out by LONP1 protease that degrades misfolded proteins and has previously been linked to regulation of mtDNA copy number (see introductory section 2.6).

During fruitful conversations with colleagues from Trifunovic´s lab, we observed that mice harbouring a heart-specific knockout of LONP1 displayed increased levels of POLγA compared with control littermates (Figure 4.36), suggesting that POLγA could be a LONP1 target. Therefore, we decided to investigate if POLγA was a target for LONP1.

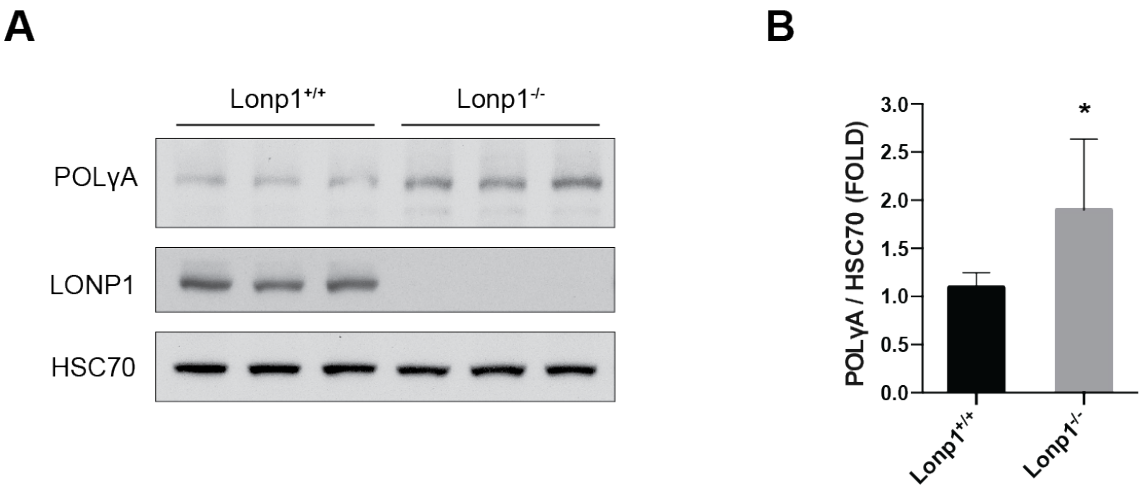

Figure 4.36. Evaluation of POLγA protein levels in *Lonp1*$^{-/-}$ *mice.*
A. Western blot analysis of steady-state levels of POLγA in heart of *Lonp1*$^{+/+}$ and *Lonp1*$^{-/-}$ animals. An anti-LONP1 antibody was used to confirm gene knockout and HSC70 was used as loading control. This blot was produced by Dieu-Hien Rozsivalova from Trifunovic´s Lab. **B.** Quantification of POLγA levels in heart of *Lonp1*$^{+/+}$ and *Lonp1*$^{-/-}$ animals (A). POLγA levels were normalized to HSC70 and presented as fold change from *Lonp1*$^{+/+}$. Data are presented as mean ± SEM. Two tailed unpaired Student's *t*-test: $^{*}P < 0.05$. ($n = 6$).

We first used siRNA interference against LONP1, POLγA and POLγB in WT and *Polg*$^{A449T/A449T}$ MEFs. However, despite several efforts, delivery of siRNAs either by liposomes or by electroporation was proven difficult in primary MEFs (data not shown). Therefore, we decided to perform these experiments using easy to transfect human HeLa cells. Interestingly, LONP1 knockdown caused a robust increase in POLγA levels (Figure 4.37 – A and B), whereas POLγB was unaffected (Figure 4.37 – A), supporting the idea that POLγA, but not POLγB, is a specific target for LONP1 degradation. In turn, knockdown of POLγB caused a reduction of POLγA levels (Figure 4.37 – A and C), further supporting stabilizing effect of POLγB over POLγA. In addition, both POLγB and POLγA knockdown resulted in an increase of LONP1 (Figure 4.37 – A). Collectively, these results suggest that LONP1 targets POLγA both in cells and *in vivo*.

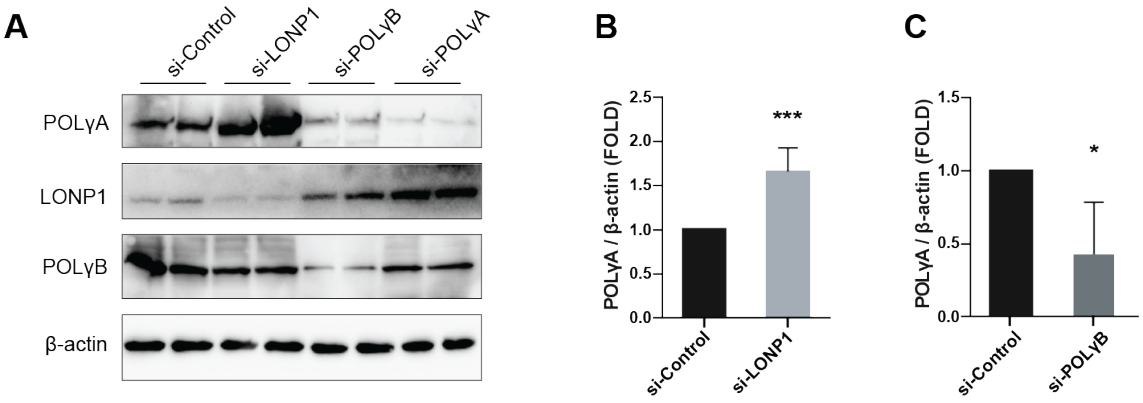

Figure 4.37. Evaluation of POLγA protein levels upon siRNA-mediated knockdown of LONP1 and POLγB *in human cells.*
A. Western blot analysis of steady-state levels of POLγA, LONP1 and POLγB upon siRNA-mediated knockdown of LONP1, POLγB and POLγA, in HeLa cells. ß-actin was used as loading control. **B.** Quantification of POLγA levels upon siRNA-mediated knockdown of LONP1 (A). POLγA levels were normalized to ß-actin and presented as FOLD change from cells treated with control siRNA. Data are presented as mean ± SEM. Two tailed unpaired Student's *t*-test: ***$P < 0.001$. ($n = 3$). **C.** Quantification of POLγA levels upon siRNA-mediated knockdown of POLγB (A). POLγA levels were normalized to ß-actin and presented as fold change from cells treated with control siRNA. Data are presented as mean ± SEM. Two tailed unpaired Student's *t*-test: *$P < 0.05$. ($n = 3$).

4.10.5. POLγA interacts with LONP1 *in vitro*

To investigate if POLγA is a direct target for LONP1 degradation, we performed a size-exclusion chromatography with recombinant proteins to assess if POLγA can form a complex with LONP1. Proteolytic degradation by LONP1 is a rapid event. Thus, to ensure that POLγA was not degraded by LONP1 during the experiment, we used the mutant LONP1^{S855A}, which traps substrates without degrading them (Kereiche et al., 2016). Notably, we observed a co-elution of LONP1^{S855A} and hPOLγA (Figure 4.38), revealing an interaction between these two proteins and providing further evidence for POLγA as a target for LONP1.

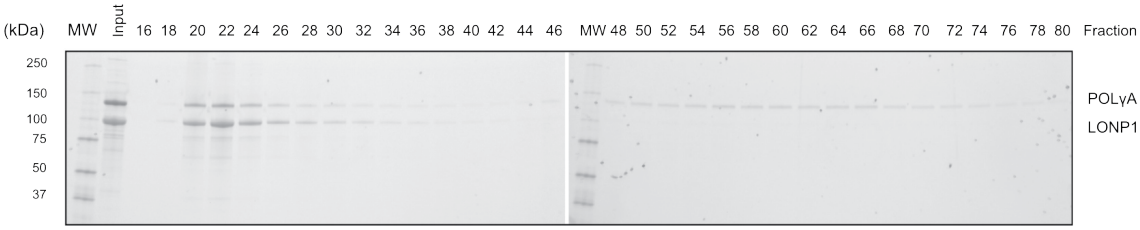

Figure 4.38. *In vitro* interaction of POLγA and LONP1.
Size-exclusion chromatography of the complex formed by human LONP1^{S855A} (catalytic dead mutant) and hPOLγA^{WT}. The mixture was incubated for 10 min, at 37°C, in the presence of 10 mM MgCl2 and 2 mM ATP before being loaded on the chromatography. Note the co-elution of POLγA and LONP1 in fractions 20-24.

4.10.6. POLγA but not POLγB is degraded by LONP1

Next, we determined whether LONP1 could degrade the WT version of mPOLγA and mPOLγB *in vitro*. To this end, we mixed LONP1 with either mPOLγA^{WT} alone, mPOLγB alone or mPOLγA^{WT} complexed with mPOLγB and followed the reactions over time. Individual mPOLγB was not degraded by LONP1, confirming that the accessory subunit is not a substrate of the protease (Figure 3.39 – A, lanes 6 to 10). In contrast, mPOLγA^{WT} alone was degraded progressively in the presence of LONP1, with 50% being degraded after 20 minutes (Figure 3.39 – A, lanes 1 to 5), supporting POLγA as a specific target for LONP1. Importantly, LONP1 is an ATP-dependent enzyme, and no degradation of POLγA was therefore observed in the absence of ATP, confirming the degradation LONP1-mediated and not due to other external causes (Figure 3.39 - A, lanes 1, 6 and 11).

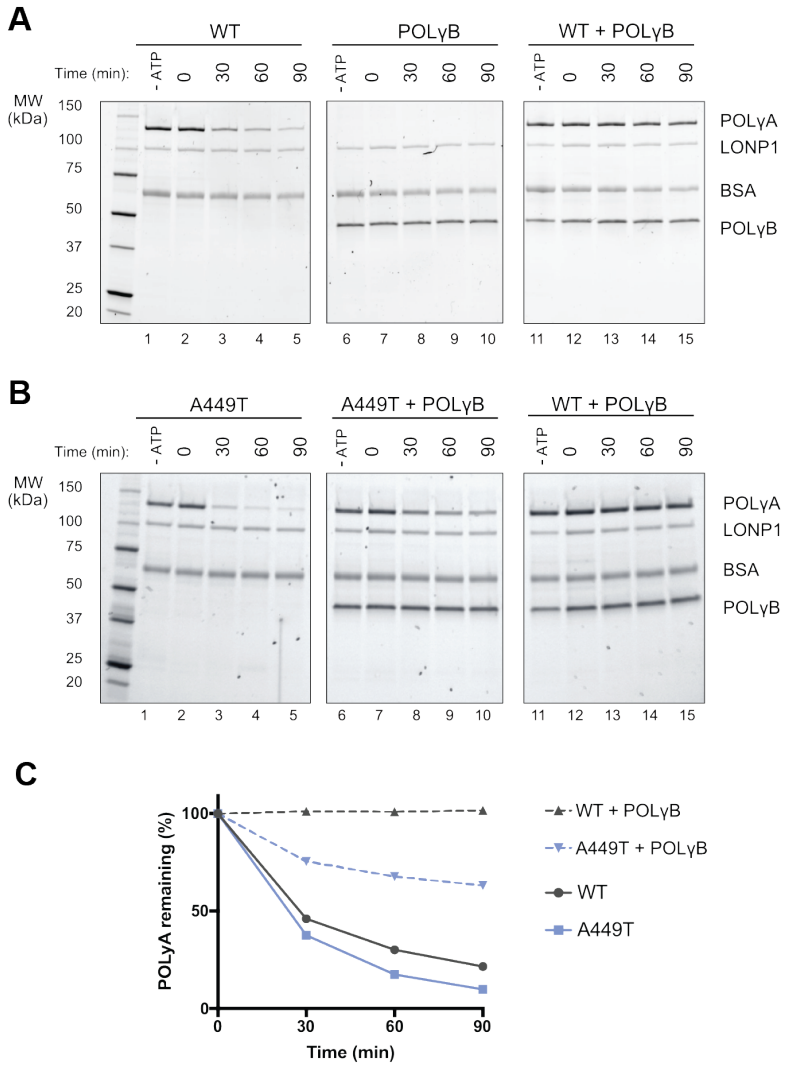

Figure 4.39. *In vitro* degradation of mouse POLγA^{A449T} by LONP1.
A. SDS-PAGE of the LONP1 proteolysis assay of isolated mPOLγA^{WT} (left), mPOLγB (middle), and mPOLγA^{WT} complexed with mPOLγB, over time. The reactions were incubated for the indicated times (top). In the absence of ATP (-ATP control), LONP1 does not exert proteolysis. **B.** SDS-PAGE of the LONP1 proteolysis assay of mPOLγA^{A449T} in absence (left) or presence (middle) of mPOLγB, over time. Reactions with mPOLγA^{WT} + mPOLγB (right) were added for reference. The reactions were incubated for the indicated times (top). In the absence of ATP (-ATP control), LONP1 does not exert proteolysis. **C.** Quantification of POLγA degradation over time (0–90 min) by LONP1, related to (A and B). mPOLγA^{WT} (black) and mPOLγA^{A449T} (blue), in absence (solid line) or presence (dashed line) of POLγB. Data are presented as mean ± SD. (n = 3). These set of assays were performed in collaboration with Carlos Pardo-Hernandez from Falkenberg´s lab.

4.10.7. POLγB protects POLγA against LONP1 degradation

We then examined POLγA in complex with POLγB. Interestingly, the presence of mPOLγB completely blocked mPOLγA^{WT} degradation, with 100% of mPOLγA^{WT} left after 90 minutes (Figure 3.39 – A, lanes 11 to 15). This data suggests that POLγB exerts a protective role over POLγA from LONP1 degradation.

4.10.8. Loss of interaction with mPOLγB predisposes mPOLγA^{A449T} and hPOLγA^{A467T} for LONP1 degradation

In previous sections, we showed that mPOLγA^{A449T} presents a weaker interaction with mPOLγB and that mPOLγA^{A449T} alone is partially unfolded. In addition, mPOLγB protected mPOLγA^{WT} against LONP1 degradation. We thus investigated whether mPOLγB could also protect mPOLγA^{A449T} and whether loss of interaction between the two could influence LONP1 proteolytic activity over mPOLγA^{A449T}.

The mutant POLγA^{A449T} alone was degraded over time by LONP1, with values similar to POLγA^{WT}, although the mutant protein was degraded slightly faster (A449T: 10% vs WT: 21% left after 90 minutes) (Figure 3.39 – B, lanes 1 to 5 and C). In turn, mPOLγB was unable to efficiently block degradation of mPOLγA^{A449T}, with only 63% left after 90 minutes (Figure 3.39 – B, lanes 6 to 10 and C), with remarkable contrast with POLγA^{WT}, that presents 100% of the initial input after the same incubation period (Figure 3.39 – A, lanes 11 to 15 and C).

To further validate our findings, we extended our analysis to the human WT and A467T mutant versions of POLγA. Similar to the results obtained with mouse proteins, both isolated hPOLγA^{WT} and hPOLγA^{A467T} were efficiently degraded, with a 60% reduction in about 30 min (Figure 3.40 – A and B, lanes 1 to 5, and C). The presence of hPOLγB also completely blocked hPOLγA^{WT} degradation by LONP1. (Figure 3.40 – A, lanes 6 to 10, and C). In addition, as expected hPOLγB was unable to efficiently block degradation of hPOLγA^{A467T} and the levels of the mutant protein decreased significantly over the time of the experiment (Figure 3.40 – B, lanes 6 to 10, and C).

These results indicate that the impaired interaction between POLγB and mutants mPOLγA^{A449T} and hPOLγA^{A467T} leads to increased LONP1-dependent degradation of POLγA. This observation could explain the lower levels of POLγA observed in the tissues of *Polg*$^{A449T/A449T}$ mice.

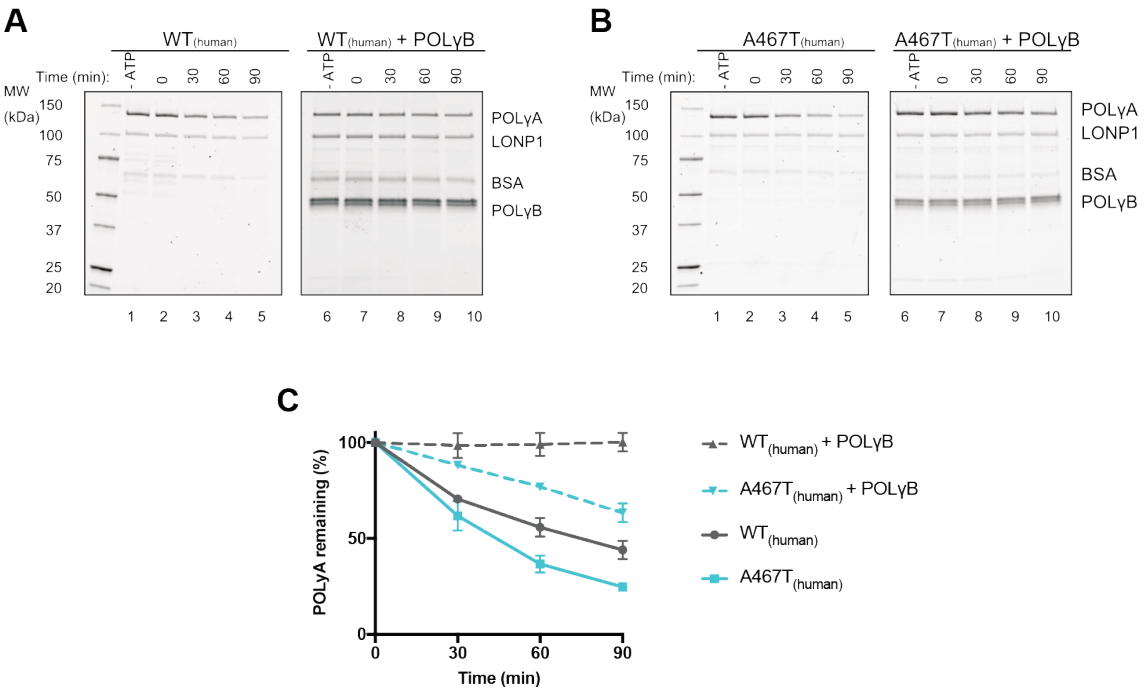

Figure 4.40. *In vitro* degradation of human POLγA^{A467T} by LONP1.
A. SDS-PAGE of the LONP1 proteolysis assay of hPOLγA^{WT} in absence (left) or presence (right) of hPOLγB, over time. The reactions were incubated for the indicated times (top). In the absence of ATP (-ATP control), LONP1 does not exert proteolysis. **B.** SDS-PAGE of the LONP1 proteolysis assay of hPOLγA^{A467T} in absence (left) or presence (right) of hPOLγB, over time. The reactions were incubated for the indicated times (top). In the absence of ATP (-ATP control), LONP1 does not exert proteolysis. **C.** Quantification of human POLγA degradation over time (0–90 min) by LONP1, related to (A and B). hPOLγA^{WT} (gray) and hPOLγA^{A467T} (blue), in absence (solid line) or presence (dashed line) of POLγB. Data are presented as mean ± SD. (n = 3). These set of assays were performed in collaboration with Carlos Pardo-Hernandez from Falkenberg´s lab.

4.10.9. mPOLγB is present in excess relative to mPOLγA in mouse tissues

Finally, our *in vitro* results implied that the POLγB dimer must be present in at least stoichiometric amounts *in vivo* to prevent POLγA degradation. To determine the *in vivo* ratio of the two proteins, we performed quantitative immunoblotting using antibodies against the POLγA and POLγB in various mouse tissues (liver, skeletal muscle, brain, kidney and heart). Protein levels were determined by comparison with known amounts of recombinant POLγA and POLγB. As predicted, the levels of the POLγB dimer were higher than POLγA in all tissue types investigated. The ratio varied between 4:1 and 15:1 of the POLγB dimer relative POLγA (Figure 4.41). Overall, these data provide evidence that POLγB stabilises and protects POLγA from degradation. In turn, disrupted interaction between the two proteins triggered by the Polγ A449T mutation biases the mutant mPOLγA^{A449T} for degradation, which can have pathophysiologic consequences.

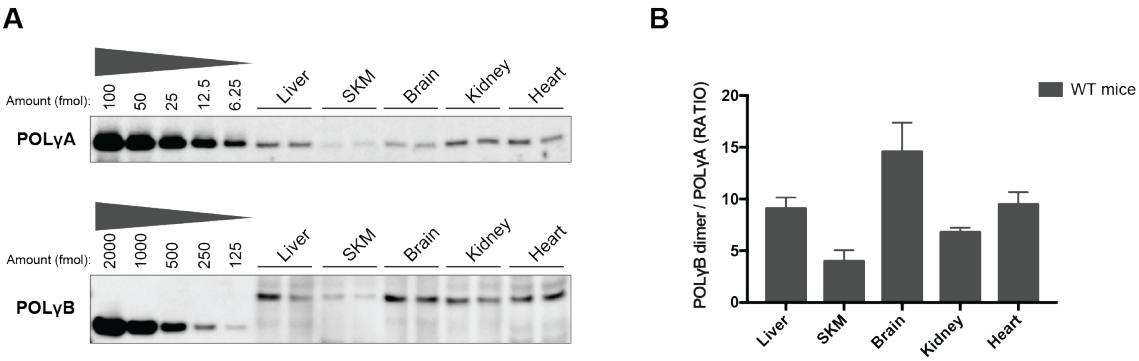

Figure 4.41. Analysis of molecular ratios of POLγA and POLγB in tissues of *Polg*$^{A449T/A449T}$ mice

A. Western blot analysis of endogenous POLγA and POLγB proteins in liver, skeletal muscle (SKM), brain, kidney and heart of WT mice. Each lane was loaded with 10 µg of crude mitochondria protein extracts from the indicated tissue from an individual mouse. Purified recombinant POLγA and POLγB were used to create a standard curve with known protein concentrations (as indicated in the figure). SKM - skeletal muscle. **B.** Ratio between POLγB (calculated as a dimer) and POLγA in liver, skeletal muscle (SKM), brain, kidney and heart of WT mice based on quantifications obtained from (B). Data are presented as mean ± SEM. (n = 3).

4.11. Summary of the main findings

- The clinical phenotype of *Polg*$^{A449T/A449T}$ mice is characterized by a mild lethargy quantified by a decrease of spontaneous motility and mild exercise intolerance in the treadmill.
- *Polg*$^{A449T/A449T}$ mice present a mild depletion of mtDNA in skeletal muscle, but no mtDNA deletions were found in any of the analysed tissues.
- *Polg*$^{A449T/A449T}$ mice display impaired liver regeneration after drug-induced liver damage with Carbon Tetrachloride.
- MEFs isolated from *Polg*$^{A449T/A449T}$ embryos present abnormal mtDNA replication characterised by inability to restore mtDNA copy number after EtBr-mediated depletion and an increase number of replicating mtDNA foci in basal conditions, despite normal mtDNA levels.
- *Polg*$^{A449T/A449T}$ and *Polg*$^{A449T//KO}$ tissues present unusual mtDNA replication, characterised by reduction of 7S DNA levels in several tissues and accumulation of mtDNA replication intermediates, despite normal mtDNA *in organello* replication rates.

- *In vitro*, purified mutant mPOLγA^{A449T} displays less affinity to DNA templates absence and in presence of mPOLγB.
- mPOLγA^{A449T} is virtually inert without mPOLγB.
- mPOLγA^{A449T} displays decreases polymerase activity rates in ssDNA and dsDNA. The same was also observed using hPOLγA^{A467T}.

- *Polg*$^{A449T/A449T}$ tissues present a marked decrease in POLγA steady-state levels, while POLγB levels remains the same.
- The A449T mutation affects negatively the interaction between mPOLγA^{A449T} and mPOLγB.
- *In vitro*, the loss of interaction between mPOLγA^{A449T} and mPOLγB predisposes mPOLγA^{A449T} for LONP1-mediated degradation. These findings were also replicated using hPOLγA^{A467T}.

Chapter 5 Results

AAV-mediated gene delivery as therapeutic option for Mitochondrial diseases

5. AAV-mediated gene delivery as therapeutic option for Mitochondrial diseases

5.1. Introduction

Currently, no curative therapies for mitochondrial disorders are available. Of many trial treatments, gene replacement therapy has been proposed as a therapeutic option for mitochondrial patients, particularly due to the encouraging advances of this field in the treatment of other non-mitochondrial disorders (Garone and Viscomi, 2018, Wang et al., 2019). Adeno-associated viral vectors (AAVs) are currently the leading platform for *in vivo* delivery of gene therapies, providing efficient transduction in several tissues (Naso et al., 2017). Nevertheless, gene delivery to the central nervous system (CNS), is still very challenging mainly because of the presence of the blood-brain barrier (BBB). This presents a limitation for several mitochondrial diseases, including many of those *POLG*-related, which have a strong neurological involvement, highlighting an important unmet medical need. Recently, an engineered AAV-PHP.B has demonstrated a remarkable capacity to cross the BBB when intravenously injected in adult C57BL/6 mice, leading to widespread CNS transduction and targeting both neurons and glial cells (Deverman et al., 2016).

Our initial plan was to study the therapeutic potential of AAV-PHP.B-mediated gene replacement in the brain of *Polg*$^{A449T/A449T}$ mice, given the strong neurological phenotypes presented by human patients homozygous for this mutation. However, *Polg*$^{A449T/A449T}$ mice presented a limited brain phenotype (see chapter 4), constraining their use to study AAV-PHP.B as therapeutic option for neurological symptoms. Therefore, we made use of another model available in the lab, the *Ndufs4*$^{-/-}$ mouse.

The *Ndufs4*$^{-/-}$ mouse presents a knockout of the mitochondrial NADH dehydrogenase ubiquinone iron-sulphur protein 4 (Ndufs4), which encodes an 18 kDA subunit of the ETC complex I (CI). Absence of NDUFS4 in mice results in failure of proper CI assembly which leads to undetectable levels of CI activity by spectrophotometric assays (Kruse et al., 2008). Phenotypically, *Ndufs4*$^{-/-}$ mice seem healthy until 5 weeks of age, however quickly degenerate, progressing to

death around 7 weeks of age. Some of *Ndufs4*$^{-/-}$ mice clinical signs include retarded growth rate and loss of motor skills (Kruse et al., 2008). In addition, histological analysis of the brain revealed progressive neuronal degeneration and gliosis in specific areas of the brain, including early involvement of the olfactory bulb and vestibular nuclei (Quintana et al., 2010). Importantly, inactivation of *Ndufs4* selectively in neurons and glia (by crossing with a *Nestin*-Cre mouse) reproduces all the clinical, histological and molecular findings of the full body knockout, confirming that the *Ndufs4*$^{-/-}$ phenotype results mainly from neurological complications (Quintana et al., 2010). Thus, the *Ndufs4*$^{-/-}$ mouse presents itself as an ideal model to evaluate the therapeutic potential of AAV-PHP.B-mediated gene replacement in the brain.

In this chapter, I describe the therapeutic outcomes of a single-dose systemic injection of AAV-PHP.B encoding the human *NDUFS4*, in adult and newborn *Ndufs4*$^{-/-}$ mice.

5.2. Evaluation of the therapeutic outcomes of gene rescue in adult *Ndufs4*$^{-/-}$ mice using AAV-PHP.B

To investigate the therapeutic effects of AAV-mediated gene therapy in the brain, the human wild-type *NDUFS4* cDNA (h*NDUFS4*) was cloned into a suitable single-stranded AAV2-based viral vector under the control of the strong, general promoter of the cytomegalovirus (CMV). This construct was then used to produce viral particles with the PHP.B capsid generating the final AAV-PHP.B-h*NDUFS4*.

A single dose of AAV-PHP.B-h*NDUFS4* was systemically injected via tail vein into two cohorts of *Ndufs4*$^{-/-}$ mice between postnatal day 26 (P26) and P28 with 1-2 × 10^{12} viral genomes (vg). Two months after the injection, mice from one cohort (n = 7) were sacrificed for histopathological characterization and molecular analyses, including quantification of viral genomes, hNDUFS4 expression and CI activity and assembly. The remaining (n = 22) were kept alive for phenotypic characterization and to construct a survival curve.

5.2.1. AAV-PHP.B-h*NDUFS4* rescues body weight loss

Until up to 26-28 days of age, *Ndufs4*$^{-/-}$ mice hardly presented any neurological symptom. However, at the injection day *Ndufs4*$^{-/-}$ mice were slightly but notably smaller than the WT littermates (Figure 5.1). Ten days after injection of AAV-PHP.B-h*NDUFS4*, treated *Ndufs4*$^{-/-}$ started to gain weight and became virtually indistinguishable from the WT controls (Figure 5.1). In turn, the untreated *Ndufs4*$^{-/-}$ littermates started to lose weight and eventually died between 45 and 60 days after birth. These results show that AAV-PHP.B-h*NDUFS4* can revert the progression of weight loss commonly seen in *Ndufs4*$^{-/-}$ mice.

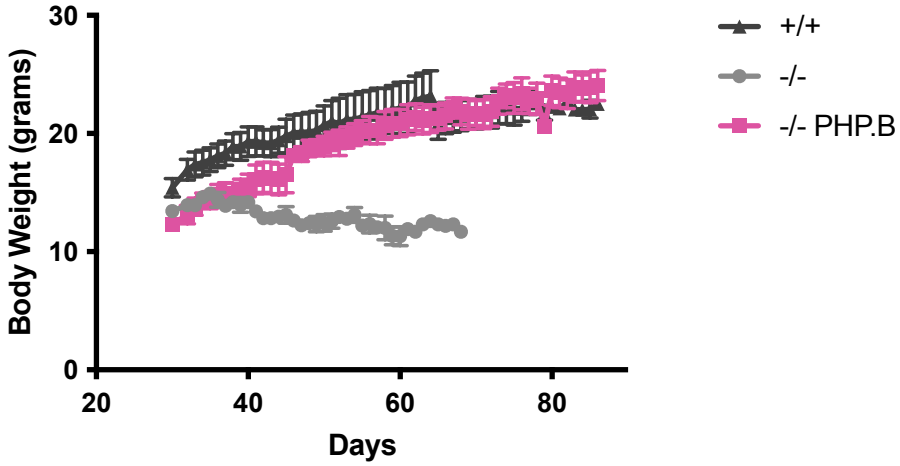

Figure 5.1 Analysis of body weight upon AAV-PHP.B-h*NDUFS4* treatment in *Ndufs4*$^{-/-}$ mice. Body weights measured from P26-28 until 90 days of age of WT (+/+), untreated (-/-) and AAV-treated (-/- PHP.B) *Ndufs4*$^{-/-}$ mice. Note the recovery up to normal levels of treated *Ndufs4*$^{-/-}$ mice about 10 days after the injection.

5.2.2. AAV-PHP.B-h*NDUFS4* improves rotarod performance

Between 5 and 7 weeks of age, *Ndufs4*$^{-/-}$ mice quickly degenerated and developed several neurological symptoms, which included loss of motor skill. To assess the effects of treatment AAV-PHP.B-h*NDUFS4* on motor coordination, mice were submitted to a standard accelerating rotarod test. At seven weeks of age, untreated mice could barely stand on the rotating bar, confirming degenerated motor skill. In turn, AAV-treated *Ndufs4*$^{-/-}$ mice could stay on the bar and perform for up to

150 s, indicating a marked improvement on their motor coordination compared to untreated animals (Figure 5.2). Although, treated mice still performed significantly worse than the WT animals (220 ± 15 s, $p < 0.01$) the difference with untreated affected littermates was highly significant ($p < 0.0001$). The benefits of AAV-PHP.B-h*NDUFS4* treatment were further supported by a similar performance by treated *Ndufs4*$^{-/-}$ mice at 12 weeks of age (Figure 5.2), while no untreated animals survived beyond 7-8 weeks of age.

These results indicate that AAV-PHP.B-h*NDUFS4* can stall the progression of neurological symptoms in *Ndufs4*$^{-/-}$ mice.

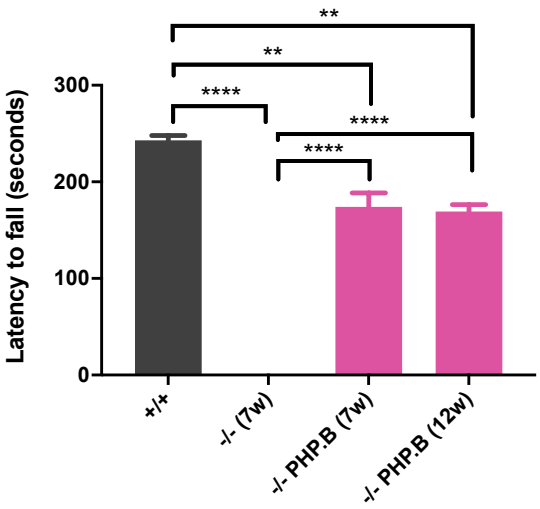

Figure 5.2 Motor skills evaluation upon AAV-PHP.B-h*NDUFS4* treatment in *Ndufs4*$^{-/-}$ mice. Motor coordination measured as latency to fall on an accelerating rotarod apparatus of WT (+/+), untreated (-/-) and AAV-treated (-/- PHP.B) *Ndufs4*$^{-/-}$ mice at 7 weeks of age. AAV-treated *Ndufs4*$^{-/-}$ mice were also evaluated at 12 weeks of age, while no untreated *Ndufs4*$^{-/-}$ mice were alive. Data are presented as mean ± SEM. $^{**}P < 0.01$, $^{****}P < 0.0001$; two-way ANOVA (n = 6).

5.2.3. AVV-PHP.B efficiently delivers h*NDUFS4* to mouse brain

Given that the *Ndufs4*$^{-/-}$ mice symptoms are attributed mainly to brain anomalies, we evaluated if *NDUFS4* expression was restored in the brain. In addition, we extended some analyses to other tissues relevant for mitochondrial disease, including liver, skeletal muscle and heart.

First, we analysed the biodistribution of the viral vector in different tissues of treated *Ndufs4*$^{-/-}$ mice. Approximately 10 vg/diploid genome (dg) were detected in brain and liver, 2–3 vg/dg in heart, and 0.3 vg/dg in skeletal muscle (Figure 5.3 - A), suggesting that the AAV-PHP.B effectively crossed the BBB and infected brain cells. Importantly, the viral genome copies found in the different tissues were consistent with the ones from the original published data for AAV-PHP.B serotype (Deverman et al., 2016). To further confirm effective delivery of hNDUFS4 across the BBB, we used an anti-hNDUFS4 antibody to evaluate protein expression in brain homogenates. The hNDUFS4 protein was detected in the brains of all AAV-treated mice analysed, while expression was virtually absent in untreated mice (Figure 5.3 - B). However, the amount of NDUFS4 protein in treated mice was lower than in the WT control brains. In addition, hNDUFS4 was similarly detected in liver, skeletal muscle and heart (Figure 5.3 - C). We then investigated in greater detail the hNDUFS4 expression in brain regions of interest of AAV-PHP.B-injected animals, such as the olfactory bulb and vestibular nuclei. Immunohistochemistry using the same anti-NDUFS4 antibody showed positive areas and cells in the olfactory bulb and vestibular nuclei (Figure 5.4). Importantly, no anti-NDUFS4-positive staining was present in untreated *Ndufs4*$^{-/-}$ mice. Together these results demonstrate that treatment with AAV-PHP.B-h*NDUFS4* can restore NDUFS4 protein expression in the mouse brain.

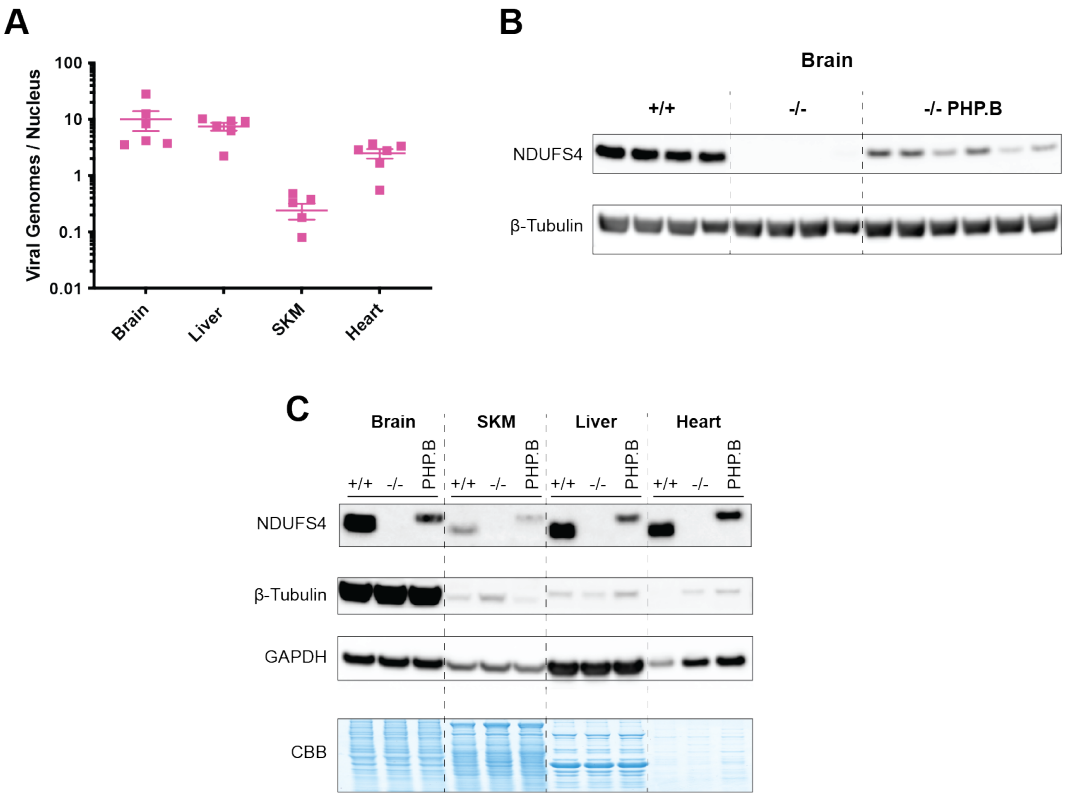

Figure 5.3 Delivery of h*NDUFS4* into tissues of *Ndufs4*$^{-/-}$ mice upon AAV-PHP.B-h*NDUFS4* treatment.
A. Real-Time qPCR quantification of AAV-PHP.B viral genomes in brain, liver, skeletal muscle (SKM), and heart of AAV-PHP.B treated *Ndufs4*$^{-/-}$ mice. Data are presented as mean ± SEM. Each symbol represents a biological replicate. **B.** Western blot analysis of the levels of NDUFS4 in brain of WT (+/+), untreated (-/-) and AAV-treated (-/- PHP.B) Ndufs4$^{-/-}$ mice. ß-tubulin was used as loading control. Each lane represents an individual mouse. **C.** Western blot analysis of the levels of NDUFS4 in brain, skeletal muscle (SKM), liver and heart of WT (+/+), untreated (-/-) and AAV-treated (-/- PHP.B) Ndufs4$^{-/-}$ mice. ß-tubulin, GAPDH and coomassie brilliant blue (CBB) were used as loading controls. Each lane represents an individual mouse.

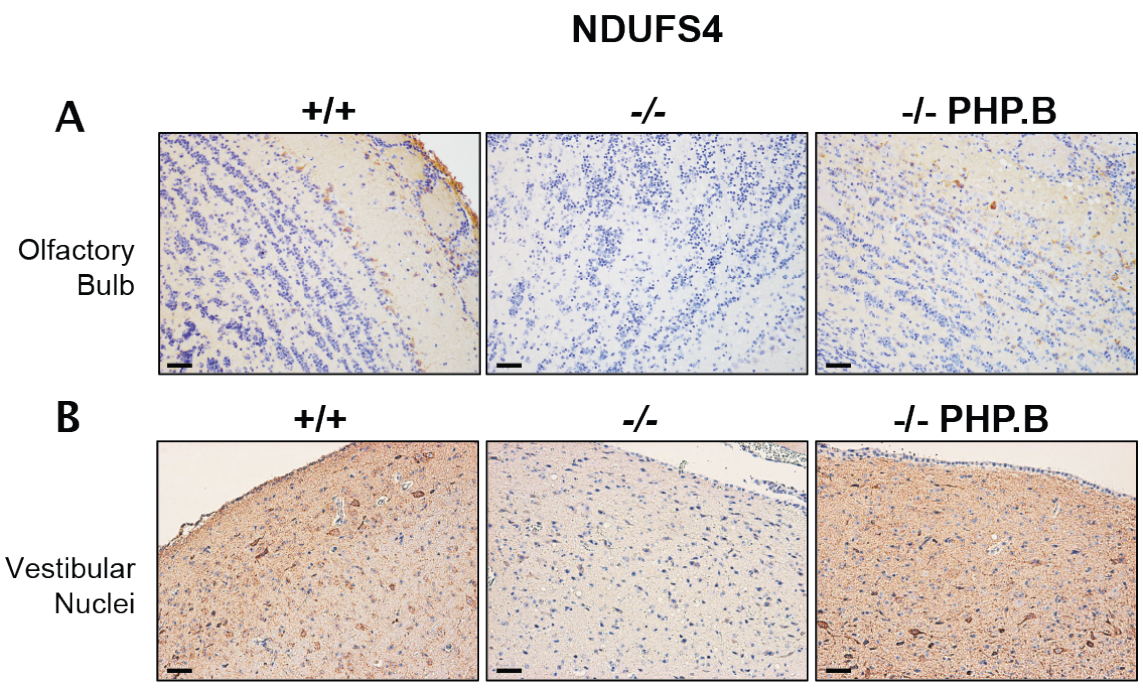

Figure 5.4 Detection of hNDUFS4 in relevant brain regions of *Ndufs4*$^{-/-}$ mice upon AAV-PHP.B-h*NDUFS4* treatment.
Representative immunohistochemical staining using an anti-NDUFS4 antibody on sections of the (**A**) olfactory bulb and (**B**) vestibular nuclei of WT (+/+), untreated (-/-) and AAV-treated (-/-PHP.B) *Ndufs4*$^{-/-}$ mice. Scale bars: 50 µm.

5.2.4. AAV-PHP.B-h*NDUFS4* ameliorates some brain histological findings

Next, we decided to evaluate if AAV-PHP.B-h*NDUFS4* treatment could circumvent some of the histopathological features observed in *Ndufs4*$^{-/-}$ mice in the same olfactory bulb and vestibular nuclei regions, such as gliosis and neuronal degeneration.

We first analysed microgliosis using an anti-CD68 immunostaining. Microgliosis is consequence of an intense reaction of microglia to pathogenic insults, that include expression of CD68 by these cells. Scattered CD68-positive cells were found across the olfactory bulb and vestibular nuclei of untreated *Ndufs4*$^{-/-}$ mice (Figure 5.5). The same CD68-positive cells were also found in treated mice, however to a lesser extend in both regions, suggesting a scarcer neurological damage (Figure 5.5). In contrast, investigation of astrogliosis (reaction of astrocytes to pathogenic insults) using an anti-GFAP antibody showed evident astrogliosis present in the olfactory bulb and vestibular nuclei regions of both treated and untreated *Ndufs4*$^{-/-}$ mice (Figure 5.6). We also evaluated

neurodegeneration by PathoGreen staining, which selectively stains degenerating neurons. Massive neurodegeneration was detected in the olfactory bulb of both treated and untreated *Ndufs4*$^{-/-}$ mice, however we found trend to a decrease in the AAV-treated animal (Figure 5.7 - A). In turn, neurodegeneration detected by PathoGreen staining in the vestibular nuclei was comparable between treated and untreated *Ndufs4*$^{-/-}$ mice and WT controls (Figure 5.7 - B). Together these results suggest that histopathological alterations found in *Ndufs4*$^{-/-}$ mice were partially prevented by AAV-PHP.B-h*NDUFS4* treatment, although some pathological features remain present.

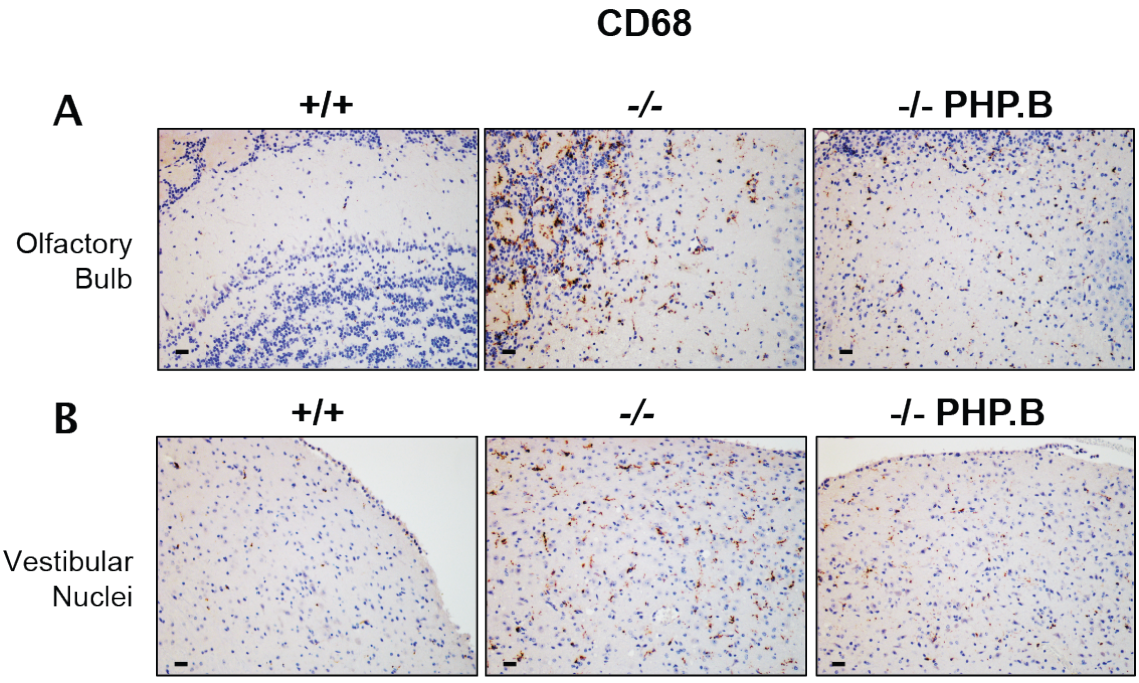

Figure 5.5 Increased microgliosis in relevant brain regions of *Ndufs4*$^{-/-}$ mice is reversed by AAV-PHP.B-h*NDUFS4* treatment.
Representative immunohistochemical staining using an anti-CD68 antibody on sections of the (**A**) olfactory bulb and (**B**) vestibular nuclei of WT (+/+), untreated (-/-) and AAV-treated (-/- PHP.B) *Ndufs4*$^{-/-}$ mice. Scale bars: 10 µm.

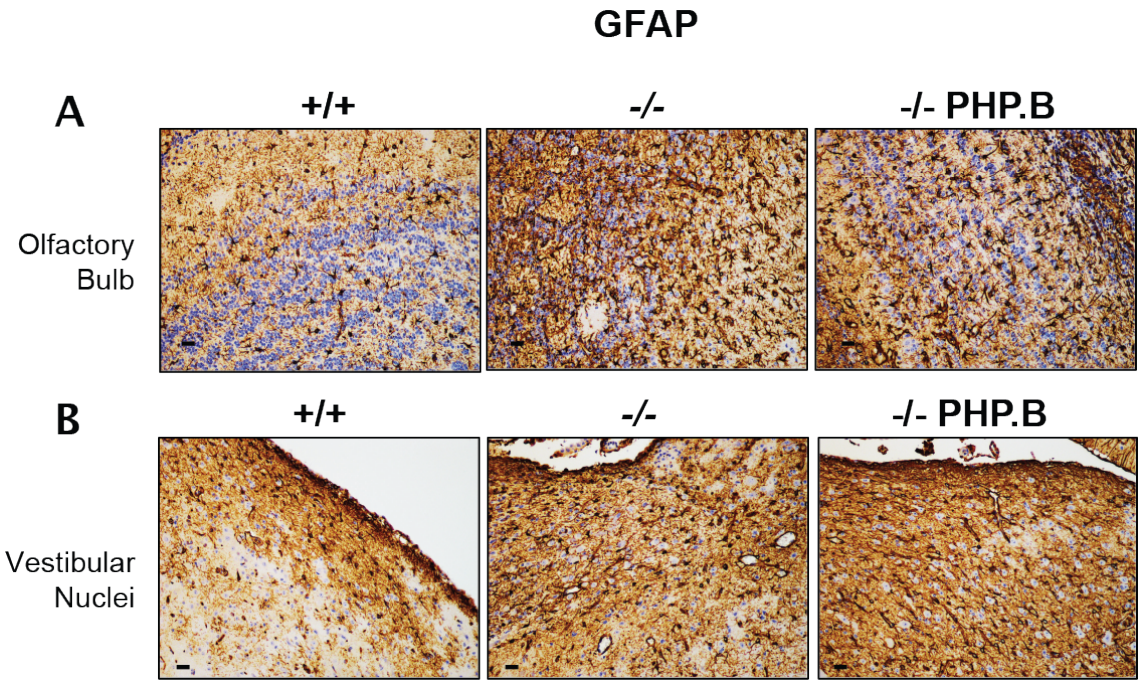

Figure 5.6 Increased astrogliosis in relevant brain regions of *Ndufs4*$^{-/-}$ mice is not reversed AAV-PHP.B h*NDUFS4* treatment.
Representative immunohistochemical staining using an anti-GFAP antibody on sections of the (**A**) olfactory bulb and (**B**) vestibular nuclei of WT (+/+), untreated (-/-) and AAV-treated (-/- PHP.B) *Ndufs4*$^{-/-}$ mice. Scale bars: 10 µm.

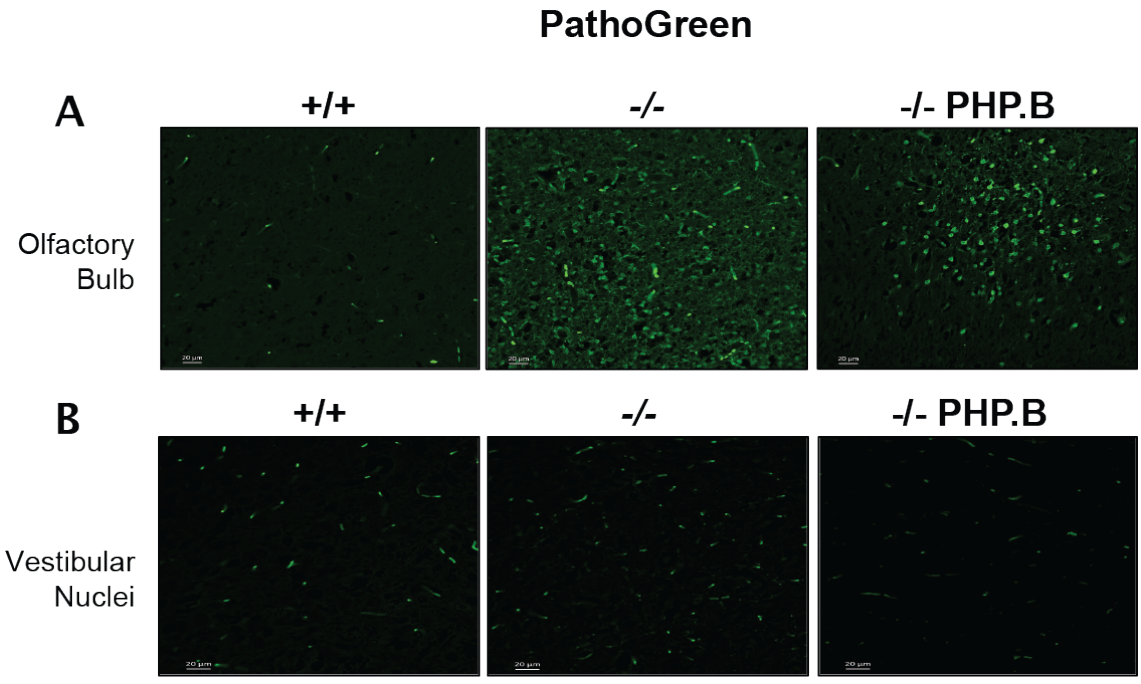

Figure 5.7 Massive neurodegeneration in olfactory bulb of *Ndufs4*$^{-/-}$ mice is partially reversed upon AAV-PHP.B-h*NDUFS4* treatment.
Representative PathoGreen staining on sections of the (**A**) olfactory bulb and (**B**) vestibular nuclei of WT (+/+), untreated (-/-) and AAV-treated (-/- PHP.B) *Ndufs4*$^{-/-}$ mice. Scale bars: 20 µm.

5.2.5. AAV-PHP.B-mediated expression of h*NDUFS4* increases Complex I activity in brain

The phenotype of *Ndufs4*$^{-/-}$ mice is attributed to loss of NDUFS4 which leads to CI assembly defects (failure to assemble the N-module) and thereby a reduction of CI activity. We thus measured CI activity in brain homogenates of untreated and AAV-treated mice. As expected, rotenone-sensitive NADH (reduced nicotinamide adenine dinucleotide)-CoQ (coenzyme Q) reductase activity was profoundly decreased in *Ndufs4*$^{-/-}$ mice (16.3% ± 3.86% compared to WT, $p < 0.001$). In contrast, CI activity was 63.5% ± 11.26% of the WT ($p < 0.05$) in AAV-treated animals, demonstrating a biochemical rescue of CI in these animals (Figure 5.8 - A). Furthermore, BNGE and in-gel activity on isolated brain mitochondria revealed that the activity associated with fully assembled CI was restored in AAV-treated *Ndufs4*$^{-/-}$mice, while it was completely absent in untreated animals (Figure 5.8 - B). Accordingly, western blot immunovisualization of the BNGE revealed robust recovery of fully assembled CI, although there was persistency of the N-module-less 830-kDa subassembly, typically observed in *Ndufs4*$^{-/-}$mice (Figure 5.8 - C). These data indicate that AAV-PHP.B-mediated restoration of NDUFS4 levels salvages CI activity and assembly, although not to WT-like levels.

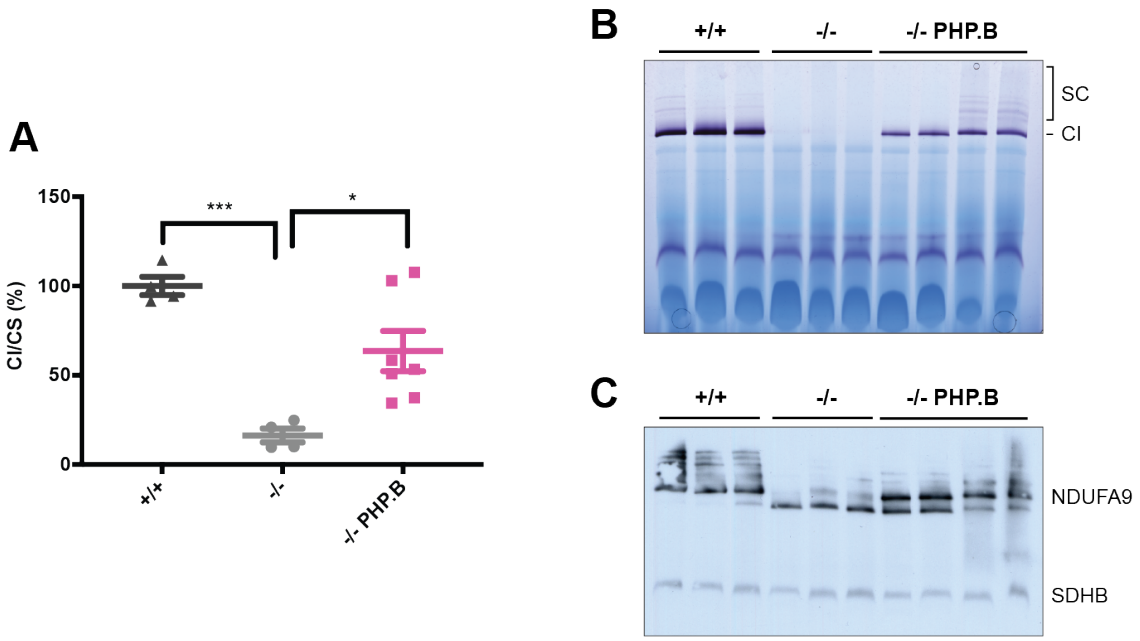

Figure 5.8 Assessment of complex I activity and assembly in brain of *Ndufs4*$^{-/-}$ mice upon AAV-PHP.B-h*NDUFS4* treatment.
A. Spectrophotometric activity of complex I (CI), normalized to citrate synthase (CS), in brain homogenates of WT (+/+), untreated (-/-) and AAV-treated (-/- PHP.B) *Ndufs4*$^{-/-}$ mice. Data are presented as mean ± SEM. *P < 0.05, ***P < 0.001; one-way ANOVA. Each symbol represents a biological replicate. **B.** In-gel activity of complex I (CI) on a first-dimension BNGE in mitochondrial protein isolated from brain of WT (+/+), untreated (-/-) and AAV-treated (-/- PHP.B) *Ndufs4*$^{-/-}$ mice. Each lane represents a sample from an individual mouse. SC- super complexes. **C.** Western blot analysis of a first-dimension BNGE in mitochondrial protein isolated from brain of WT (+/+), untreated (-/-) and AAV-treated (-/- PHP.B) *Ndufs4*$^{-/-}$ mice, with an antibody specific for complex I (NDUFA9). Note that only the 830-kDa subassembly band is present in untreated *Ndufs4*$^{-/-}$ samples, while both fully assembled and subassembly bands are present after treatment with AAV-PHP.B-h*NDUFS4*. An antibody specific for complex II was used as loading control (SDHB). SC- super complexes.

5.2.6. AAV-PHP.B-h*NDUFS4* prolongs lifespan *Ndufs4*$^{-/-}$ mice

We then analysed the survival probability of AAV-PHP.B-h*NDUFS4*-treated versus untreated *Ndufs4*$^{-/-}$mice by Kaplan-Meier distribution and log rank analysis in the second cohort of animals. AAV-PHP.B-h*NDUFS4* treatment significantly improved the median lifespan of *Ndufs4*$^{-/-}$mice compared untreated littermates (100 versus 55 days, log rank test; p < 0.0001) (Figure 5.9).

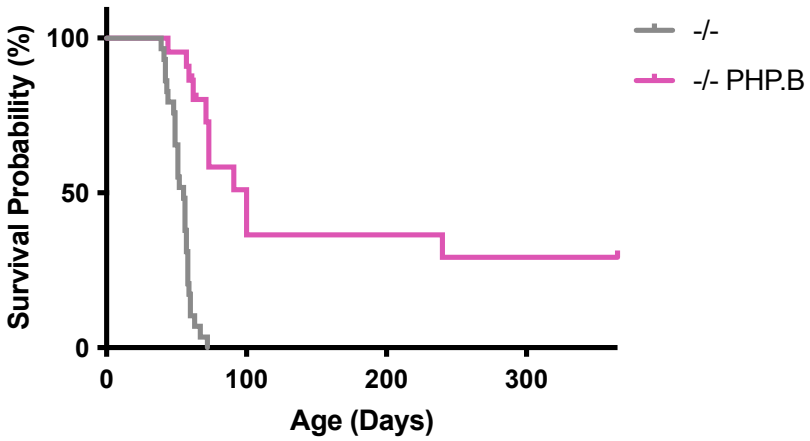

Figure 5.9 Lifespan of *Ndufs4*$^{-/-}$ mice upon AAV-PHP.B-h*NDUFS4* treatment.

Kaplan-Meier survival probability in untreated (-/-) and AAV-treated (-/- PHP.B) *Ndufs4*$^{-/-}$ mice. Significance was calculated with a log rank test (median lifespan 55 days for untreated *Ndufs4*$^{-/-}$ vs 100 for AAV-PHP.B-h*NDUFS4*-treated; log rank test; p<0.0001). No WT (+/+) mouse was loss during the one-year evaluation.

Remarkably, approximatively 30% of the treated animals survived up to 1 year of age and were culled in apparently good health. Unexpectedly, four animals injected in different days died suddenly between 90 and 100 days after birth. Post-mortem analysis showed a massively enlarged stomach (Figure 5.10), but analysis of the stomach, small intestine, and large intestine failed to reveal any obvious histological alteration (not shown). In addition, we failed to identify the presence of viral genomes in these tissues by Real-Time qPCR (not shown). Other AAV-treated mice developed the typical signs of the disease, although at a later stage than untreated littermates, and were sacrificed when body weight dropped by 20%. All the mice that were sacrificed because of poor health conditions showed some degree of neurodegeneration by PathoGreen staining in the olfactory bulb and vestibular nuclei regions as shown previously in (Figure 5.7), but also in regions that were not previously affected in untreated *Ndufs4*$^{-/-}$mice, such as the preoptic region (Figure 5.11). These findings demonstrate that treatment with AAV-PHP.B-h*NDUFS4* at P26–P28 is highly effective in delaying, if not blocking, the disease progression in a subset of *Ndufs4*$^{-/-}$mice (extending the lifespan up to 1 year). However, disease still slowly progresses in some mice, suggesting that some of the neurological insults might already be present at the time of injection.

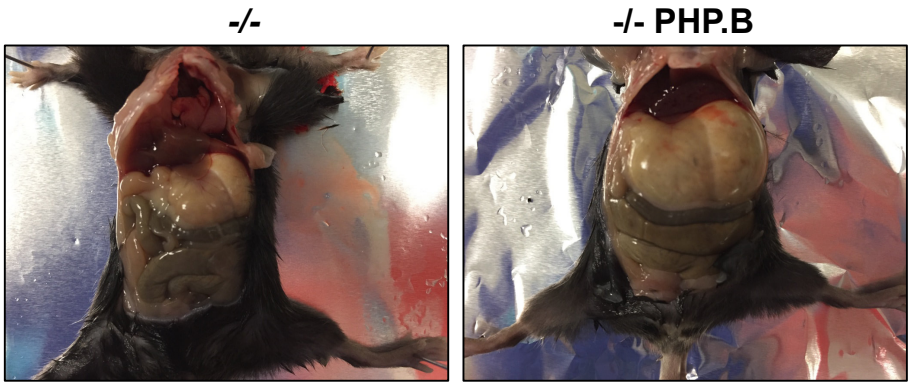

Figure 5.10 Post-mortem examination of suddenly deceased *Ndufs4*$^{-/-}$ mice after AAV-PHP.B-h*NDUFS4* treatment.
Representative necropsy photographs of AAV-treated (-/- PHP.B) *Ndufs4*$^{-/-}$ mice that died unexpectedly. A massively enlarged stomach was observed in several *Ndufs4*$^{-/-}$ mice treated with AAV-PHP.B-h*NDUFS4*. An untreated (-/-) *Ndufs4*$^{-/-}$ was added for comparison purposes.

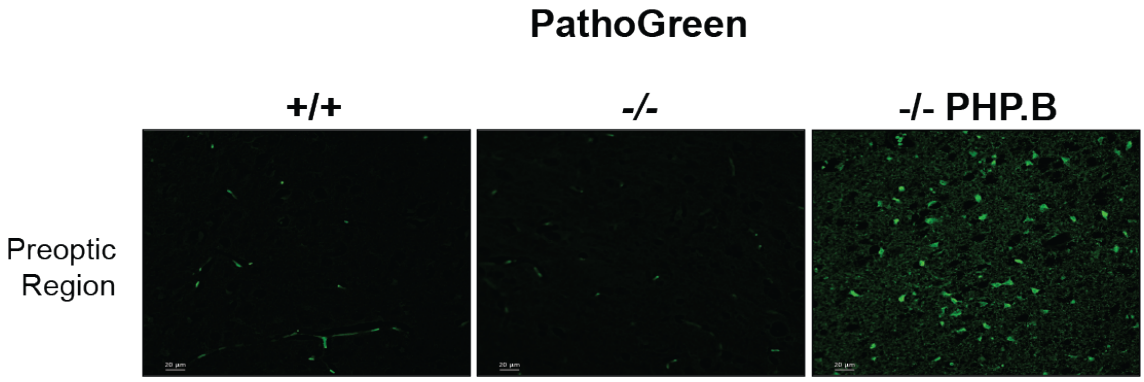

Figure 5.11 Evaluation of neurodegeneration in the preoptic region of *Ndufs4*$^{-/-}$ mice upon AAV-PHP.B-h*NDUFS4* treatment.
Representative PathoGreen staining on sections of the preoptic region in the brain of WT (+/+), untreated (-/-) and AAV-treated (-/- PHP.B) *Ndufs4*$^{-/-}$ mice. Scale bars: 20 µm.

5.3. Evaluation of the therapeutic outcomes of gene rescue in newborn *Ndufs4*$^{-/-}$ mice using AAV-PHP.B

Because some of the neurological damage might be present when injecting AAV-PHP.B-h*NDUFS4* at P26–P28, we hypothesized that anticipating the treatment could improve the clinical outcome. We thus treated a group of newborn *Ndufs4*$^{-/-}$mice at P1 with a single dose of AAV-PHP.B-h*NDUFS4* of 1×10^{12} viral genomes systemically delivered via the temporal vein.

5.3.1. Early intervention with AAV-PHP.B-h*NDUFS4* does not improve lifespan *Ndufs4*$^{-/-}$ mice

Mice injected with AAV-PHP.B-h*NDUFS4* at birth developed normally until 5 weeks. However, in contrast to our expectations, around 40 days of age P1-treated *Ndufs4*$^{-/-}$ mice started to present signs of disease progression similar to untreated *Ndufs4*$^{-/-}$ mice, such as weight loss and neurological defects and were eventually sacrificed. Analysis of the survival curve showed a rough overlap between untreated and P1-treated mice (Figure 5.12). Thus, an early intervention with AAV-PHP.B-h*NDUFS4* was ineffective in improving lifespan of *Ndufs4*$^{-/-}$mice.

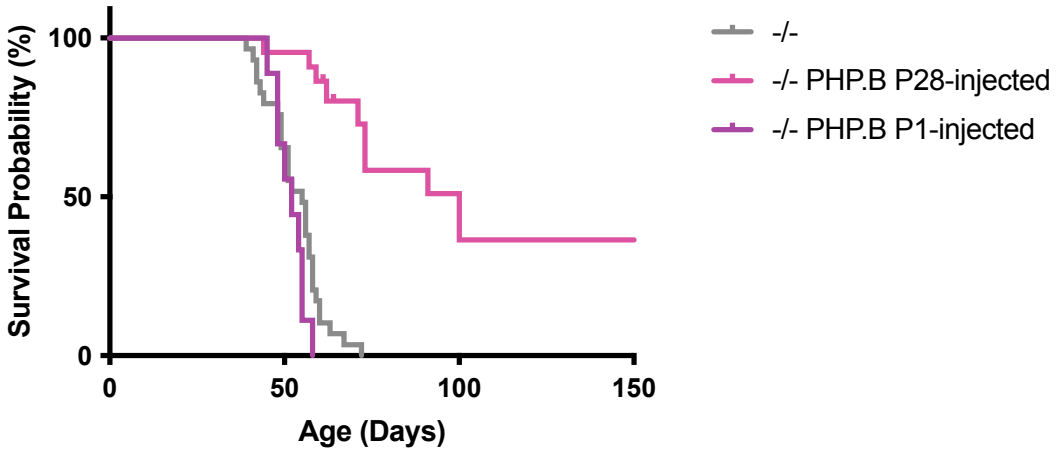

Figure 5.12 Lifespan of *Ndufs4*$^{-/-}$ mice upon early intervention of AAV-PHP.B-h*NDUFS4* treatment.
Kaplan-Meier survival probability in untreated (-/-) and AAV-treated *Ndufs4*$^{-/-}$ mice injected P1 (-/- PHP.B P1-injected). Significance was calculated with a log rank test (not significant). *Ndufs4*$^{-/-}$ mice injected at P26-28 (-/- PHP.B P28-injected) were added for comparison purposes. No WT (+/+) mouse was loss during the one-year evaluation.

5.3.2. AVV-PHP.B does not effectively deliver h*NDUFS4* to newborn mouse brain

We then analysed the biodistribution of the viral vector in different tissues of P1-treated *Ndufs4*$^{-/-}$ mice. The AAV-PHP.B copy number in the tissues of P1-injected pups was similar to that of the P28-injected adults, with even higher AAV-PHP.B copy numbers in skeletal muscle (Figure 5.13 - A). Notably, the viral genome copies in the brain were lower than in adults and showed much higher variability (Figure 5.13 - A). Accordingly, the hNDUFS4 protein levels were barely detectable in the brains of AAV-PHP.B-treated animals (Figure 5.13 - B).

These data suggest that the AAV-PHP.B crossed the BBB much less effectively in pups than in adults.

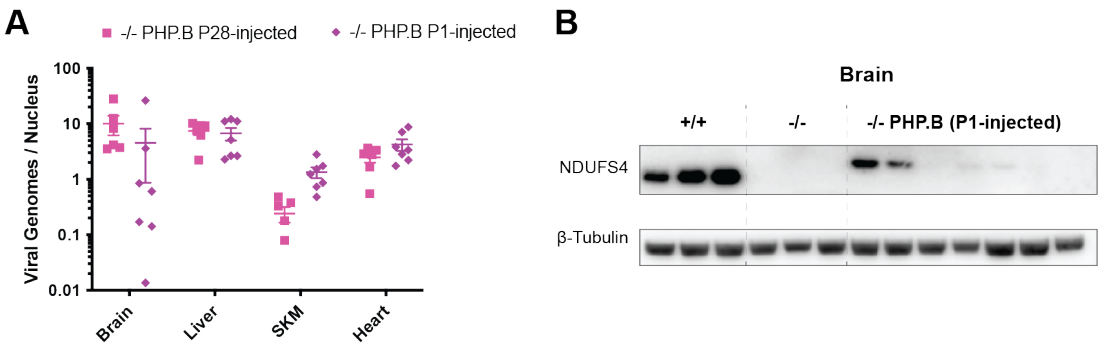

Figure 5.13 Delivery of h*NDUFS4* into tissues of *Ndufs4*$^{-/-}$ mice upon early intervention of AAV-PHP.B-h*NDUFS4* treatment.
A. Real-Time qPCR quantification of AAV-PHP.B viral genomes in brain, liver, skeletal muscle (SKM), and heart of AAV-treated *Ndufs4*$^{-/-}$ mice injected at P1 (-/- PHP.B P1-injected) and injected at P26-28 (-/- PHP.B P28-injected). Data are presented as mean ± SEM. Each symbol represents a biological replicate. **B.** Western blot analysis of the levels of NDUFS4 in brain of WT (+/+), untreated (-/-) and AAV-treated (-/- PHP.B) *Ndufs4*$^{-/-}$ mice injected at P1. ß-tubulin was used as loading control. Each lane represents an individual mouse.

5.3.3. Newborn mouse brains present an immature import system for AAV-PHP.B

The AAV-PHP.B capacity of crossing the BBB has been associated with the expression of membrane glycoproteins of the brain endothelia, in particular the LY6A receptor (Batista et al., 2020). We thus hypothesized that the observed inefficiency of AAV-PHP.B could be due to lower expression of the LY6A receptor in newborn mice. To test if LY6A was decreased in newborn mice, we used an anti-LY6A antibody on brain homogenates from P1 and P30 mice. Indeed, western blot immunovisualization showed a marked decrease of LY6A in P1 mice compared with P30 animals (Figure 5.14). This result suggests that newborn mice have an immature import system for AAV-PHP.B, demonstrated by low levels of the LY6A, and thus justify the relatively inefficiency of this serotype at early-life interventions.

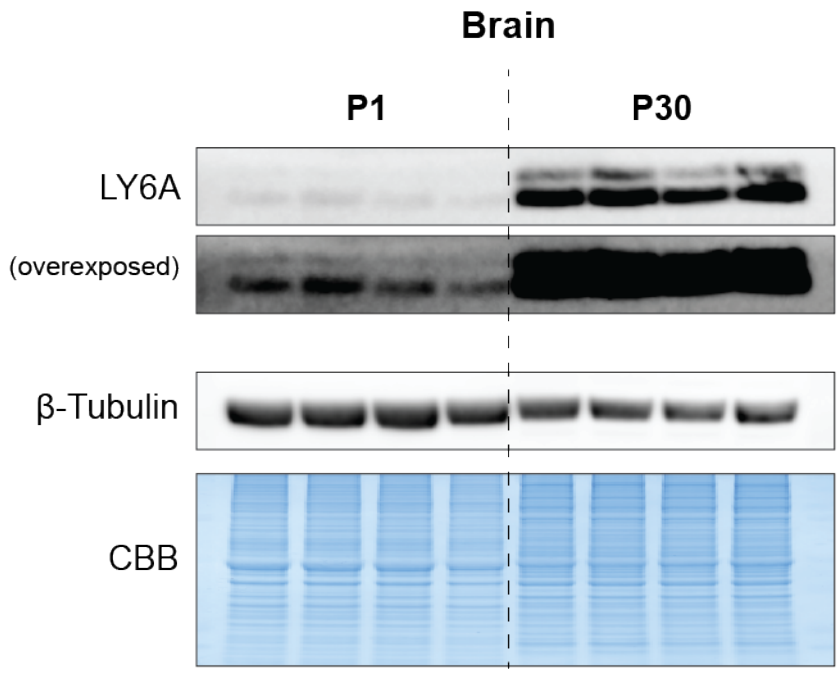

Figure 5.14 Detection of LY6A receptor in the mouse brain at different development stages. Western blot analysis of the levels of LY6A in brain of WT (+/+) mice, sacrificed at birth (P1) or at 30 days after birth (P30). ß-tubulin and coomassie brilliant blue (CBB) were used as loading control. Each lane represents an individual mouse. Note the marked higher LY6A levels in P30 mice compared to P1 mice.

5.4. Summary of the main Findings

- A single dose of AAV-PHP.B-h*NDUFS4* can rescue some of the clinical phenotypes presented by *Ndufs4*$^{-/-}$ mice, such as body weight loss and degeneration rapid of motor coordination, as tested with a rotarod apparatus.
- AAV-PHP.B crosses efficiently the BBB of adult mice, supported by a detection of a reasonable number of viral genomes and immunodetection of the NDUFS4 protein in treated mice brains. Liver, skeletal muscle and heart are also transduced with relative efficiency.
- AAV-PHP.B-h*NDUFS4* treatment can improve some of the histopathological findings in some regions of *Ndufs4*$^{-/-}$ brains, such as reduction of microgliosis in the olfactory bulb and vestibular nuclei and reduce neurodegeneration in the olfactory bulb.
- A single dose of AAV-PHP.B-h*NDUFS4* can rescue complex I activity and assembly in brains of treated mice, supported by spectrophotometer and BNGE analysis.
- AAV-PHP.B-h*NDUFS4* treatment significantly improves the lifespan of *Ndufs4*$^{-/-}$ mice. Some mice were apparently healthy up to 1 year of age, while untreated mice normally do not survive over 8 weeks.
- An early intervention with AAV-PHP.B-h*NDUFS4* treatment at birth (P1) provided a lifespan comparable of untreated mice, which is probably associated with the inability of AAV-PHP.B to cross the BBB, as shown with a variable number of viral genomes and week immunodetection of NDUFS4 P1-treated brains (sacrificed after 40 days).
- The inefficiency of AAV-PHP.B to cross BBB in newborns compared with adult mice is likely due to a weak expression of the LY6A receptor at birth (P1) compared with early adulthood (P30).

Chapter 6 Discussion and Future Directions

6. Discussion and Future Directions

Mutations in *POLG* are a common cause of a spectrum of mitochondrial disease. The substantial lack of relevant *in vivo* models has hampered our understanding of the pathogenesis of the *POLG*-related disorders. In chapter 3, we developed two *POLG* knockin mouse models, corresponding to the human A467T and Y955C mutations, the most common recessive and dominant *POLG* mutations, respectively. The human POLγA residues A467 and Y955 are evolutionary conserved from chimpanzee (*Pan troglodytes*) to fruit fly (*Drosophila melanogaster*), including mice (*Mus musculus*). The high evolutionary conservation among species further supports the importance of residues A467 and Y955 in POLγA function and upholds the pathogenicity of mutations affecting them in human patients (Camps et al., 2007).

The generation of the *Polg*$^{A449T/A449T}$ mouse model (human A467T equivalent) was performed using a double-nickase CRISPR/Cas9 D10A approach. The use of two gRNAs ameliorates the off-target activity of Cas9 (Ran et al., 2013) and injection of all the components (Cas9-D10A, gRNAs and HDR template) directly in mouse zygotes enabled us to obtain heterozygous *Polg*$^{WT/A449T}$ in a pure FVB/NJ strain background after just one attempt. The reduction of off-targets and generation in a pure background allowed for direct characterization of the *Polg*^{A449T} strain without the need of extensive breeding programs.

The generation of the *Polg*$^{WT/Y933C}$ mouse model (human Y955C equivalent) faced more challenges. The use of double-nickase CRISPR/Cas9 D10A approach failed to produce *Polg*^{Y933C} mutants despite several attempts. Factors such as genomic locus, secondary structure and gRNA selection can have an impact on overall CRISPR/Cas9-mediated knockin efficiency (Balci et al., 2021). The two gRNAs targeting the Y933C locus were validated individually in mouse cultured cells, however their efficiency as a nickase pair was not evaluated. Given that all the pups obtained using the double-nickase CRISPR/Cas9 D10A had WT sequences with no evidence of indels, we thus presumed a low efficiency of cleavage at the targeted locus using this strategy. The use of single nuclease CRISPR/Cas9 WT using only one gRNA increases the targeting efficiency, but using this strategy directly into

mouse embryos also failed to produce mutant mice. Positive results were eventually obtained by delivering the CRISPR-Cas9 reagents into mouse ES cells, in which screening can be scaled up considerably. Surprisingly, we found a high number of CRISPR-Cas9 edited clones with efficiencies up to 25%, which contradicts the low efficiencies found when injecting zygotes. Most positive clones were invalidated by the presence of a deletion of two Guanines (c.2802_2804del), which was co-segregating with the intended p.Y933C modification. In our strategy, Cas9 cut the locus in the region of four guanines upstream of the PAM sequence (see Figure 3.7), which could justify the presence of the c.2802_2804del in ~94% of the edited clones. This is consistent with the reports showing that the highest indel rate occurs at the cut site (Edmondson et al., 2021). Nevertheless, ES clones with the expected p.Y933C knockin were identified and used to generate heterozygous *Polg*$^{WT/Y933C}$. The human *POLG* Y955C mutation was only found in heterozygous patients (Human DNA POLγA Mutation Database http://tools.niehs.nih.gov/polg/). Accordingly, crossing heterozygous *Polg*^{Y933C} mutant mice revealed complete embryonic lethality of *Polg*$^{Y933C/Y933C}$ mutants. Thus, the mouse *Polg*^{Y933C} replicates the dominant inheritance pattern seen in humans, providing encouraging preliminary data for the use of *Polg*^{Y933C} mutant mice to elucidate some aspects of the pathogenesis of *POLG*-related disorders. Future work is warranted to investigate and characterize the phenotype of *Polg*^{Y933C} mice.

In chapter 4, we focused on the homozygous *Polg*$^{A449T/A449T}$ mice to study the molecular pathogenesis of the *POLG* A467T mutation *in vivo* and complemented this analysis with a detailed biochemical characterization of the corresponding events *in vitro*.

The homozygous *Polg*$^{A449T/A449T}$ mice present an early adulthood onset phenotype which does not progress between 3 and 12 months of age characterized by a mild lethargy and exercise intolerance. Despite a mild depletion of mtDNA in skeletal muscle, no alterations in mtDNA transcripts levels and OXPHOS activities were detected. Accordingly, no obvious lesions were detected in several tissues of mutant mice by histological analysis. In addition, the mutant mice were resilient

to various challenges, including administration of valproic acid (VPA), which is known to trigger acute liver failure in *POLG* patients (Stewart et al., 2010). Although drug-induced toxicity was not detected in *Polg*$^{A449T/A449T}$ mice with the doses and administration regimens used in this work, VPA seems to accelerate the onset of an already existent pathology of *POLG* patients. In support of this notion, liver histopathology findings of VPA-treated *POLG* patients are indistinguishable from those not treated with VPA, supporting the pre-existence of a pathology (Harding, 1990). The absence of a pre-stablished liver-related phenotype in *Polg*$^{A449T/A449T}$ mice could justify their higher resilience to VPA-induced toxicity. VPA is also known to inhibit fatty acid β-oxidation, which mainly occurs in liver mitochondria (Silva et al., 2008). Therefore, metabolic differences in the β-oxidation pathway between mice and humans could also account for the different outcomes. The only obvious phenotype seen was after administration of CCl_4, which resulted in a reduced recovery rate to liver damage, demonstrating that effective mtDNA replication is necessary for liver regeneration. Similar results have previously been reported for a knockout mouse model of mitochondrial topoisomerase I (TOP1mt), in which defective mtDNA replication promoted by absence of TOP1mt, stimulates impaired liver regeneration upon CCl_4-induced liver damage (Khiati et al., 2015).

Despite the mild clinical phenotype, *Polg*$^{A449T/A449T}$ mice revealed a clear effect on mtDNA replication compared to WT controls. In *Polg*$^{A449T/A449T}$ mouse tissues, we observed a reduction of 7S DNA and increased levels of replication intermediates (RIs), suggestive of mtDNA replication stalling. Similar effects have been previously described in knock-out models for other components of the mitochondrial replication machinery, in which a decrease in 7S DNA steady state levels is detected upon depletion of POLγB, TWINKLE and mtSSB (Milenkovic et al., 2013, Ruhanen et al., 2010, Di Re et al., 2009). In addition, experiments carried out in *Polg*$^{A449T/A449T}$ MEFs revealed a striking reduction of mtDNA recovery after depletion with EtBr, thus demonstrating that POLγ activity is severely impaired in this model. This result is in line with another report showing the inability of human

fibroblasts harbouring distinct POLγA mutations to recover mtDNA content after EtBr-induced mtDNA depletion (Stewart et al., 2011).

Although we do not have an obvious explanation for the phenotypic differences between POLγA-defective mice and patients, our results suggest that the mutant mice may have effective compensatory mechanisms which mitigate POLγ dysfunction. Such compensatory mechanism was highlighted by the observation that *Polg*$^{A449T/A449T}$ mitochondria display *in organello* replication rates similar to WT controls but present a higher accumulation rate of mtDNA RIs and lower levels of 7S DNA. It is then tempting to hypothesise that somehow, to maintain adequate mtDNA levels, PolgA449T/A449T mitochondria increase the number of replication events that proceed to full-length molecules to compensate for a slower replication carried by the mutant POLγA449T. About 95% of the mammalian mtDNA replication events terminate prematurely originating the 7S DNA. Why 7S DNA is synthesised and turned over at considerable energetic expense is still not well understood, but is suggestive of a process of physiological relevance (Nicholls and Minczuk, 2014). Therefore, a compensatory mechanism at the replication initiation level could justify the observed decreased in 7S DNA levels, as the 7S DNA would be used to prime full-length replication (and less events will be prematurely terminated). Also, it would justify the increase in RIs, as more mtDNA molecules would be engaged in replication to normalise mtDNA synthesis rates. Interestingly, experiments carried out using *Polg*$^{A449T/A449T}$ MEFs showed an increased number of actively replicating nucleoids, while retaining normal mtDNA copy number. In further support of this putative compensatory mechanism, the *Polg*$^{A449T/KO}$ double mutants presented a very similar phenotype to homozygous *Polg*$^{A449T/A449T}$ mice. However, *Polg*$^{A449T/KO}$ mice display an even sharper decrease in 7S DNA steady-state levels and a higher accumulation of RIs than *Polg*$^{A449T/A449T}$ while sustaining mtDNA replication rates. Thus, these observations suggest that the compensatory mechanism is further enhanced in these mice possibly to account for the higher degree of mtDNA replication constrain caused by a 50% reduction of POLγA levels. Although evidence for such compensatory mechanism is merely observational in this work, a deeper mechanistic investigation could

provide meaningful insights on how cells sense and regulate mtDNA copy number, a matter that has been debated for several decades but remains to be elucidated. In future work, *Polg*^{A449T} mutant mice and cells could be used to unravel important key factors mediating control of mtDNA copy number, for example by identifying genes that are up or downregulated in these models.

Furthermore, in agreement with the irregular mtDNA replication observed *in vivo*, our analysis of mPOLγA^{A449T} *in vitro* revealed less affinity to DNA template and a decrease in exonuclease and polymerase activities, which were partially rescued in the presence of POLγB. This observation highlights the importance of POLγB for the activity of POLγA. In addition, size-exclusion chromatography demonstrates that the A449T mutation impairs interactions between POLγA and POLγB, disturbing POLγ holoenzyme formation. This latter observation is supported by structural modelling of human A467T, which suggested that this mutation locates in the region of POLγA required for interactions with POLγB (Lee et al., 2009). The results obtained with mPOLγA^{A449T} are in line with the data previously obtained for hPOLγA^{A467T}, showing that the human mutation also impaired the interaction with hPOLγB and compromised polymerase catalytic activity (Chan et al., 2005). We therefore conclude that the main cause of the A449T mutation pathogenicity can be attributed to the weaker interaction of mPOLγA^{A449T} with mPOLγB, which constrains the stimulatory effects of POLγB on POLγA, including the binding affinity to DNA as well as exonuclease and polymerase activities.

Interestingly, *in vitro* comparison between the mouse POLγA^{A449T} and human POLγA^{A467T} proteins, revealed comparable but more pronounced replication defects for the human polymerase, which can also help to explain why the human A467T mutation causes more severe phenotypes in patients. These findings also demonstrate that the mouse model reproduces the molecular signature of the human disease, despite the milder phenotypes observed.

During characterisation of *Polg*$^{A449T/A449T}$ mice, we noticed a marked reduction of POLγA^{A449T} protein levels in mouse tissues, and thus in the last part of Chapter 4, we investigated the possible causes of this reduction. Using an *in vitro* thermofluor stability assay, we found that in isolation, both mPOLγA^{WT} and mPOLγA^{A449T} are

structurally unstable at physiological temperatures, but strongly stabilized in complex with mPOLγB. Importantly, mPOLγA^{A449T} was partially unfolded already at 20-30°C, a range of temperatures at which mPOLγA^{WT} was stable. Led by this observation, we hypothesised that POLγA when not bound to POLγB could be a target for proteases that degrade misfolded proteins and that weaker interactions between POLγA^{A449T} and POLγB could prompt the unstable POLγA^{A449T} for enhanced degradation. An obvious candidate to mediate such degradation was LONP1, a mitochondrial protease known to promote direct degradation of misfolded proteins in the mitochondrial matrix (Bezawork-Geleta et al., 2015). The idea that POLγA is a substrate of LONP1 was further ignited by the *in vivo* observation that LONP1 knockout mice have elevated steady-state levels of POLγA.

We followed this hypothesis using both cellular model and *in vitro* biochemical evidence and confirmed that POLγA^{A449T} is indeed a substrate of LONP1 and that POLγB serves as a stabilizing, protective factor against LONP1 degradation. Notably, knockdown of LONP1 causes an increase in POLγA levels in human HeLa cells, confirming the results observed in tissues of LONP1 knockout mice. In contrast, knockdown of POLγB leads to lower levels of POLγA, whereas depletion of POLγA has no discernible effect on POLγB. This result is consistent with a similar severe decrease of POLγA observed by another group upon CRISPR/Cas9-mediated knockout of POLγB in human HeLa cells (Do et al., 2020). Accordingly, *in vitro* LONP1 degrades POLγA but not POLγB and degradation of POLγA^{WT} by LONP1 is blocked by adding POLγB in the reaction, confirming the protective role of the accessory subunit. Interestingly, mPOLγA^{A449T} protection by POLγB is compromised due to the impaired interaction between the two subunits caused by the A449T mutation, which in turn presents as reasonable explanation for the lower levels of POLγA in *Polg*$^{A449T/A449T}$ tissues. The relevance of these results was further supported by a similar effect using the human POLγA mutant, in which hPOLγA^{A467T} was also degraded by LONP1 with hPOLγB in the reaction. Despite the strong evidence presented here for LONP1-mediated degradation of POLγA, it should be noted that we cannot rule out that other proteases can contribute to POLγA degradation *in vivo* (Lee et al., 2021). Future work will be required to

evaluate the relevance of other mitochondrial matrix proteases, such as ClpXP, on the levels of POLγA levels in physiological and pathological conditions.

In addition, the hypothesis that POLγB protects POLγA from proteolysis was also supported by the super-stoichiometric levels of POLγB relative to POLγA in mouse tissues. The rapid degradation of POLγA in the absence of POLγB could be of physiological relevance, since on its own, the POLγA displays low polymerase activity but high exonuclease activity, which may disturb mtDNA replication (see Figure 4.26). During our quantifications, we found different POLγB: POLγA ratios between the different mouse tissues analysed. In future work, it would be interesting to evaluate if tissue-specific POLγB: POLγA ratios could contribute to the observed tissue-specificity of some of the *POLG*-related syndromes.

Furthermore, during our analysis we also noted that native POLγB has slightly higher molecular weight compared to the recombinant protein when analysed by SDS-PAGE (see Figure 4.41). The reason for the difference between the predicted and observed size of the protein is not known, but could indicate that the cleavage site for the MTS is different from the previously reported (Kasiviswanathan et al., 2010). Alternatively, POLγB may contain post-translational modifications that affect its migration in SDS-PAGE. In support of the later, during analysis of POLγB levels we also observed an additional lower molecular weight band in both WT and mutant mouse brains. While we considered this band as corresponding to an unspecific protein detected by anti-POLγB antibody, we cannot exclude the presence of post-translational modifications or different POLγB isoforms in this tissue. However, we were not able to identify any reports of such modifications or isoforms in the available literature. Clarifying these points warrants additional work and may have consequences for our understanding of POLγ function. The presence of additional POLγB isoforms in the brain could also help to understand the tissue specificity of certain neurological phenotypes presented by *POLG*-patients.

In conclusion, in Chapter 4 we describe in detail the *in vivo* and *in vitro* features of the most common POLγA mutation, with potential implications for the pathogenesis of a previously poorly understood condition. Our findings suggest

the existence of a compensatory mechanism, at least in mice, that could be explored to understand not only pathological mechanisms, but also provide insights in normal processes of regulation of mtDNA replication. Our findings also imply that in addition to the *Polg* A449T mutation, other mutations in *POLG* or *POLG2*, which cause weaker interactions within the POLγ holoenzyme, would lead to degradation of POLγA, resulting in protein depletion *in vivo* with pathological consequences. We thus speculate that interventions aimed at increasing POLγA stability, either by directly stabilizing the protein or increasing interactions with POLγB may have therapeutic value in affected patients.

Aetiological therapies for mitochondrial disorders, including POLG-related disorders, are currently unavailable. In Chapter 5, we used the pre-clinical model Ndufs4-/- mouse to evaluate the therapeutic outcomes of gene replacement therapy in the amelioration of neurological-derived symptoms of mitochondrial diseases caused by mutations in nuclear-encoded genes using a novel AAV-PHP.B serotype.

We showed that a single, systemic injection of AAV-PHP.B-h*NDUFS4* in pre-symptomatic, young adult *Ndufs4*$^{-/-}$ mice could significantly prolong their lifespan up to 1 year and improve their clinical and molecular phenotype. These results are more encouraging than those presented previously delivering h*NDUFS4* into *Ndufs4*$^{-/-}$ mice using the WT AAV9 serotype (Di Meo et al., 2017). In this study, a systemic delivery of 2 x 10^{12} vg of AAV9-h*NDUFS4* did not improve the fate of *Ndufs4*$^{-/-}$ mice. Moderate positive results were only obtained with a systemic delivery of AAV9-h*NDUFS4* in conjunction with an invasive intracerebroventricular injection, in which no mice lived beyond 85 days (Di Meo et al., 2017). We attribute the improvement presented here to the intrinsic tropism of AAV-PHP.B for both neuronal and glial cell types, allowing an extensive distribution of the vector throughout the brain even when delivered by a minimal invasive intravenous injection. Such widespread transduction of the CNS was confirmed in this work by restoration of NDUFS4 levels in different part of the mouse brain and partial rescue of CI activity and assembly in brain homogenates.

Despite the improvement of lifespan up to 1 year in several animals, some mice died during the observation time. We hypothesised that premature death (but still above the lifespan of untreated mice) was caused at least in part due to the disease progression. In treated mice, some histopathological findings were not fully reverted and in some cases, new areas of the brain were affected, such as the preoptic area. In addition, some of the treated mice deceased as a consequence of a sudden and so far, unexplained gastroparesis. Gastroparesis has been reported as a complication in several mitochondrial diseases, including MELAS (mitochondrial encephalopathy, lactic acidosis, and stroke-like episodes), MNGIE (mitochondrial neurogastrointestinal encephalopathy) and some patients with *POLG*-associated mutations (Finsterer and Frank, 2017). We therefore, hypothesise that the observed effects in new brain regions and involvement of other organ are partly a consequence of prolonging the lifespan of treated *Ndufs4*$^{-/-}$ mice. Consequently, the reduced lifespan of untreated *Ndufs4*$^{-/-}$ mice, leads to premature death of these animals prior to the onset of such symptoms. In future studies, clarification of these points could be achieved, for example, by studying the effects of tissue-specific depletion of *Ndufs4* in mouse models using a gastrointestinal-specific CRE (Ireland et al., 2004).

We did not find any obvious reason for the variable outcome of the treatment between subjects. One possible explanation could be that, although no obvious signs of neurodegeneration are detected at the age of injection (Quintana et al., 2010), we cannot exclude that the disease was already variably progressing among young *Ndufs4*$^{-/-}$ mice. This idea is suggested by recent data showing that mutations in *NDUFS4* and *SURF1*, common causes of mitochondrial disease, impair neuronal morphogenesis (Inak et al., 2021). A second hypothesis stems from the observation that CI activity is only partially restored in treated mice, despite the widespread expression of hNDUFS4 in different areas of the mouse brain upon AAV-PHP.B delivery. Accordingly, the amount of hNDUFS4 is consistently lower than physiological levels of the endogenous protein. In addition, substantial amounts of the 830-kDa assembly intermediate typically detected in *Ndufs4*$^{-/-}$ mitochondria (Kruse et al., 2008) are still present. These data suggest that the

expression levels accomplished in this work are not sufficient to ensure full rescue of the phenotype, despite the relatively high titres used. Another possibility to be explored is if the hNDUFS4 used in this work is incorporated into the mouse fully assembled complex I with similar efficiency as mNDUFS4. While suboptimal levels of a therapeutic protein can be a limitation, a high steady-state levels of such protein can also interfere with mitochondrial function. Well-adjusted ratios of the components of the ETC are necessary for efficient OXPHOS. Over-representation (like under-representation) of a certain component of the ETC can create imbalances in such ratios leading to the build-up of reactive intermediates and reducing the levels of fully assembled complexes (Slone and Huang, 2020). Therefore, controlled transgene expression should be taken into consideration when developing gene therapies for mitochondrial diseases.

Further supporting our findings, the work presented here is consistent with the study presented later by an independent group (Reynaud-Dulaurier et al., 2020). Reynaud-Dulaurier *et al.*, used the same AAV-PHP.B to systemically deliver h*NDUFS4* to *Ndufs4*$^{-/-}$ mice. The group used the same AAV-PHP.B-h*NDUFS4* dose presented in this study, however they expressed h*NDUFS4* under a CAG promoter, while we used a CMV-driven expression. Similar to our findings, Reynaud-Dulaurier *et al.,* reported an improvement in lifespan, body weight and motor performance of treated mice and reversal of some histopathological findings. Remarkably, they also showed only a partial restoration of CI activity and very similar Kaplan-Meier survival curve with some of the treated mice deceasing early on, despite the survival of others over 250 days (Reynaud-Dulaurier et al., 2020). However, there is no mention of any gastrointestinal symptoms. The consistency between both studies invalidates hypothesis attributing user-related technical differences in performing the experiments as the cause of the variable outcome of the treatment between mice.

Currently, the only AAV-based therapy under clinical trials of gene replacement therapy to treat mitochondrial diseases is based on re-expression of the mtDNA-encoded MT-ND4 gene, mutated in patients with Leber hereditary optic neuropathy (LHON). Most of LHON patients present a single organ involvement

with the optic nerve being affected exclusively. Accordingly, current clinical trials focus on delivery of the therapeutic transgene directly to the eyes of affected patients using the AAV2 serotype, with favourable results recently reported in a phase 3 trial (Yu-Wai-Man et al., 2020). Success of AAV-based gene therapy for LHON subjects in these trials is partly related to the requirement of transgene delivery only to a very specific region, in this case the optic nerves. However, most mitochondrial diseases present multiple organ involvement, and thus the therapeutic transgenes would have to be delivered throughout the body to ameliorate patient´s symptoms. While the aim of this work was to study transduction of the brain, we show that the AAV-PHP.B serotype presents a diversified tropism and can also transduce with relative efficiency other tissues, for example liver, skeletal muscle and heart, a feature that, as mentioned, should be of particularly consideration for multi-systemic disorders such mitochondrial diseases.

The development of the AAV-PHP.B serotype raised great expectations for the gene therapy of neurological and neurodegenerative diseases. In addition to the work presented here, other reports have also highlighted the potential of AAV-PHP.B to ameliorate neurological symptoms in mouse models of mitochondria hyper-fusion (Yang et al., 2020), *Cdlk5* deficiency disorder (Gao et al., 2020), Sandhoff disease (Lahey et al., 2020) and Pompe disease (Lim et al., 2019). However, these expectations have been challenged by the discovery of a critical role for the LY6A receptor in enabling this serotype to cross the BBB. Unfortunately, LY6A is mutated in some mouse strains and is absent in humans (Hordeaux et al., 2019, Huang et al., 2019, Loughner et al., 2016). For this reason, when tested in non-human primates, the AAV-PHP.B presented a very inefficient transduction of the CNS compared with mouse experiments (Liguore et al., 2019, Matsuzaki et al., 2018), limiting the applicability of this novel serotype in the treatment of human neurological diseases. In line with this, we also showed that an additional limitation of AAV-PHP.B is related to low expression of LY6A in newborn mice. Accordingly, barely detectable levels of hNDUFS4 were present in

the brains of animals injected at P1, justifying the inefficacy of an early intervention with AAV-PHP.B-h*NDUFS4* treatment.

To conclude the findings presented in Chapter 5, we showed the beneficial therapeutic effects of a single dose of AAV-PHP.B-h*NDUFS4* in the treatment of the neurological symptoms of a *Ndufs4*$^{-/-}$ mouse model. Despite the limitations of the AAV-PHP.B serotype, this work supports the notion that AAV-mediated gene therapy can be life-changing for patients with severe, neurological mitochondrial disease. Pre-clinical studies like the one presented here, provide an important proof-of-concept and serve as preliminary clues for the efficacy and safety of gene therapies, paving the way for potential new, yet to discover, AAV serotypes. Future efforts are thus needed to identify additional candidate vectors with the same BBB permeability of AAV-PHP.B, but improved applicability in humans.

References

AGARONYAN, K., MOROZOV, Y. I., ANIKIN, M. & TEMIAKOV, D. 2015. Mitochondrial biology. Replication-transcription switch in human mitochondria. *Science,* 347**,** 548-51.

AGBANDJE-MCKENNA, M. & KLEINSCHMIDT, J. 2011. AAV capsid structure and cell interactions. *Methods Mol Biol,* 807**,** 47-92.

AL-BEHADILI, A., UHLER, J. P., BERGLUND, A. K., PETER, B., DOIMO, M., REYES, A., WANROOIJ, S., ZEVIANI, M. & FALKENBERG, M. 2018. A two-nuclease pathway involving RNase H1 is required for primer removal at human mitochondrial OriL. *Nucleic Acids Res,* 46**,** 9471-9483.

ALEXEYEV, M. 2020. On separation and coding capacity of mtDNA strands. *Protein Sci,* 29**,** 1070.

ALLEN, J. F. 2017. The CoRR hypothesis for genes in organelles. *J Theor Biol,* 434**,** 50-57.

ALTMANN, R. 1894. *Die Elementarorganismen und ihre Beziehungen zu den Zellen*.

ANDERSON, S., BANKIER, A. T., BARRELL, B. G., DE BRUIJN, M. H., COULSON, A. R., DROUIN, J., EPERON, I. C., NIERLICH, D. P., ROE, B. A., SANGER, F., SCHREIER, P. H., SMITH, A. J., STADEN, R. & YOUNG, I. G. 1981. Sequence and organization of the human mitochondrial genome. *Nature,* 290**,** 457-65.

ANDERSSON, S. G., ZOMORODIPOUR, A., ANDERSSON, J. O., SICHERITZ-PONTEN, T., ALSMARK, U. C., PODOWSKI, R. M., NASLUND, A. K., ERIKSSON, A. S., WINKLER, H. H. & KURLAND, C. G. 1998. The genome sequence of Rickettsia prowazekii and the origin of mitochondria. *Nature,* 396**,** 133-40.

APOSHIAN, H. V. 1970. The use of DNA for gene therapy--the need, experimental approach, and implications. *Perspect Biol Med,* 14**,** 98-108.

ARNAUDO, E., DALAKAS, M., SHANSKE, S., MORAES, C. T., DIMAURO, S. & SCHON, E. A. 1991. Depletion of muscle mitochondrial DNA in AIDS patients with zidovudine-induced myopathy. *Lancet,* 337**,** 508-10.

ARNBERG, A., VAN BRUGGEN, E. F. & BORST, P. 1971. The presence of DNA molecules with a displacement loop in standard mitochondrial DNA preparations. *Biochim Biophys Acta,* 246**,** 353-7.

ATANASSOVA, N., FUSTE, J. M., WANROOIJ, S., MACAO, B., GOFFART, S., BACKSTROM, S., FARGE, G., KHVOROSTOV, I., LARSSON, N. G., SPELBRINK, J. N. & FALKENBERG, M. 2011. Sequence-specific stalling of DNA polymerase gamma and the effects of mutations causing progressive ophthalmoplegia. *Hum Mol Genet,* 20**,** 1212-23.

ATCHISON, R. W., CASTO, B. C. & HAMMON, W. M. 1965. Adenovirus-Associated Defective Virus Particles. *Science,* 149**,** 754-6.

BALCI, H., GLOBYTE, V. & JOO, C. 2021. Targeting G-quadruplex Forming Sequences with Cas9. *ACS Chem Biol,* 16**,** 596-603.

BATISTA, A. R., KING, O. D., REARDON, C. P., DAVIS, C., SHANKARACHARYA, PHILIP, V., GRAY-EDWARDS, H., ARONIN, N., LUTZ, C., LANDERS, J. & SENA-ESTEVES, M. 2020. Ly6a Differential Expression in Blood-Brain Barrier Is Responsible for Strain Specific Central Nervous System Transduction Profile of AAV-PHP.B. *Hum Gene Ther,* 31**,** 90-102.

BAUM, C., KUSTIKOVA, O., MODLICH, U., LI, Z. & FEHSE, B. 2006. Mutagenesis and oncogenesis by chromosomal insertion of gene transfer vectors. *Hum Gene Ther,* 17**,** 253-63.

BENDA, C. 1898. Ueber die spermatogenese der vertebraten und höherer evertebraten, II. Theil: Die histiogenese der spermien. *Arch. Anat. Physiol***,** 393-398.

BENSASSON, D., ZHANG, D., HARTL, D. L. & HEWITT, G. M. 2001. Mitochondrial pseudogenes: evolution's misplaced witnesses. *Trends Ecol Evol,* 16**,** 314-321.

BERRY, E. A., GUERGOVA-KURAS, M., HUANG, L. S. & CROFTS, A. R. 2000. Structure and function of cytochrome bc complexes. *Annu Rev Biochem,* 69**,** 1005-75.

BESSIS, N., GARCIACOZAR, F. J. & BOISSIER, M. C. 2004. Immune responses to gene therapy vectors: influence on vector function and effector mechanisms. *Gene Ther,* 11 Suppl 1**,** S10-7.

BEZAWORK-GELETA, A., BRODIE, E. J., DOUGAN, D. A. & TRUSCOTT, K. N. 2015. LON is the master protease that protects against protein aggregation in human mitochondria through direct degradation of misfolded proteins. *Sci Rep,* 5**,** 17397.

BEZAWORK-GELETA, A., ROHLENA, J., DONG, L., PACAK, K. & NEUZIL, J. 2017. Mitochondrial Complex II: At the Crossroads. *Trends Biochem Sci,* 42**,** 312-325.

BIANCO, A., BISCEGLIA, L., TREROTOLI, P., RUSSO, L., D'AGRUMA, L., GUERRIERO, S. & PETRUZZELLA, V. 2017. Leber's hereditary optic neuropathy (LHON) in an Apulian cohort of subjects. *Acta Myol,* 36**,** 163-177.

BIANCO, A., MARTINEZ-ROMERO, I., BISCEGLIA, L., D'AGRUMA, L., FAVIA, P., RUIZ-PESINI, E., GUERRIERO, S., MONTOYA, J. & PETRUZZELLA, V. 2016. Mitochondrial DNA copy number differentiates the Leber's hereditary optic neuropathy affected individuals from the unaffected mutation carriers. *Brain,* 139**,** e1.

BIBB, M. J., VAN ETTEN, R. A., WRIGHT, C. T., WALBERG, M. W. & CLAYTON, D. A. 1981. Sequence and gene organization of mouse mitochondrial DNA. *Cell,* 26**,** 167-80.

BLAESE, R. M., CULVER, K. W., MILLER, A. D., CARTER, C. S., FLEISHER, T., CLERICI, M., SHEARER, G., CHANG, L., CHIANG, Y., TOLSTOSHEV, P., GREENBLATT, J. J., ROSENBERG, S. A., KLEIN, H., BERGER, M., MULLEN, C. A., RAMSEY, W. J., MUUL, L., MORGAN, R. A. & ANDERSON, W. F. 1995. T lymphocyte-directed gene therapy for ADA- SCID: initial trial results after 4 years. *Science,* 270**,** 475-80.

BOGENHAGEN, D. & CLAYTON, D. A. 1978. Mechanism of mitochondrial DNA replication in mouse L-cells: kinetics of synthesis and turnover of the initiation sequence. *J Mol Biol,* 119**,** 49-68.

BOGENHAGEN, D. F. 2012. Mitochondrial DNA nucleoid structure. *Biochim Biophys Acta,* 1819**,** 914-20.

BOLENDER, N., SICKMANN, A., WAGNER, R., MEISINGER, C. & PFANNER, N. 2008. Multiple pathways for sorting mitochondrial precursor proteins. *EMBO Rep,* 9**,** 42-9.

BONORA, M., PATERGNANI, S., RIMESSI, A., DE MARCHI, E., SUSKI, J. M., BONONI, A., GIORGI, C., MARCHI, S., MISSIROLI, S., POLETTI, F., WIECKOWSKI, M. R. & PINTON, P. 2012. ATP synthesis and storage. *Purinergic Signal,* 8**,** 343-57.

BOTA, D. A. & DAVIES, K. J. 2002. Lon protease preferentially degrades oxidized mitochondrial aconitase by an ATP-stimulated mechanism. *Nat Cell Biol,* 4**,** 674-80.

BOURDON, A., MINAI, L., SERRE, V., JAIS, J. P., SARZI, E., AUBERT, S., CHRETIEN, D., DE LONLAY, P., PAQUIS-FLUCKLINGER, V., ARAKAWA, H., NAKAMURA, Y., MUNNICH, A. & ROTIG, A. 2007. Mutation of RRM2B, encoding p53-controlled ribonucleotide reductase (p53R2), causes severe mitochondrial DNA depletion. *Nat Genet,* 39**,** 776-80.

BRIX, J., DIETMEIER, K. & PFANNER, N. 1997. Differential recognition of preproteins by the purified cytosolic domains of the mitochondrial import receptors Tom20, Tom22, and Tom70. *J Biol Chem,* 272**,** 20730-5.

BROWN, G. G., GADALETA, G., PEPE, G., SACCONE, C. & SBISA, E. 1986. Structural conservation and variation in the D-loop-containing region of vertebrate mitochondrial DNA. *J Mol Biol,* 192**,** 503-11.

BROWN, T. A. & CLAYTON, D. A. 2002. Release of replication termination controls mitochondrial DNA copy number after depletion with 2',3'-dideoxycytidine. *Nucleic Acids Res,* 30**,** 2004-10.

BRUSER, C., KELLER-FINDEISEN, J. & JAKOBS, S. 2021. The TFAM-to-mtDNA ratio defines inner-cellular nucleoid populations with distinct activity levels. *Cell Rep,* 37**,** 110000.

BUGIANI, M., INVERNIZZI, F., ALBERIO, S., BRIEM, E., LAMANTEA, E., CARRARA, F., MORONI, I., FARINA, L., SPADA, M., DONATI, M. A., UZIEL, G. & ZEVIANI, M. 2004. Clinical and molecular findings in children with complex I deficiency. *Biochim Biophys Acta,* 1659**,** 136-47.

BULAKLAK, K. & GERSBACH, C. A. 2020. The once and future gene therapy. *Nat Commun,* 11**,** 5820.

BURTON, A. C. & EDHOLM, O. G. 1956. Man in a Cold Environment: Physiological and Pathological Effects of Exposure to Low Temperatures. *Proceedings of the Royal Society of Medicine,* 49(12), 1061.

CAMASAMUDRAM, V., FANG, J. K. & AVADHANI, N. G. 2003. Transcription termination at the mouse mitochondrial H-strand promoter distal site requires an A/T rich sequence motif and sequence specific DNA binding proteins. *Eur J Biochem,* 270**,** 1128-40.

CAMPS, M., HERMAN, A., LOH, E. & LOEB, L. A. 2007. Genetic constraints on protein evolution. *Crit Rev Biochem Mol Biol,* 42**,** 313-26.

CANNON, B. & NEDERGAARD, J. 2011. Nonshivering thermogenesis and its adequate measurement in metabolic studies. *J Exp Biol,* 214**,** 242-53.

CARRACEDO, A., CANTLEY, L. C. & PANDOLFI, P. P. 2013. Cancer metabolism: fatty acid oxidation in the limelight. *Nat Rev Cancer,* 13**,** 227-32.

CAVALIER-SMITH, T. 1987. The origin of eukaryotic and archaebacterial cells. *Ann N Y Acad Sci,* 503**,** 17-54.

CAVALIER-SMITH, T. 2006. Cell evolution and Earth history: stasis and revolution. *Philos Trans R Soc Lond B Biol Sci,* 361**,** 969-1006.

CECCHINI, G. 2003. Function and structure of complex II of the respiratory chain. *Annu Rev Biochem,* 72**,** 77-109.

CHA, S. S., AN, Y. J., LEE, C. R., LEE, H. S., KIM, Y. G., KIM, S. J., KWON, K. K., DE DONATIS, G. M., LEE, J. H., MAURIZI, M. R. & KANG, S. G. 2010. Crystal structure of Lon protease: molecular architecture of gated entry to a sequestered degradation chamber. *EMBO J,* 29**,** 3520-30.

CHAN, S. S., LONGLEY, M. J. & COPELAND, W. C. 2005. The common A467T mutation in the human mitochondrial DNA polymerase (POLG) compromises catalytic efficiency and interaction with the accessory subunit. *J Biol Chem,* 280**,** 31341-6.

CHANG, D. D. & CLAYTON, D. A. 1985. Priming of human mitochondrial DNA replication occurs at the light-strand promoter. *Proc Natl Acad Sci U S A,* 82**,** 351-5.

CHEN, S. H., SUZUKI, C. K. & WU, S. H. 2008. Thermodynamic characterization of specific interactions between the human Lon protease and G-quartet DNA. *Nucleic Acids Res,* 36**,** 1273-87.

CHEN, Y. H., CHANG, M. & DAVIDSON, B. L. 2009. Molecular signatures of disease brain endothelia provide new sites for CNS-directed enzyme therapy. *Nat Med,* 15**,** 1215-8.

CHIABRANDO, D., VINCHI, F., FIORITO, V., MERCURIO, S. & TOLOSANO, E. 2014. Heme in pathophysiology: a matter of scavenging, metabolism and trafficking across cell membranes. *Front Pharmacol,* 5**,** 61.

CHINNERY, P. F., ELLIOTT, H. R., HUDSON, G., SAMUELS, D. C. & RELTON, C. L. 2012. Epigenetics, epidemiology and mitochondrial DNA diseases. *Int J Epidemiol,* 41**,** 177-87.

CHINNERY, P. F. & HUDSON, G. 2013. Mitochondrial genetics. *Br Med Bull,* 106**,** 135-59.

CHINNERY, P. F. & SAMUELS, D. C. 1999. Relaxed replication of mtDNA: A model with implications for the expression of disease. *Am J Hum Genet,* 64**,** 1158-65.

CHOMYN, A., MARIOTTINI, P., CLEETER, M. W., RAGAN, C. I., MATSUNO-YAGI, A., HATEFI, Y., DOOLITTLE, R. F. & ATTARDI, G. 1985. Six unidentified reading frames of human mitochondrial DNA encode components of the respiratory-chain NADH dehydrogenase. *Nature,* 314**,** 592-7.

CHRISTIANSON, T. W. & CLAYTON, D. A. 1988. A tridecamer DNA sequence supports human mitochondrial RNA 3'-end formation in vitro. *Mol Cell Biol,* 8**,** 4502-9.

CLAY MONTIER, L. L., DENG, J. J. & BAI, Y. 2009. Number matters: control of mammalian mitochondrial DNA copy number. *J Genet Genomics,* 36**,** 125-31.

CLAYTON, D. A. 1991. Replication and transcription of vertebrate mitochondrial DNA. *Annu Rev Cell Biol,* 7**,** 453-78.

CONG, L., RAN, F. A., COX, D., LIN, S., BARRETTO, R., HABIB, N., HSU, P. D., WU, X., JIANG, W., MARRAFFINI, L. A. & ZHANG, F. 2013. Multiplex genome engineering using CRISPR/Cas systems. *Science,* 339**,** 819-23.

D'ERCHIA, A. M., ATLANTE, A., GADALETA, G., PAVESI, G., CHIARA, M., DE VIRGILIO, C., MANZARI, C., MASTROPASQUA, F., PRAZZOLI, G. M., PICARDI, E., GISSI, C., HORNER, D., REYES, A., SBISA, E., TULLO, A. & PESOLE, G. 2015. Tissue-specific mtDNA abundance from exome data and its correlation with mitochondrial transcription, mass and respiratory activity. *Mitochondrion,* 20**,** 13-21.

D'SOUZA, A. R. & MINCZUK, M. 2018. Mitochondrial transcription and translation: overview. *Essays Biochem,* 62**,** 309-320.

DAIRAGHI, D. J., SHADEL, G. S. & CLAYTON, D. A. 1995. Human mitochondrial transcription factor A and promoter spacing integrity are required for transcription initiation. *Biochim Biophys Acta,* 1271**,** 127-34.

DALAKAS, M. C., ILLA, I., PEZESHKPOUR, G. H., LAUKAITIS, J. P., COHEN, B. & GRIFFIN, J. L. 1990. Mitochondrial myopathy caused by long-term zidovudine therapy. *N Engl J Med,* 322**,** 1098-105.

DANEMAN, R. & PRAT, A. 2015. The blood-brain barrier. *Cold Spring Harb Perspect Biol,* 7**,** a020412.

DARSHI, M., MENDIOLA, V. L., MACKEY, M. R., MURPHY, A. N., KOLLER, A., PERKINS, G. A., ELLISMAN, M. H. & TAYLOR, S. S. 2011. ChChd3, an inner mitochondrial membrane protein, is essential for maintaining crista integrity and mitochondrial function. *J Biol Chem,* 286**,** 2918-32.

DE HAAS, R., DAS, D., GARANTO, A., RENKEMA, H. G., GREUPINK, R., VAN DEN BROEK, P., PERTIJS, J., COLLIN, R. W. J., WILLEMS, P., BEYRATH, J., HEERSCHAP, A., RUSSEL, F. G. & SMEITINK, J. A. 2017. Therapeutic effects of the mitochondrial ROS-redox modulator KH176 in a mammalian model of Leigh Disease. *Sci Rep,* 7**,** 11733.

DE VRIES, M. C., RODENBURG, R. J., MORAVA, E., VAN KAAUWEN, E. P., TER LAAK, H., MULLAART, R. A., SNOECK, I. N., VAN HASSELT, P. M., HARDING, P., VAN DEN HEUVEL, L. P. & SMEITINK, J. A. 2007. Multiple oxidative phosphorylation deficiencies in severe childhood multi-system disorders due to polymerase gamma (POLG1) mutations. *Eur J Pediatr,* 166**,** 229-34.

DEBALSI, K. L., LONGLEY, M. J., HOFF, K. E. & COPELAND, W. C. 2017. Synergistic Effects of the in cis T251I and P587L Mitochondrial DNA Polymerase gamma Disease Mutations. *J Biol Chem,* 292**,** 4198-4209.

DEL DOTTO, V., ULLAH, F., DI MEO, I., MAGINI, P., GUSIC, M., MARESCA, A., CAPORALI, L., PALOMBO, F., TAGLIAVINI, F., BAUGH, E. H., MACAO, B., SZILAGYI, Z., PERON, C., GUSTAFSON, M. A., KHAN, K., LA MORGIA, C., BARBONI, P., CARBONELLI, M., VALENTINO, M. L., LIGUORI, R., SHASHI, V., SULLIVAN, J., NAGARAJ, S., EL-DAIRI, M., IANNACCONE, A., CUTCUTACHE, I., BERTINI, E., CARROZZO, R., EMMA, F., DIOMEDI-CAMASSEI, F., ZANNA, C., ARMSTRONG, M., PAGE, M., STONG, N., BOESCH, S., KOPAJTICH, R., WORTMANN, S., SPERL, W., DAVIS, E. E., COPELAND, W. C., SERI, M., FALKENBERG, M., PROKISCH, H., KATSANIS, N., TIRANTI, V., PIPPUCCI, T. & CARELLI, V. 2020. SSBP1 mutations cause mtDNA depletion underlying a complex optic atrophy disorder. *J Clin Invest,* 130**,** 108-125.

DEMISHTEIN-ZOHARY, K., GUNSEL, U., MAROM, M., BANERJEE, R., NEUPERT, W., AZEM, A. & MOKRANJAC, D. 2017. Role of Tim17 in coupling the import motor to the translocation channel of the mitochondrial presequence translocase. *Elife,* 6.

DEVERMAN, B. E., PRAVDO, P. L., SIMPSON, B. P., KUMAR, S. R., CHAN, K. Y., BANERJEE, A., WU, W. L., YANG, B., HUBER, N., PASCA, S. P. & GRADINARU, V. 2016. Cre-dependent selection yields AAV variants for widespread gene transfer to the adult brain. *Nat Biotechnol,* 34**,** 204-9.

DI MEO, I., MARCHET, S., LAMPERTI, C., ZEVIANI, M. & VISCOMI, C. 2017. AAV9-based gene therapy partially ameliorates the clinical phenotype of a mouse model of Leigh syndrome. *Gene Ther,* 24**,** 661-667.

DI RE, M., SEMBONGI, H., HE, J., REYES, A., YASUKAWA, T., MARTINSSON, P., BAILEY, L. J., GOFFART, S., BOYD-KIRKUP, J. D., WONG, T. S., FERSHT, A. R., SPELBRINK, J. N. & HOLT, I. J. 2009. The accessory subunit of mitochondrial DNA polymerase gamma determines the DNA content of mitochondrial nucleoids in human cultured cells. *Nucleic Acids Res,* 37**,** 5701-13.

DIAZ, F., BAYONA-BAFALUY, M. P., RANA, M., MORA, M., HAO, H. & MORAES, C. T. 2002. Human mitochondrial DNA with large deletions repopulates organelles faster than full-length genomes under relaxed copy number control. *Nucleic Acids Res,* 30**,** 4626-33.

DING, W. X. & YIN, X. M. 2012. Mitophagy: mechanisms, pathophysiological roles, and analysis. *Biol Chem,* 393**,** 547-64.

DO, Y., MATSUDA, S., INATOMI, T., NAKADA, K., YASUKAWA, T. & KANG, D. 2020. The accessory subunit of human DNA polymerase gamma is required for mitochondrial DNA maintenance and is able to stabilize the catalytic subunit. *Mitochondrion,* 53**,** 133-139.

DODA, J. N., WRIGHT, C. T. & CLAYTON, D. A. 1981. Elongation of displacement-loop strands in human and mouse mitochondrial DNA is arrested near specific template sequences. *Proc Natl Acad Sci U S A,* 78**,** 6116-20.

DOGAN, S. A., CERUTTI, R., BENINCA, C., BREA-CALVO, G., JACOBS, H. T., ZEVIANI, M., SZIBOR, M. & VISCOMI, C. 2018. Perturbed Redox Signaling Exacerbates a Mitochondrial Myopathy. *Cell Metab,* 28**,** 764-775 e5.

DOOLITTLE, W. F. 1998. You are what you eat: a gene transfer ratchet could account for bacterial genes in eukaryotic nuclear genomes. *Trends Genet,* 14**,** 307-11.

DROGE, W. 2002. Free radicals in the physiological control of cell function. *Physiol Rev,* 82**,** 47-95.

DZBEK, J. & KORZENIEWSKI, B. 2008. Control over the contribution of the mitochondrial membrane potential (DeltaPsi) and proton gradient (DeltapH) to the protonmotive force (Deltap). In silico studies. *J Biol Chem,* 283**,** 33232-9.

EDMONDSON, C., ZHOU, Q. & LIU, X. 2021. Analysis of conventional and alternative CRISPR/Cas9 genome editing to enhance a single-base pair knock-in mutation. *BMC Biotechnol,* 21**,** 45.

EKSTRAND, M. I., FALKENBERG, M., RANTANEN, A., PARK, C. B., GASPARI, M., HULTENBY, K., RUSTIN, P., GUSTAFSSON, C. M. & LARSSON, N. G. 2004. Mitochondrial transcription factor A regulates mtDNA copy number in mammals. *Hum Mol Genet,* 13**,** 935-44.

EMBLEY, T. M. & MARTIN, W. 2006. Eukaryotic evolution, changes and challenges. *Nature,* 440**,** 623-30.

ERNSTER, L., IKKOS, D. & LUFT, R. 1959. Enzymic activities of human skeletal muscle mitochondria: a tool in clinical metabolic research. *Nature,* 184**,** 1851-4.

ERNSTER, L. & SCHATZ, G. 1981. Mitochondria: a historical review. *J Cell Biol,* 91**,** 227s-255s.

FALKENBERG, M. & GUSTAFSSON, C. M. 2020. Mammalian mitochondrial DNA replication and mechanisms of deletion formation. *Crit Rev Biochem Mol Biol,* 55**,** 509-524.

FALKENBERG, M., LARSSON, N. G. & GUSTAFSSON, C. M. 2007. DNA replication and transcription in mammalian mitochondria. *Annu Rev Biochem,* 76**,** 679-99.

FARGE, G., MEHMEDOVIC, M., BACLAYON, M., VAN DEN WILDENBERG, S. M., ROOS, W. H., GUSTAFSSON, C. M., WUITE, G. J. & FALKENBERG, M. 2014. In vitro-reconstituted nucleoids can block mitochondrial DNA replication and transcription. *Cell Rep,* 8**,** 66-74.

FERRARI, G., LAMANTEA, E., DONATI, A., FILOSTO, M., BRIEM, E., CARRARA, F., PARINI, R., SIMONATI, A., SANTER, R. & ZEVIANI, M. 2005. Infantile hepatocerebral syndromes associated with mutations in the mitochondrial DNA polymerase-gammaA. *Brain,* 128**,** 723-31.

FINSTERER, J. & FRANK, M. 2017. Gastrointestinal manifestations of mitochondrial disorders: a systematic review. *Therap Adv Gastroenterol,* 10**,** 142-154.

FISHER, R. P., TOPPER, J. N. & CLAYTON, D. A. 1987. Promoter selection in human mitochondria involves binding of a transcription factor to orientation-independent upstream regulatory elements. *Cell,* 50**,** 247-58.

FOLKER, E. S. & BAYLIES, M. K. 2013. Nuclear positioning in muscle development and disease. *Front Physiol,* 4**,** 363.

FONTANA, R. J., WATKINS, P. B., BONKOVSKY, H. L., CHALASANI, N., DAVERN, T., SERRANO, J., ROCHON, J. & GROUP, D. S. 2009. Drug-Induced Liver Injury Network (DILIN) prospective study: rationale, design and conduct. *Drug Saf,* 32**,** 55-68.

FOUST, K. D., NURRE, E., MONTGOMERY, C. L., HERNANDEZ, A., CHAN, C. M. & KASPAR, B. K. 2009. Intravascular AAV9 preferentially targets neonatal neurons and adult astrocytes. *Nat Biotechnol,* 27**,** 59-65.

FOX, M. S. & LITTLEFIELD, J. W. 1971. Reservations concerning gene therapy. *Science,* 173**,** 195.

FRIDLENDER, B., FRY, M., BOLDEN, A. & WEISSBACH, A. 1972. A new synthetic RNA-dependent DNA polymerase from human tissue culture cells (HeLa-fibroblast-synthetic oligonucleotides-template-purified enzymes). *Proc Natl Acad Sci U S A,* 69**,** 452-5.

FUKE, S., KUBOTA-SAKASHITA, M., KASAHARA, T., SHIGEYOSHI, Y. & KATO, T. 2011. Regional variation in mitochondrial DNA copy number in mouse brain. *Biochim Biophys Acta,* 1807**,** 270-4.

FUSTE, J. M., WANROOIJ, S., JEMT, E., GRANYCOME, C. E., CLUETT, T. J., SHI, Y., ATANASSOVA, N., HOLT, I. J., GUSTAFSSON, C. M. & FALKENBERG, M. 2010. Mitochondrial RNA polymerase is needed for activation of the origin of light-strand DNA replication. *Mol Cell,* 37**,** 67-78.

GAO, G., VANDENBERGHE, L. H., ALVIRA, M. R., LU, Y., CALCEDO, R., ZHOU, X. & WILSON, J. M. 2004. Clades of Adeno-associated viruses are widely disseminated in human tissues. *J Virol,* 78**,** 6381-8.

GAO, G. P., ALVIRA, M. R., WANG, L., CALCEDO, R., JOHNSTON, J. & WILSON, J. M. 2002. Novel adeno-associated viruses from rhesus monkeys as vectors for human gene therapy. *Proc Natl Acad Sci U S A,* 99**,** 11854-9.

GAO, Y., IRVINE, E. E., ELEFTHERIADOU, I., NARANJO, C. J., HEARN-YEATES, F., BOSCH, L., GLEGOLA, J. A., MURDOCH, L., CZERNIAK, A., MELONI, I., RENIERI, A., KINALI, M. & MAZARAKIS, N. D. 2020. Gene replacement ameliorates deficits in mouse and human models of cyclin-dependent kinase-like 5 disorder. *Brain,* 143**,** 811-832.

GARNEAU, J. E., DUPUIS, M. E., VILLION, M., ROMERO, D. A., BARRANGOU, R., BOYAVAL, P., FREMAUX, C., HORVATH, P., MAGADAN, A. H. & MOINEAU, S. 2010. The CRISPR/Cas bacterial immune system cleaves bacteriophage and plasmid DNA. *Nature,* 468**,** 67-71.

GARONE, C., GARCIA-DIAZ, B., EMMANUELE, V., LOPEZ, L. C., TADESSE, S., AKMAN, H. O., TANJI, K., QUINZII, C. M. & HIRANO, M. 2014. Deoxypyrimidine monophosphate bypass therapy for thymidine kinase 2 deficiency. *EMBO Mol Med,* 6**,** 1016-27.

GARONE, C. & VISCOMI, C. 2018. Towards a therapy for mitochondrial disease: an update. *Biochem Soc Trans,* 46**,** 1247-1261.

GASPARI, M., FALKENBERG, M., LARSSON, N. G. & GUSTAFSSON, C. M. 2004. The mitochondrial RNA polymerase contributes critically to promoter specificity in mammalian cells. *EMBO J,* 23**,** 4606-14.

GENSLER, S., WEBER, K., SCHMITT, W. E., PEREZ-MARTOS, A., ENRIQUEZ, J. A., MONTOYA, J. & WIESNER, R. J. 2001. Mechanism of mammalian mitochondrial DNA replication: import of mitochondrial transcription factor A into isolated mitochondria stimulates 7S DNA synthesis. *Nucleic Acids Res,* 29**,** 3657-63.

GHEZZI, D. & ZEVIANI, M. 2018. Human diseases associated with defects in assembly of OXPHOS complexes. *Essays Biochem,* 62**,** 271-286.

GILLET, J. P., MACADANGDANG, B., FATHKE, R. L., GOTTESMAN, M. M. & KIMCHI-SARFATY, C. 2009. The development of gene therapy: from monogenic recessive disorders to complex diseases such as cancer. *Methods Mol Biol,* 542**,** 5-54.

GILLUM, A. M. & CLAYTON, D. A. 1979. Mechanism of mitochondrial DNA replication in mouse L-cells: RNA priming during the initiation of heavy-strand synthesis. *J Mol Biol,* 135**,** 353-68.

GIORDANO, C., IOMMARINI, L., GIORDANO, L., MARESCA, A., PISANO, A., VALENTINO, M. L., CAPORALI, L., LIGUORI, R., DECEGLIE, S., ROBERTI, M., FANELLI, F., FRACASSO, F., ROSS-CISNEROS, F. N., D'ADAMO, P., HUDSON, G., PYLE, A., YU-WAI-MAN, P., CHINNERY, P. F., ZEVIANI, M., SALOMAO, S. R., BEREZOVSKY, A., BELFORT, R., JR., VENTURA, D. F., MORAES, M., MORAES FILHO, M., BARBONI, P., SADUN, F., DE NEGRI, A., SADUN, A. A., TANCREDI, A., MANCINI, M., D'AMATI, G., LOGUERCIO POLOSA, P., CANTATORE, P. & CARELLI, V. 2014. Efficient mitochondrial biogenesis drives incomplete penetrance in Leber's hereditary optic neuropathy. *Brain,* 137**,** 335-53.

GORMAN, G. S., CHINNERY, P. F., DIMAURO, S., HIRANO, M., KOGA, Y., MCFARLAND, R., SUOMALAINEN, A., THORBURN, D. R., ZEVIANI, M. & TURNBULL, D. M. 2016. Mitochondrial diseases. *Nat Rev Dis Primers,* 2**,** 16080.

GORMAN, G. S., SCHAEFER, A. M., NG, Y., GOMEZ, N., BLAKELY, E. L., ALSTON, C. L., FEENEY, C., HORVATH, R., YU-WAI-MAN, P., CHINNERY, P. F., TAYLOR, R. W., TURNBULL, D. M. & MCFARLAND, R. 2015. Prevalence of nuclear and

mitochondrial DNA mutations related to adult mitochondrial disease. *Ann Neurol,* 77**,** 753-9.

GRANGE, R. M. H., SHARMA, R., SHAH, H., REINSTADLER, B., GOLDBERGER, O., COOPER, M. K., NAKAGAWA, A., MIYAZAKI, Y., HINDLE, A. G., BATTEN, A. J., WOJTKIEWICZ, G. R., SCHLEIFER, G., BAGCHI, A., MARUTANI, E., MALHOTRA, R., BLOCH, D. B., ICHINOSE, F., MOOTHA, V. K. & ZAPOL, W. M. 2021. Hypoxia ameliorates brain hyperoxia and NAD(+) deficiency in a murine model of Leigh syndrome. *Mol Genet Metab,* 133**,** 83-93.

GRAY, H. & WONG, T. W. 1992. Purification and identification of subunit structure of the human mitochondrial DNA polymerase. *J Biol Chem,* 267**,** 5835-41.

GRAZIEWICZ, M. A., LONGLEY, M. J., BIENSTOCK, R. J., ZEVIANI, M. & COPELAND, W. C. 2004. Structure-function defects of human mitochondrial DNA polymerase in autosomal dominant progressive external ophthalmoplegia. *Nat Struct Mol Biol,* 11**,** 770-6.

GROSS, N. J., GETZ, G. S. & RABINOWITZ, M. 1969. Apparent turnover of mitochondrial deoxyribonucleic acid and mitochondrial phospholipids in the tissues of the rat. *J Biol Chem,* 244**,** 1552-62.

GUSTAFSSON, C. M., FALKENBERG, M. & LARSSON, N. G. 2016. Maintenance and Expression of Mammalian Mitochondrial DNA. *Annu Rev Biochem,* 85**,** 133-60.

HALLBERG, B. M. & LARSSON, N. G. 2011. TFAM forces mtDNA to make a U-turn. *Nat Struct Mol Biol,* 18**,** 1179-81.

HALLIWELL, B. & CROSS, C. E. 1994. Oxygen-derived species: their relation to human disease and environmental stress. *Environ Health Perspect,* 102 Suppl 10**,** 5-12.

HANCE, N., EKSTRAND, M. I. & TRIFUNOVIC, A. 2005. Mitochondrial DNA polymerase gamma is essential for mammalian embryogenesis. *Hum Mol Genet,* 14**,** 1775-83.

HANSON, P. I. & WHITEHEART, S. W. 2005. AAA+ proteins: have engine, will work. *Nat Rev Mol Cell Biol,* 6**,** 519-29.

HARDING, B. N. 1990. Progressive neuronal degeneration of childhood with liver disease (Alpers-Huttenlocher syndrome): a personal review. *J Child Neurol,* 5**,** 273-87.

HATEFI, Y. 1985. The mitochondrial electron transport and oxidative phosphorylation system. *Annu Rev Biochem,* 54**,** 1015-69.

HILLEN, H. S., MOROZOV, Y. I., SARFALLAH, A., TEMIAKOV, D. & CRAMER, P. 2017a. Structural Basis of Mitochondrial Transcription Initiation. *Cell,* 171**,** 1072-1081 e10.

HILLEN, H. S., PARSHIN, A. V., AGARONYAN, K., MOROZOV, Y. I., GRABER, J. J., CHERNEV, A., SCHWINGHAMMER, K., URLAUB, H., ANIKIN, M., CRAMER, P. & TEMIAKOV, D. 2017b. Mechanism of Transcription Anti-termination in Human Mitochondria. *Cell,* 171**,** 1082-1093 e13.

HIMMS-HAGEN, J. 1984. Nonshivering thermogenesis. *Brain Res Bull,* 12**,** 151-60.

HINDERER, C., KATZ, N., BUZA, E. L., DYER, C., GOODE, T., BELL, P., RICHMAN, L. K. & WILSON, J. M. 2018. Severe Toxicity in Nonhuman Primates and Piglets Following High-Dose Intravenous Administration of an Adeno-Associated Virus Vector Expressing Human SMN. *Hum Gene Ther,* 29**,** 285-298.

HIRST, J. 2013. Mitochondrial complex I. *Annu Rev Biochem,* 82**,** 551-75.

HOLEC, A. D., MANDAL, S., PRATHIPATI, P. K. & DESTACHE, C. J. 2017. Nucleotide Reverse Transcriptase Inhibitors: A Thorough Review, Present Status and Future Perspective as HIV Therapeutics. *Curr HIV Res,* 15**,** 411-421.

HOLMES, J. B., AKMAN, G., WOOD, S. R., SAKHUJA, K., CERRITELLI, S. M., MOSS, C., BOWMAKER, M. R., JACOBS, H. T., CROUCH, R. J. & HOLT, I. J. 2015. Primer retention owing to the absence of RNase H1 is catastrophic for mitochondrial DNA replication. *Proc Natl Acad Sci U S A,* 112**,** 9334-9.

HOLT, I. J., LORIMER, H. E. & JACOBS, H. T. 2000. Coupled leading- and lagging-strand synthesis of mammalian mitochondrial DNA. *Cell,* 100**,** 515-24.

HOPPINS, S., LACKNER, L. & NUNNARI, J. 2007. The machines that divide and fuse mitochondria. *Annu Rev Biochem,* 76**,** 751-80.

HORDEAUX, J., YUAN, Y., CLARK, P. M., WANG, Q., MARTINO, R. A., SIMS, J. J., BELL, P., RAYMOND, A., STANFORD, W. L. & WILSON, J. M. 2019. The GPI-Linked Protein LY6A Drives AAV-PHP.B Transport across the Blood-Brain Barrier. *Mol Ther,* 27**,** 912-921.

HORVATH, R., HUDSON, G., FERRARI, G., FUTTERER, N., AHOLA, S., LAMANTEA, E., PROKISCH, H., LOCHMULLER, H., MCFARLAND, R., RAMESH, V., KLOPSTOCK, T., FREISINGER, P., SALVI, F., MAYR, J. A., SANTER, R., TESAROVA, M., ZEMAN, J., UDD, B., TAYLOR, R. W., TURNBULL, D., HANNA, M., FIALHO, D., SUOMALAINEN, A., ZEVIANI, M. & CHINNERY, P. F. 2006. Phenotypic spectrum associated with mutations of the mitochondrial polymerase gamma gene. *Brain,* 129**,** 1674-84.

HUANG, Q., CHAN, K. Y., TOBEY, I. G., CHAN, Y. A., POTERBA, T., BOUTROS, C. L., BALAZS, A. B., DANEMAN, R., BLOOM, J. M., SEED, C. & DEVERMAN, B. E. 2019. Delivering genes across the blood-brain barrier: LY6A, a novel cellular receptor for AAV-PHP.B capsids. *PLoS One,* 14**,** e0225206.

HUDRY, E. & VANDENBERGHE, L. H. 2019. Therapeutic AAV Gene Transfer to the Nervous System: A Clinical Reality. *Neuron,* 101**,** 839-862.

HUG, L. A., STECHMANN, A. & ROGER, A. J. 2010. Phylogenetic distributions and histories of proteins involved in anaerobic pyruvate metabolism in eukaryotes. *Mol Biol Evol,* 27**,** 311-24.

HUMBLE, M. M., YOUNG, M. J., FOLEY, J. F., PANDIRI, A. R., TRAVLOS, G. S. & COPELAND, W. C. 2013. Polg2 is essential for mammalian embryogenesis and is required for mtDNA maintenance. *Hum Mol Genet,* 22**,** 1017-25.

INAGAKI, K., FUESS, S., STORM, T. A., GIBSON, G. A., MCTIERNAN, C. F., KAY, M. A. & NAKAI, H. 2006. Robust systemic transduction with AAV9 vectors in mice: efficient global cardiac gene transfer superior to that of AAV8. *Mol Ther,* 14**,** 45-53.

INAK, G., RYBAK-WOLF, A., LISOWSKI, P., PENTIMALLI, T. M., JUTTNER, R., GLAZAR, P., UPPAL, K., BOTTANI, E., BRUNETTI, D., SECKER, C., ZINK, A., MEIERHOFER, D., HENKE, M. T., DEY, M., CIPTASARI, U., MLODY, B., HAHN, T., BERRUEZO-LLACUNA, M., KARAISKOS, N., DI VIRGILIO, M., MAYR, J. A., WORTMANN, S. B., PRILLER, J., GOTTHARDT, M., JONES, D. P., MAYATEPEK, E., STENZEL, W., DIECKE, S., KUHN, R., WANKER, E. E., RAJEWSKY, N., SCHUELKE, M. & PRIGIONE, A. 2021. Defective metabolic programming impairs early neuronal

morphogenesis in neural cultures and an organoid model of Leigh syndrome. *Nat Commun,* 12**,** 1929.

IRELAND, H., KEMP, R., HOUGHTON, C., HOWARD, L., CLARKE, A. R., SANSOM, O. J. & WINTON, D. J. 2004. Inducible Cre-mediated control of gene expression in the murine gastrointestinal tract: effect of loss of beta-catenin. *Gastroenterology,* 126**,** 1236-46.

JASTROCH, M., DIVAKARUNI, A. S., MOOKERJEE, S., TREBERG, J. R. & BRAND, M. D. 2010. Mitochondrial proton and electron leaks. *Essays Biochem,* 47**,** 53-67.

JAZAYERI, M., ANDREYEV, A., WILL, Y., WARD, M., ANDERSON, C. M. & CLEVENGER, W. 2003. Inducible expression of a dominant negative DNA polymerase-gamma depletes mitochondrial DNA and produces a rho0 phenotype. *J Biol Chem,* 278**,** 9823-30.

JEMT, E., PERSSON, O., SHI, Y., MEHMEDOVIC, M., UHLER, J. P., DAVILA LOPEZ, M., FREYER, C., GUSTAFSSON, C. M., SAMUELSSON, T. & FALKENBERG, M. 2015. Regulation of DNA replication at the end of the mitochondrial D-loop involves the helicase TWINKLE and a conserved sequence element. *Nucleic Acids Res,* 43**,** 9262-75.

JIANG, M., XIE, X., ZHU, X., JIANG, S., MILENKOVIC, D., MISIC, J., SHI, Y., TANDUKAR, N., LI, X., ATANASSOV, I., JENNINGER, L., HOBERG, E., ALBARRAN-GUTIERREZ, S., SZILAGYI, Z., MACAO, B., SIIRA, S. J., CARELLI, V., GRIFFITH, J. D., GUSTAFSSON, C. M., NICHOLLS, T. J., FILIPOVSKA, A., LARSSON, N. G. & FALKENBERG, M. 2021. The mitochondrial single-stranded DNA binding protein is essential for initiation of mtDNA replication. *Sci Adv,* 7.

JIANG, S., KOOLMEISTER, C., MISIC, J., SIIRA, S., KUHL, I., SILVA RAMOS, E., MIRANDA, M., JIANG, M., POSSE, V., LYTOVCHENKO, O., ATANASSOV, I., SCHOBER, F. A., WIBOM, R., HULTENBY, K., MILENKOVIC, D., GUSTAFSSON, C. M., FILIPOVSKA, A. & LARSSON, N. G. 2019. TEFM regulates both transcription elongation and RNA processing in mitochondria. *EMBO Rep,* 20.

JIMENEZ-MENENDEZ, N., FERNANDEZ-MILLAN, P., RUBIO-COSIALS, A., ARNAN, C., MONTOYA, J., JACOBS, H. T., BERNADO, P., COLL, M., USON, I. & SOLA, M. 2010. Human mitochondrial mTERF wraps around DNA through a left-handed superhelical tandem repeat. *Nat Struct Mol Biol,* 17**,** 891-3.

JOHANNESSEN, C. U. 2000. Mechanisms of action of valproate: a commentatory. *Neurochem Int,* 37**,** 103-10.

KANDUC, D., MITTELMAN, A., SERPICO, R., SINIGAGLIA, E., SINHA, A. A., NATALE, C., SANTACROCE, R., DI CORCIA, M. G., LUCCHESE, A., DINI, L., PANI, P., SANTACROCE, S., SIMONE, S., BUCCI, R. & FARBER, E. 2002. Cell death: apoptosis versus necrosis (review). *Int J Oncol,* 21**,** 165-70.

KANG, S. G., ORTEGA, J., SINGH, S. K., WANG, N., HUANG, N. N., STEVEN, A. C. & MAURIZI, M. R. 2002. Functional proteolytic complexes of the human mitochondrial ATP-dependent protease, hClpXP. *J Biol Chem,* 277**,** 21095-102.

KASAMATSU, H., ROBBERSON, D. L. & VINOGRAD, J. 1971. A novel closed-circular mitochondrial DNA with properties of a replicating intermediate. *Proc Natl Acad Sci U S A,* 68**,** 2252-7.

KASIVISWANATHAN, R., LONGLEY, M. J., YOUNG, M. J. & COPELAND, W. C. 2010. Purification and functional characterization of human mitochondrial DNA polymerase gamma harboring disease mutations. *Methods,* 51**,** 379-84.

KAUFMAN, B. A., DURISIC, N., MATIVETSKY, J. M., COSTANTINO, S., HANCOCK, M. A., GRUTTER, P. & SHOUBRIDGE, E. A. 2007. The mitochondrial transcription factor TFAM coordinates the assembly of multiple DNA molecules into nucleoid-like structures. *Mol Biol Cell,* 18**,** 3225-36.

KELLY, R. D., MAHMUD, A., MCKENZIE, M., TROUNCE, I. A. & ST JOHN, J. C. 2012. Mitochondrial DNA copy number is regulated in a tissue specific manner by DNA methylation of the nuclear-encoded DNA polymerase gamma A. *Nucleic Acids Res,* 40**,** 10124-38.

KEREICHE, S., KOVACIK, L., BEDNAR, J., PEVALA, V., KUNOVA, N., ONDROVICOVA, G., BAUER, J., AMBRO, L., BELLOVA, J., KUTEJOVA, E. & RASKA, I. 2016. The N-terminal domain plays a crucial role in the structure of a full-length human mitochondrial Lon protease. *Sci Rep,* 6**,** 33631.

KHIATI, S., BAECHLER, S. A., FACTOR, V. M., ZHANG, H., HUANG, S. Y., DALLA ROSA, I., SOURBIER, C., NECKERS, L., THORGEIRSSON, S. S. & POMMIER, Y. 2015. Lack of mitochondrial topoisomerase I (TOP1mt) impairs liver regeneration. *Proc Natl Acad Sci U S A,* 112**,** 11282-7.

KIRKMAN, M. A., YU-WAI-MAN, P., KORSTEN, A., LEONHARDT, M., DIMITRIADIS, K., DE COO, I. F., KLOPSTOCK, T. & CHINNERY, P. F. 2009. Gene-environment interactions in Leber hereditary optic neuropathy. *Brain,* 132**,** 2317-26.

KOONIN, E. V. 2010. The origin and early evolution of eukaryotes in the light of phylogenomics. *Genome Biol,* 11**,** 209.

KORHONEN, J. A., GASPARI, M. & FALKENBERG, M. 2003. TWINKLE Has 5' -> 3' DNA helicase activity and is specifically stimulated by mitochondrial single-stranded DNA-binding protein. *J Biol Chem,* 278**,** 48627-32.

KORHONEN, J. A., PHAM, X. H., PELLEGRINI, M. & FALKENBERG, M. 2004. Reconstitution of a minimal mtDNA replisome in vitro. *EMBO J,* 23**,** 2423-9.

KORNBERG, A. & BAKER, T. A. 1972. *DNA replication*, New York: Wh Freeman.

KORNBLUM, C., NICHOLLS, T. J., HAACK, T. B., SCHOLER, S., PEEVA, V., DANHAUSER, K., HALLMANN, K., ZSURKA, G., RORBACH, J., IUSO, A., WIELAND, T., SCIACCO, M., RONCHI, D., COMI, G. P., MOGGIO, M., QUINZII, C. M., DIMAURO, S., CALVO, S. E., MOOTHA, V. K., KLOPSTOCK, T., STROM, T. M., MEITINGER, T., MINCZUK, M., KUNZ, W. S. & PROKISCH, H. 2013. Loss-of-function mutations in MGME1 impair mtDNA replication and cause multisystemic mitochondrial disease. *Nat Genet,* 45**,** 214-9.

KOSHIBA, T., DETMER, S. A., KAISER, J. T., CHEN, H., MCCAFFERY, J. M. & CHAN, D. C. 2004. Structural basis of mitochondrial tethering by mitofusin complexes. *Science,* 305**,** 858-62.

KRUSE, S. E., WATT, W. C., MARCINEK, D. J., KAPUR, R. P., SCHENKMAN, K. A. & PALMITER, R. D. 2008. Mice with mitochondrial complex I deficiency develop a fatal encephalomyopathy. *Cell Metab,* 7**,** 312-20.

KU, C., NELSON-SATHI, S., ROETTGER, M., SOUSA, F. L., LOCKHART, P. J., BRYANT, D., HAZKANI-COVO, E., MCINERNEY, J. O., LANDAN, G. & MARTIN, W. F. 2015.

Endosymbiotic origin and differential loss of eukaryotic genes. *Nature,* 524**,** 427-32.

KUHL, I., MIRANDA, M., POSSE, V., MILENKOVIC, D., MOURIER, A., SIIRA, S. J., BONEKAMP, N. A., NEUMANN, U., FILIPOVSKA, A., POLOSA, P. L., GUSTAFSSON, C. M. & LARSSON, N. G. 2016. POLRMT regulates the switch between replication primer formation and gene expression of mammalian mtDNA. *Sci Adv,* 2**,** e1600963.

KUHLBRANDT, W. 2015. Structure and function of mitochondrial membrane protein complexes. *BMC Biol,* 13**,** 89.

KUKAT, C., DAVIES, K. M., WURM, C. A., SPAHR, H., BONEKAMP, N. A., KUHL, I., JOOS, F., POLOSA, P. L., PARK, C. B., POSSE, V., FALKENBERG, M., JAKOBS, S., KUHLBRANDT, W. & LARSSON, N. G. 2015. Cross-strand binding of TFAM to a single mtDNA molecule forms the mitochondrial nucleoid. *Proc Natl Acad Sci U S A,* 112**,** 11288-93.

KUKAT, C., WURM, C. A., SPAHR, H., FALKENBERG, M., LARSSON, N. G. & JAKOBS, S. 2011. Super-resolution microscopy reveals that mammalian mitochondrial nucleoids have a uniform size and frequently contain a single copy of mtDNA. *Proc Natl Acad Sci U S A,* 108**,** 13534-9.

KUNJI, E. R. 2004. The role and structure of mitochondrial carriers. *FEBS Lett,* 564**,** 239-44.

KUNJI, E. R., ALEKSANDROVA, A., KING, M. S., MAJD, H., ASHTON, V. L., CERSON, E., SPRINGETT, R., KIBALCHENKO, M., TAVOULARI, S., CRICHTON, P. G. & RUPRECHT, J. J. 2016. The transport mechanism of the mitochondrial ADP/ATP carrier. *Biochim Biophys Acta,* 1863**,** 2379-93.

LAHEY, H. G., WEBBER, C. J., GOLEBIOWSKI, D., IZZO, C. M., HORN, E., TAGHIAN, T., RODRIGUEZ, P., BATISTA, A. R., ELLIS, L. E., HWANG, M., MARTIN, D. R., GRAY-EDWARDS, H. & SENA-ESTEVES, M. 2020. Pronounced Therapeutic Benefit of a Single Bidirectional AAV Vector Administered Systemically in Sandhoff Mice. *Mol Ther,* 28**,** 2150-2160.

LANE, N. & MARTIN, W. 2010. The energetics of genome complexity. *Nature,* 467**,** 929-34.

LARSSON, N. G., OLDFORS, A., HOLME, E. & CLAYTON, D. A. 1994. Low levels of mitochondrial transcription factor A in mitochondrial DNA depletion. *Biochem Biophys Res Commun,* 200**,** 1374-81.

LARSSON, N. G., WANG, J., WILHELMSSON, H., OLDFORS, A., RUSTIN, P., LEWANDOSKI, M., BARSH, G. S. & CLAYTON, D. A. 1998. Mitochondrial transcription factor A is necessary for mtDNA maintenance and embryogenesis in mice. *Nat Genet,* 18**,** 231-6.

LEBON, S., CHOL, M., BENIT, P., MUGNIER, C., CHRETIEN, D., GIURGEA, I., KERN, I., GIRARDIN, E., HERTZ-PANNIER, L., DE LONLAY, P., ROTIG, A., RUSTIN, P. & MUNNICH, A. 2003. Recurrent de novo mitochondrial DNA mutations in respiratory chain deficiency. *J Med Genet,* 40**,** 896-9.

LEE, Y. G., KIM, H. W., NAM, Y., SHIN, K. J., LEE, Y. J., PARK, D. H., RHEE, H. W., SEO, J. K. & CHAE, Y. C. 2021. LONP1 and ClpP cooperatively regulate mitochondrial proteostasis for cancer cell survival. *Oncogenesis,* 10**,** 18.

LEE, Y. S., KENNEDY, W. D. & YIN, Y. W. 2009. Structural insight into processive human mitochondrial DNA synthesis and disease-related polymerase mutations. *Cell,* 139**,** 312-24.

LEGROS, F., MALKA, F., FRACHON, P., LOMBES, A. & ROJO, M. 2004. Organization and dynamics of human mitochondrial DNA. *J Cell Sci,* 117**,** 2653-62.

LEWIS, W., DAY, B. J. & COPELAND, W. C. 2003. Mitochondrial toxicity of NRTI antiviral drugs: an integrated cellular perspective. *Nat Rev Drug Discov,* 2**,** 812-22.

LI, C. & SAMULSKI, R. J. 2020. Engineering adeno-associated virus vectors for gene therapy. *Nat Rev Genet,* 21**,** 255-272.

LIGUORE, W. A., DOMIRE, J. S., BUTTON, D., WANG, Y., DUFOUR, B. D., SRINIVASAN, S. & MCBRIDE, J. L. 2019. AAV-PHP.B Administration Results in a Differential Pattern of CNS Biodistribution in Non-human Primates Compared with Mice. *Mol Ther,* 27**,** 2018-2037.

LIM, J. A., YI, H., GAO, F., RABEN, N., KISHNANI, P. S. & SUN, B. 2019. Intravenous Injection of an AAV-PHP.B Vector Encoding Human Acid alpha-Glucosidase Rescues Both Muscle and CNS Defects in Murine Pompe Disease. *Mol Ther Methods Clin Dev,* 12**,** 233-245.

LIM, S. E., LONGLEY, M. J. & COPELAND, W. C. 1999. The mitochondrial p55 accessory subunit of human DNA polymerase gamma enhances DNA binding, promotes processive DNA synthesis, and confers N-ethylmaleimide resistance. *J Biol Chem,* 274**,** 38197-203.

LIMA, W. F., ROSE, J. B., NICHOLS, J. G., WU, H., MIGAWA, M. T., WYRZYKIEWICZ, T. K., SIWKOWSKI, A. M. & CROOKE, S. T. 2007. Human RNase H1 discriminates between subtle variations in the structure of the heteroduplex substrate. *Mol Pharmacol,* 71**,** 83-91.

LINDMARK, D. G. & MULLER, M. 1973. Hydrogenosome, a cytoplasmic organelle of the anaerobic flagellate Tritrichomonas foetus, and its role in pyruvate metabolism. *J Biol Chem,* 248**,** 7724-8.

LIVAK, K. J. & SCHMITTGEN, T. D. 2001. Analysis of relative gene expression data using real-time quantitative PCR and the 2(-Delta Delta C(T)) Method. *Methods,* 25**,** 402-8.

LODISH, H. F. 2000. *Molecular cell biology*, New York : W.H. Freeman, c2000.

LONGLEY, M. J., CLARK, S., YU WAI MAN, C., HUDSON, G., DURHAM, S. E., TAYLOR, R. W., NIGHTINGALE, S., TURNBULL, D. M., COPELAND, W. C. & CHINNERY, P. F. 2006. Mutant POLG2 disrupts DNA polymerase gamma subunits and causes progressive external ophthalmoplegia. *Am J Hum Genet,* 78**,** 1026-34.

LONGLEY, M. J., NGUYEN, D., KUNKEL, T. A. & COPELAND, W. C. 2001. The fidelity of human DNA polymerase gamma with and without exonucleolytic proofreading and the p55 accessory subunit. *J Biol Chem,* 276**,** 38555-62.

LONGLEY, M. J., PRASAD, R., SRIVASTAVA, D. K., WILSON, S. H. & COPELAND, W. C. 1998. Identification of 5'-deoxyribose phosphate lyase activity in human DNA polymerase gamma and its role in mitochondrial base excision repair in vitro. *Proc Natl Acad Sci U S A,* 95**,** 12244-8.

LOUGHNER, C. L., BRUFORD, E. A., MCANDREWS, M. S., DELP, E. E., SWAMYNATHAN, S. & SWAMYNATHAN, S. K. 2016. Organization, evolution and functions of the human and mouse Ly6/uPAR family genes. *Hum Genomics,* 10**,** 10.

LU, B., LEE, J., NIE, X., LI, M., MOROZOV, Y. I., VENKATESH, S., BOGENHAGEN, D. F., TEMIAKOV, D. & SUZUKI, C. K. 2013. Phosphorylation of human TFAM in mitochondria impairs DNA binding and promotes degradation by the AAA+ Lon protease. *Mol Cell,* 49**,** 121-32.

LU, B., YADAV, S., SHAH, P. G., LIU, T., TIAN, B., PUKSZTA, S., VILLALUNA, N., KUTEJOVA, E., NEWLON, C. S., SANTOS, J. H. & SUZUKI, C. K. 2007. Roles for the human ATP-dependent Lon protease in mitochondrial DNA maintenance. *J Biol Chem,* 282**,** 17363-74.

MACREADIE, I. G., NOVITSKI, C. E., MAXWELL, R. J., JOHN, U., OOI, B. G., MCMULLEN, G. L., LUKINS, H. B., LINNANE, A. W. & NAGLEY, P. 1983. Biogenesis of mitochondria: the mitochondrial gene (aap1) coding for mitochondrial ATPase subunit 8 in Saccharomyces cerevisiae. *Nucleic Acids Res,* 11**,** 4435-51.

MAGNUSSON, J., ORTH, M., LESTIENNE, P. & TAANMAN, J. W. 2003. Replication of mitochondrial DNA occurs throughout the mitochondria of cultured human cells. *Exp Cell Res,* 289**,** 133-42.

MAHESHRI, N., KOERBER, J. T., KASPAR, B. K. & SCHAFFER, D. V. 2006. Directed evolution of adeno-associated virus yields enhanced gene delivery vectors. *Nat Biotechnol,* 24**,** 198-204.

MAIO, N. & ROUAULT, T. A. 2015. Iron-sulfur cluster biogenesis in mammalian cells: New insights into the molecular mechanisms of cluster delivery. *Biochim Biophys Acta,* 1853**,** 1493-512.

MANIBUSAN, M. K., ODIN, M. & EASTMOND, D. A. 2007. Postulated carbon tetrachloride mode of action: a review. *J Environ Sci Health C Environ Carcinog Ecotoxicol Rev,* 25**,** 185-209.

MARTIN, M., CHO, J., CESARE, A. J., GRIFFITH, J. D. & ATTARDI, G. 2005. Termination factor-mediated DNA loop between termination and initiation sites drives mitochondrial rRNA synthesis. *Cell,* 123**,** 1227-40.

MARTIN, W. & MULLER, M. 1998. The hydrogen hypothesis for the first eukaryote. *Nature,* 392**,** 37-41.

MARTINEZ-CAYUELA, M. 1995. Oxygen free radicals and human disease. *Biochimie,* 77**,** 147-61.

MATIC, S., JIANG, M., NICHOLLS, T. J., UHLER, J. P., DIRKSEN-SCHWANENLAND, C., POLOSA, P. L., SIMARD, M. L., LI, X., ATANASSOV, I., RACKHAM, O., FILIPOVSKA, A., STEWART, J. B., FALKENBERG, M., LARSSON, N. G. & MILENKOVIC, D. 2018. Mice lacking the mitochondrial exonuclease MGME1 accumulate mtDNA deletions without developing progeria. *Nat Commun,* 9**,** 1202.

MATSUSHIMA, Y., GOTO, Y. & KAGUNI, L. S. 2010. Mitochondrial Lon protease regulates mitochondrial DNA copy number and transcription by selective degradation of mitochondrial transcription factor A (TFAM). *Proc Natl Acad Sci U S A,* 107**,** 18410-5.

MATSUZAKI, Y., KONNO, A., MOCHIZUKI, R., SHINOHARA, Y., NITTA, K., OKADA, Y. & HIRAI, H. 2018. Intravenous administration of the adeno-associated virus-PHP.B capsid fails to upregulate transduction efficiency in the marmoset brain. *Neurosci Lett,* 665**,** 182-188.

MATTHEWS, L., ENZINGER, C., FAZEKAS, F., ROVIRA, A., CICCARELLI, O., DOTTI, M. T., FILIPPI, M., FREDERIKSEN, J. L., GIORGIO, A., KUKER, W., LUKAS, C., ROCCA, M.

A., DE STEFANO, N., TOOSY, A., YOUSRY, T., PALACE, J. & NETWORK, M. 2015. MRI in Leber's hereditary optic neuropathy: the relationship to multiple sclerosis. *J Neurol Neurosurg Psychiatry,* 86**,** 537-42.

MCCARRON, J. G., WILSON, C., SANDISON, M. E., OLSON, M. L., GIRKIN, J. M., SAUNTER, C. & CHALMERS, S. 2013. From structure to function: mitochondrial morphology, motion and shaping in vascular smooth muscle. *J Vasc Res,* 50**,** 357-71.

MCFARLAND, R., TAYLOR, R. W. & TURNBULL, D. M. 2010. A neurological perspective on mitochondrial disease. *Lancet Neurol,* 9**,** 829-40.

MEDEIROS, T. C., THOMAS, R. L., GHILLEBERT, R. & GRAEF, M. 2018. Autophagy balances mtDNA synthesis and degradation by DNA polymerase POLG during starvation. *J Cell Biol,* 217**,** 1601-1611.

MENDELL, J. R., AL-ZAIDY, S., SHELL, R., ARNOLD, W. D., RODINO-KLAPAC, L. R., PRIOR, T. W., LOWES, L., ALFANO, L., BERRY, K., CHURCH, K., KISSEL, J. T., NAGENDRAN, S., L'ITALIEN, J., SPROULE, D. M., WELLS, C., CARDENAS, J. A., HEITZER, M. D., KASPAR, A., CORCORAN, S., BRAUN, L., LIKHITE, S., MIRANDA, C., MEYER, K., FOUST, K. D., BURGHES, A. H. M. & KASPAR, B. K. 2017. Single-Dose Gene-Replacement Therapy for Spinal Muscular Atrophy. *N Engl J Med,* 377**,** 1713-1722.

MENTEL, M. & MARTIN, W. 2008. Energy metabolism among eukaryotic anaerobes in light of Proterozoic ocean chemistry. *Philos Trans R Soc Lond B Biol Sci,* 363**,** 2717-29.

MERESCHKOWSKY, K. S. 1905. Über Natur und Ursprung der Chromatophoren im Pflanzenreiche. *Biol. Centralbl.***,** 593–604.

MILENKOVIC, D., MATIC, S., KUHL, I., RUZZENENTE, B., FREYER, C., JEMT, E., PARK, C. B., FALKENBERG, M. & LARSSON, N. G. 2013. TWINKLE is an essential mitochondrial helicase required for synthesis of nascent D-loop strands and complete mtDNA replication. *Hum Mol Genet,* 22**,** 1983-93.

MINTZER, M. A. & SIMANEK, E. E. 2009. Nonviral vectors for gene delivery. *Chem Rev,* 109**,** 259-302.

MIRALLES FUSTE, J., SHI, Y., WANROOIJ, S., ZHU, X., JEMT, E., PERSSON, O., SABOURI, N., GUSTAFSSON, C. M. & FALKENBERG, M. 2014. In vivo occupancy of mitochondrial single-stranded DNA binding protein supports the strand displacement mode of DNA replication. *PLoS Genet,* 10**,** e1004832.

MITCHELL, P. & MOYLE, J. 1969. Estimation of membrane potential and pH difference across the cristae membrane of rat liver mitochondria. *Eur J Biochem,* 7**,** 471-84.

MONTOYA, J., CHRISTIANSON, T., LEVENS, D., RABINOWITZ, M. & ATTARDI, G. 1982. Identification of initiation sites for heavy-strand and light-strand transcription in human mitochondrial DNA. *Proc Natl Acad Sci U S A,* 79**,** 7195-9.

MORAES, C. T. 2001. What regulates mitochondrial DNA copy number in animal cells? *Trends Genet,* 17**,** 199-205.

MOYES, C. D., BATTERSBY, B. J. & LEARY, S. C. 1998. Regulation of muscle mitochondrial design. *J Exp Biol,* 201**,** 299-307.

MURPHY, M. P. 2009. How mitochondria produce reactive oxygen species. *Biochem J,* 417**,** 1-13.

NADANACIVA, S. & WILL, Y. 2011. New insights in drug-induced mitochondrial toxicity. *Curr Pharm Des,* 17**,** 2100-12.

NASO, M. F., TOMKOWICZ, B., PERRY, W. L., 3RD & STROHL, W. R. 2017. Adeno-Associated Virus (AAV) as a Vector for Gene Therapy. *BioDrugs,* 31**,** 317-334.

NASS, M. M. 1966. The circularity of mitochondrial DNA. *Proc Natl Acad Sci U S A,* 56**,** 1215-22.

NAU, H. 1985. Teratogenic valproic acid concentrations: infusion by implanted minipumps vs conventional injection regimen in the mouse. *Toxicol Appl Pharmacol,* 80**,** 243-50.

NAVIAUX, R. K. & NGUYEN, K. V. 2005. POLG mutations associated with Alpers syndrome and mitochondrial DNA depletion. *Ann Neurol,* 58**,** 491.

NEDERGAARD, J., GOLOZOUBOVA, V., MATTHIAS, A., ASADI, A., JACOBSSON, A. & CANNON, B. 2001. UCP1: the only protein able to mediate adaptive non-shivering thermogenesis and metabolic inefficiency. *Biochim Biophys Acta,* 1504**,** 82-106.

NGUYEN, K. V., SHARIEF, F. S., CHAN, S. S., COPELAND, W. C. & NAVIAUX, R. K. 2006. Molecular diagnosis of Alpers syndrome. *J Hepatol,* 45**,** 108-16.

NICHOLLS, D. G. 1974. The influence of respiration and ATP hydrolysis on the proton-electrochemical gradient across the inner membrane of rat-liver mitochondria as determined by ion distribution. *Eur J Biochem,* 50**,** 305-15.

NICHOLLS, T. J. & MINCZUK, M. 2014. In D-loop: 40 years of mitochondrial 7S DNA. *Exp Gerontol,* 56**,** 175-81.

NICHOLLS, T. J., ZSURKA, G., PEEVA, V., SCHOLER, S., SZCZESNY, R. J., CYSEWSKI, D., REYES, A., KORNBLUM, C., SCIACCO, M., MOGGIO, M., DZIEMBOWSKI, A., KUNZ, W. S. & MINCZUK, M. 2014. Linear mtDNA fragments and unusual mtDNA rearrangements associated with pathological deficiency of MGME1 exonuclease. *Hum Mol Genet,* 23**,** 6147-62.

NIKKANEN, J., FORSSTROM, S., EURO, L., PAETAU, I., KOHNZ, R. A., WANG, L., CHILOV, D., VIINAMAKI, J., ROIVAINEN, A., MARJAMAKI, P., LILJENBACK, H., AHOLA, S., BUZKOVA, J., TERZIOGLU, M., KHAN, N. A., PIRNES-KARHU, S., PAETAU, A., LONNQVIST, T., SAJANTILA, A., ISOHANNI, P., TYYNISMAA, H., NOMURA, D. K., BATTERSBY, B. J., VELAGAPUDI, V., CARROLL, C. J. & SUOMALAINEN, A. 2016. Mitochondrial DNA Replication Defects Disturb Cellular dNTP Pools and Remodel One-Carbon Metabolism. *Cell Metab,* 23**,** 635-48.

NISHINO, I., SPINAZZOLA, A. & HIRANO, M. 1999. Thymidine phosphorylase gene mutations in MNGIE, a human mitochondrial disorder. *Science,* 283**,** 689-92.

NONNENMACHER, M. & WEBER, T. 2012. Intracellular transport of recombinant adeno-associated virus vectors. *Gene Ther,* 19**,** 649-58.

NURMINEN, A., FARNUM, G. A. & KAGUNI, L. S. 2017. Pathogenicity in POLG syndromes: DNA polymerase gamma pathogenicity prediction server and database. *BBA Clin,* 7**,** 147-156.

OSAWA, S., JUKES, T. H., WATANABE, K. & MUTO, A. 1992. Recent evidence for evolution of the genetic code. *Microbiol Rev,* 56**,** 229-64.

OSELLAME, L. D., BLACKER, T. S. & DUCHEN, M. R. 2012. Cellular and molecular mechanisms of mitochondrial function. *Best Pract Res Clin Endocrinol Metab,* 26**,** 711-23.

OSTERMAN, J. V., WADDELL, A. & APOSHIAN, H. V. 1970. DNA and gene therapy: uncoating of polyoma pseudovirus in mouse embryo cells. *Proc Natl Acad Sci U S A,* 67**,** 37-40.

PACK, D. W., HOFFMAN, A. S., PUN, S. & STAYTON, P. S. 2005. Design and development of polymers for gene delivery. *Nat Rev Drug Discov,* 4**,** 581-93.

PAGLIARINI, D. J., CALVO, S. E., CHANG, B., SHETH, S. A., VAFAI, S. B., ONG, S. E., WALFORD, G. A., SUGIANA, C., BONEH, A., CHEN, W. K., HILL, D. E., VIDAL, M., EVANS, J. G., THORBURN, D. R., CARR, S. A. & MOOTHA, V. K. 2008. A mitochondrial protein compendium elucidates complex I disease biology. *Cell,* 134**,** 112-23.

PAGLIARINI, D. J. & RUTTER, J. 2013. Hallmarks of a new era in mitochondrial biochemistry. *Genes Dev,* 27**,** 2615-27.

PALADE, G. E. 1953. An electron microscope study of the mitochondrial structure. *J Histochem Cytochem,* 1**,** 188-211.

PEARCE, S. F., REBELO-GUIOMAR, P., D'SOUZA, A. R., POWELL, C. A., VAN HAUTE, L. & MINCZUK, M. 2017. Regulation of Mammalian Mitochondrial Gene Expression: Recent Advances. *Trends Biochem Sci,* 42**,** 625-639.

PEREIRA, F., SOARES, P., CARNEIRO, J., PEREIRA, L., RICHARDS, M. B., SAMUELS, D. C. & AMORIM, A. 2008. Evidence for variable selective pressures at a large secondary structure of the human mitochondrial DNA control region. *Mol Biol Evol,* 25**,** 2759-70.

PFANNER, N., WARSCHEID, B. & WIEDEMANN, N. 2019. Mitochondrial proteins: from biogenesis to functional networks. *Nat Rev Mol Cell Biol,* 20**,** 267-284.

PHAN, L. M., YEUNG, S. C. & LEE, M. H. 2014. Cancer metabolic reprogramming: importance, main features, and potentials for precise targeted anti-cancer therapies. *Cancer Biol Med,* 11**,** 1-19.

PICKETT, S. J., GRADY, J. P., NG, Y. S., GORMAN, G. S., SCHAEFER, A. M., WILSON, I. J., CORDELL, H. J., TURNBULL, D. M., TAYLOR, R. W. & MCFARLAND, R. 2018. Phenotypic heterogeneity in m.3243A>G mitochondrial disease: The role of nuclear factors. *Ann Clin Transl Neurol,* 5**,** 333-345.

PICKLES, S., VIGIE, P. & YOULE, R. J. 2018. Mitophagy and Quality Control Mechanisms in Mitochondrial Maintenance. *Curr Biol,* 28**,** R170-R185.

PIECZENIK, S. R. & NEUSTADT, J. 2007. Mitochondrial dysfunction and molecular pathways of disease. *Exp Mol Pathol,* 83**,** 84-92.

PIRINEN, E., AURANEN, M., KHAN, N. A., BRILHANTE, V., URHO, N., PESSIA, A., HAKKARAINEN, A., ULLA HEINONEN, J. K., SCHMIDT, M. S., HAIMILAHTI, K., PIIRILA, P., LUNDBOM, N., TASKINEN, M. R., BRENNER, C., VELAGAPUDI, V., PIETILAINEN, K. H. & SUOMALAINEN, A. 2020. Niacin Cures Systemic NAD(+) Deficiency and Improves Muscle Performance in Adult-Onset Mitochondrial Myopathy. *Cell Metab,* 32**,** 144.

POMATTO, L. C., RAYNES, R. & DAVIES, K. J. 2017. The peroxisomal Lon protease LonP2 in aging and disease: functions and comparisons with mitochondrial Lon protease LonP1. *Biol Rev Camb Philos Soc,* 92**,** 739-753.

POSSE, V., AL-BEHADILI, A., UHLER, J. P., CLAUSEN, A. R., REYES, A., ZEVIANI, M., FALKENBERG, M. & GUSTAFSSON, C. M. 2019. RNase H1 directs origin-specific

initiation of DNA replication in human mitochondria. *PLoS Genet,* 15**,** e1007781.

POSSE, V., SHAHZAD, S., FALKENBERG, M., HALLBERG, B. M. & GUSTAFSSON, C. M. 2015. TEFM is a potent stimulator of mitochondrial transcription elongation in vitro. *Nucleic Acids Res,* 43**,** 2615-24.

PULICHERLA, N., SHEN, S., YADAV, S., DEBBINK, K., GOVINDASAMY, L., AGBANDJE-MCKENNA, M. & ASOKAN, A. 2011. Engineering liver-detargeted AAV9 vectors for cardiac and musculoskeletal gene transfer. *Mol Ther,* 19**,** 1070-8.

QU, J., YASUKAWA, T. & KANG, D. 2016. Suppression of mitochondrial transcription initiation complexes changes the balance of replication intermediates of mitochondrial DNA and reduces 7S DNA in cultured human cells. *J Biochem,* 160**,** 49-57.

QUINTANA, A., KRUSE, S. E., KAPUR, R. P., SANZ, E. & PALMITER, R. D. 2010. Complex I deficiency due to loss of Ndufs4 in the brain results in progressive encephalopathy resembling Leigh syndrome. *Proc Natl Acad Sci U S A,* 107**,** 10996-1001.

RAHMAN, S. & COPELAND, W. C. 2019. POLG-related disorders and their neurological manifestations. *Nat Rev Neurol,* 15**,** 40-52.

RAJAKULENDRAN, S., PITCEATHLY, R. D., TAANMAN, J. W., COSTELLO, H., SWEENEY, M. G., WOODWARD, C. E., JAUNMUKTANE, Z., HOLTON, J. L., JACQUES, T. S., HARDING, B. N., FRATTER, C., HANNA, M. G. & RAHMAN, S. 2016. A Clinical, Neuropathological and Genetic Study of Homozygous A467T POLG-Related Mitochondrial Disease. *PLoS One,* 11**,** e0145500.

RAN, F. A., HSU, P. D., LIN, C. Y., GOOTENBERG, J. S., KONERMANN, S., TREVINO, A. E., SCOTT, D. A., INOUE, A., MATOBA, S., ZHANG, Y. & ZHANG, F. 2013. Double nicking by RNA-guided CRISPR Cas9 for enhanced genome editing specificity. *Cell,* 154**,** 1380-9.

RATH, D., AMLINGER, L., RATH, A. & LUNDGREN, M. 2015. The CRISPR-Cas immune system: biology, mechanisms and applications. *Biochimie,* 117**,** 119-28.

REBELO-GUIOMAR, P., POWELL, C. A., VAN HAUTE, L. & MINCZUK, M. 2019. The mammalian mitochondrial epitranscriptome. *Biochim Biophys Acta Gene Regul Mech,* 1862**,** 429-446.

REYES, A., YASUKAWA, T., CLUETT, T. J. & HOLT, I. J. 2009. Analysis of mitochondrial DNA by two-dimensional agarose gel electrophoresis. *Methods Mol Biol,* 554**,** 15-35.

REYNAUD-DULAURIER, R., BENEGIAMO, G., MARROCCO, E., AL-TANNIR, R., SURACE, E. M., AUWERX, J. & DECRESSAC, M. 2020. Gene replacement therapy provides benefit in an adult mouse model of Leigh syndrome. *Brain,* 143**,** 1686-1696.

RINGEL, R., SOLOGUB, M., MOROZOV, Y. I., LITONIN, D., CRAMER, P. & TEMIAKOV, D. 2011. Structure of human mitochondrial RNA polymerase. *Nature,* 478**,** 269-73.

ROBBERSON, D. L. & CLAYTON, D. A. 1972. Replication of mitochondrial DNA in mouse L cells and their thymidine kinase - derivatives: displacement replication on a covalently-closed circular template. *Proc Natl Acad Sci U S A,* 69**,** 3810-4.

ROBBERSON, D. L., KASAMATSU, H. & VINOGRAD, J. 1972. Replication of mitochondrial DNA. Circular replicative intermediates in mouse L cells. *Proc Natl Acad Sci U S A,* 69**,** 737-41.

ROGERS, S. 1971. Gene therapy: a potentially invaluable aid to medicine and mankind. *Res Commun Chem Pathol Pharmacol,* 2**,** 587-600.

RUHANEN, H., BORRIE, S., SZABADKAI, G., TYYNISMAA, H., JONES, A. W., KANG, D., TAANMAN, J. W. & YASUKAWA, T. 2010. Mitochondrial single-stranded DNA binding protein is required for maintenance of mitochondrial DNA and 7S DNA but is not required for mitochondrial nucleoid organisation. *Biochim Biophys Acta,* 1803**,** 931-9.

RUSSELL, O. M., GORMAN, G. S., LIGHTOWLERS, R. N. & TURNBULL, D. M. 2020. Mitochondrial Diseases: Hope for the Future. *Cell,* 181**,** 168-188.

RUSSELL, S., BENNETT, J., WELLMAN, J. A., CHUNG, D. C., YU, Z. F., TILLMAN, A., WITTES, J., PAPPAS, J., ELCI, O., MCCAGUE, S., CROSS, D., MARSHALL, K. A., WALSHIRE, J., KEHOE, T. L., REICHERT, H., DAVIS, M., RAFFINI, L., GEORGE, L. A., HUDSON, F. P., DINGFIELD, L., ZHU, X., HALLER, J. A., SOHN, E. H., MAHAJAN, V. B., PFEIFER, W., WECKMANN, M., JOHNSON, C., GEWAILY, D., DRACK, A., STONE, E., WACHTEL, K., SIMONELLI, F., LEROY, B. P., WRIGHT, J. F., HIGH, K. A. & MAGUIRE, A. M. 2017. Efficacy and safety of voretigene neparvovec (AAV2-hRPE65v2) in patients with RPE65-mediated inherited retinal dystrophy: a randomised, controlled, open-label, phase 3 trial. *Lancet,* 390**,** 849-860.

SACCONE, C., PESOLE, G. & SBISA, E. 1991. The main regulatory region of mammalian mitochondrial DNA: structure-function model and evolutionary pattern. *J Mol Evol,* 33**,** 83-91.

SAGAN, L. 1967. On the origin of mitosing cells. *J Theor Biol,* 14**,** 255-74.

SANETO, R. P., LEE, I. C., KOENIG, M. K., BAO, X., WENG, S. W., NAVIAUX, R. K. & WONG, L. J. 2010. POLG DNA testing as an emerging standard of care before instituting valproic acid therapy for pediatric seizure disorders. *Seizure,* 19**,** 140-6.

SANGER, F., NICKLEN, S. & COULSON, A. R. 1977. DNA sequencing with chain-terminating inhibitors. *Proc Natl Acad Sci U S A,* 74**,** 5463-7.

SATOH, M. & KUROIWA, T. 1991. Organization of multiple nucleoids and DNA molecules in mitochondria of a human cell. *Exp Cell Res,* 196**,** 137-40.

SBISA, E., TANZARIELLO, F., REYES, A., PESOLE, G. & SACCONE, C. 1997. Mammalian mitochondrial D-loop region structural analysis: identification of new conserved sequences and their functional and evolutionary implications. *Gene,* 205**,** 125-40.

SHI, Y., DIERCKX, A., WANROOIJ, P. H., WANROOIJ, S., LARSSON, N. G., WILHELMSSON, L. M., FALKENBERG, M. & GUSTAFSSON, C. M. 2012. Mammalian transcription factor A is a core component of the mitochondrial transcription machinery. *Proc Natl Acad Sci U S A,* 109**,** 16510-5.

SHOSHAN-BARMATZ, V., DE PINTO, V., ZWECKSTETTER, M., RAVIV, Z., KEINAN, N. & ARBEL, N. 2010. VDAC, a multi-functional mitochondrial protein regulating cell life and death. *Mol Aspects Med,* 31**,** 227-85.

SICHERITZ-PONTEN, T., KURLAND, C. G. & ANDERSSON, S. G. 1998. A phylogenetic analysis of the cytochrome b and cytochrome c oxidase I genes supports an origin of mitochondria from within the Rickettsiaceae. *Biochim Biophys Acta,* 1365**,** 545-51.

SIEKEVITZ, P. 1957. Powerhouse of the Cell. *Scientific American*.

SILVA, M. F., AIRES, C. C., LUIS, P. B., RUITER, J. P., L, I. J., DURAN, M., WANDERS, R. J. & TAVARES DE ALMEIDA, I. 2008. Valproic acid metabolism and its effects on mitochondrial fatty acid oxidation: a review. *J Inherit Metab Dis,* 31**,** 205-16.

SIRRENBERG, C., BAUER, M. F., GUIARD, B., NEUPERT, W. & BRUNNER, M. 1996. Import of carrier proteins into the mitochondrial inner membrane mediated by Tim22. *Nature,* 384**,** 582-5.

SJOSTRAND, F. S. 1953. Electron microscopy of mitochondria and cytoplasmic double membranes. *Nature,* 171**,** 30-2.

SKLADAL, D., HALLIDAY, J. & THORBURN, D. R. 2003. Minimum birth prevalence of mitochondrial respiratory chain disorders in children. *Brain,* 126**,** 1905-12.

SLONE, J. & HUANG, T. 2020. The special considerations of gene therapy for mitochondrial diseases. *NPJ Genom Med,* 5**,** 7.

STARKOV, A. A. 2008. The role of mitochondria in reactive oxygen species metabolism and signaling. *Ann N Y Acad Sci,* 1147**,** 37-52.

STENTON, S. L. & PROKISCH, H. 2018. Advancing genomic approaches to the molecular diagnosis of mitochondrial disease. *Essays Biochem,* 62**,** 399-408.

STENTON, S. L. & PROKISCH, H. 2020. Genetics of mitochondrial diseases: Identifying mutations to help diagnosis. *EBioMedicine,* 56**,** 102784.

STEWART, J. B. & CHINNERY, P. F. 2021. Extreme heterogeneity of human mitochondrial DNA from organelles to populations. *Nat Rev Genet,* 22**,** 106-118.

STEWART, J. B. & LARSSON, N. G. 2014. Keeping mtDNA in shape between generations. *PLoS Genet,* 10**,** e1004670.

STEWART, J. D., HORVATH, R., BARUFFINI, E., FERRERO, I., BULST, S., WATKINS, P. B., FONTANA, R. J., DAY, C. P. & CHINNERY, P. F. 2010. Polymerase gamma gene POLG determines the risk of sodium valproate-induced liver toxicity. *Hepatology,* 52**,** 1791-6.

STEWART, J. D., SCHOELER, S., SITARZ, K. S., HORVATH, R., HALLMANN, K., PYLE, A., YU-WAI-MAN, P., TAYLOR, R. W., SAMUELS, D. C., KUNZ, W. S. & CHINNERY, P. F. 2011. POLG mutations cause decreased mitochondrial DNA repopulation rates following induced depletion in human fibroblasts. *Biochim Biophys Acta,* 1812**,** 321-5.

SZCZEPANOWSKA, K., SENFT, K., HEIDLER, J., HERHOLZ, M., KUKAT, A., HOHNE, M. N., HOFSETZ, E., BECKER, C., KASPAR, S., GIESE, H., ZWICKER, K., GUERRERO-CASTILLO, S., BAUMANN, L., KAUPPILA, J., RUMYANTSEVA, A., MULLER, S., FRESE, C. K., BRANDT, U., RIEMER, J., WITTIG, I. & TRIFUNOVIC, A. 2020. A salvage pathway maintains highly functional respiratory complex I. *Nat Commun,* 11**,** 1643.

SZCZEPANOWSKA, K. & TRIFUNOVIC, A. 2021. Mitochondrial matrix proteases: quality control and beyond. *FEBS J*.

TAIT, S. W. & GREEN, D. R. 2010. Mitochondria and cell death: outer membrane permeabilization and beyond. *Nat Rev Mol Cell Biol,* 11**,** 621-32.

TATSUTA, T. 2009. Protein quality control in mitochondria. *J Biochem,* 146**,** 455-61.

TATSUTA, T. & LANGER, T. 2008. Quality control of mitochondria: protection against neurodegeneration and ageing. *EMBO J,* 27**,** 306-14.

TATUCH, Y., CHRISTODOULOU, J., FEIGENBAUM, A., CLARKE, J. T., WHERRET, J., SMITH, C., RUDD, N., PETROVA-BENEDICT, R. & ROBINSON, B. H. 1992. Heteroplasmic mtDNA mutation (T----G) at 8993 can cause Leigh disease when the percentage of abnormal mtDNA is high. *Am J Hum Genet,* 50**,** 852-8.

TERZIOGLU, M., RUZZENENTE, B., HARMEL, J., MOURIER, A., JEMT, E., LOPEZ, M. D., KUKAT, C., STEWART, J. B., WIBOM, R., MEHARG, C., HABERMANN, B., FALKENBERG, M., GUSTAFSSON, C. M., PARK, C. B. & LARSSON, N. G. 2013. MTERF1 binds mtDNA to prevent transcriptional interference at the light-strand promoter but is dispensable for rRNA gene transcription regulation. *Cell Metab,* 17**,** 618-26.

THORBURN, D. R. 2004. Mitochondrial disorders: prevalence, myths and advances. *J Inherit Metab Dis,* 27**,** 349-62.

TILOKANI, L., NAGASHIMA, S., PAUPE, V. & PRUDENT, J. 2018. Mitochondrial dynamics: overview of molecular mechanisms. *Essays Biochem,* 62**,** 341-360.

TRIFUNOVIC, A., WREDENBERG, A., FALKENBERG, M., SPELBRINK, J. N., ROVIO, A. T., BRUDER, C. E., BOHLOOLY, Y. M., GIDLOF, S., OLDFORS, A., WIBOM, R., TORNELL, J., JACOBS, H. T. & LARSSON, N. G. 2004. Premature ageing in mice expressing defective mitochondrial DNA polymerase. *Nature,* 429**,** 417-23.

TYYNISMAA, H., SEMBONGI, H., BOKORI-BROWN, M., GRANYCOME, C., ASHLEY, N., POULTON, J., JALANKO, A., SPELBRINK, J. N., HOLT, I. J. & SUOMALAINEN, A. 2004. Twinkle helicase is essential for mtDNA maintenance and regulates mtDNA copy number. *Hum Mol Genet,* 13**,** 3219-27.

TZOULIS, C., ENGELSEN, B. A., TELSTAD, W., AASLY, J., ZEVIANI, M., WINTERTHUN, S., FERRARI, G., AARSETH, J. H. & BINDOFF, L. A. 2006. The spectrum of clinical disease caused by the A467T and W748S POLG mutations: a study of 26 cases. *Brain,* 129**,** 1685-92.

TZOULIS, C., TRAN, G. T., COXHEAD, J., BERTELSEN, B., LILLENG, P. K., BALAFKAN, N., PAYNE, B., MILETIC, H., CHINNERY, P. F. & BINDOFF, L. A. 2014. Molecular pathogenesis of polymerase gamma-related neurodegeneration. *Ann Neurol,* 76**,** 66-81.

UHLER, J. P. & FALKENBERG, M. 2015. Primer removal during mammalian mitochondrial DNA replication. *DNA Repair (Amst),* 34**,** 28-38.

UHLER, J. P., THORN, C., NICHOLLS, T. J., MATIC, S., MILENKOVIC, D., GUSTAFSSON, C. M. & FALKENBERG, M. 2016. MGME1 processes flaps into ligatable nicks in concert with DNA polymerase gamma during mtDNA replication. *Nucleic Acids Res,* 44**,** 5861-71.

UUSIMAA, J., GOWDA, V., MCSHANE, A., SMITH, C., EVANS, J., SHRIER, A., NARASIMHAN, M., O'ROURKE, A., RAJABALLY, Y., HEDDERLY, T., COWAN, F., FRATTER, C. & POULTON, J. 2013. Prospective study of POLG mutations presenting in children with intractable epilepsy: prevalence and clinical features. *Epilepsia,* 54**,** 1002-11.

VAFAI, S. B. & MOOTHA, V. K. 2012. Mitochondrial disorders as windows into an ancient organelle. *Nature,* 491**,** 374-83.

VAN DEN AMEELE, J., LI, A. Y. Z., MA, H. & CHINNERY, P. F. 2020. Mitochondrial heteroplasmy beyond the oocyte bottleneck. *Semin Cell Dev Biol,* 97**,** 156-166.

VAN GOETHEM, G., DERMAUT, B., LOFGREN, A., MARTIN, J. J. & VAN BROECKHOVEN, C. 2001. Mutation of POLG is associated with progressive external ophthalmoplegia characterized by mtDNA deletions. *Nat Genet,* 28**,** 211-2.

VAN GOETHEM, G., LOFGREN, A., DERMAUT, B., CEUTERICK, C., MARTIN, J. J. & VAN BROECKHOVEN, C. 2003. Digenic progressive external ophthalmoplegia in a sporadic patient: recessive mutations in POLG and C10orf2/Twinkle. *Hum Mutat,* 22**,** 175-6.

VENKATESH, S., LEE, J., SINGH, K., LEE, I. & SUZUKI, C. K. 2012. Multitasking in the mitochondrion by the ATP-dependent Lon protease. *Biochim Biophys Acta,* 1823**,** 56-66.

VISCOMI, C., BOTTANI, E., CIVILETTO, G., CERUTTI, R., MOGGIO, M., FAGIOLARI, G., SCHON, E. A., LAMPERTI, C. & ZEVIANI, M. 2011. In vivo correction of COX deficiency by activation of the AMPK/PGC-1alpha axis. *Cell Metab,* 14**,** 80-90.

VISCOMI, C. & ZEVIANI, M. 2017. MtDNA-maintenance defects: syndromes and genes. *J Inherit Metab Dis,* 40**,** 587-599.

VON HEIJNE, G. 1986. Why mitochondria need a genome. *FEBS Lett,* 198**,** 1-4.

WAI, T., AO, A., ZHANG, X., CYR, D., DUFORT, D. & SHOUBRIDGE, E. A. 2010. The role of mitochondrial DNA copy number in mammalian fertility. *Biol Reprod,* 83**,** 52-62.

WALBERG, M. W. & CLAYTON, D. A. 1981. Sequence and properties of the human KB cell and mouse L cell D-loop regions of mitochondrial DNA. *Nucleic Acids Res,* 9**,** 5411-21.

WALKER, J. E. 2013. The ATP synthase: the understood, the uncertain and the unknown. *Biochem Soc Trans,* 41**,** 1-16.

WANG, D., TAI, P. W. L. & GAO, G. 2019. Adeno-associated virus vector as a platform for gene therapy delivery. *Nat Rev Drug Discov,* 18**,** 358-378.

WANG, N., GOTTESMAN, S., WILLINGHAM, M. C., GOTTESMAN, M. M. & MAURIZI, M. R. 1993. A human mitochondrial ATP-dependent protease that is highly homologous to bacterial Lon protease. *Proc Natl Acad Sci U S A,* 90**,** 11247-51.

WANG, N., MAURIZI, M. R., EMMERT-BUCK, L. & GOTTESMAN, M. M. 1994. Synthesis, processing, and localization of human Lon protease. *J Biol Chem,* 269**,** 29308-13.

WANROOIJ, P. H., UHLER, J. P., SHI, Y., WESTERLUND, F., FALKENBERG, M. & GUSTAFSSON, C. M. 2012. A hybrid G-quadruplex structure formed between RNA and DNA explains the extraordinary stability of the mitochondrial R-loop. *Nucleic Acids Res,* 40**,** 10334-44.

WANROOIJ, S. & FALKENBERG, M. 2010. The human mitochondrial replication fork in health and disease. *Biochim Biophys Acta,* 1797**,** 1378-88.

WANROOIJ, S., FUSTE, J. M., FARGE, G., SHI, Y., GUSTAFSSON, C. M. & FALKENBERG, M. 2008. Human mitochondrial RNA polymerase primes lagging-strand DNA synthesis in vitro. *Proc Natl Acad Sci U S A,* 105**,** 11122-7.

WARRINGTON, K. H., JR., GORBATYUK, O. S., HARRISON, J. K., OPIE, S. R., ZOLOTUKHIN, S. & MUZYCZKA, N. 2004. Adeno-associated virus type 2 VP2 capsid protein is nonessential and can tolerate large peptide insertions at its N terminus. *J Virol,* 78**,** 6595-609.

WEI, W. & CHINNERY, P. F. 2020. Inheritance of mitochondrial DNA in humans: implications for rare and common diseases. *J Intern Med,* 287**,** 634-644.

WELLS, R. D. & LARSON, J. E. 1972. Buoyant density studies on natural and synthetic deoxyribonucleic acids in neutral and alkaline solutions. *J Biol Chem,* 247**,** 3405-9.

WIEDEMANN, N., FRAZIER, A. E. & PFANNER, N. 2004. The protein import machinery of mitochondria. *J Biol Chem,* 279**,** 14473-6.

WIEDEMANN, N. & PFANNER, N. 2017. Mitochondrial Machineries for Protein Import and Assembly. *Annu Rev Biochem,* 86**,** 685-714.

XU, B. & CLAYTON, D. A. 1995. A persistent RNA-DNA hybrid is formed during transcription at a phylogenetically conserved mitochondrial DNA sequence. *Mol Cell Biol,* 15**,** 580-9.

YANG, D., OYAIZU, Y., OYAIZU, H., OLSEN, G. J. & WOESE, C. R. 1985. Mitochondrial origins. *Proc Natl Acad Sci U S A,* 82**,** 4443-7.

YANG, L., SLONE, J., LI, Z., LOU, X., HU, Y. C., QUEME, L. F., JANKOWSKI, M. P. & HUANG, T. 2020. Systemic administration of AAV-Slc25a46 mitigates mitochondrial neuropathy in Slc25a46-/- mice. *Hum Mol Genet,* 29**,** 649-661.

YASUKAWA, T., REYES, A., CLUETT, T. J., YANG, M. Y., BOWMAKER, M., JACOBS, H. T. & HOLT, I. J. 2006. Replication of vertebrate mitochondrial DNA entails transient ribonucleotide incorporation throughout the lagging strand. *EMBO J,* 25**,** 5358-71.

YIN, H., KANASTY, R. L., ELTOUKHY, A. A., VEGAS, A. J., DORKIN, J. R. & ANDERSON, D. G. 2014. Non-viral vectors for gene-based therapy. *Nat Rev Genet,* 15**,** 541-55.

YOSHIKAWA, S., MURAMOTO, K. & SHINZAWA-ITOH, K. 2011. Proton-pumping mechanism of cytochrome C oxidase. *Annu Rev Biophys,* 40**,** 205-23.

YOSHIKAWA, S. & SHIMADA, A. 2015. Reaction mechanism of cytochrome c oxidase. *Chem Rev,* 115**,** 1936-89.

YOUNG, M. J. 2017. Off-Target Effects of Drugs that Disrupt Human Mitochondrial DNA Maintenance. *Front Mol Biosci,* 4**,** 74.

YU, A. Y. & HOURY, W. A. 2007. ClpP: a distinctive family of cylindrical energy-dependent serine proteases. *FEBS Lett,* 581**,** 3749-57.

YU-WAI-MAN, P., NEWMAN, N. J., CARELLI, V., MOSTER, M. L., BIOUSSE, V., SADUN, A. A., KLOPSTOCK, T., VIGNAL-CLERMONT, C., SERGOTT, R. C., RUDOLPH, G., LA MORGIA, C., KARANJIA, R., TAIEL, M., BLOUIN, L., BURGUIERE, P., SMITS, G., CHEVALIER, C., MASONSON, H., SALERMO, Y., KATZ, B., PICAUD, S., CALKINS, D. J. & SAHEL, J. A. 2020. Bilateral visual improvement with unilateral gene therapy injection for Leber hereditary optic neuropathy. *Sci Transl Med,* 12.

ZEVIANI, M., SERVIDEI, S., GELLERA, C., BERTINI, E., DIMAURO, S. & DIDONATO, S. 1989. An autosomal dominant disorder with multiple deletions of mitochondrial DNA starting at the D-loop region. *Nature,* 339**,** 309-11.

ZEVIANI, M., SPINAZZOLA, A. & CARELLI, V. 2003. Nuclear genes in mitochondrial disorders. *Curr Opin Genet Dev,* 13**,** 262-70.

ZURITA RENDON, O. & SHOUBRIDGE, E. A. 2018. LONP1 Is Required for Maturation of a Subset of Mitochondrial Proteins, and Its Loss Elicits an Integrated Stress Response. *Mol Cell Biol,* 38.